Novel XFEM Variable Strain Damage Model for Predicting Fracture in Small-scale SENT and Full-scale Pipeline Fracture Tests

by

Meng Lin

A thesis submitted in partial fulfillment of the requirements for the degree of

Doctor of Philosophy

in

Structural Engineering

Department of Civil and Environmental Engineering
University of Alberta

Abstract

Of all the common integrity threats of steel pipelines, cracking is the most dangerous and potentially resulting in the immediate loss of pressure containment capacity. Industry pipeline operators should ensure that the tensile train capacity (TSC) of welded pipeline exceeds the longitudinal tensile strains caused by substantial bending and/or tension due to external loads such as the seasonal ground temperature difference and soil differential movement. The tearing resistance curve (R-curve), such as the J-integral against the crack extension, quantifying the material's inherent resistance to fracture, plays a critical role in predicting the TSC of welded pipeline. The R-curves of a pipeline material have recently been recommended to be measured from small-scale single edge notched tension (SENT) specimens, which can produce a relatively lower level of crack tip constraint similar to that of full-scale circumferentially cracked pipe specimens subjected to tension or even if it is globally loaded in bending.

The extended finite element method (XFEM) has been increasingly implemented to predict the TSC of welded pipeline as well as the R-curves of SENT tests to assist with the pipeline integrity assessment. This method provides a robust approach allowing discontinuities such as cracks to be freely laid within the finite elements by introducing special enrichment functions. It alleviates the requirement for remeshing during crack propagation which is generally challenging to implement and computationally expensive in the conventional finite element method (FEM). The XFEM-based cohesive segments approach available in commercial finite element software Abaqus has been employed in predicting the crack initiation and propagation of pipelines since the last decade, but current damage criteria have not been well calibrated. Available criteria assume a fixed critical stress or strain value as the damage initiation, such as the maximum principal stress (Maxps) and

maximum principal strain (Maxpe) damage criterion. Once an initiation criterion is met, the material cohesive stiffness is degraded with a specific damage evolution law till eventual failure, which can be simply characterized by the critical fracture energy release rate (G_c). However, the fracture behaviour predicted may be inaccurate due to its simplicity by ignoring important factors such as crack-tip constraint, which has a profound effect on fracture resistance.

This doctoral thesis developed a novel XFEM variable strain-based damage criterion by introducing a variable critical strain profile as a function of stress triaxiality and Lode angle parameters accounting for crack-tip constraint. The new criterion was derived from the strain-based modified Mohr-Coulomb (MMC) fracture criterion developed for uncracked specimens and was applied to the small-scale SENT and full-scale pipeline fracture tests on cracked specimens. This criterion was implemented using Fortran programmed in Abaqus user subroutine-UDMGINI, and calibrated through models based on experimental data. The TSC of circumferentially surfaced-cracked X52 pipe specimens in full-scale pressurized tests and the J-R curves of X100 pipe specimens in small-scale SENT tests were well predicted with novel XFEM damage criterion. An optimal set of damage parameters (c_1 = 0.1, c_2 = 1.9, c_3 = 0.9, c_4 = 1, and G_c =200 N/mm) was calibrated specific to X52 with a given strain hardening exponent (n = 0.119) through 8 full-scale simulations based on experimental data of force against crack mouth opening displacement (CMOD) and end plate rotation, tensile strains along the pipe length at failure and fracture surface appearances. An optimal set of damage parameters (c_1 = 0.03, c_2 = 1.9, c_3 = 0.9, c_4 = 1, and G_c = 100 N/mm) was calibrated specific to X100 with a given strain hardening exponent (n = 0.0923) through 4 SENT simulations based on experimental data of force against CMOD and J-R curve. The effect of crack tip simulation using notch or planar crack and the differences of numerical predictions adopting fixed Maxps, fixed Maxpe or novel variable strain damage initiation criterion

were carefully investigated in both X52 full-scale and X100 SENT models.

This work is the first to couple XFEM with strain-based modified Mohr-Coulomb fracture criterion developed from uncracked specimens into full-scale and small-scale models of cracked specimens and validated from experiments. This work attempts to unify the classical fracture mechanics assuming a pre-existing crack and damage mechanics of uncracked bodies to form a unified theory in predicting fracture.

Preface

All the research work presented for this thesis forms part of a research collaboration between the University of Alberta and Enbridge Inc. and TC Energy Corporation with Professor Dr. Samer Adeeb being the lead collaborator at the University of Alberta and various industry professionals responsible for facilitation and acquisition of research funding.

All chapters in this doctoral thesis are all my original work and include appropriate citations of references as required. The Chapters 3 to 5 are derived from either conference proceedings, journal publications or research articles intended for publication. Chapter 3 is derived from a journal publication [1]: M. Lin, S. Agbo, D.-M. Duan, J.J.R. Cheng, S. Adeeb, Simulation of crack propagation in API 5L X52 pressurized pipes using XFEM-based cohesive segment approach, Journal of Pipeline Systems Engineering and Practice. 11 (2020) 04020009. https://doi.org/10.1061/(asce)ps.1949-1204.0000444. Chapter 4 is derived from a conference publication [2]: M. Lin, Y. Li, M. Salem, J.J.R. Cheng, S. Adeeb, M. Kainat, A parametric study of variable crack initiation criterion in XFEM on pipeline steel, in: Pressure Vessels and Piping Conference Volume 6: Materials and Fabrication, American Society of Mechanical Engineers (ASME), Virtual, Online, 2020. https://doi.org/10.1115/PVP2020-21664. Chapter 5 are derived from two research articles with one submitted for publication in 2021 Technology for Future and Aging Pipelines Conference [3] (under review), and the other prepared to be submitted for a journal - Engineering Fracture Mechanics.

I was the lead investigator for all the research conducted herein and, therefore, responsible for concept formation, data collection and analysis, and manuscript composition. Being the supervisory author, Dr. Samer Adeeb was involved in concept improvement and manuscript

editing. All other co-authors provided extensive and resourceful technical input for methodology formulation and result validation.

M. Lin

Dedicated with infinite love to my dearest parents:

Yujin Lin and Dagang Xue

My academic journey would not have been such successful without your unconditional love, understanding and support throughout my life.

Acknowledgements

First and foremost, my deepest gratitude goes to my exceptional supervisor and life mentor, Professor Samer Adeeb, for his unconditional and endless motivation, patience, guidance, support and friendship throughout my whole academic and professional journey at the University of Alberta. To date he has supervised me for a total of 9 years including my master's study, research assistant working experience, and this doctoral program. I am extremely grateful to his continuous encouragement giving me confidence and optimism, consideration and understanding in dealing with my difficult emotions, and share of his rich life experiences and expertise to help me succeed. He is definitely the person who has inspired my passion to research, shaped my rigorous work habits, and promoted my personal and professional growth.

My sincere appreciation also goes to additional members of my doctoral supervisory committee, Dr. J. J. Roger Cheng and Dr. Yong Li. Their invaluable insight and knowledge, abundant engineering experience, and innovative thinking never cease to amaze me. My heartfelt appreciation is extended to my external examiner, Dr. Xin Wang from Carleton University, for his investment of time and professional feedback advice to help this doctoral thesis in achieving a higher quality. Further thanks to Dr. Lindsey Westover, Dr. Ali Imanpour, Dr. Ben Jar, Dr. Ying-Hei Chui, and other professors who have imparted knowledge and contributed to my academic accomplishments.

I wish to express my gratitude to my colleagues in C-FER Technologies with the deepest gratitude going to my former manager Dr. Smitha Koduru who consistently support me to pursue my PhD during my employment and provide my intelligent advice through the industry perspectives. As a talented and successful female engineer, she is my role model.

Last but not least, I would like to acknowledge all my caring friends at the University of Alberta. I only list the names below for their extensive collaborative supports throughout my doctoral program but if you are reading this as my friend, you definitely have the right to be included in the list: Liying Huang, Xinfang Zhang, Mohammad Salem, Sylvester Agbo, Allan Okodi and Qipei Mei.

Table of Contents

List of Tables

List of Figures

List of Abbreviations

CMOD	Crack mouth opening displacement
$CMOD_{critical}$	CMOD at the point of time when the applied load is almost constant but CMOD increases sharply, which is simply represented by the time when the load reaches 98% of the maximum applied load in a full-scale test and model.
$CMOD_{failure}$	CMOD at failure when the water starts to seep out of the crack in a full-scale test or the crack tip (or crack tip element damage) reaches the inner surface (or innermost element) of pipe in a full-scale model
$CMOD_{pl}$	Plastic part of CMOD of SENT specimen
CTOD	crack-tip opening displacement
CZM	cohesive zone model
DIC	digital image correlation
FEM	finite element method
HAZ	heat-affected zone
Maxpe	maximum principal strain
Maxps	maximum principal stress
NPS	nominal pipe size
PEEQ	equivalent plastic strain
SENT	single edge notched tension test
SMYS	specified minimum yield strength

STATUSXFEM	status of the enriched element, ranging from 0 (no damage) to 1 (fully damaged), and the value between 0 and 1 indicates the enriched element is partially damaged
TSC	tensile strain capacity
TSL	traction–separation law
XFEM	extended finite element method

List of Symbols

a	crack size of SENT specimen
$a_{(i)}$	crack size at i_{th} unloading of SENT specimen
a_0	original crack size of SENT specimen
Δa	crack extension of SENT specimen
A	strength coefficient
A_{pl}	plastic area under the SENT load-CMOD curve
B	thickness of SENT specimen
BCE	normalized CMOD compliance, where B is plain-sided SENT specimen's thickness or side-grooved SENT specimen effective thickness $B-(B-B_N)^2/B$
B_N	net thickness of SENT specimen
c_1, c_2, c_3 and c_4	damage parameters in novel XFEM damage initiation criterion
$C_{(i)}$	CMOD compliance at i_{th} unloading which is equivalent to the inverse of the slope of SENT load-CMOD curve
D	pipe outer diameter
E	young's modulus or modulus of elasticity
G_c	critical fracture energy release rate
H	span between grips of SENT specimen
J	J-integral
J_{el}	elastic part of J-integral
J_{pl}	plastic part of J-integral

K	stress intensity factor
n	strain hardening exponent
p	hydrostatic pressure
q	von Mises stress
r	third stress invariant
t	pipe wall thickness
t_x, ϕ_x, Ψ_x	coefficients in J-integral equations for SENT specimen
T_0 or T_{max}	cohesive strength or maximum cohesive traction
T_n	cohesive traction
W	width of SENT specimen
$\gamma_{LLD(i)}$, $\eta_{CMOD(i)}$	factors in J-integral equations for SENT specimen
$\eta_{LLD(i)}$, $\eta'_{LLD(i)}$	
Γ_0	cohesive energy
δ_0 or δ_c	complete surface separation
δ_n	surface separation
$\varepsilon_{0.5L}$	tensile strain measured at a quarter of the pipe length ($1/4 \times 2L = 0.5L$) away from the end plate at 90 degree intervals around the pipe circumference where $2L$ is the total pipe length in a full-scale test and model
ε_{avg}	averaged tensile strain measured from the outer surface along the pipe length and at an angle of 0 degree from the crack, in a range from 10% to 40% of pipe length ($0.2L \sim 0.8L$) in both sides away

	from the crack (185 mm to 730 mm away from the crack for tests/models 1-4; 120 mm to 490 mm away from the crack for tests/models 5-8) in a full-scale test and model
$\bar{\varepsilon}_f$	equivalent strain at the point of fracture
ε_{maxp}	maximum principal strain
ε^o_{maxp}	maximum allowable principal strain
η	stress triaxiality parameter
$\bar{\theta}$	Load angle parameter or normalized Lode angle
ν	poisson's ratio
ξ	normalized third deviatoric stress invariant
σ_{maxps}	maximum principal stress
σ_n	normal stress
σ_y	yield strength
σ_u	ultimate tensile strength
τ	shear stress

1. Introduction

1.1 Background

Pipeline systems in transporting the energy products, such as natural gas and petroleum, are commonly made of low carbon steel, which is an alloy primarily composed of iron (98-99% iron) and small percentages of alloying elements including carbon (0.1-0.28% by weight), manganese, phosphorus, sulfur, vanadium, niobium, and titanium, silicon, to increase the strength, toughness, and hardness of steel [4,5]. The American Petroleum Institute specification API 5L provides two product specification levels, PSL 1 (standard quality) and PSL 2 (additional mandatory requirements), for the manufacture of seamless and welded steel pipes, covering multiple steel grades, designated as Grade A, Grade B, Grade X42 to X120 [4]. The digit numbers following the letter 'X' indicates the specified minimum yield strength (SMYS) expressed in ksi (kilopound per square inch) of pipe produced to this grade. Tracking back the history of manufacturing of pipelines, it can be categorized by vintage and modern pipelines. At present, the vintage pipelines (no longer manufactured but still exist), may generally refer to those manufactured from 1950 through 1970, before modern manufacturing and testing processes were employed as early as 1950s. For example, the vintage pipelines' chemical composition were not measured explicitly other than major elements [6]; vintage pipelines may contain some manufacturing-related anomalies, e.g., silver-type flaw, which were not treated as integrity threats [7]; only pieces of vintage pipes were tested in hydrostatic testing[1] to 90% of their maximum operating pressure, while all new constructed modern pipes were tested in

[1] Hydrostatic testing refers to pressure tests to validate the integrity of a newly constructed or existing pipeline for strength and leakage, involving filling the pipeline with water, and pumping and maintaining the test pressure to a level higher than the maximum operating pressure over a specific amount of time without leaking.

hydrostatic testing to 125% of their maximum operating pressure by late 1960s [5]; the longitudinal seams of vintage pipelines were made with old manufacturing processes which had been discontinued in 1960s, e.g, furnace butt-welding, furnace lap-welding, low frequency electric-resistance-welding (ERW), electric flash-welding (EFW), single-submerged-arc welding, while the modern pipelines' seams were made with high frequency ERW and double-submerged-arc-welding [5,8].

Of all the common integrity threats for steel pipelines, cracking is the most dangerous and potentially resulting in the immediate loss of pressure containment capacity. If the longitudinal cracking occurs in a pipeline, the burst pressure plays a critical role in identifying the limits on the operating pressure that the operator needs to maintain. In severe cases, rupture rather than leaking can occur resulting in a devastating failure, and the pressure capacity is significantly affected by the crack length. Such situations are found frequently in a pipeline in which the crack is developed within a dent, commonly known as a dent-crack defect, and often lead to the need for replacement of the affected pipe segment [9]. At present, the most common analytical models in the literature for predicting the burst pressure of longitudinally cracked pipelines are Battelle model [10], CorLAS^{TM} model [11], and the failure assessment diagram (FAD) methodologies recommended by British nuclear industry's R6 procedure [12,13], British Standard BS7910 [14], and API-579/ASME FFS-1 [15]. The Battelle model (or called modified log-secant model or NG-18 equation) is a semi-empirical model evaluating failure by plastic collapse. CorLAS^{TM} (Corrosion Life Assessment Software) is a simplified J-integral based fracture model based on flat plate solution with effective-area method. The FAD evaluates the independent failure by brittle fracture or plastic collapse and combine the evaluation graphically to represent the mixed failure, and thus a limit curve of toughness-strength controlled failure is demonstrated. However, there are no agreed upon guidelines for predicting burst pressures of pipelines containing cracks with any other anomalies.

If circumferential cracking occurs in a pipeline, the longitudinal tensile strain capacity (TSC) of girth welds plays a critical role in pipelines integrity assessments. Due to the presence of inevitable welding flaws, girth welds including the heat-affected zones (HAZ) form the weakest link in pipelines resisting longitudinal tension. Pipeline operators should ensure that the TSC is higher than the longitudinal strains caused by substantial bending and/or tension due to external loads such as the seasonal ground temperature difference and soil differential movement. The only Canadian code-based equation (Rupture, Tier 2 approach) proposed in Canadian Standard Association CSA Z662-11 [16] in predicting the longitudinal tensile strain capacity of a circumferentially cracked pipeline has been removed in the revision CSA Z662-15 [17], because it was only limited to high strength steel pipes and inaccurately neglected the effect of internal pressure. Instead, the revision guides to adopt proven methods validated from physical tests. Alternatively, the North American pipeline industry has developed various empirical tensile strain models, such as the PRCI-CRES model developed by Pipeline Research Council International (PRCI) and Center for Reliable Energy Systems (CRES) which is applicable for pipeline grades from X65 to X100 [18–24], and the ExxonMobil model that is applicable for grades from X60 to X80 [25–27]. All these models were developed and validated for modern pipelines, although the PRCI-CRES model was extended to vintage girth welds by Wang et al. [28] last year based on limited eight curved wide plate (CWP) tests. There lacks an assessment model targeting the vintage pipelines, such as the vintage X52 steel which is still present in existing pipeline systems and is ubiquitous in the North American pipeline network. According to data published by Pipeline and Hazardous Materials Safety Administration (PHMSA), vintage pipelines account for almost half portion of total transmission pipelines in the United States. The 2020 records indicates that 41.7% and 54.5% of total pipeline mileages were constructed before 1970 for hazardous liquid pipelines and gas transmission pipelines respectively [29]. At present, the integrity decisions for either longitudinally and

circumferentially cracked pipelines are either based on engineering experience–making the decisions inconsistent–or based on numerical tools.

Current numerical tools are mostly based on the conventional finite element method (FEM), which is generally challenging to implement and computationally expensive, especially in complex geometric and three-dimensional domains. This method requires a considerable mesh refinement in the near tip field to adequately capture the singular asymptotic fields. Additionally, it requires adaptive mesh refinement requiring the mesh to continuously conform to the geometric discontinuities as the crack propagates along the predefined path [30,31]. The mesh contribution and maintenance are significant for the success of FEM. Due to the complexity and inefficiency associated with meshing the crack surfaces, numerous researchers have been pursuing potentially more simplified methods. The extended finite element method (XFEM) was proposed in 1999 by Belytschko and collaborators [32,33] based on the partition of unity method of Melenk and Babuska [34]. The finite element analysis commercial software Abaqus has a variety of fracture mechanics capabilities including the XFEM supported in Abaqus/Standard which employs the implicit integration scheme to solve static and low-speed dynamic events [30]. It provides a robust approach to incorporate the discontinuities and discontinuous solution field into standard finite element functions by introducing special enrichment functions in conjunction with additional degrees of freedom. It enables both stationary crack analysis and propagating or moving crack analysis. The propagating crack analysis can be performed by XFEM-based cohesive segments method, i.e., cohesive zone model (CZM) within XFEM framework, which allows the crack initiation and propagation along an arbitrary solution-dependent path [30]. The phantom nodes are adopted by Belytschko and collaborators [35] to represent the discontinuities of cracked elements, based on the superposed element formulation of Hansbo and Hansbo [36]. Once a crack cuts through an enriched element, the phantom nodes and their superposed original real nodes move apart. The

level set method offers a way to track the motion of interfaces and was used to model the arbitrary crack propagation path without remeshing, in which the crack surface and crack front are determined by two level set signed distance functions [30,31]. The crack propagation is freely laid within finite element (interior) in XFEM and not tied to element boundaries in FEM which is strongly mesh dependent [31]. The reduced meshing effort makes XFEM more efficient than FEM in solving discontinuous problems.

1.2 Problem Statement

Although the XFEM-based cohesive segments method has been increasingly employed in the crack propagation analysis in pipelines since the last decade, current damage criteria have not been well calibrated. Available damage criteria within the XFEM framework typically assume a fixed critical stress or strain value as the damage initiation, such as those built-in procedure of Abaqus/Standard [30]. Once an initiation criterion is satisfied, the material cohesive stiffness is degraded following a specific damage evolution law till eventual failure. The built-in damaged traction-separation response follows either a linearly or exponentially softening model based on either the effective displacement at failure or the energy dissipated due to fracture i.e., the critical fracture energy release rate G_c which is the work needed to create an extended unit area of crack surfaces equivalent to the area under the traction-separation curve.

The first step of my doctoral research is to introduce XFEM as a tool for predicting the TSC of pipeline, validate the XFEM-based cohesive segment method available Abaqus/Standard and evaluate the the built-in damage criterion. This work was included in Chapter 0 where eight full-scale models were developed to reproduce eight full-scale tests [37] on circumferentially surface-cracked X52 pipe specimens subjected to internal pressure and external eccentric tension. A fixed damage initiation criterion with critical maximum principal stress (Maxps) of 750 MPa and fracture energy release rate (G_C) of 900 N/mm was adopted. Although this work

successfully predicted similar Traction-Separation Law (TSL) with those measured from tests, there were some limitations in predicting plasticity indicated by growth of crack mouth opening displacement (CMOD) and reduction of pipe wall thickness at failure. The Maxps damage initiation criterion was later extended to the prediction of CTOD-R curves of X42 pipe steel based on six small-scale single edge notched tension (SENT) tests by Ameli et al. [38]. The calibrated Maxps and G_C are 1400 MPa and G_C= 200 N/mm. Although the numerical CTOD-R curves matched with experimental curves, this damage initiation stress value may be impractical because it is approximately 4.5 times the yield stress of X42. This implies that a strain-based rather than a stress-based damage criterion may be more suitable in predicting the ductile fracture of pipelines. Subsequent work by Agbo et al. [39] based on a damage initiation criterion with critical maximum principal strain (Maxpe) demonstrated its success in predicting the tensile strain capacity of circumferentially cracked X42 pipes based on eight full-scale four-point bending tests. The calibrated Maxpe and G_C are 0.013 and G_C= 450 N/mm. In addition, the Maxpe damage initiation criterion was extended to the prediction of burst pressure of longitudinally cracked X60 pipes by Okodi et al. [40]. Due to the limited test data, three sets of damage parameters were calibrated from three full-scale burst tests containing different crack size (Maxpe = 0.02, G_C= 50 N/mm; Maxpe = 0.03, G_C= 10 N/mm; Maxpe = 0.065, G_C= 10 N/mm), and one set of damage parameters were calibrated from a SENT test for a specimen cut from X60 pipe (Maxpe = 0.034, G_C= 150 N/mm). Furthermore, the Maxpe criterion was extended to the prediction of burst pressure of X42 and X52 pipes containing cracks in corrosion defects by Zhang et al. [41]. One set of damage parameters (Maxpe = 0.02, G_C= 150 N/mm) were calibrated for both pipe grades. A more systematic literature review of the application of XFEM in fracture prediction of pipelines has been published by Shahzamanian et al. [42].

Overall, all mentioned literature work shows the calibrated damage parameters are quite case

dependent. This motivated me to develop a novel XFEM variable damage initiation criterion that is accurate and applicable to various pipe grades and cracks with any other anomalies. The major limitation of using either fixed Maxps or Maxpe criterion is the simplicity by ignoring important factors such as the crack-tip constraint, which has a profound effect on fracture resistance. In the simulation of a side-grooved SENT model using a fixed Maxpe damage initiation criterion, an irregular fracture profile of ductile tearing was obtained, while a physical test demonstrated a basically parabolic curve with slight growth at the side groove [2]. The novel damage initiation criterion, taking account of crack tip constrains, aims to modify the inaccurate crack propagating path allowing the specimen center to be more susceptible to crack extension rather than the specimen side even though high strains are concentrated at the crack tip due to the presence of the side groove.

In addition to the simple damage criterion, there is another concern associated with the simulation of crack propagation. Researchers in the literature, including all work mentioned above, adopted the typical use of XFEM crack by inserting a planar crack into the finite element mesh. It was the firstly proposed by Zhang et al. [41] that such simulation accompanied by initial cohesion around the crack tip field would artificially increase the fracture resistance for crack opening. Noticeable differences were found between the simulation of a planar crack and a V-shape notch in the prediction of burst pressure of X42 and X52 pipes containing cracks in corrosion defects using the same fixed Maxpe damage initiation criterion. Although an optimal set of damage parameters could be found based on simulation with XFEM planar crack to predict accurate experimental data, this calibrated damage parameters were not considered accurate or practically representative. This artificial cohesion around the crack tip field requires further careful investigation. In addition, the validation of the newly developed XFEM variable damage initiation criterion shall be based on the simulations with narrow notch cutting in the finite element models.

1.3 Objectives of Thesis

This doctoral thesis aims at utilizing and evaluating the current damage initiation criteria available in XFEM built-in procedure of Abaqus/Standard, and further developing a novel and more accurate damage criterion for predicting crack initiation and propagation of pipelines. This research focuses on the Mode-I (opening mode) fracture, in which the tensile stress pulls the crack surfaces apart, or in other words, the critical Maxps or Maxpe are normal to the crack plane and propagation. The novel variable strain damage initiation criterion is developed from the modified Mohr-Coulomb (MMC) fracture criterion as a function of stress triaxiality and Lode angle. The criterion is implemented using a Fortran code programmed in Abaqus user subroutine-UDMGINI, applied to various numerical models, and calibrated from experimental test data. This novel variable strain damage initiation criterion would provide significant numerical convenience with accuracy in predicting both brittle and ductile fracture of pipeline steel, dependent on the crack-tip constraint, but independent of the specimen geometry, pre-cracking size, or loading conditions. The followings are the main objectives for this doctoral thesis along with their specific aims:

Objective 1: To validate the capability of XFEM tool and calibrate fixed Maxps damage initiation criterion in predicting the fracture of circumferentially surface-cracked X52 pipeline in full-scale tests.

Specific aim 1.1: Develop eight full-scale models with different initial crack size and internal pressure where initial crack was simulated by XFEM planar crack inserted into the mesh.

Specific aim 1.2: Calibrate damage parameters (Maxps and G_C) based on experimental TSC, force-CMOD curves, pipe end rotation, and reduction of pipe wall at failure.

Specific aim 1.3: Investigate mesh size sensitivity.

Objective 2: To develop a novel XFEM variable strain damage initiation criterion from stain-based MMC fracture criterion.

Specific aim 2.1: Create a Fortran code to be used to implement novel criterion programmed in Abaqus user subroutine-UDMGINI.

Specific aim 2.2: Perform a parametric study and investigate effect of damage parameters on the fracture locus curve.

Specific aim 2.3: Validate the use of novel criterion in a side-grooved SENT model.

Objective 3: To calibrate fixed Maxpe damage initiation criterion in predicting the fracture of X52 full-scale tests.

Specific aim 3.1: Develop eight full-scale models with different initial crack size simulated by 0.5 mm- wide notch cut in the pipe model.

Specific aim 3.2: Calibrate damage parameters (Maxpe and G_C)

Objective 4: To calibrate the novel variable damage initiation criterion in predicting fracture of X52 full-scale tests.

Specific aim 4.1: Calibrate the damage parameters through the above eight full-scale models with initial notch.

Specific aim 4.2: Compare the numerical difference among fixed Maxps, fixed Maxpe and variable strain damage initiation criterion.

Specific aim 4.3: Identify the relationship between crack growth and TSC.

Specific aim 4.4: Investigate the effect of initial crack tip simulation using planar crack or notch.

Objective 5: To calibrate novel variable strain damage strain criterion in predicting J-resistance curves of X100 pipe specimens in SENT tests.

Specific aim 5.1: Develop four SENT models with each specimen either side-grooved or plain-sided and either shallow-cracked or deep-cracked.

Specific aim 5.2: Calibrate damage parameters.

Specific aim 5.3: Investigate crack-tip constraint.

Specific aim 5.4: Investigate the effect of initial crack tip simulation using planar crack or notch and with fixed Maxpe and variable strain damage initiation criterion on predictions.

Objective 6: To compare my calibrated damage parameters with literature available MMC fracture model parameters.

Specific aim 6.1: Conduct literature study for API 5L X grade of pipeline using MMC fracture model.

1.4 Organization of Thesis

This doctoral thesis consists of six Chapters plus three supplementary Appendixes.

Chapter 1 provides the overall introduction of cracking in pipelines along with current methodologies and numerical tools, the problem statement, and the objective and the organization of this thesis.

Chapter 2 consists of a comprehensive literature review of cracking in pipelines, fracture tests, fracture models, and XFEM-based cohesive segment approach.

Chapter 3 focuses on the validation of capability of XFEM using fixed Maxps damage criterion in predicting the fracture of circumferentially surface-cracked X52 pipe in full-scale tests. The eight full-scale models are developed with different sizes of initial cracks created by inserting an XFEM planar crack into the mesh. The damage parameters (Maxps and G_C) are calibrated from experimental data. The mesh size sensitivity study is performed. This Chapter

corresponds to a peer-reviewed research article published in the ASCE Journal of Pipeline System Engineering Practice, Volume 11 Issue 2, 2020.

Chapter 4 introduces my novel variable strain damage initiation criterion accounting of crack-tip constraint. It is developed from a stain-based MMC fracture criterion as a function of stress triaxiality and Lode angle. A sensitivity study of damage parameters influencing the damage locus curve is performed. A Fortran code is created to implement the novel damage criterion in XFEM and programmed in Abaqus user subroutine-UDMGINI. This novel damage criterion is adopted in Chapter 5. The majority content of this Chapter is derived from a peer-reviewed research article published in the ASME Pressure Vessels and Piping Conference, Volumn 6, 2020.

Chapter 5 focus on the validation of the novel variable strain damage initiation criterion in predicting fracture of small-scale and full-scale pipeline fracture tests. Two optimal sets of damage parameters (n, c_1, c_2, c_3, c_4, and G_c) are calibrated for X52 based on eight full-scale models and X100 based on four small-scale SENT models. Additional optimal damage parameters using fixed Maxpe and G_C were also calibrated for X52. The effect of crack tip simulation using notch or planar crack, and the differences of fixed Maxps, fixed Maxpe and variable strain damage initiation criterion were all discussed. My calibrated damage parameters are compared with literature available strain-based MMC fracture model parameters for various API 5L X grade of pipeline. Some content in this Chapter is derived from a research article submitted for publication in 2021 Technology for Future and Aging Pipelines Conference (under review), while the others are prepared to be submitted for a journal - Engineering Fracture Mechanics. To maintain a paper-based thesis, some of the literature review is inevitably repeated in the introduction section in Chapter 5.

Chapter 6 provides a general summary, conclusions and contributions of this doctoral thesis, as well as the recommendations for future research work.

Appendix A includes the Fortran code in defining the variable strain damage initiation criterion modified from strain-based MMC fracture criterion to be programmed in Abaqus user subroutine-UDMGINI.

Appendix B includes equations of J-integral developed by CANMET-MTL for SENT specimens.

Appendix C includes the numerical results of eight X52 full-scale models adopting fixed Maxpe damage criterion.

2. Literature Review

2.1 Cracking in Pipelines

Cracking constitutes one of the most common integrity threats for steel pipelines in the transportation of natural gas and petroleum, which results in the immediate loss of pressure containment capacity. Pipeline operators are required to assess and manage crack threats and address related integrity issues in accordance with applicable industry standards, recommended practices, and regulations, such as Canadian Standard Association CSA Z662 [43], American Society of Mechanical Engineers ASME B31.8S [44], and API RP 1176 [45] and API RP 1160 [46]. Cracks or crack-like defects can be formed in industry pipelines at any stage. During the manufacturing of pipe body or pipe seam, cracks may originate in pipe body hard spots or hard heat-affected zones (HAZ), or in the longitudinal seam welds such as lack-of-fusion, hook cracks, weld metal cracks, and toe cracks [45,46]. In the construction, fabrication, and installation stages, cracks may occur in the circumferential (girth) welds, fabrication welds, winkles, fittings, branch connection, and sleeves [46]. In general, most pre-service cracks can be detected, repaired or removed during mill hydrostatic testing of a pipeline and in-line inspection (ILI), while those undetected or surviving from the initial testing may be enlarged in long-term operation due to pressure-cycle-induced fatigue, or cause any other in-service failure [45].

Once the pipeline enters service, environmentally assisted cracking (EAC) or mechanically driven cracking constitute the two primary failure causes or mechanisms. Examples of EAC include stress corrosion cracking (SCC), sulphide stress cracking (SSC), hydrogen-induced cracking (HIC), and corrosion fatigue cracking (CFC) [45]. Mechanically driven cracking can initiate due to external mechanical damage to the surface of pipeline and can propagate over

time in service till eventual failure. Examples are cracking occurring in highly localized indentations or sharp dents or in metal loss associated with gouging, or fatigue crack growth due to pressure cycles [45].

Recognizing the crack types and corresponding failure time is important for operators to maintenance pipeline integrity. Although the time dependency may be hard to observe, the crack threats can be generally categorized as time-dependent (e.g., EAC and fatigue), potentially time-dependent (e.g., Manufacture or construction related cracks, or mechanically driven cracking in cyclic service), and time-independent or random (e.g., mechanically driven cracking resulting in sudden failure) [45,46]. Generally speaking, periodic assessment, monitoring and preventive maintenance (e.g. repairment or replacement) of a pipeline are essential and necessary for time-dependent crack threats, but may be inefficient or useless for time-independent crack threats. In addition, operators' decision-making process for repair or replacement of a pipeline rely on essential data including but not limited to the type and vintage of pipeline, pipe geometry and mechanical properties, type of longitudinal seam, type and locations of girth welds, type of coating and cathodic protection, operating pressure profile as a function of time, location of valves and fittings, pressure tests records, leak and rupture history.

In general, a crack propagates in a direction perpendicular to the local direction of maximum stress or strain on the pipeline. For a pressurized pipe subjected to circumferential or hoop stress due to high internal pressure, longitudinal cracks aligned parallel to longitudinal axis of the pipeline either in the pipe body or seam weld are most dangerous. On the other hand, for pipelines operating at low internal pressure but subjected to large external longitudinal or axial stresses or strains caused by seasonal ground temperature difference or soil differential movement especially in the permafrost and seismically active regions, circumferential cracks aligned parallel to pipeline girth welds are more likely to occur either in the pipe body or girth

weld. The failure mode also depends on the diameter of pipe. Due to their relatively higher pressure and larger moment of inertia, large diameter pipes are more susceptible to longitudinal cracking , while small diameter pipes are more susceptible to circumferential cracking due to the lower pressure and smaller moment of inertia [45,47].

2.2 Crack-tip Constraint

Constraint refers to the material's inability to plastic deformation prevented from surrounding material [48]. Consider a plate containing a crack, an element near the crack tip subjected to a large tensile normal stress to the crack plane (σ_{yy}) is restrained from lateral contraction by its adjacent elements. Such constraint produces lateral stresses (σ_{xx} and σ_{zz}) perpendicular to the applied stress (i.e., parallel to the crack plane) resulting in a triaxial state of stress near the crack tip [49]. Figure 2-1 (a) illustrate the crack-tip stress state conditions in cracked thin and thick plates where the origin of coordinates (x, y, z) is located at the crack tip in the mid-thickness of the plate and (b) illustrates the effect of thickness (B) on σ_{zz}. For a thick plate, the crack-tip stress state in the interior of the plate (center region) has high triaxiality which is essentially in plane strain condition, whereas that near the free surface of the plate has low triaxiality and that at both free surfaces ($z = \pm B/2$) are in pure plane stress condition [49]. As the plate thickness is decreased, the central plane strain region is reduced until it vanishes in a very thin plate. The plane strain refers to the condition of non-zero strains in a single plane (strain in the thickness direction is constrained thus $\varepsilon_{zz} = 0$) concomitant with a triaxial state of stress exists (stresses σ_{xx}, σ_{yy} and σ_{zz} acting in three directions), whereas the plane stress refers to the condition where non-zero stress exist in a single plane (stress in the thickness direction are negligible in comparison with the other stresses thus $\sigma_{zz} \approx 0$) with a concomitant biaxial state of stress exists (stresses σ_{xx} and σ_{yy} acting perpendicular to thickness direction) [50]. Figure 2-1 (c) compares the crack-tip stress state in a through-thickness crack in a plate and a

circumferential surface crack in a pipe. The high triaxiality region is predominated by the plate thickness in the plate while it is largely influenced by circumferential surface crack length in the pipe [49]. Indeed, the crack size has a profound effect on the constraint. The constraint can be elevated by increasing the crack depth (a) of a through-thickness cracked specimen and increasing the crack depth ratio (a/t) or decreasing the crack aspect ratio (a/c where c is half of the crack length) in a circumferential surface-cracked pipeline [51]. In terms of the direction relative to the crack plane, constraint can also be classified as in-plane or out-of-plane; both generally existing in the actual engineering structures [52,53]. The in-plane constraint depends on in-plane loading and specimen geometry in the direction of a propagating crack, i.e., the length of the un-cracked ligament, while the out-of-plane constraint depends on the out-of-plane loading and the specimen thickness that is parallel to the crack plane [52,53]. The high constraint, high triaxiality, and plane strain are often correlated and occur in a thick and deep cracked specimen developing little plasticity prior to fracture, whereas low constraint, low triaxiality or biaxial stress state, and plane stress are often correlated and occur in a thin and shallow cracked specimen developing a larger plastic region at the crack tip [49,52]. The reduction of constraint in a material is beneficial to raise its fracture resistance and absorbing more energy before fracture.

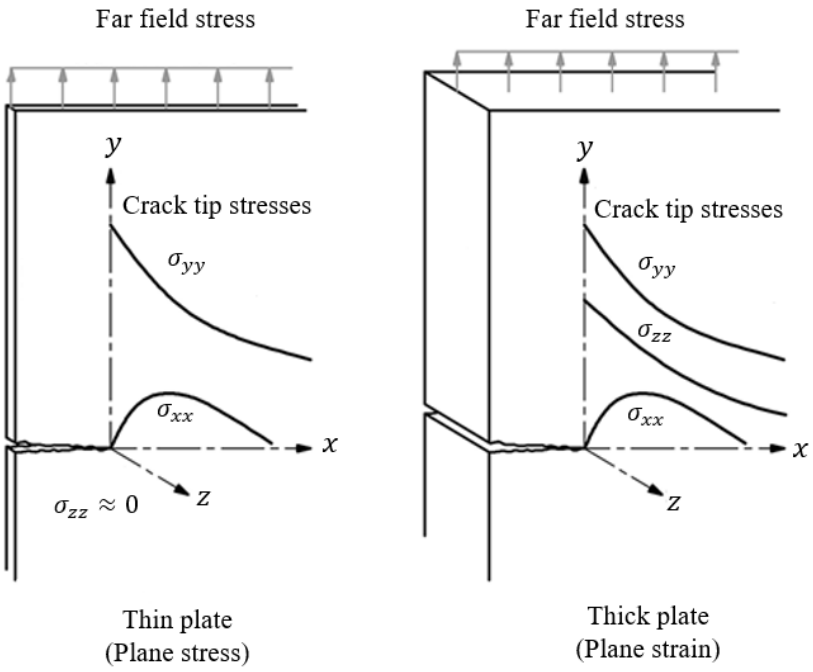

(a)

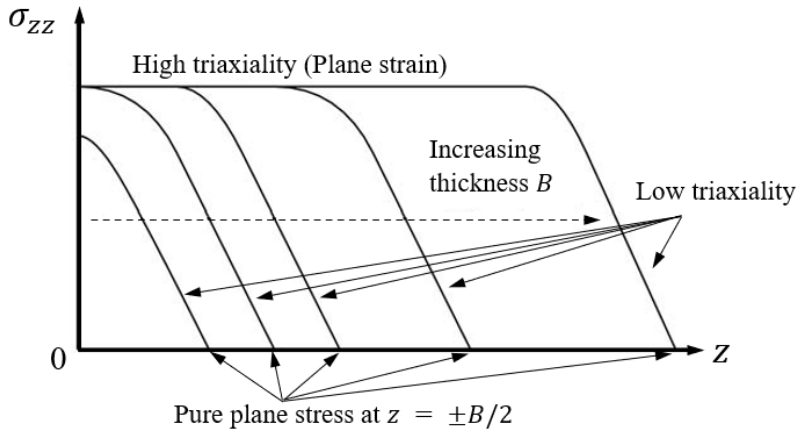

(b)

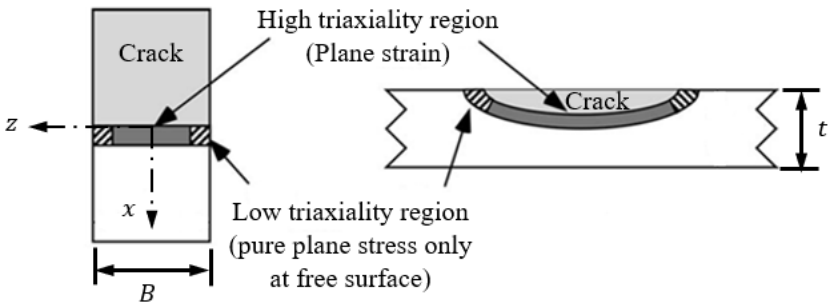

(c)

Figure 2-1. Illustration of crack-tip stress state conditions (a) in a cracked thin or thick plate;

(b) affected by plate thickness; and (c) for a though-thickness crack or circumferential surface crack. [Adapted (a) from McMullin [48] and (b and c) from Anderson [49].]

2.3 Fracture Tests

Important mechanical properties of pipe material include yield strength, ultimate tensile strength and fracture toughness. Actual yield and ultimate tensile strength of a given pipe can be higher than the specified minimum defined in API 5L, but strength properties can be easily obtained by performing tension coupon tests of specimen cut from a given pipeline. Fracture toughness in the form of either stress intensity factor (K), J-integral, crack tip opening displacement (CTOD or δ), or resistance curve (R-curve) relating any of the above toughness parameter to crack extension (Δa), quantifies the material's inherent resistance to fracture or crack extension in the presence of an existing crack. The measure of fracture toughness for a given pipeline material varies with temperature and testing technique, and should be indicative of the pipe body, HAZ, or weld metal regarding where the crack is located. Traditionally, a fracture toughness test specimen containing a fatigue pre-cracked notch is loaded with opening mode (Mode-I) at a low (quasi-static) strain rates and the fracture toughness is evaluated from the force versus load-line displacement and/or crack-mouth opening displacement monitored during the test [54]. Unstable brittle crack extension such as cleavage can be sufficiently described by a single point toughness value, indicating the unstable cracking initiation, pop-in[2] initiation, or fracture instability. Stable ductile crack extension such as stable tearing, on the other hand, can be described by either an entire continuous R-curve or a single point engineering initiation toughness parameter estimating the stable tearing initiation. The unstable

[2] Pop-in is an abrupt discontinuity in the force versus displacement record, featured by a sudden decrease in force and increase in displacement, followed by both increases in force and displacement.

crack extension including the pop-in may occur with or without significant prior stable crack extension, as illustrated in Figure 2-2 where the displacement corresponds to the notch opening displacement or load-line displacement [55].

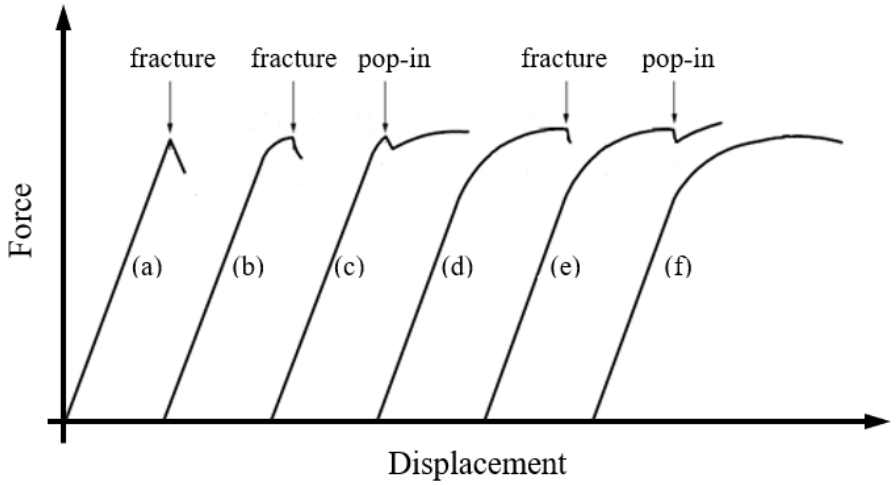

Figure 2-2. Common force-displacement curves in fracture toughness tests: (a) brittle fracture; (b) brittle fracture with little prior plastic deformation; (c) stable crack extension after a pop-in; (d) fracture after stable crack extension; (e) pop-in after stable crack extension; (f) significant stable crack extension showing a maximum force plateau prior to fracture. (Adapted from ISO 12135 [55].)

Among all factors that have a profound impact on the fracture resistance, temperature, strain rate, and the crack-tip stress state are the three major factors. Brittle fracture may be promoted by low temperature, high strain rate (i.e., rapid loading rate), and high triaxial state of stress (i.e., high constraint) such as the state of stress at the tip of a notch. Under any of these conditions, ductile materials may fail in an unfavorable brittle manner. Conventional fracture toughness tests recommend deep-cracked specimens such as the compact tension (CT) and single edge notched bending (SENB) specimens, and both result in high levels of constraints at the crack tip. This contributes to over-conservatism of fracture resistance curves as well as the crack acceptance criteria for the final application in particular the case of pressurized

pipeline. The fracture toughness of a pipeline (measured from full-scale pipe test) is higher and can rather be predicted by low crack-tip constrained specimens such as a medium-scale curved wide plate test (CWP) and small-scale single edge notched tension (SENT) specimens as illustrated in Figure 2-3 [56,57]. The CWP tests can correlate with the TSC of pipeline with a correction for internal pressure, whereas the SENT tests can provide fracture resistance serving as a key input to evaluate the TSC [58]. Recently, the SENT tests have become increasingly popular in the pipeline industry which can generate the crack-tip constraint condition similar to that of a circumferential crack in a girth weld under global bending during pipeline installation and service [59,60]. The whole ligament containing the crack is essentially in tension even if the pipeline is under global bending [60]. Experimental and numerical research conducted by ExxonMobil have validated that the CTOD-R curves in SENT tests and full-scale tests are closely matched [61]. A few SENT test procedures have been developed over the past two decades. The currently widely used test procedures are multiple-specimen technique recommended by Det Norske Veritas [62] and single-specimen technique recommended by CANMET Materials Technology Laboratory [63], and both techniques are described in the British Standard BS 8571[64]. The multiple-specimen technique requires at least six identical specimens with each providing one valid point on the resistance curve at different level of crack extension at the final fracture, while the single-specimen technique requires at least three identical specimens with each providing a completed resistance curve using the unloading-compliance method with rotation correction to measure the crack extension during the test.

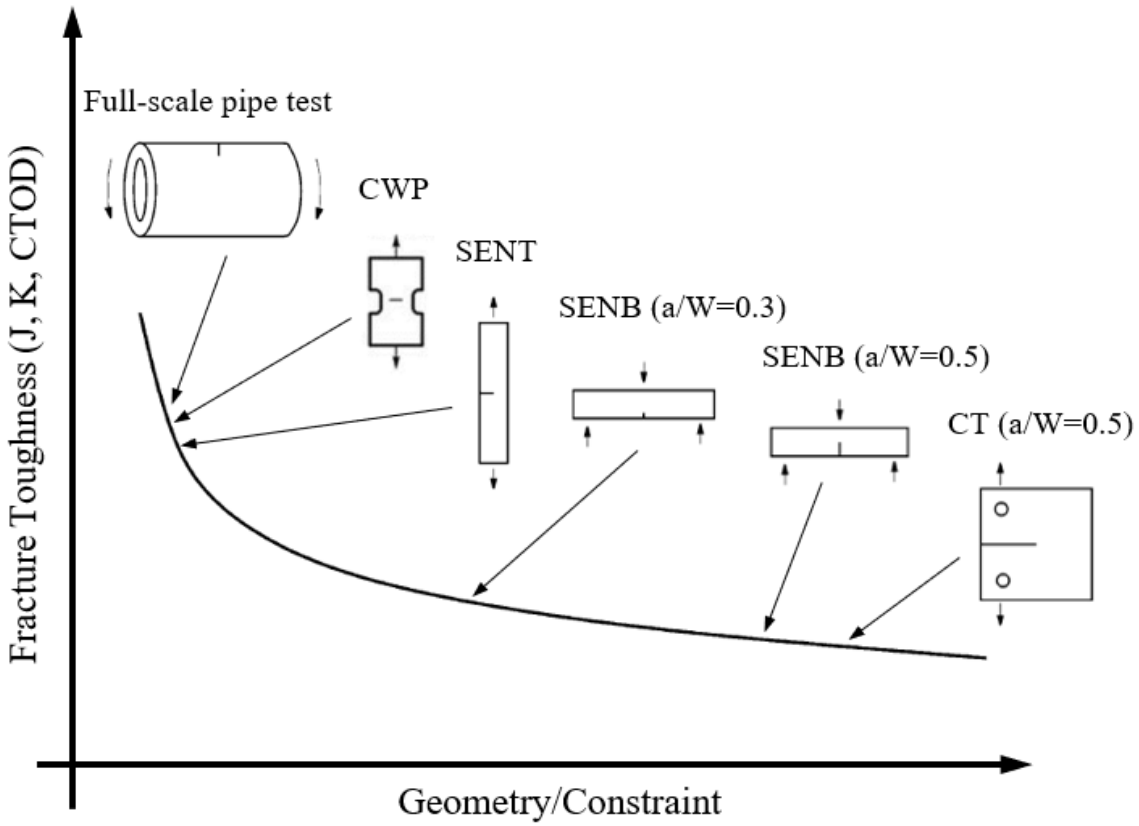

Figure 2-3. Effect of specimen geometry and constraint on fracture toughness. Note CWP, SENT, SENB, CT represents curved wide plate test, single edge notched tension test, single edge notched bending test, and compact tension test, respectively. (Adapted from Chiesa et al. [56] and Kang et al. [57].)

2.4 Fracture Models

Engineers and researchers have developed numerous computational fracture models within the finite element framework to predict the ductile fracture of structural materials. The fundamental principals of these models can be categorized by either fracture mechanics-based or damage mechanics-based models. The theory of fracture mechanics explicitly assumes the material contains cracks in the macroscopic scale and predicts the propagation of initial macro-cracks. The initial cracks are considered as discontinuities where the stress singularity exists at the crack tip making the material surrounding the crack tip weaker and thus the crack propagation

occurs [65]. There are three basic modes of fracture shown in Figure 2-4 characterizing the orientation of applied loading with respect to the crack plane: Mode I - opening mode describes a situation where the a tensile stress is normal to the plane of the crack; Mode II – slide mode (in-plane shear) describes a situation where a shear stress is parallel to the plane of the crack and perpendicular to the crack front; Mode III – tearing mode (out-of plane shear) describes a situation where a shear stress is parallel to the plane of the crack and crack front [49]. The fracture mode I is the most common fracture mode used in fracture toughness testing. Two major limitations of fracture mechanics-based models are the inability to model fracture of uncracked (crack-free) materials and predefined crack direction and path by a user.

The theory of damage mechanics assumes the material contains defects (micro-cracks) in the microscopic scale which are continuously distributed in the material [65]. It introduces the damage evolution of material degradation phenomenon from initial undamaged or predamaged condition to fully damaged condition (creation of a macro-crack). Therefore, damage mechanics-based models have advantages of predicting both crack initiation and propagation, not requiring a predefined crack path. Gurson-Tvergaard-Needleman (GTN) model [66–68] is one of the widely used model to describe failure as a sequence of void nucleation, growth and coalescence, but it has redundant calibration procedure. The original GTN model contains 7 parameters to predict the tensile stress dominated fracture, and the shear modified GTN model [69–71] contains 13 parameters that need to be calibrated to predict shear stress dominated fracture [72,73]. The strain-based modified Mohr-Coulomb (MMC) model developed by Bai and Wierzbicki [74,75] is an recent model that aims to predict ductile fracture of uncracked bodies accounting for the effects of stress triaxiality (dimensionless hydrostatic pressure) and Lode angle parameter (derived from third invariant of stress tensor). The fracture strain dependence on the Lode angle dependence is a unique feature of the MMC fracture criterion, which is generally deficient in almost all existing other ductile fracture criteria. The MMC

model has a full range of applicability of stress states (or called loading conditions) from tension, shear to compression and therefore not restricted to a single fracture mode type. Figure 2-5 illustrates the initial stress states of 10 types of uncracked specimens (marked by circles) typically used for plasticity and fracure testing, and their analytical solutions for the stress triaxiality (η) and Lode angle ($\bar{\theta}$) parameter. Four classical stress states are highlihted in the figure: (A) axial symmetry, tension ($\bar{\theta}$ = 1); (B) axial symmetry, compression ($\bar{\theta}$ = -1); (C) plastic plane strain or generalized shear ($\bar{\theta}$ = 0); and (D) plane stress (η and $\bar{\theta}$ are uniquly related due to $\sigma_3 = 0$). The performance of MMC model for predicting the behaviour of uncracked structures in the stress triaxiality range $0 \leq \eta \leq 2$ has been well evaluated in many publications [72–77] and its applications for pre-cracked structures is examined by Kofiani et al. [72,73] on SENT tests.

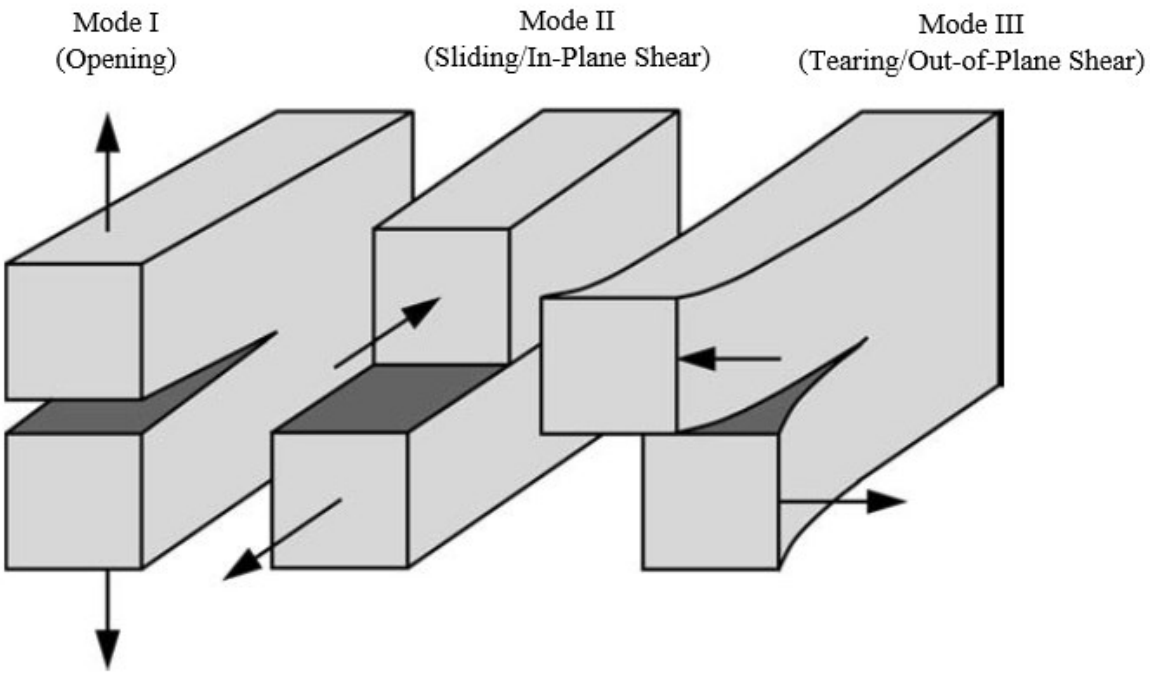

Figure 2-4. Three basic modes of fracure. (Adapted from Anderson [49].)

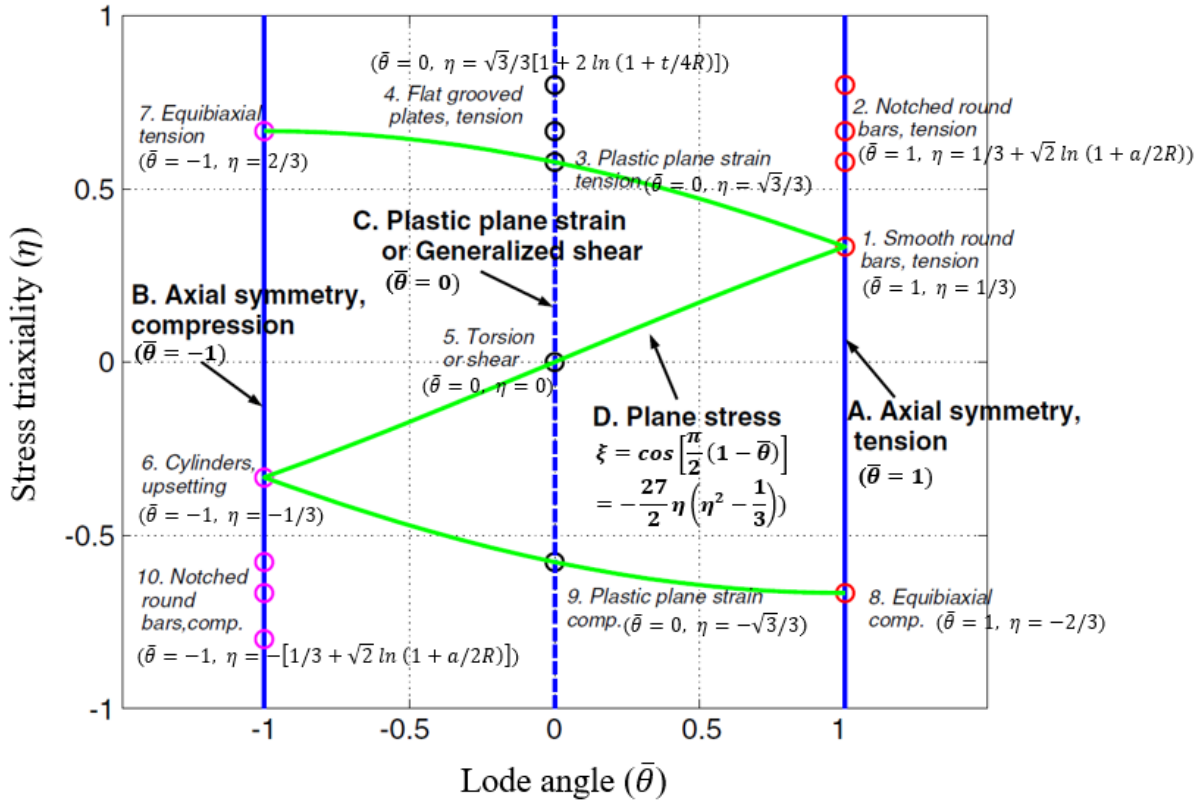

Figure 2-5. Illustation of initial stress states on the plane of stress triaxiality and Lode angle. (Adapted from Bai [74].) Note that ξ is the normalized third deviatoric stress invariant, R is the radius of a notch or a groove, a is the radius of a round bar at the notch, and t is the thickness of a flat grooved plate at the groove.

2.5 XFEM-based Cohesive Segment Approach

The idea of enriching the near tip field in FEA was first introduced by Benzley in 1974 [78] using the asymptotic solution for static fracture problems. In 1996, Melenk and Babuska proposed the concept of partition of unity [34] to describe the displacement field of a cracked element. Based on it, the first practical extended finite element method (XFEM) was introduced by Belytschko and collaborators in 1999 [32,33] for general crack propagation problems. This method was later extended from two-dimensional to three-dimensional crack modelling by defining arbitrary crack propagation with new definitions from rotational enrichments [79–81].

Overall, the XFEM provides a robust approach to incorporate the discontinuities and discontinuous solution field into standard finite element functions by introducing special enrichment functions in conjunction with additional degrees of freedom [30]. The XFEM displacement approximation u in an element is given by [30]

$$u = \sum_{I=1}^{N} N_I(x) \left[u_I + H(x) a_I + \sum_{\alpha=1}^{4} F_\alpha(x) b_I^\alpha \right] \quad (1)$$

where $N_I(x)$ are the standard nodal shape functions of node I, u_I are the nodal displacement vector associated with the continuous part of the FE solution, a_I and $H(x)$ are the nodal enriched degree of freedom vector and the associated discontinuous (generalized Heaviside) jump function across the crack surface, b_I^α and $F_\alpha(x)$ are the nodal enriched degree of freedom vector and the associated elastic asymptotic crack-tip functions. Note that $N_I(x)u_I$ applies to all nodes in the model, $H(x)a_I$ applies to nodes whose shape function is cut by the crack interior, and $\sum_{\alpha=1}^{4} F_\alpha(x) b_I^\alpha$ applies to nodes whose shape function is cut by the crack tip.

In the built-in XFEM procedure of Abaqus/Standard, accurately modeling the crack-tip asymptotic singularity requires constantly keeping track of where the crack propagates and is cumbersome in the propagation analysis. Therefore, the crack-tip enrichment is only considered in stationary crack analysis, but not considered in the propagating crack analysis [30]. As shown in Figure 2-6. (b), the crack keeps cutting each element completely and the crack tip is always located at an element edge and not arrested within an element to avoid the need to model the stress singularity. For this reason, the contour integral evaluation is only available in the stationary crack analysis, but not in the propagating crack analysis.

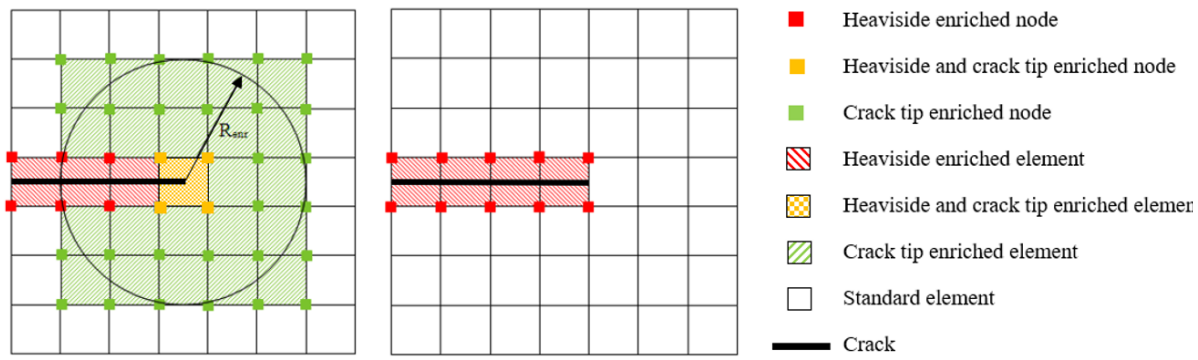

(a) (b)

Figure 2-6. Illustration of a finite element mesh cutting by a XFEM (a) stationary crack; and (b) propagating crack. (Adapted from Gigliotti [82].)

The propagating crack analysis can be performed with either XFEM-based linear elastic fracture mechanics (LEFM) or XFEM-based cohesive segments method i.e., cohesive zone model (CZM) within the XFEM framework, while the latter method has an advantage in solving problems of both brittle and ductile fracture [30]. The concept of CZM was originally introduced to fracture modelling by Barenblatt [83,84] and Dugdale [85] in the early 1960s. It was firstly implemented in FEM framework by Hillerborg et al. [86] in 1976 and in XFEM framework by Wells and Sluys [87] in 2001. The CZM (Figure 2-7) considers the fracture as a gradual phenomenon and describes a traction-separation constitutive relation (i.e., TSL), between cohesive traction acting on cracked surfaces resisted by crack propagation and the corresponding separations of crack surfaces across an extended crack tip. When the separation at the tail of the cohesive zone, i.e., physical crack tip, reaches a critical value δ_c, the crack grows, while the cohesive traction T_n vanishes. The major advantages of CZM over classical fracture mechanics include the extended validity in crack-free bodies (pre-existing crack is the priori in classical fracture mechanics), and the removal of crack tip stress singularities (difficult to capture in classical fracture mechanics without extensive remeshing). The CZM only requires three parameters, a given shape of TSL, the maximum cohesive strength T_{max} and the

cohesive energy or complete separation (or crack opening).

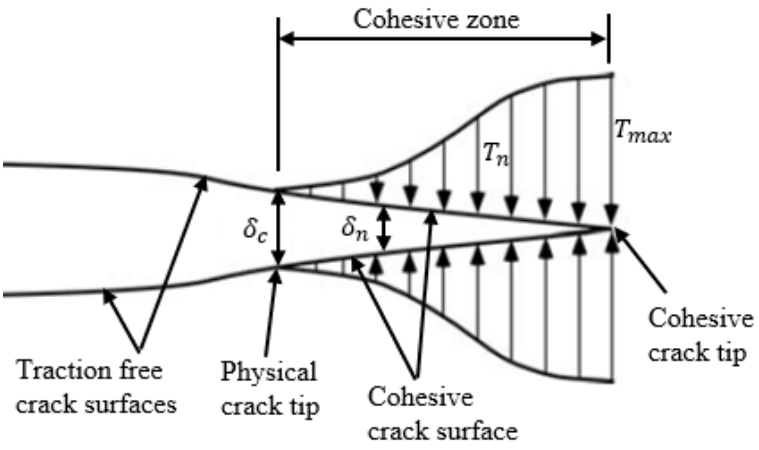

Figure 2-7. Concept of cohesive zone model. (Adapted from Anderson [49].)

XFEM-based cohesive segments method is based on the traction-separation cohesive behavior used in conventional FEM, assuming an undamaged linear elastic traction-separation model (not required to be specified in XFEM), followed by one or multiple failure mechanisms with each consisted of a damage initiation criterion and a damage evolution law [30]. The damage occurs at an enriched element once a damage initiation criterion is satisfied, e.g., its maximum principal stress (Maxps) or maximum principal strain (Maxpe) exceeds a given critical value, in which the crack plane is perpendicular to the direction of Maxps or Maxpe. Afterwards, the damage occurs according to a specific damage evolution law till eventual failure (i.e., cohesive traction is degraded until no traction across the crack surfaces). The built-in damaged traction-separation response (Figure 2-8) in XFEM capability of Abaqus/Standard, is either linear or exponential softening based on either the energy dissipated due to fracture (i.e., critical fracture energy release rate G_c) or the effective displacement at failure. The energy-based damage evolution can be defined to be mode-independent or incorporating the mixed mode behavior using an analytical formulae, e.g., power law [88] or Benzeggagh-Kenane (B-K) law [89]. $G_c = \int_0^{\delta_c} T(\delta) d\delta$ is the work needed to create an extended unit area of crack surfaces,

which is equivalent to the area under the TSL curve.

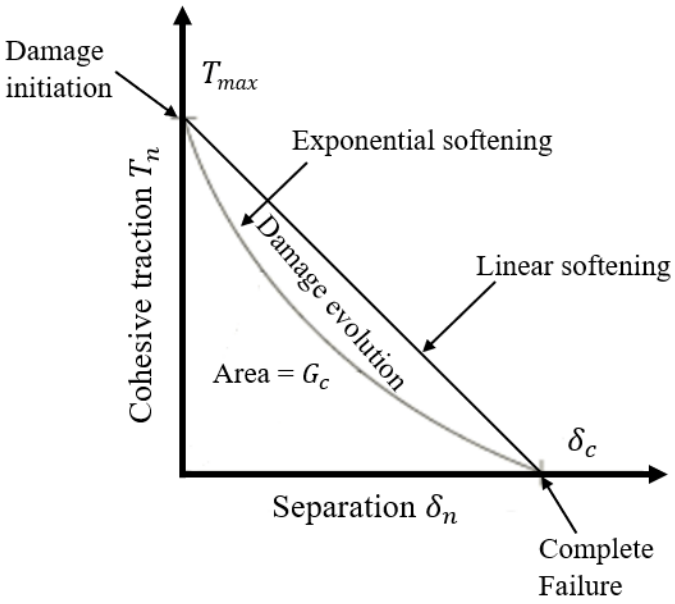

Figure 2-8. Damaged traction-separation response in XFEM. (Adapted from Abaqus documentation [30].)

For a simulation using XFEM, it is important to request three outputs PHILSM, PSILSM, and STATUSXFEM [30]. PHILSM and PSILSM are the signed distance function to describe the crack surface and initial crack front using the level set method. STATUSXFEM is the status of the enriched element, ranging from 0 (no damage or uncracked) to 1 (fully damaged or cracked), while the value between 0 and 1 indicates the enriched element is partially damaged or cracked.

Overall, XFEM is a revolutionary and powerful technique for modelling crack propagation phenomena. It has been implemented in many applications and its use in pipelines is starting to gain traction. However, current implementation of XFEM lacks proper attempts for calibration. Further, there is not a single study that attempted to include the constraint effects in XFEM. To incorporate constraint into XFEM with proper calibration is therefore the ultimate goal of this thesis.

3. Fixed Stress Damage Model for Predicting Fracture of Full-scale Pipe Tests[3]

3.1 Abstract

The cohesive zone model (CZM) is one of the most widely used damage models to describe the fracture processes of brittle and ductile materials, and has been usually combined with the conventional finite-element method (FEM). CZM in the context of the more effective extended finite-element method (XFEM) has recently been implemented in many applications, but it has not been widely used for crack propagation of pipelines. This chapter aims to investigate the capability of the XFEM-based cohesive segment approach implemented in Abaqus/Standard to predict crack propagation of pipelines by calibrating a linearly decreasing traction–separation law with two damage parameters, the maximum principal stress and the fracture energy. The damage parameters for vintage pipeline steel (API 5L Grade X52) were systematically calibrated and verified by comparing the numerical results with eight full-scale experiments of pressurized and circumferentially surface-cracked pipe specimens. A correlation between the damage parameters and material yield strength and fracture toughness is discussed and an investigation of mesh size sensitivity included.

Keywords: Extended finite element method; Traction separation law; Maximum principal stress; Fracture energy.

[3] This chapter is derived from a journal publication [1]:

M. Lin, S. Agbo, D.-M. Duan, J.J.R. Cheng, S. Adeeb, Simulation of crack propagation in API 5L X52 pressurized pipes using XFEM-based cohesive segment approach, Journal of Pipeline Systems Engineering and Practice. 11 (2020) 04020009. https://doi.org/10.1061/(asce)ps.1949-1204.0000444

3.2 Introduction

Assessment of fracture behavior of steel pipelines has been traditionally conducted by performing standard fracture toughness tests on deep-cracked specimens, such as compact tension (CT) specimens and single-edge notched bend (SENB) specimens. The valid fracture toughness results require deep-cracked specimens with high levels of constraints at the crack tip, which are too conservative especially in the study of commonly used thin-walled and high-strength steel pipeline with relatively high toughness [60,90,91]. Zhang et al. [60] stated that a crack in a thin-walled pipeline is essentially in a low-constraint configuration even when the pipe is subjected to global bending. In recent years, shallow-cracked specimens, such as single-edge notched tension (SENT) specimens, which can accurately capture the stress state at the crack tip in pipelines, have been highly recommended [91,92]. However, there is a high cost associated with specimen fabrication and testing for small-scale SENT fracture test specimens. The costs are even higher for physically conducting full-scale experiments on cracked pipes subjected to both internal pressure and external tension and/or bending to resemble the actual conditions of buried pipeline underneath the ground. For more cost-effective pipeline design, the numerical techniques based on the finite-element method (FEM) or extended finite-element method (XFEM) have offered alternative solutions in numerously simulating the crack initiation and propagation of pipelines subjected to various complex loading conditions.

In most FEM-based approaches, the cohesive zone model (CZM) is one of the most widely used numerical techniques for crack propagation analysis. The model was originally introduced by Barenblatt [83,84] and Dugdale [85] in the early 1960s, who respectively described the near-tip nonlinear processes in quasi-brittle materials and ductile materials with small-scale plasticity. The first implementation of CZM in the context of FEM was proposed by Hillerborg et al. in 1976 [86] for brittle fracture in concrete. In the late 1980s and early 1990s, ductile

fracture at the microscale was studied by Needleman [93], while ductile fracture at the macroscale was studied by Tvergaard and Hutchinson [94]. The first implementation of CZM in the context of XFEM was proposed by Wells and Sluys [87] in 2001 based on the partition of unity property of finite elements for a cohesive crack. The CZM model considers fracture as a gradual phenomenon and describes a constitutive relation [referred to as the traction–separation law (TSL)] between cohesive traction acting on crack surfaces resisted by crack propagation and the corresponding separations of surfaces across an extended crack tip (cohesive zone) [31,95–97]. When the separation at the tail of the cohesive zone (physical crack tip) reaches a critical value, the crack grows, while the cohesive traction vanishes [96]. The major advantage of CZM is the removal of crack tip stress singularities in classical fracture mechanics. The damage model following a TSL in CZM describes the loss of load or deflection-bearing capacity of material as a function of a crack surface separation (i.e., displacement jump), irrespective of the physical details of damage occurring in an actual material [97,98].Therefore, it can be applied to both brittle and ductile fracture processes [97,98]. The choice of a TSL depends on the brittle or ductile fracture behaviors of materials under consideration. For brittle materials, the TSL proposed by Hillerborg et al. [86] as shown in Figure 3-1 (a) has been suggested by many experiments, and the influence of TSL shape plays a minor role in crack propagation [99]. However, for ductile materials involving large plastic material deformation, there is not a correct shape of TSL determined from experiments and hence it has been usually assumed [99], such as the TSL proposed by Scheider [100] as shown in Figure 3-1 (b) in modeling ductile fracture. The magnitudes of cohesive parameters are dependent on the shape of TSL, but all different shapes of TSL with their related cohesive parameters are able to reproduce experimental results [98,99]. For a given shape of TSL, the material damage can be only characterized by two damage parameters, cohesive strength (T_0) and cohesive energy (Γ_0) or complete surface separation (δ_0), where $\Gamma_0 = \int_0^{\delta_0} T(\delta) d\delta$ is the

work needed to crack a unit area of fracture surfaces, equivalent to the area under the TSL curve.

Based on the concept of partition of unity by Melenk and Babuška [34], XFEM extends the conventional FEM by enriching additional discontinuous displacement in conjunction with additional degrees of freedom in the elements that can capture the physical discontinuity, such as cracks [32,33,101]. The XFEM-based CZM (typically referred to as the XFEM-based cohesive segment approach) is based on traction–separation cohesive behavior used in conventional FEM. It is based on the intraelement algorithm in which the discontinuities can be freely laid within elements and are not tied to element boundaries without the need of remeshing to match the geometry of the discontinuities [31]. Phantom nodes, first proposed by Hansbo and Hansbo [36], are introduced in the method to represent the discontinuities of the cracked elements. In the commercial finite-element system Abaqus/Standard, the software searches for critical regions of crack initiation in which the stress or strain exceeds a user-defined critical value, after which phantom nodes and their superposed original real nodes move apart. The maximum principal stress (σ_{maxps}) and the fracture energy (G_C) are two commonly used damage parameters in controlling the crack initiation and propagation.

This chapter aims to simulate the crack propagation of API 5L Grade X52 steel pipes subjected to the combined effects of internal pressure and external tension and bending using the XFEM-based cohesive segment approach implemented in the commercial finite element system Abaqus/Standard. A suitable set of damage parameters, σ_{maxps} and G_C,, was calibrated and verified using the eight full-scale experimental results. The correlation between the damage parameters and the material yield strength and fracture toughness is discussed. The effect of mesh sensitivity on the numerical results was examined in one of the models.

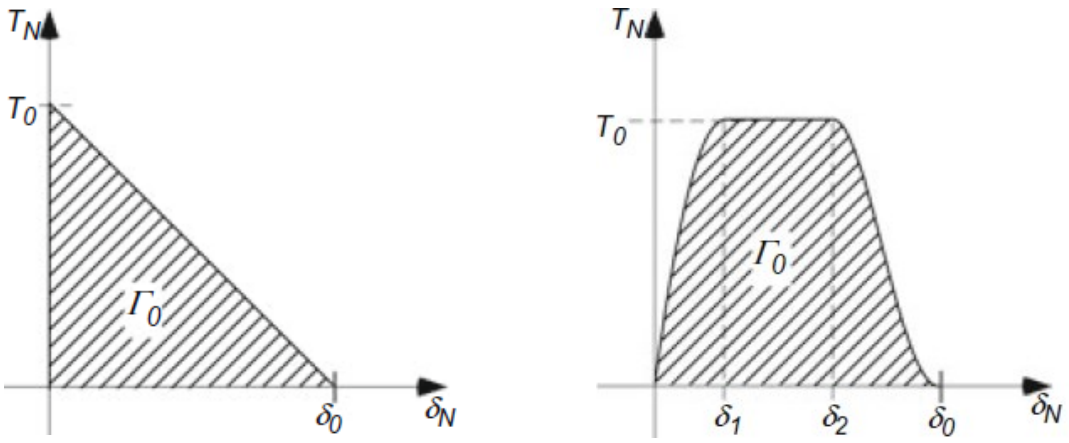

(a) (b)

Figure 3-1. Typical transition-separation laws: (a) for brittle fracture proposed by Hillerborg [86] and (b) for ductile fracture propose by Scheider [100]. (Adapted from Schwalbe et al. [98].)

3.3 Previous Research on Pipeline

3.3.1 Numerical Studies on Modern Pipelines

Recent studies over the past decade using the FEM-based CZM in simulating fracture behaviors of modern pipelines have achieved satisfying results. Shim et al. [102] successfully employed the method in the simulation of the ductile crack propagation on a circumferentially cracked pipe by modeling a three-dimensional four-point bending test on a pipe specimen made of SA-358 Type 304 stainless steel (σ_y = 220 MPa and σ_u = 682 MPa). The modeled crack was a circumferential through-wall crack with a length of 37% of pipe circumference. The spiderweb mesh technique was employed in the crack tip region with a mesh size of 2.54 mm. The TSL adopted from Scheider [100] was used in the work with the damage parameters T_0 = 618 MPa ($2.8\sigma_y$) and Γ_0 = 1084 N/mm. Nonn and Kalwa [103,104] and Scheider et al. [105] successfully calibrated and verified the damage parameters for API 5L pipeline steel with grade of X65 (σ_y = 482 MPa and σ_u = MPa), X80 (σ_y = 663 MPa and σ_u = MPa), and X100 (σ_y = 756 MPa and σ_u = 757 MPa). A number of three-dimensional drop weight tear testing (DWTT) tests and

SENT tests were simulated for specimens cut from corresponding-grade longitudinal welded pipe. By accurately reproducing the load-deformation and fracture resistance curves obtained from small-scale tests, the adequate sets of damage parameters were determined: T_0 = 1375 MPa (= $2.85\sigma_y$) and Γ_0 = 900 N/mm for X65 steel, T_0 = 1600 MPa (= $2.4\sigma_y$) and Γ_0 = 900 N/mm for X80 steel and T_0 = 1700 MPa (= $2.26\sigma_y$) and Γ_0 = 700 N/mm for X100 steel.. The mesh size in cohesive elements was 0.5 × 0.01 × 1.58 mm (=1/12 of specimen thickness) for X65 steel, and 0.5 × 0.01 × 1.15 mm (=1/12 of specimen thickness) for X80 steel, which are dimensions respectively in the direction of crack propagation, perpendicular to the crack plane (width of cohesive element layer), and in the direction of the specimen thickness [104]. The TSL used in their modelings was adapted from Scheider [100] as shown in Figure 3-1, where the adjusting shape parameters $\delta_1 = 0.001\delta_0$ and $\delta_2 = 0.5\delta_0$ resulting in $\Gamma_0 = 0.75T_0\,\delta_0$, and it was embedded in the user subroutine UEL of Abaqus/Standard.

More recently, XFEM-based CZM has been employed in pipeline fracture studies. Liu et al. [106] successfully employed the method in the simulation of crack behavior of a buried API 5L X65 pipe (σ_y = 460 MPa and σ_u = 667 MPa) during the landslide process by modeling a three-dimensional pipe in a soil model. The damage process was defined by a TSL with the damage initiation defined by the maximum principal stress σ_{maxps} = 667 MPa (= $\sigma_u = 1.45\sigma_y$) taken from the tensile strength and an exponential response for damage evolution with fracture energy G_C = 180 N/mm obtained from SENB test results. The mesh sensitivity was examined by comparing results of the meshes of 50 × 10 × 3.1 mm and 25 × 10 × 2.5 mm in the fracture process zone along the longitudinal, hoop, and depth direction, respectively, which resulted in no significant variation of numerical results. The same values of σ_{maxps} and G_C were used by Zhang et al. [107] in the simulation of the fatigue crack behaviors of X65 pipe with a circumferential elliptical embedded crack under cyclic tensile loadings and the classical Paris law–based fatigue model was added to the method. The mesh sensitivity was examined by

modeling mesh of 0.3, 0.5, and 0.7 mm in the fracture zone in three directions. Almost the same fatigue crack growth pattern was obtained using mesh sizes of 0.3 and 0.5 mm, indicating that the element size of 0.5 mm was fine enough to produce accurate results. Hojjati-Talemi et al. [108,109] employed the method in the simulation of dynamic brittle fracture of X70 pipe (σ_y = 520 MPa at 23° and σ_y = 760 MPa at -196°) low temperature by modeling a two-dimensional Charpy V-notch (CVN) impact test and a DWTT test. The damage parameters used were σ_{maxps} = 1064 MPa (= $1.4\sigma_y$) and $G_{IC} = K_{IC}^2/\left(E/(1-\nu^2)\right)$ = 2.7 N/mm, where fracture toughness $K_{IC} = 25\text{MPa}\sqrt{\text{m}}$ at -196° derived from measured CVN at the lower shelf of the ductile-to-brittle-transition curve known as Barsom-Rolfe correlation [110]. The mesh sizes used were 0.15 × 0.15 mm in the CVN model and 0.5 × 0.5 mm in the DWTT model at their potential crack propagation regions and the size increased gradually far from the area of interest. In all the studies mentioned, the damage parameters were not calibrated and verified from extensive experiments; on the contrary, they were often estimated, e.g., from tensile strength or Charpy V-notch impact energy. In fact, the implementation of XFEM-based CZM in pipeline fractures studies is still in its early stages.

3.3.2 Experimental Testing on X52 Pipe

The fracture behavior of vintage pipeline steel is starting to become the focus of much research in recent years. In this chapter, the vintage API 5L Grade X52 steel pipes that were experimentally studied by Abdulhameed et al. [37] and Lin [111] at the University of Alberta are investigated numerically. The experimental work included eight full-scale burst tests on circumferentially surface-cracked pipe sections subjected to both internal pressure and eccentric tension [37] and a number of small-scale material tests consisting of 25 tension coupon tests and 24 Charpy V-notch impact tests on specimens cut from the same pipe material [111]. In the full-scale burst tests, each pipe specimen was cut out of the Enbridge vintage X52

Norman Wells pipeline with an outer diameter of 324 mm (NPS 12) and a wall thickness of 6.9 mm (0.27”). The specimens’ length was approximately taken equal to either four or six times the pipe outer diameter, and they were capped by steel plates at two ends, on which a pair of tongue plates were welded with an eccentricity of 50 mm to the pipe longitudinal axis. Each pipe specimen was specially cut with a circumferential surface crack with a depth either 25% or 50% of the pipe wall thickness and a length of 5% or 15% of the pipe circumference, located near the girth weld at the middle length of the pipe specimen. The loading was applied in two steps. In the first step, an internal pressure causing hoop stress corresponding to approximately 70% or 30% of the specified minimum yield strength (SMYS) was applied on the pipe specimen by pressurized water through an opening at the bottom end plate. In the second step, displacement-controlled tensile loading was applied using the material testing system (MTS Systems Corporation, Eden Prairie, Minnesota) machine on the top-side tongue plate when the bottom-side tongue plate was fixed, and consequently the pipe specimen would experience an eccentric tension resulting in a certain level of bending. A digital image correlation (DIC) system was used to evaluate the tensile stain along the pipe surface on the tension side aligned with the circumferential crack. The strains were evaluated by tracking the movements of a speckle pattern produced by black and white spray paint [Figure 3-2 (b)] on the pipe surface from a sequence of recorded images. Additionally, DIC was used to measure the growth of the crack mouth opening displacement (CMOD) by tracking the displacements of two selected reference points on each side of the crack. A number of strain gauges were positioned at a quarter of pipe length, $0.5L$ (L is defined as the half-length of pipe) away from the end plate at 90° intervals around the pipe circumference to measure the tensile strain ($\varepsilon_{0.5L}$) and hoop strain at those locations. Clinometers were attached to both end plates to measure the rotation caused by the eccentric loading. A schematic representation of the test setup and location of the crack and strain gauges is shown in Figure 3-3. The experimental results showed that the burst load

and the tensile strain capacity of the pipe were affected by the level of internal pressure applied and by the initial crack configuration. Additionally, the crack depth showed greater influence on the tensile strain capacity than the crack length.

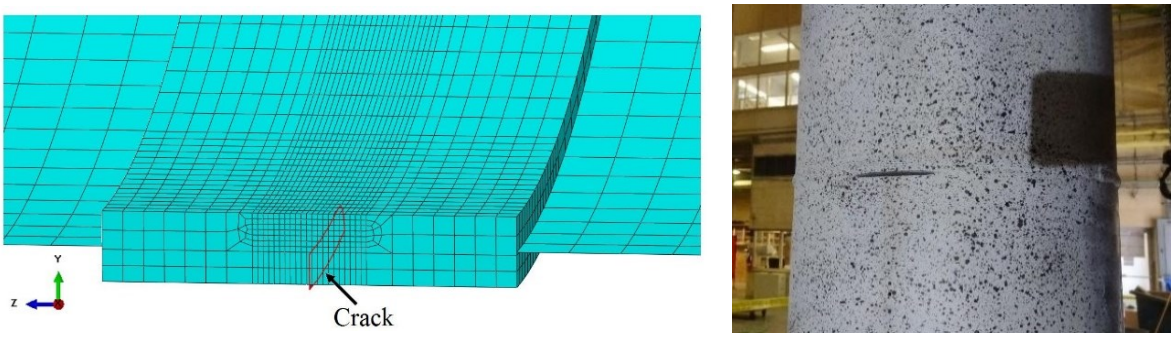

(a) (b)

Figure 3-2. Location of a circumferential crack in (a) a model; and (b) an experiment.

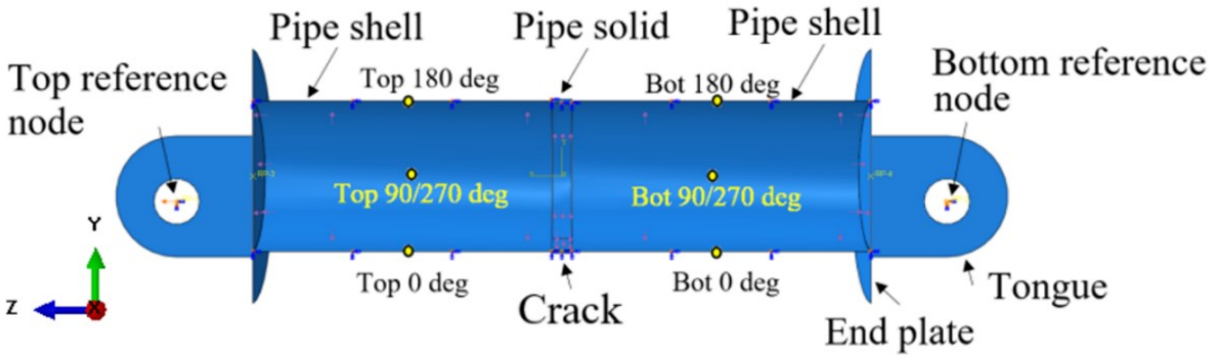

Figure 3-3. Illustration of a model configuration and locations in which $\varepsilon_{0.5L}$ were obtained.

3.4 Numerical Methods and Simulation

3.4.1 XFEM-based Cohesive Segment Approach

The XFEM-based cohesive segment approach implemented in the commercial finite-element system Abaqus/Standard was used in the simulation of the crack propagation of API 5L Grade X52 steel pipes subjected to the combined effects of internal pressure and eccentric tension. This approach was based on traction–separation cohesive behavior used in conventional FEM

to simulate a moving crack along an arbitrary, solution-dependent path in the bulk material. The near-tip asymptotic singularities were not considered, and only the displacement jump across a cracked element was considered. The fracture process defined by a traction– separation response model consists of a damage initiation criterion and a damage evolution law. The response is initially assumed to be linear elastic until a defined damage initiation criterion is satisfied (either stress or strain based), after which the material damage occurs according to a defined damage evolution law. The damage evolution law is defined either based on energy dissipated due to the fracture energy per unit area or based on the effective displacement at the completed surface separation. The available damage evolution law in Abaqus/Standard is either linearly decreasing or exponentially decreasing.

In this chapter, the crack propagation associated with the pipe fracture was assumed mainly under the Mode I fracture type (opening mode), where crack opens perpendicular to the crack plane caused by tension or bending. The maximum principal stress (σ_{maxps}) and fracture energy (G_C) were selected as two key damage parameters to characterize the fracture process, which respectively control the crack initiation and the resistance against crack propagation of Mode I fracture. A higher value of σ_{maxps} resulted in a better deflection-bearing ability of pipeline before damage initiation, while a higher value of G_C resulted in a better fracture toughness to resist the crack propagation after damage initiation. A linear softening traction–separation law shown in Figure 3-1. Typical transition-separation laws: (a) for brittle fracture proposed by Hillerborg [86] and (b) for ductile fracture propose by Scheider [100]. (Adapted from Schwalbe et al. [98].) was used for damage evolution. This shape of TSL was considered suitable to simulate the fracture behaviors of the plastic X52 pipe material because the pipe fractures demonstrated in the experiments by Abdulhameed et al. [37] were considered to be mostly brittle because of the primarily flat fracture surfaces without significant plastic tearing and dimpling.

3.4.2 Setup of Numerical Modelling

A total of eight three-dimensional finite-element models were developed using Abaqus/Standard to simulate the eight experimental full-scale tests, and a corresponding circumferential XFEM crack was respectively added at the middle length of each pipe model (Figure 3-3). Because of symmetry around the YZ-plane, only half of the pipe was modeled. The entire pipe was modeled by combining a solid part (40 mm long) at the center and two shell parts at the sides using the shell-solid coupling constraint to reduce the time required for the numerical calculations. The end plates and tongues were added at each end of the pipe using the tie constraint and were simulated as rigid bodies and represented by two reference nodes with an eccentricity of 50 mm to the longitudinal axis of the pipe. The numerical model of the pipe was first loaded with the internal pressure, then subjected to a tensile displacement assigned at the top reference node with the bottom reference node fixed but allowing rotation about the X-axis. The basic information of each test and model are summarized in Table 3-1 and the geometry of a typical numerical model is illustrated in Figure 3-3.

The two shell parts of the pipe were modeled using a 4-node linear shell element with reduced integration (S4R) and with a global mesh size of 5 mm. The solid part of the pipe was modeled using an 8-node linear brick element with reduced integration (C3D8R), and a mesh construction was carefully defined with a mesh size between 0.5 and 5 mm. In the blocked partitioned region around the crack propagating path, the fine mesh was employed with the element height l_h = 0.5mm (corresponding to 1/13 pipe wall thickness), length l_l = 0.5mm, and thickness l_t = 2mm [Figure 3-2 (a)]. Dimensions l_h, l_l and l_t are in the direction of the pipe wall thickness or crack propagation (in the radial direction), oriented perpendicular to the crack plane (in the longitudinal direction), and oriented parallel to the crack plane (in the hoop/circumferential direction), respectively.

Table 3-1. Basic information of tests and models

Test or Model	Pipe specimen dimensions			Crack dimensions		Internal pressure level	
	Outer diameter[a] (mm)	Pipe length (mm)	Wall thickness (mm)	Crack depth (mm)	Crack length[b] (mm)	Internal pressure (MPa)	Hoop stress/SMYS (%)
Test 1	324	1828.8	6.95	1.7	50	11.65	77
Model 1	304.8	1828.8	6.8	1.7	50	11.65	73
Test 2	324	1828.8	6.8	1.5	50	3.47	23
Model 2	304.8	1828.8	6.8	1.5	50	3.5	22
Test 3	324	1828.8	6.8	3.1	50	11.67	77
Model 3	304.8	1828.8	6.8	3.1	50	11.65	73
Test 4	324	1828.8	6.8	3.3	50	4.74	31
Model 4	304.8	1828.8	6.8	3.3	50	4.65	29
Test 5	324	1219.2	6.8	1.4	150	11.65	77
Model 5	304.8	1219.2	6.8	1.4	150	11.65	73
Test 6	324	1219.2	6.8	1.8	150	4.61	31

Model 6	304.8	1219.2	6.8	1.8	150	4.65	29
Test 7	324	1219.2	6.8	3.5(3.0)[c]	150	11.65	77
Model 7	304.8	1219.2	6.8	3.3	150	11.65	73
Test 8	324	1219.2	6.8	2.7(2.8)[c]	150	4.65	31
Model 8	304.8	1219.2	6.8	2.7	150	4.65	29

[a]The minor discrepancy between the outer diameter dimension of the experiment and the model is due to an initial confusion about the actual outer diameter of NPS12. It is expected to have minimum effect on the results.

[b]Actual initial crack length of each pipe specimen was not measured, thus the target value (5% or 15% pipe circumference) was used (Abdulhameed et al.2016). Simulated XFEM crack length of each model was half of the value in the table due to the symmetry around the YZ-plane.

[c]Actual initial crack depths were measured from two samples cut from pipe Specimens 7 and 8 after pipe failure using fractography (Abdulhameed et al. 2016). Additional measured values are shown in parentheses.

3.4.3 Material Properties

The pipe was simulated as an elastoplastic isotropic material. The material properties were taken from the average of true stress versus true plastic strain curves measured from six coupons cut in the longitudinal direction of the base metal of X52 pipe specimen by Lin [111]. To be more specific, the Young's modulus was 199 Gpa, the Poisson's ratio was 0.3, the 0.2% offset yield strength was 411 Mpa, and the ultimate tensile strength was 473 Mpa with a true plastic strain of 0.147. The curve of the true stress versus true plastic strain is illustrated in Figure 3-4. True stress versus true plastic strain input in the modelling (solid line). Additional true fracture stress σ_f with corresponding true plastic strain ε_f (dash line) was particularly added to assist with the crack propagation in the modeling. They can be calculated from the reduction of cross-sectional area at fracture [112]: $\sigma_f = e_f/(1-q) = 1{,}006$ MPa and $\varepsilon_f = ln\,(1/(1-q)) = 1.125$, where the engineering fracture stress e_f = 325 MPa and reduction of cross-sectional area q = 67.7% were measured from six fractured tension coupons [111].

An initial investigation in determining a suitable set of damage parameters was conducted by Lin et al. [113] and Agbo et al. [114] for Tests 3, 7, and 8. Lin et al. [113] compared the numerical developments of CMOD against the applied tension force obtained from various combinations of σ_{maxps} and G_C for Test 7 to study the effect of changing one parameter when the other was kept constant. Additionally, Agbo et al. [114] compared the numerical developments of tensile strain measured at a quarter length of the pipe away from end plate and at an angle of 90° from the crack location against the applied tension force obtained from various combinations of σ_{maxps} and G_C for Test 8. Both studies concluded that σ_{maxps} = 700 MPa and G_C = 900 N/mm based on a mesh size of $l_h \times l_l \times l_t$ = 0.85 × 0.95 × 2 mm applied in the region around the crack-propagating path were able to estimate the experimental burst load by no more than 6% difference. This research improved the numerical accuracy by using a finer

mesh $l_h \times l_l \times l_t$ = 0.5 × 0.5 × 2 mm in the critical region based on a mesh sensitivity investigation discussed subsequently. After the calibration and verification of the damage parameters using the eight tests, σ_{maxps} = 750 MPa (7% higher than previous calibration) and G_C = 900 N/mm were found to be more suitable in reproducing the overall experimental results, thus this set of values was input to the damage modeling.

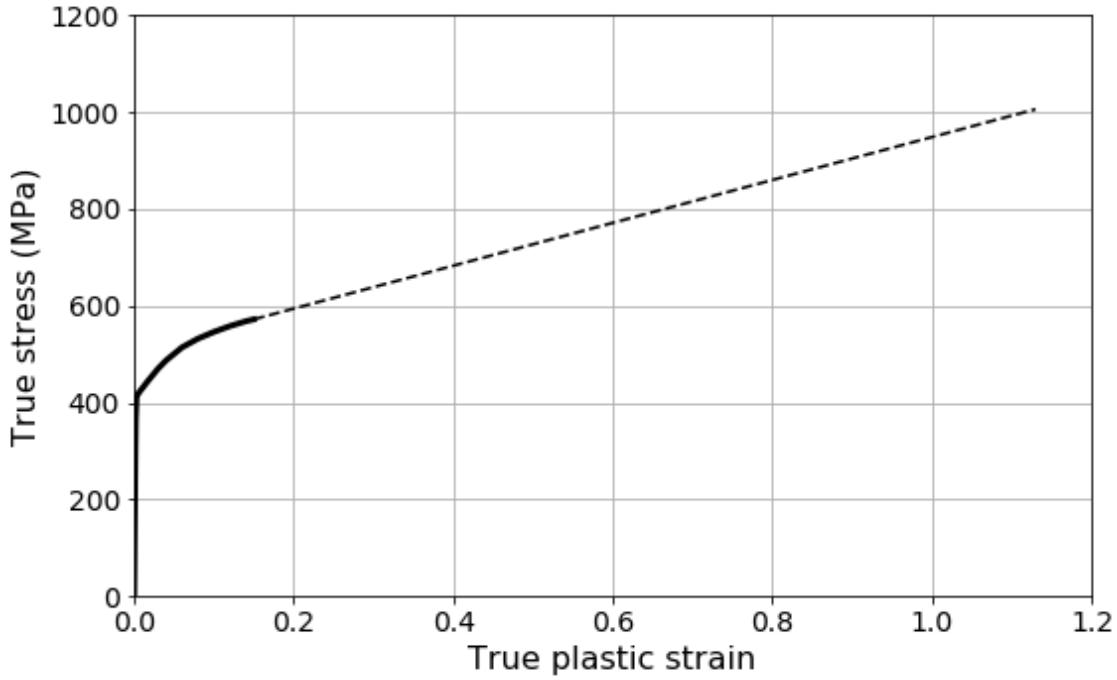

Figure 3-4. True stress versus true plastic strain input in the modelling. Note the dash line is the interpolated extension of from the true ultimate tensile stress to the true fracture stress.

3.5 Numerical Results and Discussion

3.5.1 Validation of Damage Parameter

The validation of the damage parameter set of σ_{maxps} = 750 MPa and G_C = 900 was based on the comparisons between the numerical and experimental results for the eight tests and models in terms of the hoop and tensile strains produced by the internal pressure, tensile strains produced by the combined internal pressure and external tension and bending, end plate

rotation, burst loads, CMOD, and fracture surfaces appearances, as shown in Figure 3-5 to Figure 3-8 and Table 3-2. Two definitions were used for the critical tensile strains (tensile strains at the onset of failure) produced by the experimental combined loadings ($\varepsilon_{0.5L}$ and ε_{avg}). $\varepsilon_{0.5L}$ is defined as the tensile strain at the onset of failure measured at a quarter of the pipe length away from the end plate at 90° intervals around the pipe circumference (at an angle of 0°, 90°, 270°, or 180° from the crack), and ε_{avg} is defined as the averaged tensile strain at the onset of failure measured from the outer surface at an angle of 0° from the crack (at the tension side of pipe) along the pipe length in a range from 10% to 40% of the pipe length (from $0.2L$ to $0.8L$) on both sides away from crack. For Tests and Models 1–4, this range is 185–730 mm from the crack. For Tests and Models 5–8, this range is 120–490 mm from the crack. Regarding the CMOD, there were also two critical definitions, $CMOD_{failure}$ and $CMOD_{critical}$: $CMOD_{failure}$ is the CMOD at the point in time when the water starts to seep out of the crack in the test or the crack propagates through the whole pipe wall thickness in the model, and $CMOD_{critical}$ is the CMOD at the point in time when the applied load was almost constant but the CMOD increased sharply, which is simply represented by the time when the load reaches 98% of the maximum load in each test or model.

3.5.1.1 Comparison of strains produced by internal pressure

After the first loading step of internal pressure, the numerical longitudinal or tensile strains and hoop strains produced by the applied internal pressure were examined by both experimental and theoretical strains. The averaged strains measured from critical locations shown in Figure 3-3 were used in the comparison, in which experimental strain gauges were installed at a quarter of the pipe length from the end plate at 90° intervals around the pipe circumference. The theoretical strains were calculated based on Barlow's formula. For a long section of a thin-walled pipe with capped ends, the resisting hoop and longitudinal stress and strain caused by

the internal pressure are [50] $\sigma_l = PD/4t$, $\sigma_h = PD/2t$, $\varepsilon_l = \sigma_L/E - \nu\sigma_h/E$, $\varepsilon_h = \sigma_h/E - \nu\sigma_l/E$, where σ_l, σ_h, ε_l, ε_h are longitudinal stress, hoop stress, longitudinal strain, and hoop strain respectively, P, D, and t are internal pressure, pipe outer diameter, and pipe wall thickness, respectively, and E, and ν are Young's modulus and Poisson's ratio, respectively.

For the eight models, the magnitude differences between the numerical and the theoretical hoop or tensile strain were less than 0.00003, while those between the numerical and the experimental hoop or tensile strain were less than 0.00007. To be more specific, the numerical hoop strains were roughly 3% lower to 1% higher than the theoretical hoop strains, and they were roughly 4% lower to 6% higher than the experimental hoop strains except for Model 6, which were 18% higher. The numerical tensile strains were roughly 10%–13% lower than the theoretical tensile strains, and they were roughly 15%–25% lower than the experimental tensile strains.

3.5.1.2 Comparison of tensile strains produced by combined loadings

At failure, the numerical tensile strains measured from the outer pipe surface at 0° from the crack were plotted along the pipe length for each model and were respectively compared with their experimental tensile strain profiles obtained from the DIC technique (Figure 3-5). The numerical models were able to predict the tensile strains in a region very close to the crack where the DIC technique was not able to produce meaningful results owing to the lack of speckles painted at those locations [37]. The tensile strain decreased from the pipe end to the pipe center at which the crack was located. The local compressive strain (negative values) generated around the crack was caused by a large-scale tension generated at the inside (pressurized) surface of the pipe. The averaged tensile strain ε_{avg} and tensile strain at critical locations $\varepsilon_{0.5L}$ measured at pipe failure are listed in Table 3-2. Among total tests and models, the difference between experimental and numerical tensile strain ε_{avg} or $\varepsilon_{0.5L}$were less than

30%. The general higher experimental tensile strain at failure might be caused by the original crack fabricated on pipe specimens being less sharp. Another reason might be the existence of multiple initial cracks rather than a single crack, which was observed from fractographic studies of the fracture surfaces [37]. Both possibilities would require higher energy to cause pipe fracture, resulting in higher tensile strain capacity.

3.5.1.3 Comparison of burst loads, end plate rotation and CMOD

During the second loading step of longitudinal eccentric tensile loading, the developments of the end plate rotation and CMOD for each model were respectively plotted against the reaction force generated at the top reference node and compared with the corresponding experimental results in Figure 3-6 and Figure 3-7. As shown in Table 3-2, the numerical burst loads were roughly 13% lower to 2% higher than the experimental burst loads for all tests and models, resulting in a maximum difference of 303 kN measured in Test and Model 6. Tests and Models 1 and 7 fractured at the maximum load, while Tests and Models 2–6 and 8 fractured slightly after the maximum load was reached. The numerical end plate rotations at failure were roughly 20% lower to 12% higher than experimental rotations for all tests and models, resulting in a maximum difference of 0.85° measured in Test and Model 2. The numerical $CMOD_{failure}$ values were roughly 32% lower to 22% higher than experimental $CMOD_{failure}$ resulting in a maximum difference of 0.77 mm measured in Test and Model 3. The numerical $CMOD_{critical}$ values were roughly equal to 10% higher than experimental $CMOD_{critical}$, expect for Test and Model 4, which were 31% lower. The differences in $CMOD_{critical}$ values between the models and the tests were minimal compared to the differences in $CMOD_{failure}$ between the models and tests. This is perhaps because $CMOD_{critical}$ does not consider the dynamic effects due to the sudden release of internal pressure during the test.

3.5.1.4 Comparison of fracture surfaces

The numerical fracture surfaces were compared with corresponding experimental fracture surfaces analyzed by the fractographic method [37]. A typical appearance of the experimental fracture surface (Test 1) emanating from the original machined crack (flaw) is shown in Figure 3-8 (b) viewed in the longitudinal direction of the pipe and (c) viewed in the circumferential direction of pipe. The experimental study [37] considered the experimental fracture surface to be mostly brittle because it was primarily flat without significant plastic tearing and dimpling although some plasticity was observed in the inner pipe surface owing to the internal pressure. Table 2 summarizes the reduction of pipe wall thickness for each test and model as well as their 10%–23% difference in reduction of pipe wall thickness. The higher percentage of experimental reduction of pipe wall thickness indicated that the fracture experienced more plasticity in tests than in models. This might be caused by the immense impact resulting from the sudden release of internal pressure when fracture happened during tests, while it was not simulated in the numerical modeling.

Table 3-2. Comparison between numerical and experimental results at failure

Test or model	Burst load (max load) (kN)	Rotation at end plate (°)	$CMOD_{failure}$ ($CMOD_{critical}$) (mm)	Tensile strain (%)			Reduction of pipe wall thickness (%)
				$\varepsilon_{0.5L}$		ε_{avg}	
				At 0°	At 90°/270°	In 0.2L~0.8L	
Test 1	2299	5.08	2.11 (1.19)	—	1.950	3	32.4
Model 1	2335	5.67	1.83 (1.31)	2.620	1.340	2.898	9.3
Diff.	+2%	+12%	-13% (+10%)	—	-31%	-3%	-23
Test 2	3100 (3109)	6.82	2.16 (1.09)	—	—	8	27.9
Model 2	2975 (2977)	7.67	2.16 (1.21)	5.351	4.276	7.405	9.7
Diff.	-4%	+12%	0% (+11%)	—	—	-7%	-18
Test 3	1623 (1664)	0.98	2.37 (1.18)	0.510	0.328	0.530	19.1
Model 3	1653	0.78	1.60 (1.31)	0.419	0.239	0.414	9.0
Diff.	+2%	-20%	-32% (+11%)	-18%	-27%	-22%	-10
Test 4	2061 (2075)	1.04	2.05 (1.16)	0.533	0.321	0.553	20.6
Model 4	1919	0.96	1.55 (0.80)	0.480	0.271	0.492	8.5

Diff.	-7%	-8%	-24% (-31%)	-10%	-16%	-11%	-12
Test 5	1934 (1962)	1.86	1.52 (0.77)	—	0.900	1.846	26.5
Model 5	1786 (1854)	1.86	1.85 (0.83)	1.364	0.700	1.391	10.3
Diff.	-8%	0%	+22% (+8%)	—	-22%	-25%	-16
Test 6	2261 (2268)	1.40	1.56 (0.90)	1.204	0.647	1.324	27.9
Model 6	1958 (1997)	1.28	1.74 (0.90)	0.942	0.488	0.966	9.1
Diff.	-13%	-9%	+12% (0%)	-22%	-25%	-27%	-19
Test 7	1304	0.26	1.30 (0.90)	0.208	0.177	0.217	19.1
Model 7	1261	0.25	1.42 (1.00)	0.157	0.151	0.155	8.7
Diff.	-3%	-4%	+9% (+11%)	-25%	-15%	-29%	-10
Test 8	1831 (1844)	0.42	1.27 (0.85)	0.293	0.218	0.305	20.6
Model 8	1657 (1669)	0.36	1.50 (0.89)	0.241	0.184	0.237	9.0
Diff.	-10%	-14%	+18% (+5%)	-18%	-16%	-22%	-12

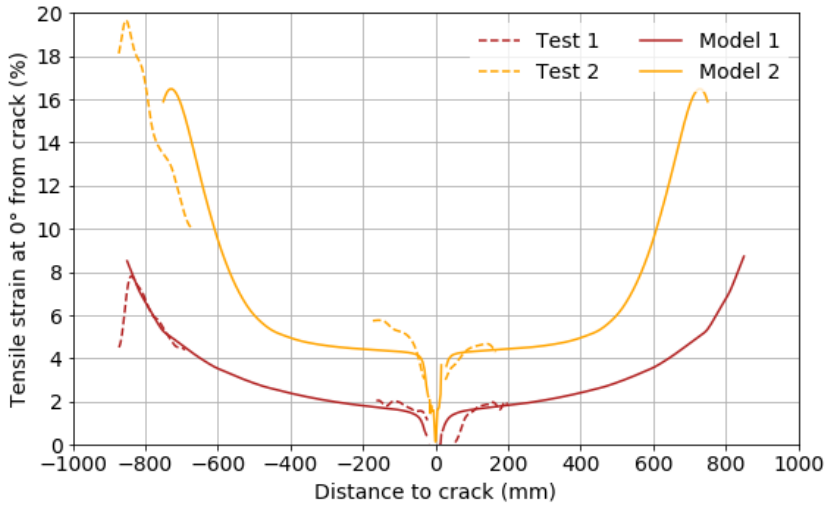

(a)

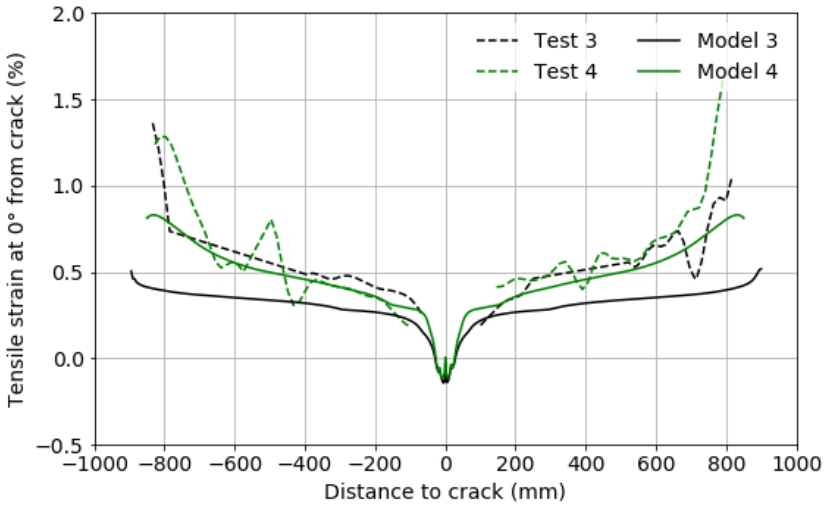

(b)

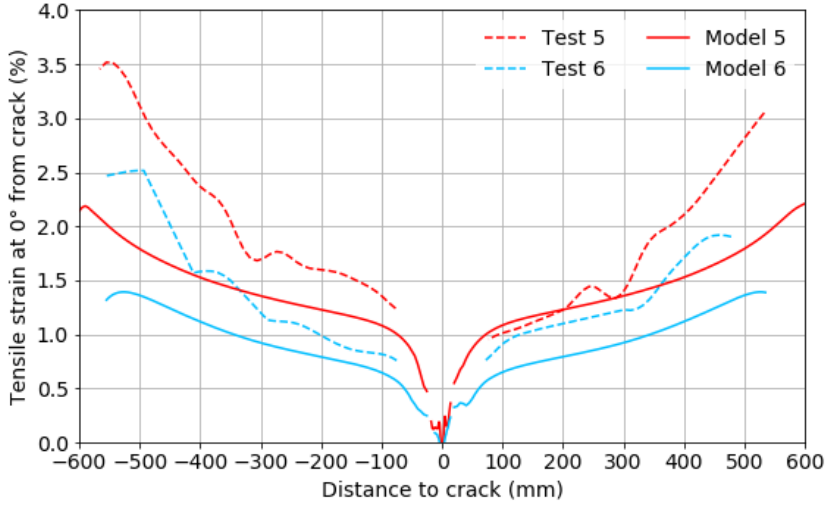

(c)

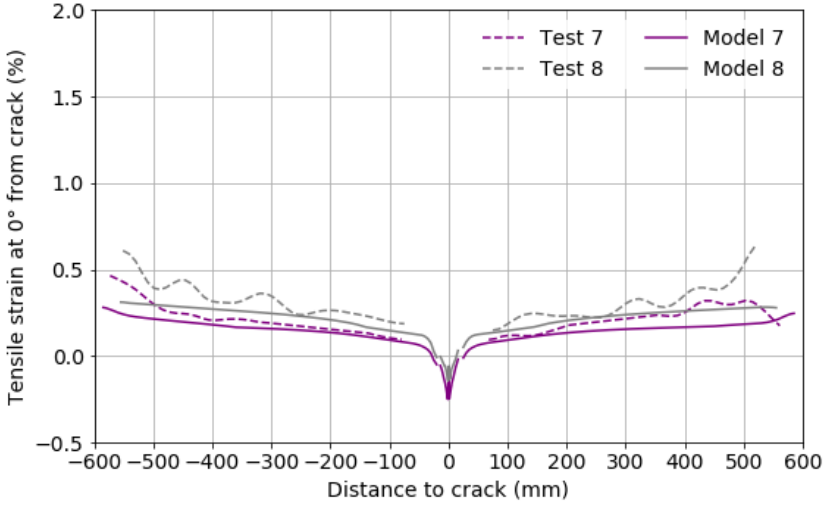

(d)

Figure 3-5. Comparison of tensile strains along the pipe length from Models and Tests (a) 1-2; (b) 3-4; (c) 5-6; and (d) 7-8.

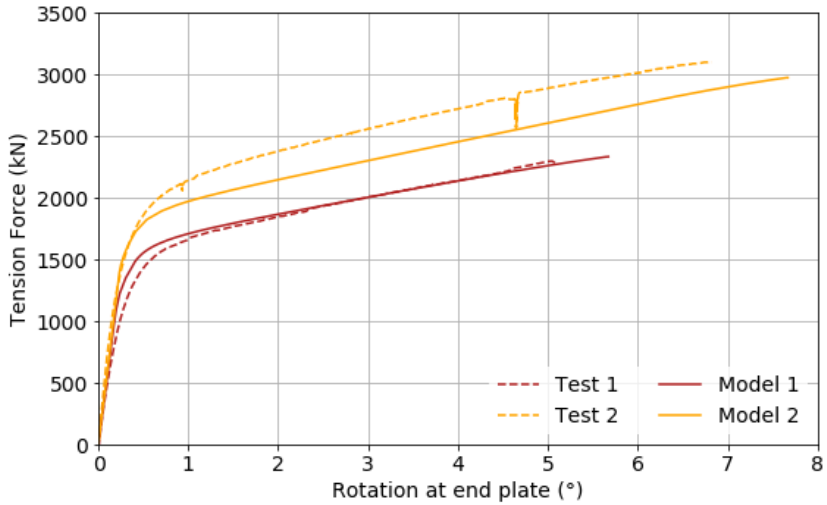

(a)

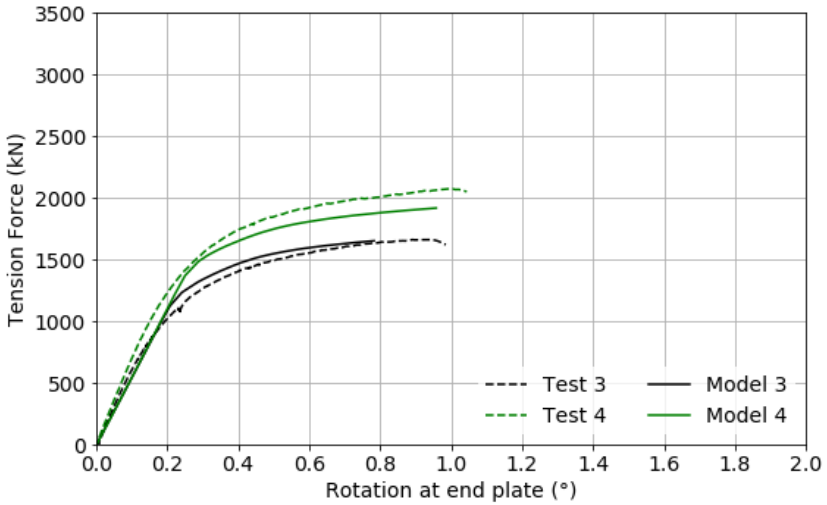

(b)

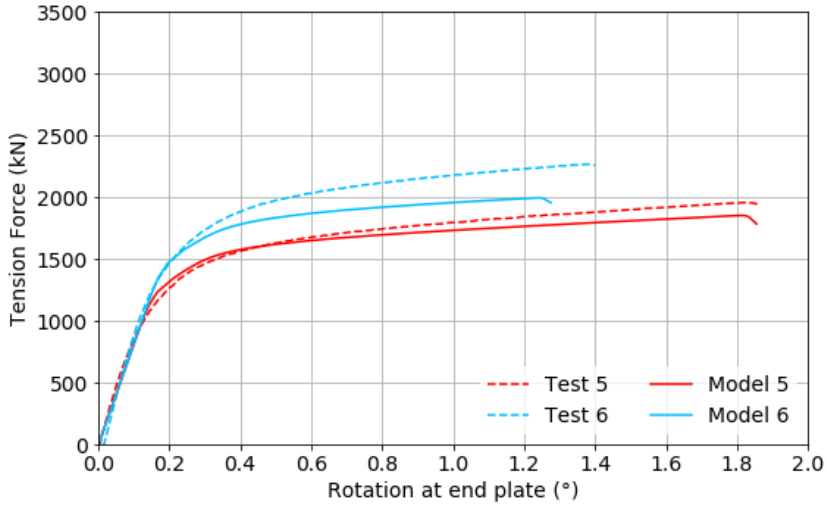

(c)

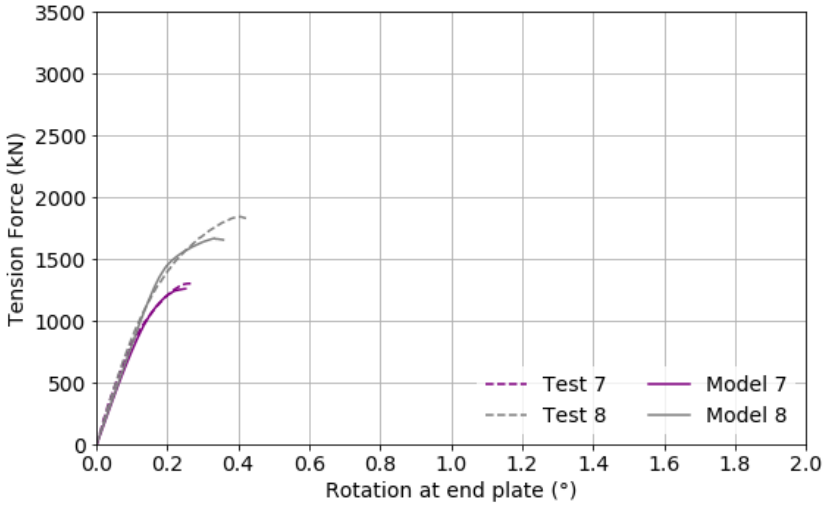

(d)

Figure 3-6. Comparison of force-rotation curves from Models and Tests (a) 1-2; (b) 3-4; (c) 5-6; and (d) 7-8.

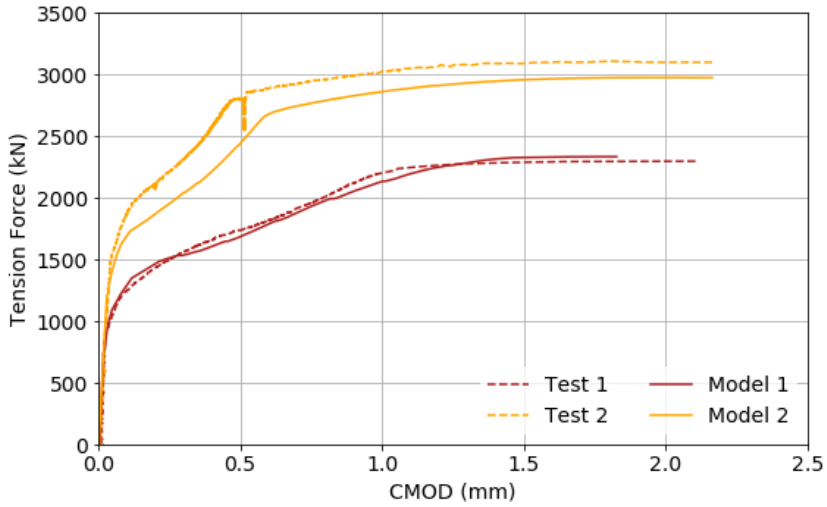

(a)

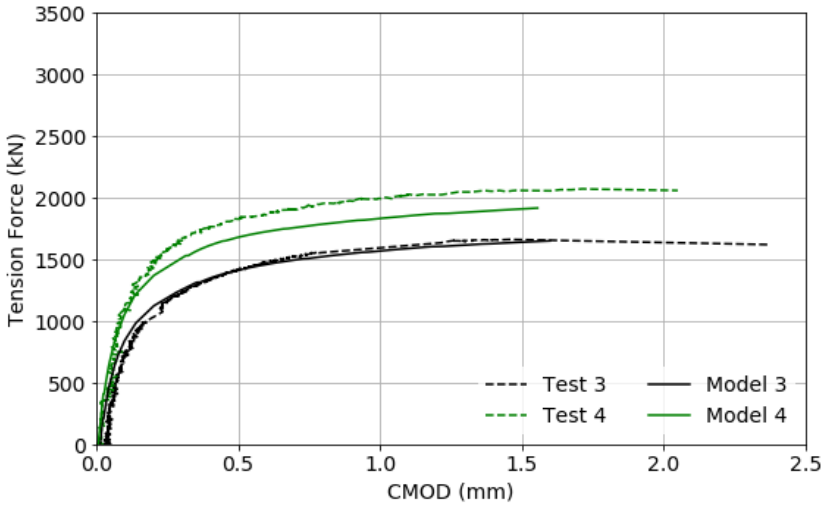

(b)

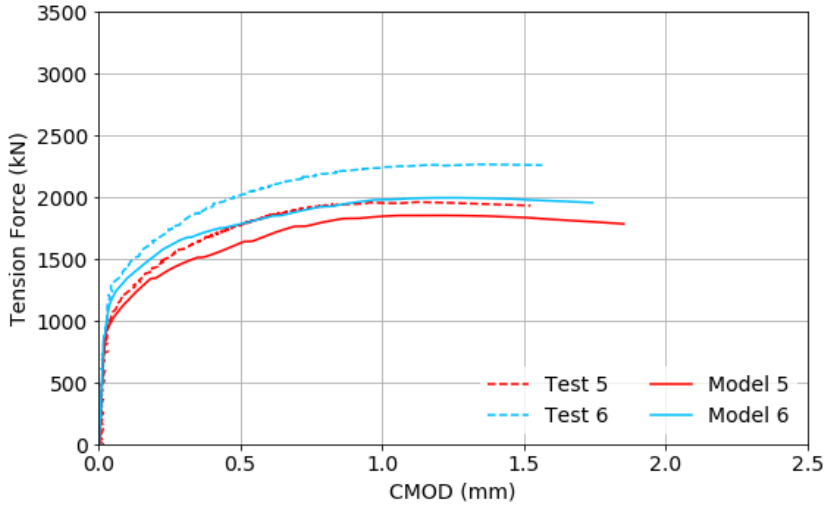

(c)

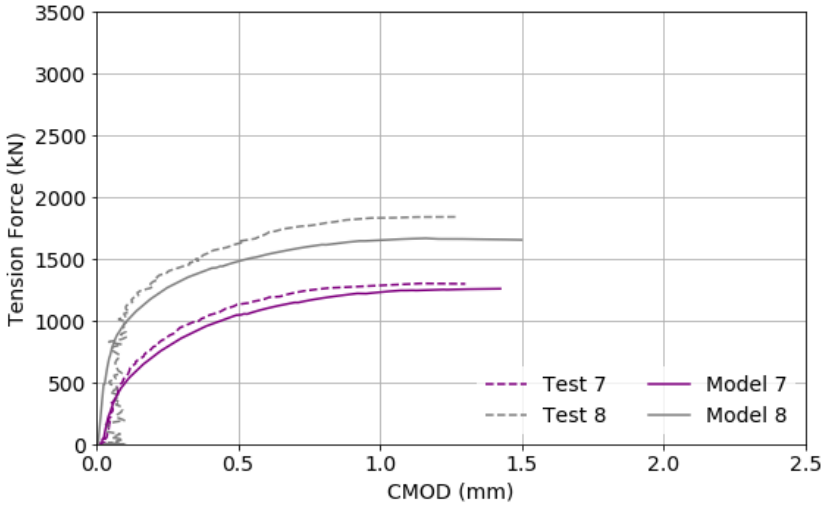

(d)

Figure 3-7. Comparison of force-CMOD curves Models and Tests (a) 1-2; (b) 3-4; (c) 5-6; and (d) 7-8.

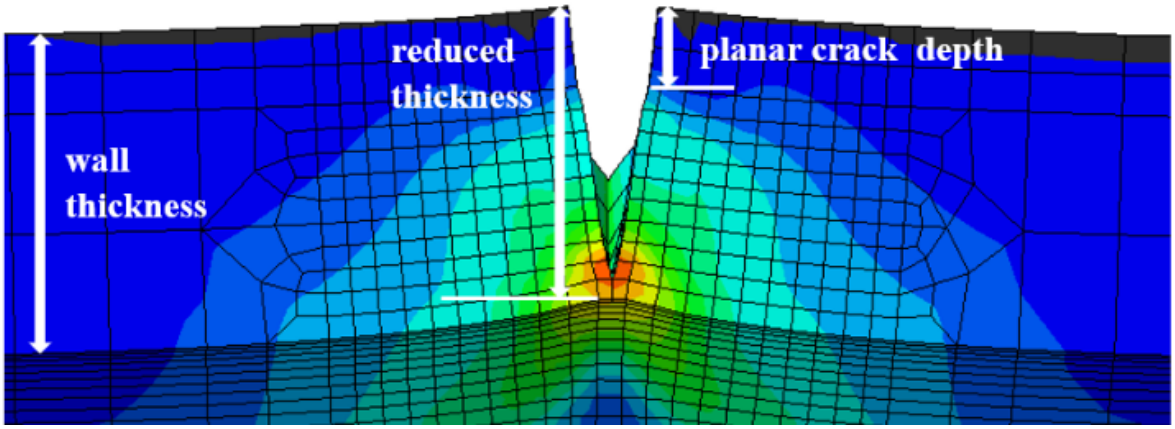

(a)

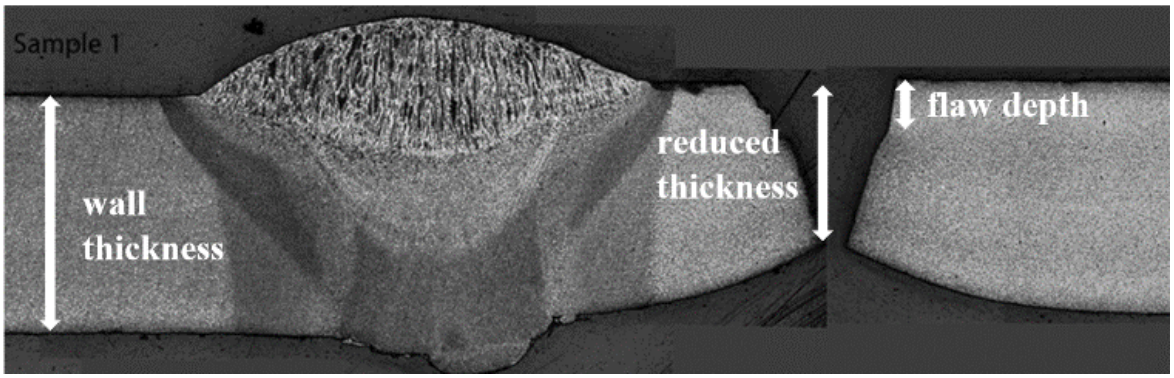

(b)

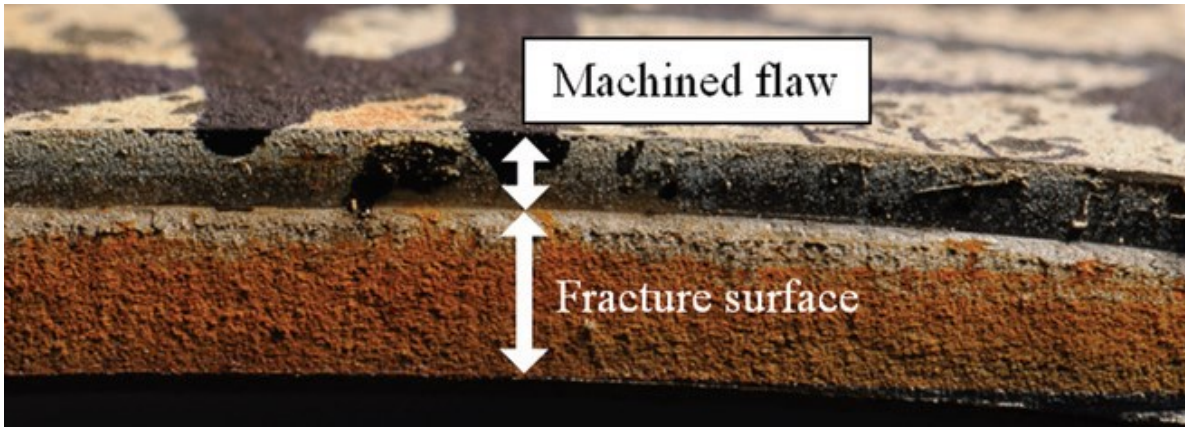

(c)

Figure 3-8. Comparison of fracture surfaces obtained from (a) Model 1; (b) Test 1 in the longitudinal direction; and (c) Test 1 in the circumferential direction.

3.5.2 Correlation between Damage Parameters and Yield Strength and Fracture Toughness

Because the XFEM-based cohesive segment method was based on traction–separation cohesive behavior used in conventional FEM, the maximum principal stress σ_{maxps} and fracture energy G_C can be correlated to the cohesive strength T_0 and cohesive energy Γ_0 in the FEM-based CZM, with the relationship $\sigma_{maxps} = T_0$ and $G_C = \Gamma_0$. The accurate damage parameters or cohesive parameters should be determined from experiments and optimized from numerical simulations. In CZM, the cohesive strength T_0 can be taken from the maximum value of stress over a notched tensile bar's instantaneous cross section at fracture, which is equal to the true tensile strength σ_u for fracture without localized necking, or higher than the true tensile strength for fracture with localized necking [98,115]. The cohesive energy Γ_0 can be taken from linear elastic energy release rate $G_{Ic} = K_{Ic}^2/E'$ within the framework of linear elastic fracture mechanics, or from the J-integral at initiation of stable ductile crack extension within the framework of elastic-plastic fracture mechanics $J_i \approx K_{Ic}^2/E'$, where $E' = E$ for plane stress assumption, while $E' = E/(1-\nu^2)$ for plane strain assumption [98,115]. For ductile structural steels, a rough estimation of cohesive parameters was suggested by Schwalbe et al. (2013) around $T_0 \approx 3\sigma_y$ and $\Gamma_0 \approx K_{Ic}^2/E'$. Recalling previous numerical studies on modern API 5L pipeline steel, Nonn and Kalwa (2013) suggested $T_0 = 2.85\sigma_y$ and $T_0 = 2.4\sigma_y$ for X65 and X80 steels, respectively, and $\Gamma_0 \approx J_i$ at initiation of ductile crack extension in the J-resistance curve obtained for DWTT tests for both materials. Hojjati-Talemi et al. [108,109] suggested $\sigma_{maxps} = 1.4\sigma_y$ and $G_{IC} \approx K_{IC}^2/\big(E/(1-\nu^2)\big)$ for dynamic brittle fracture of X70 steel at low temperature, where K_{IC} was correlated from Charpy V-notch impact energy. The difference of values of cohesive parameters was caused by selecting the different shape of TSL, which implied the TSL shape dependency for the calibration of cohesive parameters.

In this work, the material properties of X52 pipe steel under consideration measured or empirically estimated by Lin [111] included 0.2% offset yield strength σ_y = 411Mpa, Young' modulus E = 199 Gpa, Poisson's ratio ν = 0.3, estimated plane-strain stress intensity factor K_{Ic} = 207 Mpa$\sqrt{m}$ based on CVN impact energy = 167 J, and estimated plane strain fracture toughness $J_{IC} = G_{Ic} = K_{Ic}^2/\left(E/(1-\nu^2)\right)$ = 196 N/mm. Then the relationship between the damage parameters σ_{maxps} = 750 MPa and G_C = 900N/mm and yield strength and fracture toughness were $\sigma_{maxps} = 1.8\sigma_y$ and $G_C = 4.6\ K_{Ic}^2/\left(E/(1-\nu^2)\right)$. The calibration of damage parameters was based on the agreement of experimental results at pipe failure, which is defined in the model as the point of time when the crack tip (or element damage) reaches the inner surface of the numerical pipe. As shown in Figure 3-9. XFEM crack propagation obtained from Model 3 regarding (a) max principal stress and (b) status of enriched element, the original XFEM crack represented by the bottom two red layers of elements started to propagate through the first enriched Element 1 in which σ_{maxps} reached 750 MPa. Afterwards, the crack propagated mainly along the direction of pipe wall thickness until the crack tip reached the inner surface of the pipe, where the enriched Element 2 was damaged (defined as failure). The status of the enriched element in showed that all elements through the remaining ligament were damaged (STATUSXFEM > 0). This can also be seen in Figure 3-10. Comparison of the shape of TSL between the input damage parameters and the numerical model obtained from the first damaged enriched element (Element 1) on Model 3, where the shape of the TSL obtained from Element 1 in Model 3 roughly followed the linearly decreasing pattern, but the final value of σ_{maxps} did not decrease to zero when Element 2 is damaged. Also, the numerically obtained shape was slightly different from the TSL curve based on σ_{maxps} = 750 MPa and G_C = 900 N/mm because of the significant drop in the early stage caused by the crack initiation. The same behavior was obtained when using σ_{maxps} = 800 MPa and G_C = 900N/mm. For Element 1, the energy dissipated accompanying the crack opening can be roughly calculated from the

area under the resulted trapezoid shape, which was roughly 535 N/mm (=2.7$K_{Ic}^2/\left(E/(1-\nu^2)\right)$) for the case of using σ_{maxps} = 750 MPa and G_C = 900N/mm, and 600 N/mm (=3 $K_{Ic}^2/\left(E/(1-\nu^2)\right)$) for the case of using σ_{maxps} = 800 MPa and G_C = 900 N/mm. However, even though the energy dissipated until failure did not reach to 900 N/mm, a lower input G_C is not recommended because it would result in failure loads that are significantly lower than the experimental results, which was also shown previously by Lin et al. [113] and Agbo et al. [114]. Although the enriched elements were not completely damaged in the analysis, the numerical results agreed well with the experimental results.

Some researchers [98,116–118] have also proposed that the shape of TSL and their related cohesive parameters are strongly dependent on the stress triaxiality (h), defined by the hydrostatic stress (mean normal stress) over the von Mises equivalent stress $h = ((\sigma_{11}+\sigma_{22}+\sigma_{33})/3)/\sigma_v$. A typical relationship was proposed by Anvari et al. [116] who plotted curves of normalized cohesive strength (T_0/σ_y) and normalized cohesive energy ($\Gamma_0/\sigma_y D_{cell}$) against stress triaxiality (h) for rate-insensitive material based on a unit cell simulation using the Gurson-Tvergaard-Needleman (GTN) model on a ferritic steel. GTN is another widely used damage model in simulating the ductile crack process, but it require up to nine damage parameters calibrated from a fracture resistance curve test and results are strongly mesh size dependent [98]. As shown in Figure 3-11, as h increases from 1 to 5, T_0/σ_y increases from 2 to 4, while $\Gamma_0/\sigma_y D_{cell}$ decreases from 1.5 to 0.2, where D_{cell} is the element height of GTN unit cell. Lower triaxiality resulted in a decrease of cohesive strength but an increase of cohesive energy. For Model 3 in this work, the triaxiality at the crack tip at failure obtained from Element 2 was 0.677 when using σ_{maxps} = 750 MPa and G_C = 900 N/mm, while it was 0.690 when using σ_{maxps} = 800 MPa and G_C = 900 N/mm. Both cases resulted in a triaxiality value lower than 1, which explained the relatively lower ratio of σ_{maxps}/σ_y around 1.8 but

higher ratio of $G_C/\left(K_{Ic}^2/\left(E/(1-\nu^2)\right)\right)$ around 4.6 computed in these models.

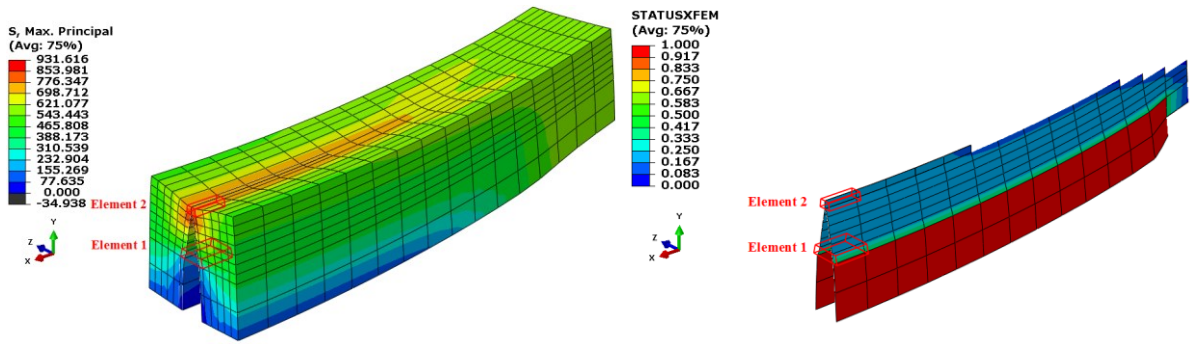

(a) (b)

Figure 3-9. XFEM crack propagation obtained from Model 3 regarding (a) max principal stress and (b) status of enriched element.

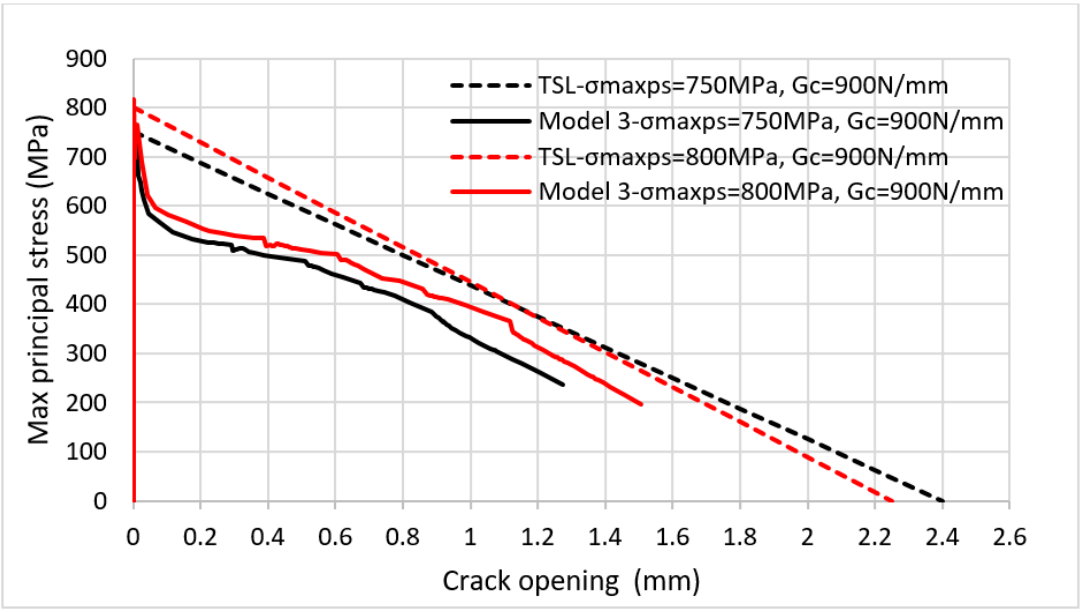

Figure 3-10. Comparison of the shape of TSL between the input damage parameters and the numerical model obtained from the first damaged enriched element (Element 1) on Model 3.

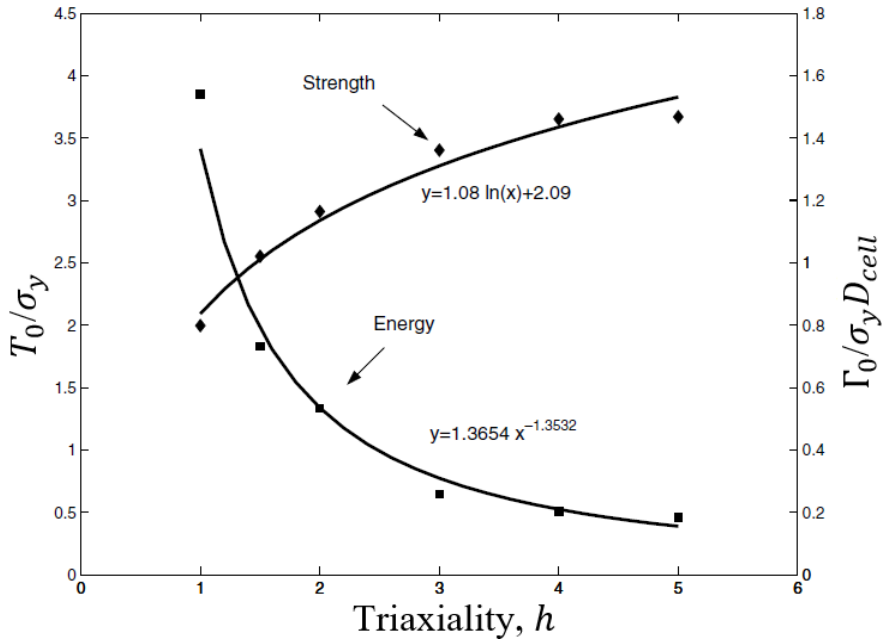

Figure 3-11. Dependence of normalized cohesive strength and energy on stress triaxiality for ferritic steel determined from GTN unit cell simulations by Anvari, et al. [116].

3.5.3 Investigation of Mesh Size Sensitivity

A suitable finite-element mesh has a significant effect on the numerical stability and computational accuracy, which has been addressed by numerous researchers in the past. As a rule of thumb, the recommended size of elements in the direction of crack propagation should be in the range of 0.05 to 0.25 mm for ductile materials in FEM [98]. Carpinteri and Colombo [119,120] examined the mesh refinement on the regularity of simulated load-deformation responses of a three-point bending beam for different brittleness numbers (s_E) using the FEM-based linear elastic fracture mechanics (LEFM) approach. For brittle material with a low value of s_E, the cohesive zone is confined to a small crack tip region, thus a refined mesh is required. They proposed a lower bound of $s_E = G_{IC}/(\sigma_u b) = G_{IC}/(\sigma_u mh) \geq 0.0008/m$ to obtain reasonable results for a brittle material with an ultimate tensile strain $\varepsilon_u = \sigma_u/E$= 0.000087, where h and m are finite element size and numbers, $b = mh$ is the beam depth. The material characteristic length $l_{ch} = G_{IC}E'/({\sigma_u}^2)$ defined by Hillerborg et al. [86] can be correlated to

brittleness number by $s_E = \varepsilon_u(l_{ch}/b) = \varepsilon_u(l_{ch}/mh)$. Then the lower bound of s_E can be rewritten as $l_{ch}/h \geq 0.0008/\varepsilon_u$ = 9.2. Based on a minimum number of 10 elements per characteristic length, the critical finite-element size h around the crack tip should satisfy $h \leq G_{Ic}E'/(10{\sigma_u}^2)$, where $E' = E$ for plane stress assumption and $E' = E/(1-\nu^2)$ for plane strain assumption. The mesh sensitivity based on the same specimen configuration and material properties were further studied by Moës and Belytschko [121] and Mojiri [122] using XFEM-based LEFM approach. Moës and Belytschko [121] examined the independence of XFEM results to the mesh matching or not matching the cohesive crack path. Mojiri [122] obtained very similar results as Carpinteri and Colombo [120] but using fewer elements, which demonstrated the accuracy and efficiency of XFEM. In addition to the critical mesh size, proper meshing technique is often recommended to ensure reliable results. Oliveira [123] suggested defining a structured mesh, such as hexahedral shape in three dimensions, with high density to achieve satisfying results in the XFEM framework. Additionally, for efficient use of computational resources, proper mesh partitions are recommend allowing a finer mesh around the crack but a coarser mesh for other regions. In the study of stationary cracks in SENT and SENB simulations, 80 elements per partition length corresponding to 0.05 mm near the crack was suggested resulting in less than 3% error of stress intensity factor (K_I). The generated computation time was significantly less than that using a constant element size of 0.2 mm for total specimen geometry [123].

Following $h \leq G_{Ic}E'/(10{\sigma_u}^2)$ proposed by Carpinteri and Colombo [119,120], the critical element size in this work was calculated to be 32 mm based on G_C = 900 N/mm and σ_{maxps} = 750 MPa replacing σ_u, which seemed too coarse. As in this chapter, the crack propagated through the pipe wall thickness direction, the critical element size of 0.085mm corresponding to 1/80 of pipe wall thickness suggested by Oliveira [123] seemed too fine. On the other hand, the element size corresponding to 1/12 of specimen thickness used in Nonn and Kalwa

[103,104] and Scheider et al. [105] was more appropriate for current analyses. The finally chosen mesh size in the partitioned critical region around the crack propagating path in current study was $l_h \times l_l \times l_t$ =0.5 × 0.5 × 2 mm, where the element height l_h corresponded to 1/13 of the pipe wall thickness. In addition, this mesh size was examined in Model 3 as the adequate size in predicting the pipe failure, in terms of burst load, end plate rotation, $CMOD_{failure}$, and tensile strains at various critical locations. Two sets of damage parameters were included in the investigation to exclude the effect caused by inputting different material properties. The first set σ_{maxps}= 750 Mpa and G_C = 900 N/mm was generally suitable for the eight models in producing experimental results, while the second set σ_{maxps} = 800 Mpa and G_C = 900 N/mm, was most suitable for Model 3 itself. The effect of mesh size on the numerical results was examined by changing the mesh size in the region around the crack propagating path in the l_h, l_l and l_t three directions (Table 3-3). In the second set, further reduction of l_h, l_l, and l_t to 0.25, 0.25 and 1 mm, respectively, resulted in less than 10% variation of the numerical results in all respects, including 0.2%, 0.8% and 0.1% variation in burst load, 2.1%, 8.2% and 1.0% variation in end plate rotation at failure, 7%, 9.7% and 1.1% variation in CMOD at failure, and 3%, 5.8% and 0.2% variation in ε_{avg}. The variations obtained from the first set were slightly higher but still acceptable to ease the computational burden caused by analyzing considerable numbers of elements. The comparisons of tensile strains at the tension side of pipe along the pipe length at failure obtained from two sets are shown in Figure 3-12. Comparison of tensile strain at the tension side of pipe at failure obtained from Test 3 and Model 3 using σ_{maxps}= 750 MPa and G_c = 900 N/mm: (a) change of l_h; (b) change of l_l; and (c) change of l_t and Figure 3-13. The higher variation caused by changing l_l indicated it was more critical in predicting fracture behaviors than the dimensions in the other two directions. Future studies may be conducted in further reducing the element length oriented perpendicular to the crack plane to minimize its sensitivity.

Table 3-3. Investigation of mesh sensitivity on fracture behaviors of Model 3

Model	Mesh size in the region around crack, $l_h \times l_l \times l_t$	Burst load (kN)	Rotation at end plate (°)	$CMOD_{failure}$ (mm)	Tensile strain at fracture (%)			
					$\varepsilon_{0.5L}$			
					At 0°	At 90°/270°	At 180°	ε_{avg}
Model 3 with σ_{maxps}= 750 Mpa and G_C = 900 N/mm	1×0.5×2	1664	0.82	1.56	0.440	0.248	0.029	0.437
	0.5×0.5×2	1653	0.78	1.60	0.419	0.239	0.031	0.414
	0.25×0.5×2	1649	0.77	1.69	0.409	0.236	0.031	0.403
	0.5×1×2	1716	1.09	2.10	0.546	0.298	0.021	0.546
	0.5×0.25×2	1617	0.66	1.40	0.367	0.216	0.035	0.360
	0.5×0.5×1	1639	0.73	1.51	0.395	0.229	0.033	0.390
			Change of l_h					
	Diff. from l_h=1 to l_h=0.5	-0.7%	-4.9%	+2.6%	-4.8%	-3.6%	+6.9%	-5.3%
	Diff. from l_h=0.5 to l_h=0.25	-0.2%	-1.3%	+5.6%	-2.4%	-1.3%	0.0%	-2.7%
			Change of l_l					
	Diff. from l_l=1 to l_l=0.5	-3.7%	-28.4%	-23.8%	-23.3%	-19.8%	+47.6%	-24.2%
	Diff. from l_l=0.5 to l_l=0.25	-2.2%	-15.4%	-12.5%	-12.4%	-9.6%	+12.9%	-13.0%
			Change of l_t					
	Diff. from l_t=2 to l_l=1	-0.8%	-6.4%	-5.6%	-5.7%	-4.2%	+6.5%	-5.8%

	1×0.5×2	1707	1.03	1.78	0.531	0.290	0.023	0.534
	0.5×0.5×2	1694	0.97	1.86	0.496	0.275	0.024	0.497
	0.25×0.5×2	1690	0.95	1.99	0.481	0.270	0.025	0.482
	0.5×1×2	1766	1.39	2.39	0.678	0.360	0.015	0.690
	0.5×0.25×2	1680	0.89	1.68	0.468	0.262	0.027	0.468
Model 3 with	0.5×0.5×1	1693	0.96	1.84	0.495	0.275	0.024	0.496
σ_{maxps}= 800				Change of l_h				
Mpa and G_C	Diff. from l_h=1 to l_h=0.5	-0.8%	-5.8%	+4.5%	-6.6%	-5.2%	+4.3%	-6.9%
= 900 N/mm	Diff. from l_h=0.5 to l_h=0.25	-0.2%	-2.1%	+7.0%	-3.0%	-1.8%	+4.2%	-3.0%
				Change of l_l				
	Diff. from l_l=1 to l_l=0.5	-4.1%	-30.2%	-22.2%	-26.8%	-23.6%	+60.0%	-28.0%
	Diff. from l_l=0.5 to l_l=0.25	-0.8%	-8.2%	-9.7%	-5.6%	-4.7%	+12.5%	-5.8%
				Change of l_t				
	Diff. from l_t=2 to l_l=1	-0.1%	-1.0%	-1.1%	-0.2%	0.0%	0.0%	-0.2%

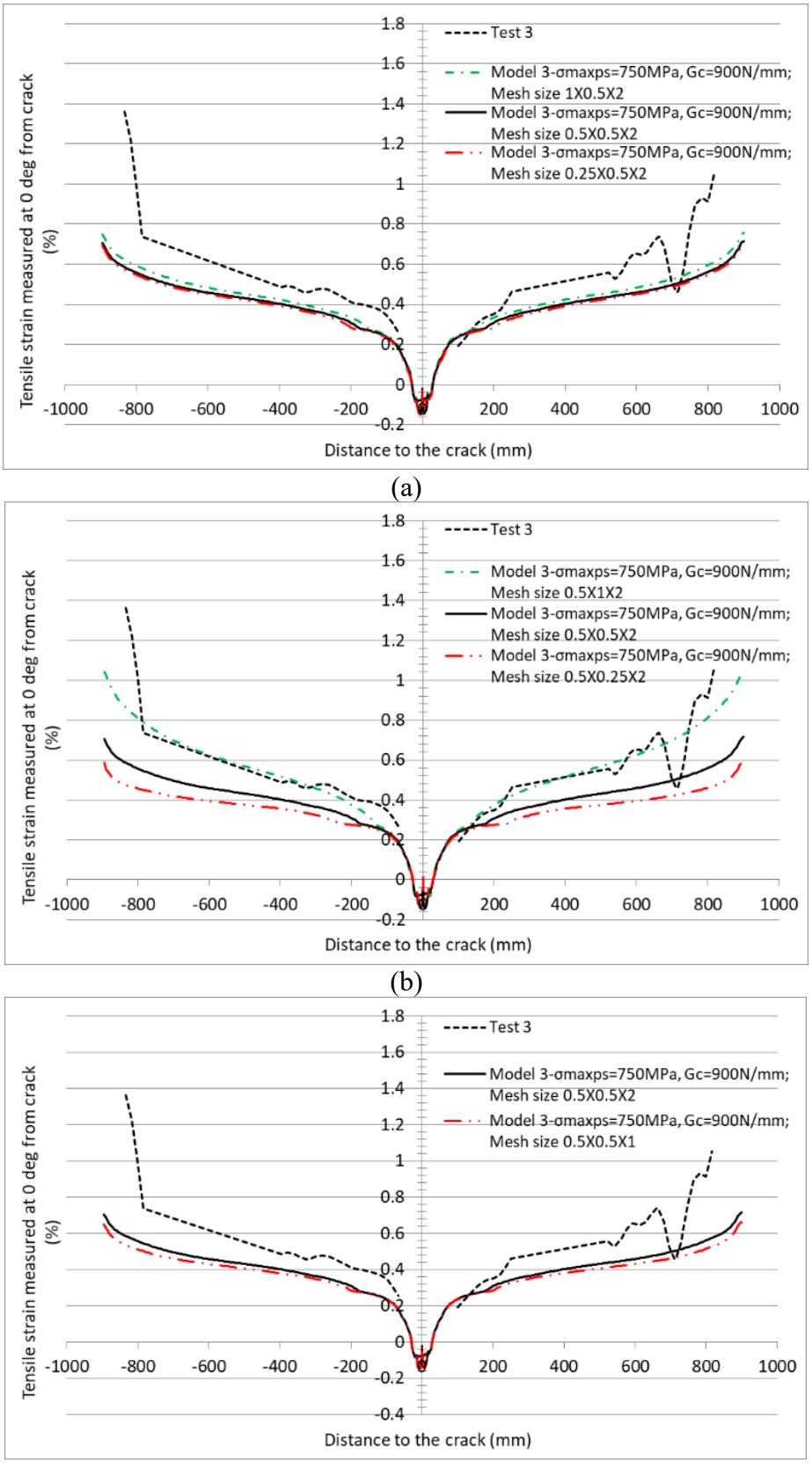

Figure 3-12. Comparison of tensile strain at the tension side of pipe at failure obtained from Test 3 and Model 3 using σ_{maxps}= 750 MPa and G_c = 900 N/mm: (a) change of l_h; (b) change of l_l; and (c) change of l_t.

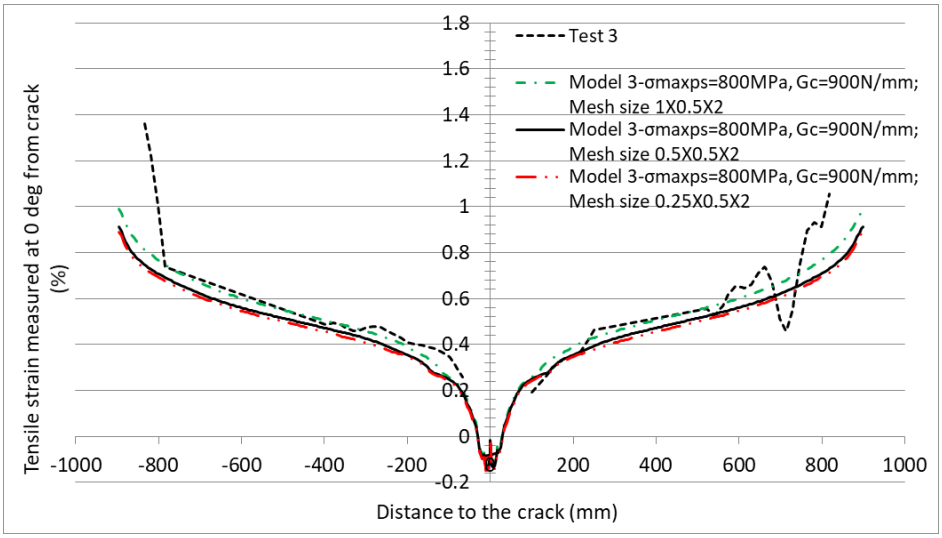

(a)

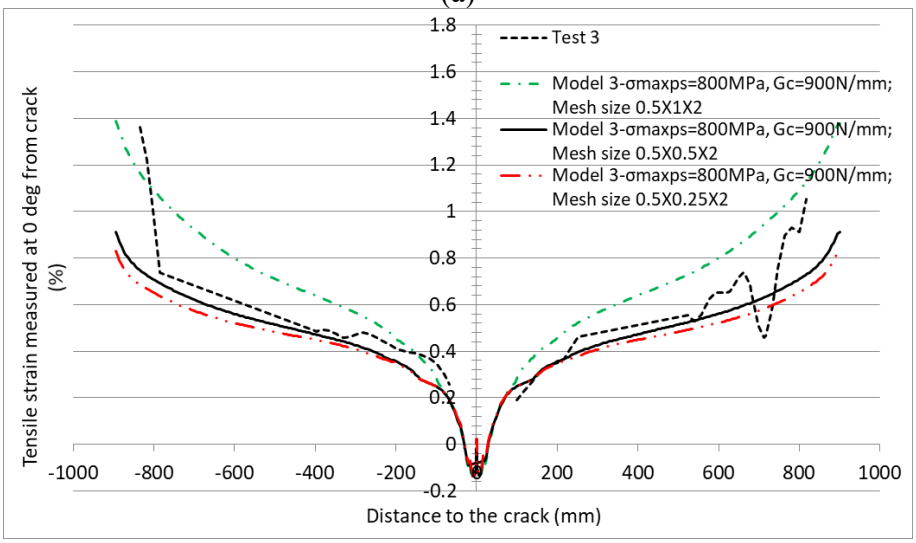

(b)

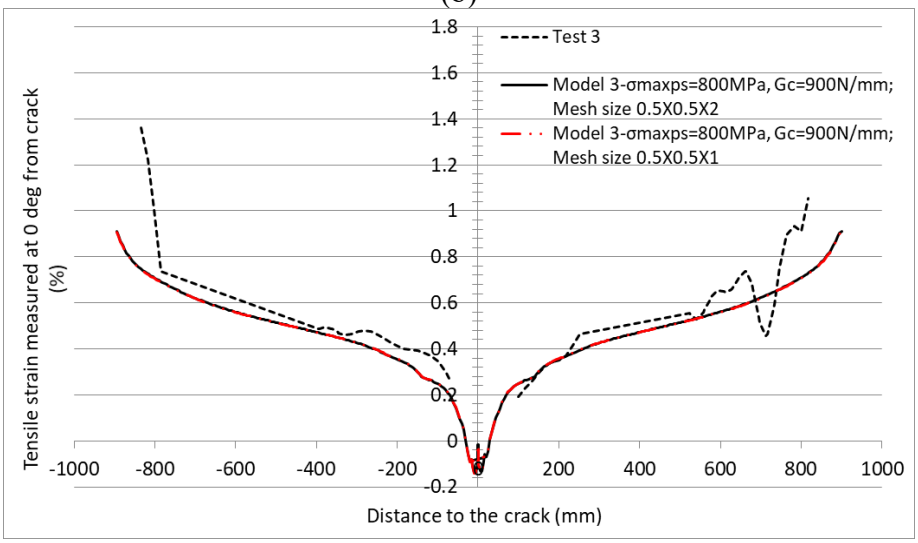

(c)

Figure 3-13. Comparison of tensile strain at the tension side of pipe at failure obtained from Test 3 and Model 3 using σ_{maxps}= 800 Mpa and G_c = 900 N/mm: (a) change of l_h; (b) change of l_l; and (c) change of l_t.

3.6 Conclusions

This chapter qualified the use of XFEM-based cohesive segment approach implemented in the commercial finite-element analysis Abaqus/Standard for crack propagation analysis of pipes. It is the first to systematically calibrate and verify the damage parameters for vintage pipeline steel (API 5L grade of X52) from eight full-scale pressurized and circumferentially surface-cracked pipe models until a good agreement is achieved between the numerical and experimental results. Based on a linearly deceasing traction–separation law, the most suitable set of damage parameters is σ_{maxps} = 750 MPa and G_C = 900 N/mm, which can be correlated to the material yield strength and fracture toughness around $\sigma_{maxps} = 1.8\,\sigma_y$ and $G_C = 4.6\,K_{Ic}^2/(E/(1-\nu^2))$. An investigation of mesh sensitivity was conducted to achieve the numerical stability and computational accuracy. The mesh size $l_h \times l_l \times l_t$ = 0.5 × 0.5 × 2 mm around the crack-propagating path resulted in 10% variation of numerical results, while l_l oriented perpendicular to the crack plane might be further reduced to minimize its sensitivity. This chapter serves as a good basis in effectively predicting crack propagation of pipelines with various steel grades using XFEM. Future work will focus on exploring new damage initiation criterion that take the constraints around the crack tip into consideration.

4. Introduction of Variable Strain Damage Initiation Criterion[4]

4.1 Abstract

This chapter develops a novel variable strain damage initiation criterion modified from the Mohr-Coulomb (MMC) fracture criterion as a function of stress triaxiality and Lode angle parameters. By introducing the crack-tip constraint into the damage criterion, the damage strain locus exponentially decreases as the stress triaxiality increases. A parametric study is presented to investigate the effect of each material parameter considered in the MMC fracture criterion on the fracture locus curve. A user-defined Fortran code is created to incorporate the novel damage criterion into XFEM through the programming with Abaqus user subroutine-UDMGINI. The code is validated in a side-grooved SENT model and the variable strain damage criterion modifies the inaccurate crack propagating path and fracture profile generated from the same model adopting the built-in fixed strain damage criterion.

Keywords: modified Mohr-Coulomb fracture criterion; stress triaxiality; Lode angle; XFEM; UDMGINI.

[4] This chapter is derived from a conference publication [2]:

M. Lin, Y. Li, M. Salem, J.J.R. Cheng, S. Adeeb, M. Kainat, A parametric study of variable crack initiation criterion in XFEM on pipeline steel, in: Pressure Vessels and Piping Conference Volume 6: Materials and Fabrication, American Society of Mechanical Engineers (ASME), Virtual, Online, 2020. https://doi.org/10.1115/PVP2020-21664.

4.2 Characterization of Stress State

The hydrostatic pressure p, von Mises stress q, and third stress invariant r are the three invariants of a stress tensor $[\sigma]$ given by [74,75]

$$p = -\frac{1}{3}(\sigma_1 + \sigma_2 + \sigma_3) \tag{4-1}$$

$$q = \sqrt{\frac{1}{2}[(\sigma_1 - \sigma_2)^2 + (\sigma_2 - \sigma_3)^2 + (\sigma_1 - \sigma_3)^2]} \tag{4-2}$$

$$r = \left[\frac{27}{2}(\sigma_1 + p)(\sigma_2 + p)(\sigma_3 + p)\right]^{1/3} \tag{4-3}$$

where σ_1, σ_2, σ_3 are three principal stresses of $[\sigma]$; hydrostatic pressure p is positive in compression and negative in tension.

The stress state parameters, stress triaxiality η and normalized Load angle $\bar{\theta}$ can be can be formulated in terms of the above three invariants given by [74,75]

$$\eta = -\frac{p}{q} \tag{4-4}$$

$$\xi = \left(\frac{r}{q}\right)^3 = cos(3\theta) \text{ and } -1 \le \xi \le 1 \tag{4-5}$$

$$\bar{\theta} = 1 - \frac{6\theta}{\pi} = 1 - \frac{2}{\pi} arccos\xi \text{ and } -1 \le \bar{\theta} \le 1 \tag{4-6}$$

where θ is the Lode angle with the range $0 \le \theta \le \pi/3$ and is related to the normalized third deviatoric stress invariant ξ; $\bar{\theta}$ is the normalized Load angle (referred to Lode angle parameter hereinafter); $\bar{\theta} = -1$, 0, and 1 respectively correspond to axisymmetric compression or equi-biaxial tension, plastic plane strain or generalized shear, and axisymmetric tension [75].

4.3 Strain-based Modified Mohr-Coulomb (MMC) Fracture Criterion

The Mohr–Coulomb fracture criterion has been extensively employed to describe the brittle fracture of geo-materials given by [74,75]

$$(\tau + c_1\sigma_n)_f = c_2 \tag{4-7}$$

where σ_n and τ are normal stress and shear stress; c_1 and c_2 are friction coefficient and shear resistance, respectively, with the range $c_1 \geq 0$ and $c_2 > 0$; c_1 controls the orientation of fracture plane, while c_1 and c_2 control the onset of fracture [75].

Recently, Bai and Wierzbicki [74,75] extended the stress-based formulae to a strain-based formulae to describe the ductile fracture of uncracked bodies, as a function of triaxiality parameter (η) and Lode angle parameter ($\bar{\theta}$) to account for the constraints at the crack tip, given by Eq. (4-8).

$$\bar{\varepsilon}_f = \left\{\frac{A}{c_2}\left[1 - c_\eta(\eta - \eta_0)\right] \times \left[c_\theta^s + \frac{\sqrt{3}}{2-\sqrt{3}}(c_\theta^{ax} - c_\theta^s)\left(sec\left(\frac{\bar{\theta}\pi}{6}\right) - 1\right)\right]\left[\sqrt{\frac{1+c_1^2}{3}}cos\left(\frac{\bar{\theta}\pi}{6}\right) + c_1\left(\eta + \frac{1}{3}sin\left(\frac{\bar{\theta}\pi}{6}\right)\right)\right]\right\}^{-\frac{1}{n}} \text{ and } c_\theta^{ax} = \begin{cases} 1 \ for \ \bar{\theta} \geq 0 \\ c_\theta^c \ for \ \bar{\theta} < 0 \end{cases} \tag{4-8}$$

where A and n are parameters of material strain hardening, following a power law stress-strain relationship; $c_1$and c_2 are primary fracture parameters that need to be calibrated from fracture tests; c_η and η_0 are additional parameters of pressure dependence; c_θ^s and c_θ^c are additional parameters of Lode angle dependence; by fixing $c_\eta = 0$ and $c_\theta^c = 1$, $c_\theta^s = 1$ and $\sqrt{3}/2$ respectively correspond to the von-Mises yield condition and Tresca yield condition [75].

It has been suggested to neglect the pressure dependence effect of c_η and η_0 due to the similarity with c_1 regarding the stress triaxiality [75]. By replacing c_θ^s and c_θ^c respectively to equivalent c_3 and c_4, Eq. (4-9) is obtained. Furthermore, if A/c_2 is replaced by an equivalent new c_2 to remove the strength coefficient A from the formula, Eq. (4-10) is developed, which only consists of five parameters (n, c_1, c_2, c_3 and c_4) as unknown variables. The strain hardening exponent n can be determined from power curve fitting of a true stress-strain curve in the strain hardening region in material tension coupon tests as $\sigma = A\varepsilon^n$ or $\sigma = A{\varepsilon_p}^n$. The

fracture parameters c_1, c_2, c_3 and c_4 shall be calibrated from fracture tests, e.g., SENT tests. c_4 can be simply taken as 1 to remove this parameter from the formular if the loading condition is dominated by $\bar{\theta} \geq 0$.

$$\bar{\varepsilon}_f = \left\{ \frac{A}{c_2} \times \left[c_3 + \frac{\sqrt{3}}{2-\sqrt{3}} (c_4 - c_3) \left(sec\left(\frac{\bar{\theta}\pi}{6}\right) - 1 \right) \right] \left[\sqrt{\frac{1+c_1^2}{3}} cos\left(\frac{\bar{\theta}\pi}{6}\right) + c_1 \left(\eta + \frac{1}{3} sin\left(\frac{\bar{\theta}\pi}{6}\right) \right) \right] \right\}^{-\frac{1}{n}} \text{ and } c_4 = 1 \text{ for } 0 \leq \bar{\theta} \leq 1 \quad (4\text{-}9)$$

$$\bar{\varepsilon}_f = \left\{ c_2 \times \left[c_3 + \frac{\sqrt{3}}{2-\sqrt{3}} (c_4 - c_3) \left(sec\left(\frac{\bar{\theta}\pi}{6}\right) - 1 \right) \right] \left[\sqrt{\frac{1+c_1^2}{3}} cos\left(\frac{\bar{\theta}\pi}{6}\right) + c_1 \left(\eta + \frac{1}{3} sin\left(\frac{\bar{\theta}\pi}{6}\right) \right) \right] \right\}^{-\frac{1}{n}} \text{ and } c_4 = 1 \text{ for } 0 \leq \bar{\theta} \leq 1 \quad (4\text{-}10)$$

4.4 Parametric Study of Fracture Criterion

A parametric study was performed to investigate the effect of each material parameter considered in the MMC fracture criterion on the fracture locus curve. An example of fracture locus curve in the space of $\bar{\varepsilon}_f$, η, and $\bar{\theta}$ is given in Figure 4-1, which is determined from Eq. (4-10) with A = 1129.6 MPa, n = 0.0923, c_1 = 0.03, c_2 = 535 MPa, c_3 = 0.9 and c_4 = 1. The fracture locus demonstrates an exponentially decreasing relationship between $\bar{\varepsilon}_f$ and η, and an asymmetric parabolic relationship between $\bar{\varepsilon}_f$ and $\bar{\theta}$. The effect of each material parameter on the magnitude, pressure dependence (i.e., extent of exponential decay of curve with increase of η), and Lode angle dependence (i.e., asymmetry of near-parabolic curve with respect to $\bar{\theta}$) of fracture locus were carefully investigated by generating relationship between $\bar{\varepsilon}_f$ and η and $\bar{\varepsilon}_f$ and $\bar{\theta}$ respectively. Three typical loading condition $\bar{\theta}$ = -1, 0, and 1 and three levels of stress triaxiality η = 0, 1, and 2 were considered. Each parameter under the analysis was varied while all others were kept constant.

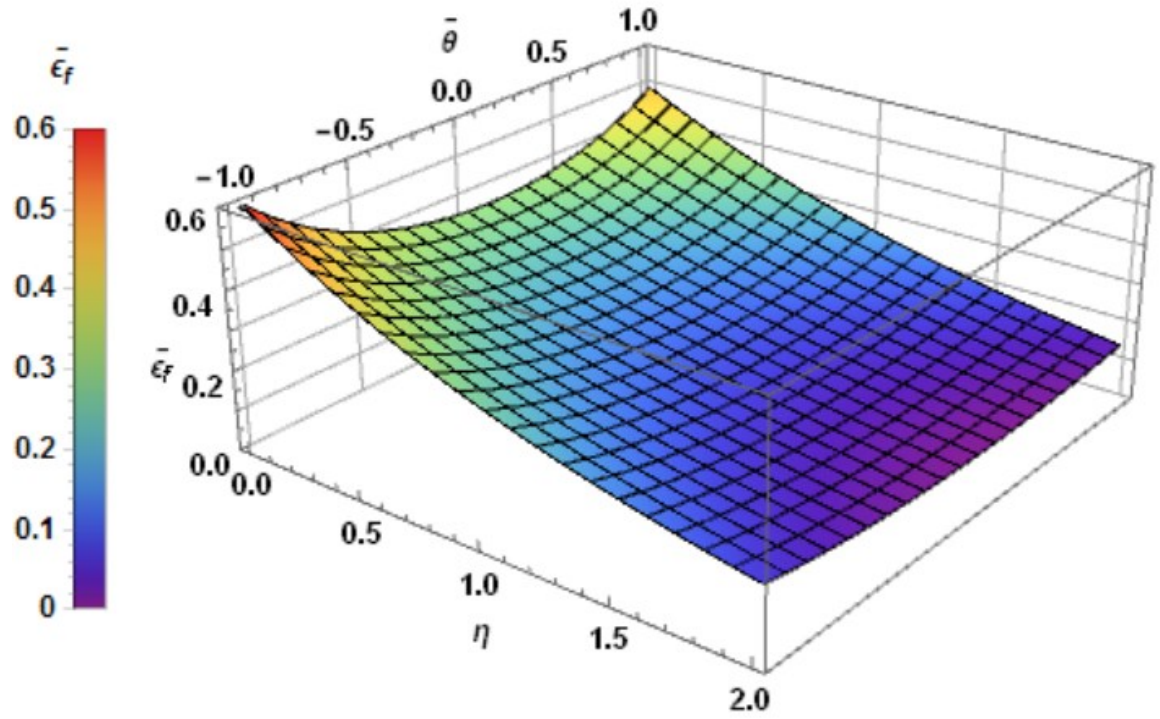

Figure 4-1. MMC fracture locus (A = 1129.6 MPa, n = 0.0923, c_1=0.03, c_2 = 535 MPa, c_3 = 0.9, c_4 = 1).

4.4.1 Effect of c_1 and c_2

Figure 4-2 shows that as c_1 increases from 0 to 0.05, the exponential decay of $\bar{\varepsilon}_f$ from η = 0 to 2 is more significant, when $\bar{\theta}$ = -1, 0, and 1. The near-parabolic curve of $\bar{\varepsilon}_f$ with respect to $\bar{\theta}$ seems more asymmetric as the increase of c_1, especially when η = 0. The limiting case c_1= 0 corresponds to the maximum shear stress fracture criterion, and the fracture locus is pressure independent and Lode angle dependent showing a symmetric locus with respect to $\bar{\theta}$. Figure 4-3 shows that as c_2 increases, $\bar{\varepsilon}_f$ is linearly raised without the shape change. As c_2 increases from 486 to 535 MPa, and from 535 to 588 MPa, $\bar{\varepsilon}_f$ is scaled up about $1.1^{1/n} = 1.1^{1/0.0923} =$ 2.8.

In summary, c_1 affects the pressure and Lode angle dependences of the fracture locus, and both dependences are improved with increase of c_1. c_2 affects the magnitude of the fracture locus

without the change of the shape, and the magnitude is linearly raised with the increase of c_2.

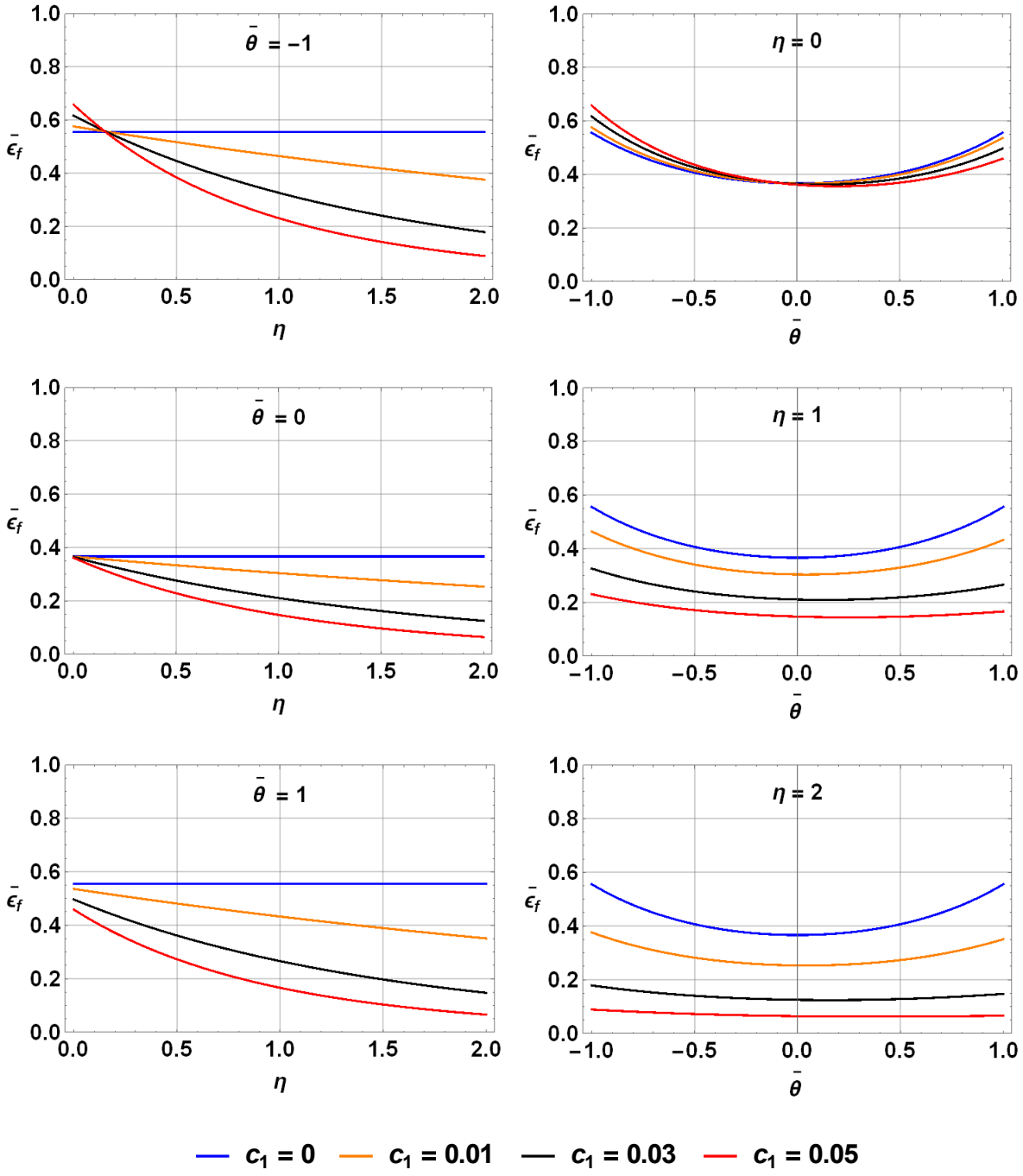

Figure 4-2. Effect of c_1 on MMC fracture criterion.

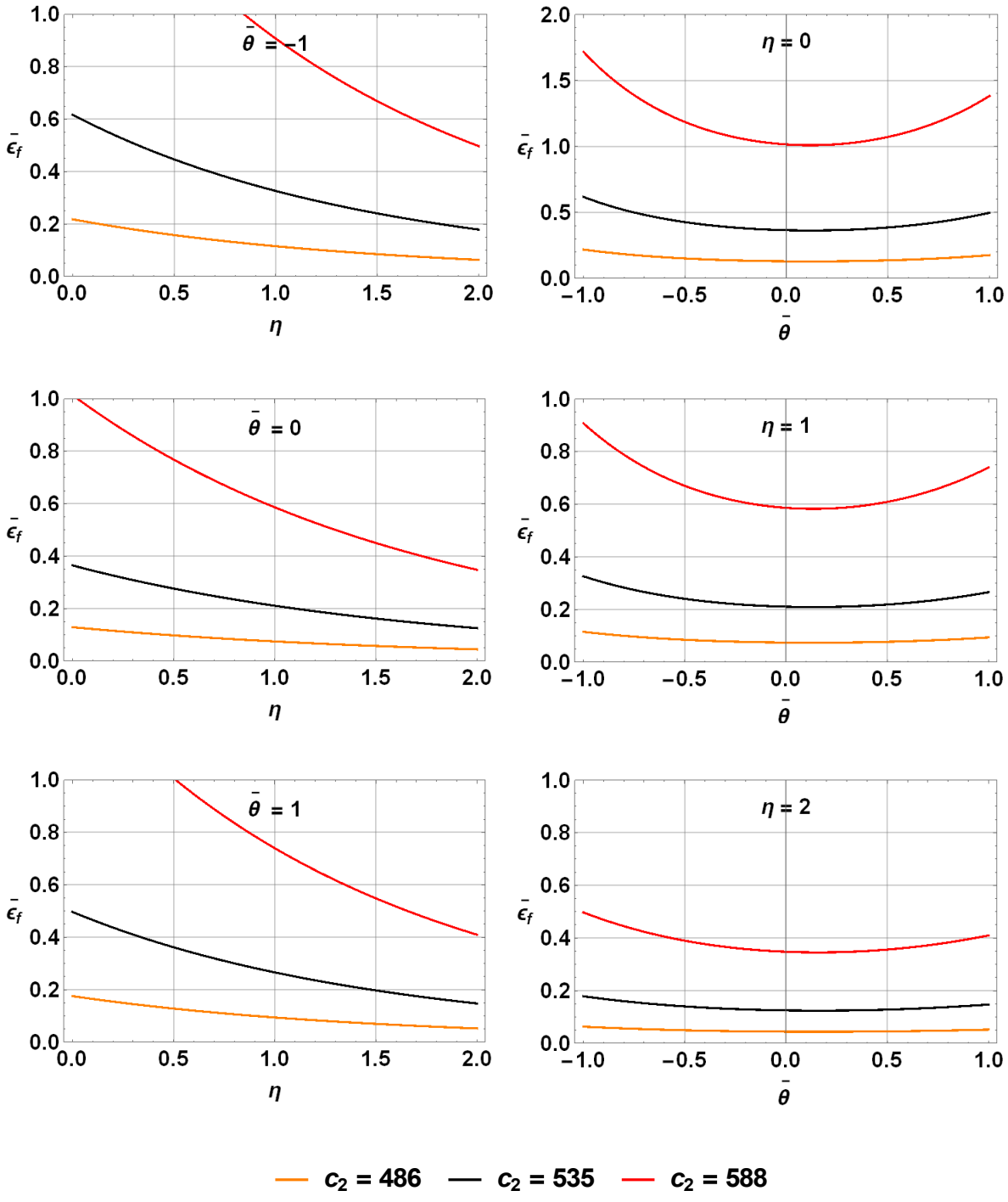

Figure 4-3. Effect of c_2 on MMC fracture criterion.

4.4.2 Effect of c_3 and c_4

Figure 4-4 shows that the fracture locus falls with the increase of c_3 when $-1 < \bar{\theta} < 1$, while it is not influenced by c_3 when $\bar{\theta}$ = -1 and 1. In addition, the near-parabolic curve of fracture locus with respect to $\bar{\theta}$ is more asymmetric with the increase of c_3. In a case that $c_3 = c_4 = 1$ in a von-Mises yield condition, the fracture locus is a near-parabolic curve opening upward when $\eta \geq 0$. In a case that $c_3 = \sqrt{3}/2$ and $c_4 = 1$ in a Tresca yield condition, the fracture locus is a nearly straight line when $\eta = 0$, but a near-parabolic curve opening downward when $\eta > 0$. Figure 4-5 shows that the fracture locus falls with the increase of c_4 when $\bar{\theta} < 0$, while it is not influenced by c_4 when $\bar{\theta} \geq 0$. When $\bar{\theta} < 0$, c_4 significantly affects the asymmetry of fracture locus, and the amount of dependence seems minor in the case when $c_4 = 1$, in comparison with other cases when $c_4 = 0.9$ and 1.1. Additionally, the case when $c_3 = c_4 = 1$ corresponds to the Mises yielding condition.

In summary, c_3 affects the Lode angle dependence of fracture locus, and the magnitude of fracture locus is reduced with the increase of c_3 when $-1 < \bar{\theta} < 1$. c_3 has no effect on the fracture locus when $\bar{\theta}$ = -1 and 1. $\bar{\theta}$ = -1 corresponds to the axisymmetric compression or equi-biaxial tension, and $\bar{\theta}$ = 1 corresponds to axisymmetric tension or equi-biaxial compression. The direction of opening for the near-parabolic curve with respect to $\bar{\theta}$ can be changed from opening upward to downward with the decrease of c_3 from 1 to$\sqrt{3}/2$. c_4 has no effect on fracture locus when $\bar{\theta} \geq 0$, but the magnitude of fracture locus is reduced with the increase of $c_4$when $\bar{\theta} < 0$. In addition, c_4 affects the Lode angle dependences of fracture locus and c_4 =1 seems an optimal value to minimize such dependence.

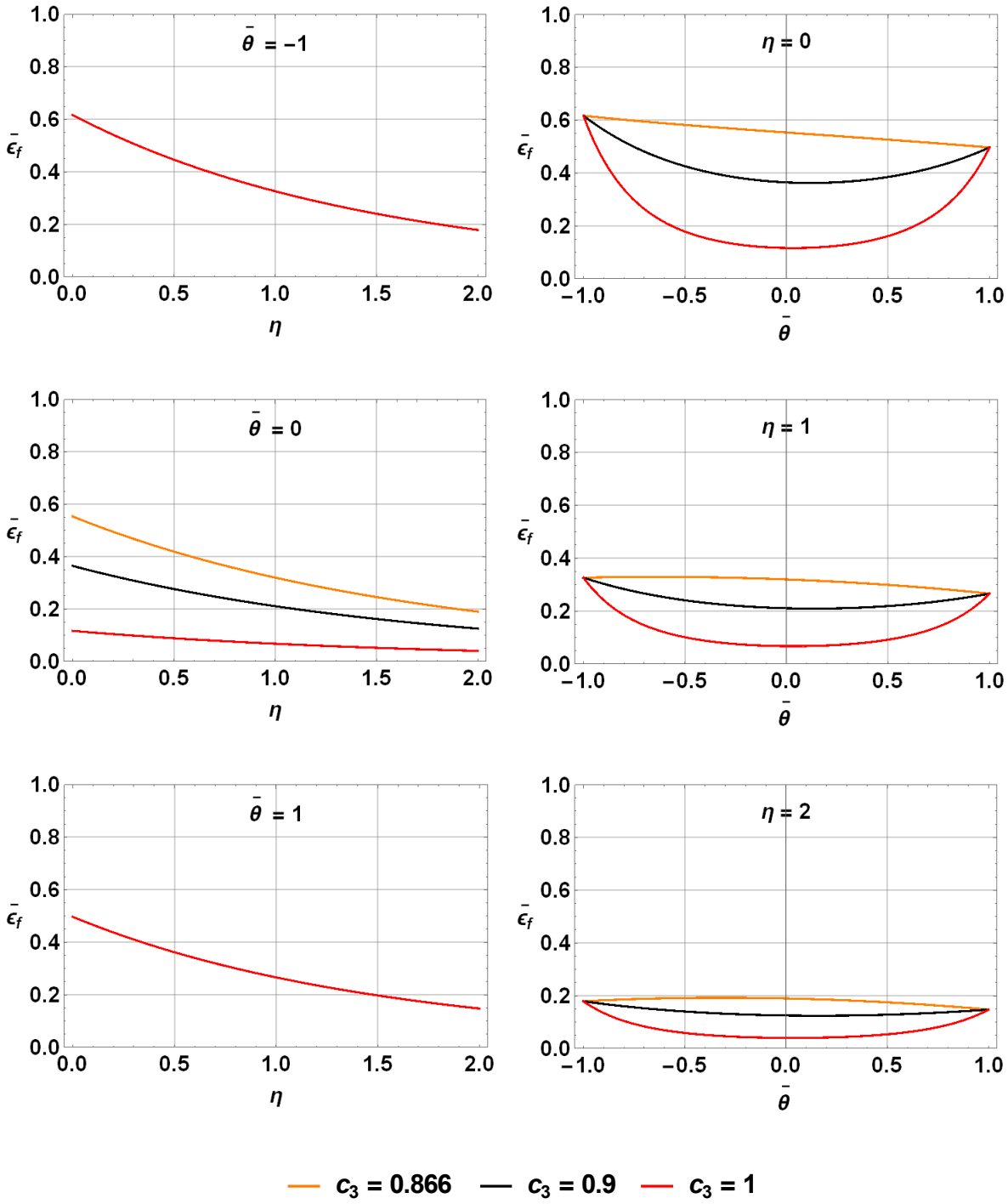

Figure 4-4. Effect of c_3 on MMC fracture criterion.

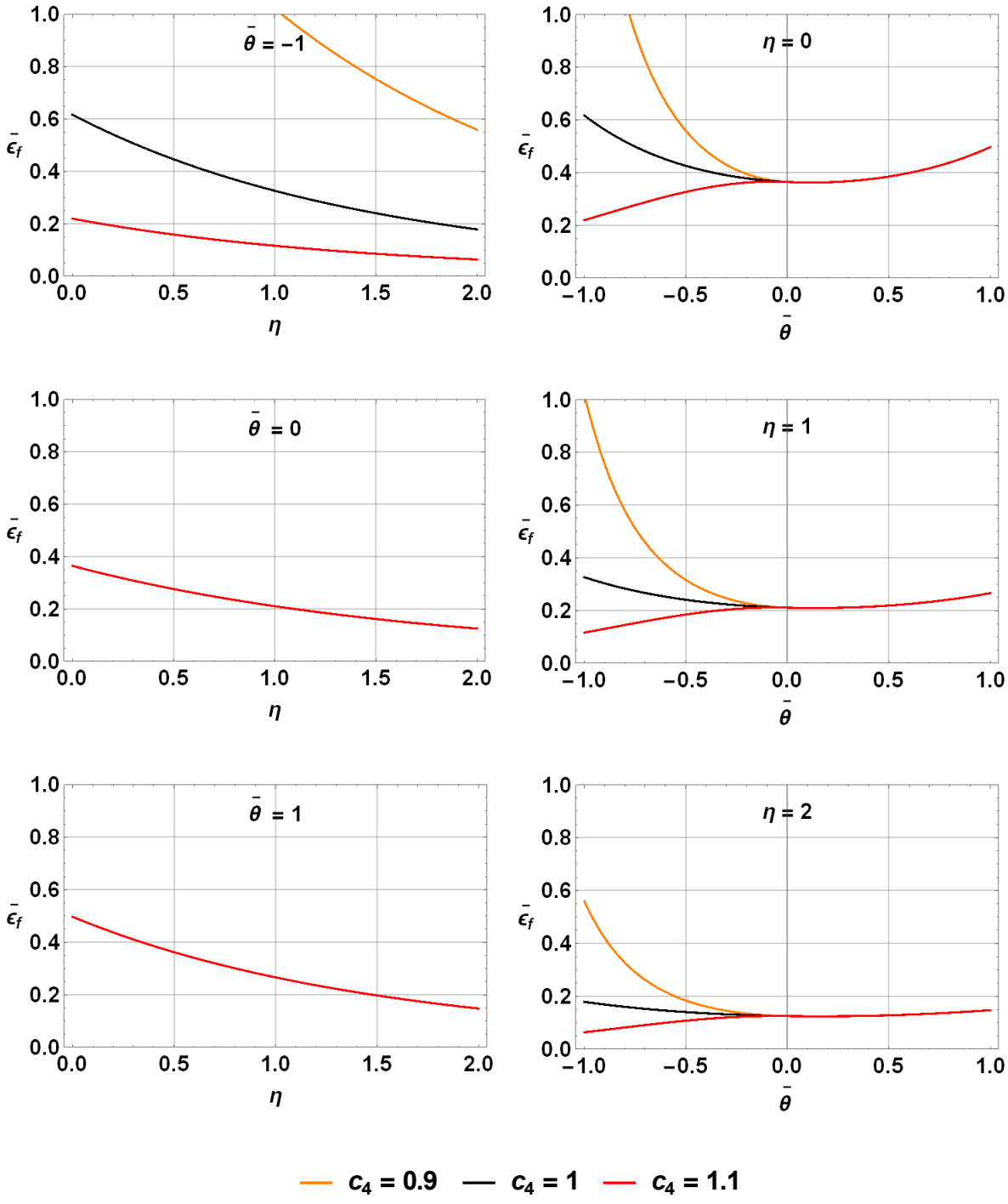

Figure 4-5. Effect of c_4 on MMC fracture criterion.

4.4.3 Effect of A and n

The strain hardening material parameters A and n can be calibrated from the power fit of true stress-strain curve, which are independent of the calibration of the optimal fracture locus for a specific material in fracture tests. The change of A on fracture locus is shown in Figure 4-6. Opposite to the effect of c_2, the fracture locus is linearly reduced about $1.1^{1/n} = 2.8$, as A is increased from 1026.9 to 1129.6 MPa, and from 1129.6 to 1242.5 MPa. It agrees with the statement that the stronger material is less ductile, resulting in a lower fracture strain. Figure 4-7 shows that as n increases, the exponential decay of $\bar{\varepsilon}_f$ due to the change of η is less dependent, and the near-parabolic curve of $\bar{\varepsilon}_f$ with respect to $\bar{\theta}$ is less asymmetric. The fracture locus is raised by the power of 1/2, as n is increased from 0.0462 to 0.0923, and from 0.0923 to 0.1846.

In summary, A affects the magnitude of fracture locus without the change of the shape, and the magnitude is linearly reduced with increase of A. The effects of A and c_2 on fracture locus are similar but right in the opposite direction. n affects the magnitude of fracture locus and the magnitude is raised by a power with the increase of n. In addition, n affects the pressure and Lode angle dependences of fracture locus and both dependences are decreased with the increase of n.

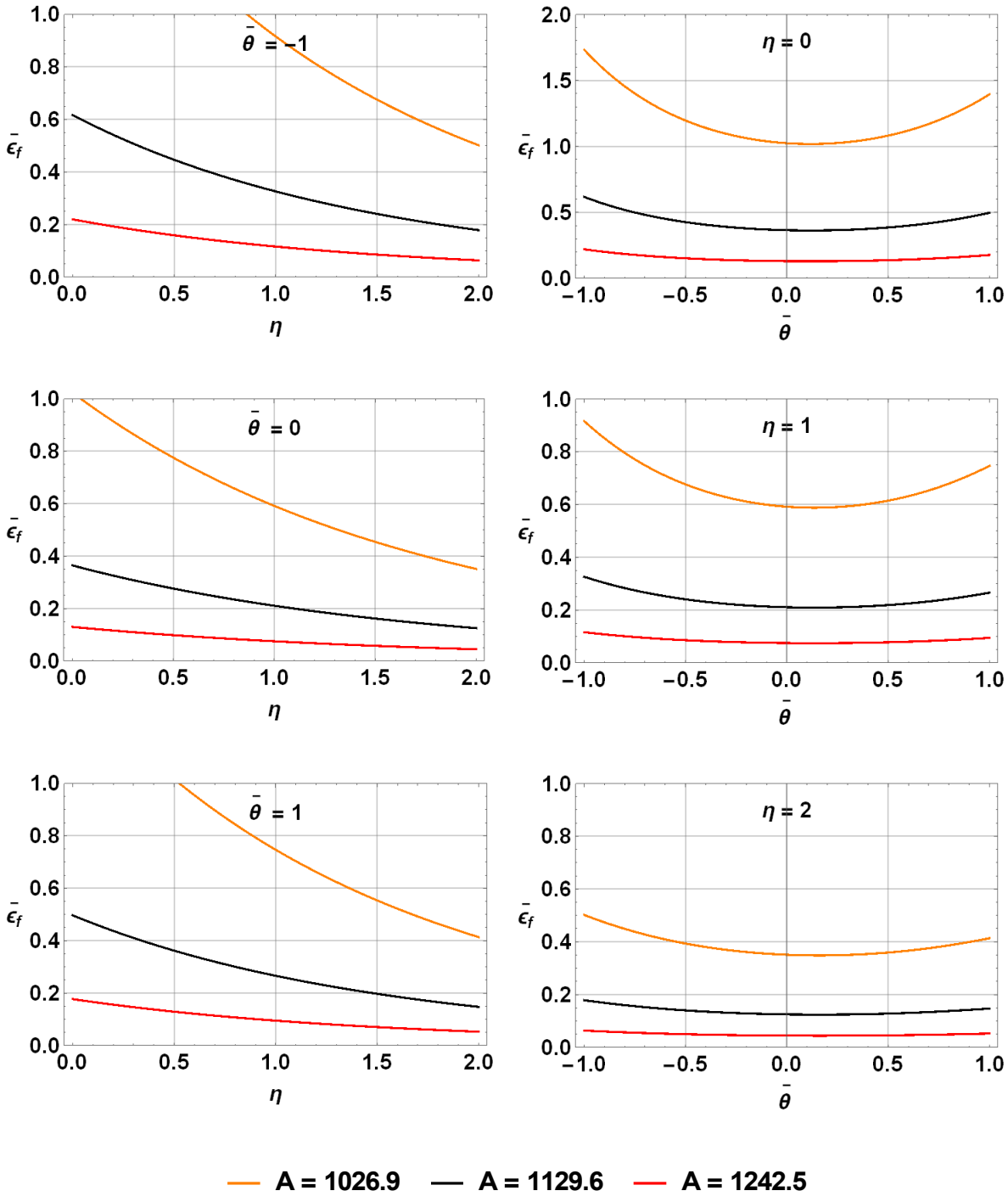

Figure 4-6. Effect of A on MMC fracture criterion.

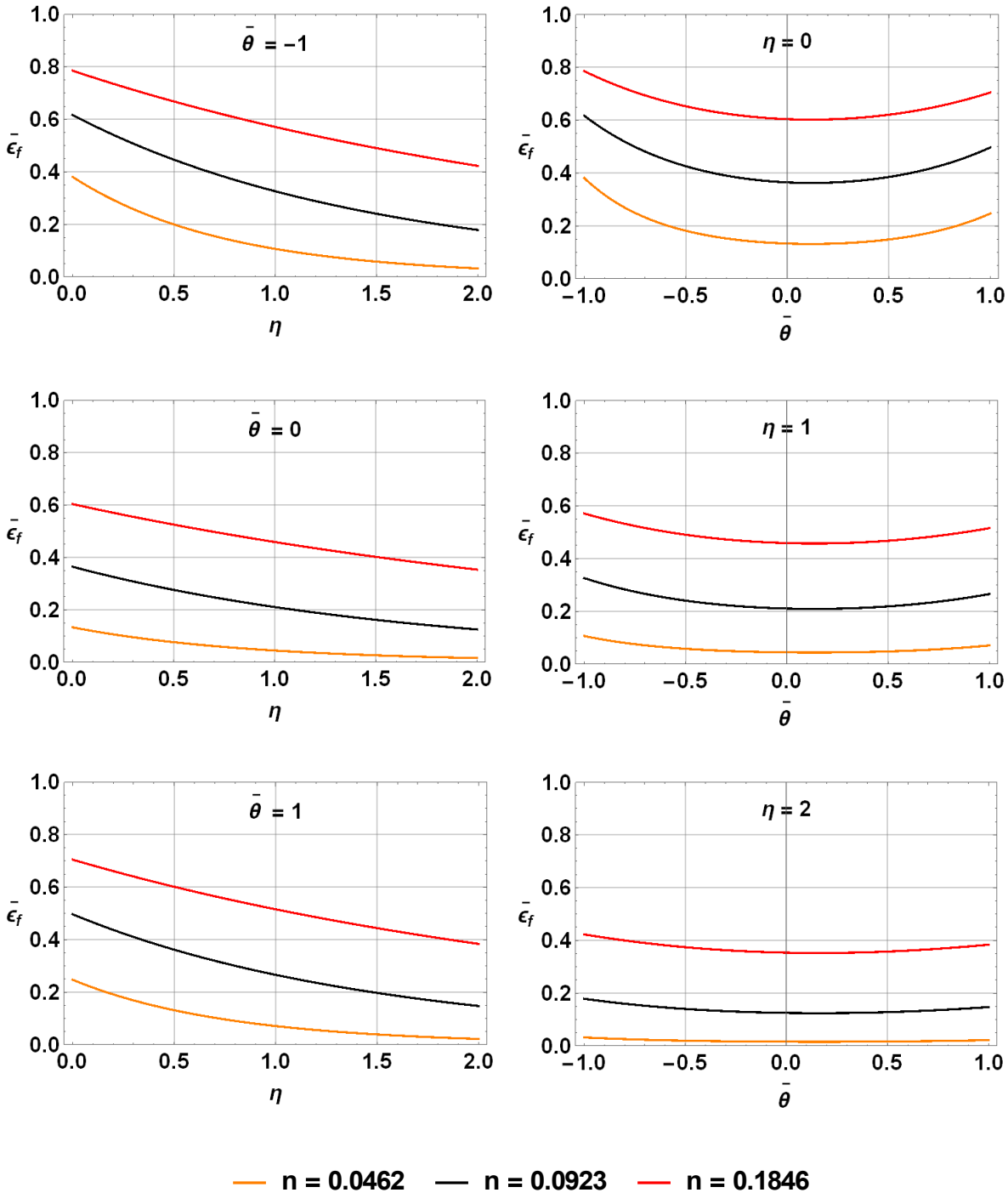

Figure 4-7. Effect of n on MMC fracture criterion.

4.4.4 Effect of c_η and η_0

The effects of additional parameters of pressure dependence c_η and η_0 on the fracture locus in Eq. (4-8) are studied and shown in Figure 4-8 and Figure 4-9 respectively. Assume $\eta_0 = 0$, Figure 4-8 shows that the fracture locus is less dependent to the change of η as c_η increases from 0 to 0.05, while further increase of c_η will change the original exponential decay of $\bar{\varepsilon}_f$ to the exponential growth. In addition, the fracture locus with respect to $\bar{\theta}$ is independent to the change of c_η when $\eta = 0$, while its magnitude is raised as the increase of c_η when $\eta > 0$. Assume $c_\eta = 0$, Eq. (4-8) is simplified to Eq. (4-10), the fracture locus with respect to η and $\bar{\theta}$ are independent of η_0. In order to further investigate the effect of η_0, $c_\eta = 0.05$ is assumed in Figure 4-9, which show that the fracture locus is scaled down with the increase of η_0.

In summary, c_η affects the pressure dependence of fracture locus. Assuming $\eta_0 = 0$, the pressure dependence is decreased with the increase of c_η when $c_\eta \leq 0.05$, while further increase of c_η changes the original exponential decay of $\bar{\varepsilon}_f$ to the exponential growth. η_0 has no effect on the fracture locus if $c_\eta = 0$ because η_0 is crossed out from the equation. η_0 affects the magnitude of fracture locus only if $c_\eta \neq 0$, and the fracture locus is scaled down with the increase of η_0.

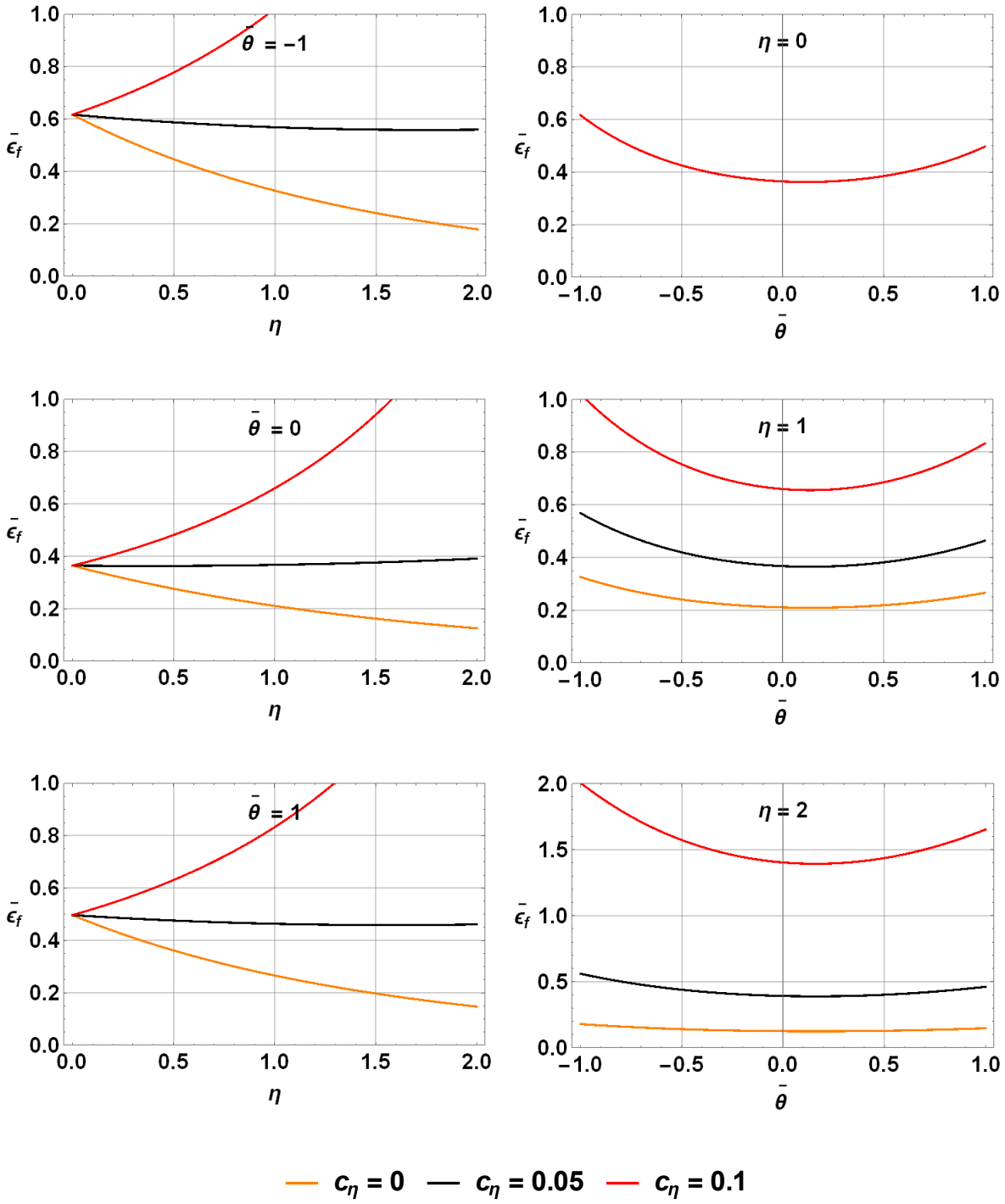

Figure 4-8. Effect of c_η (based on $\eta_0 = 0$) on MMC fracture criterion.

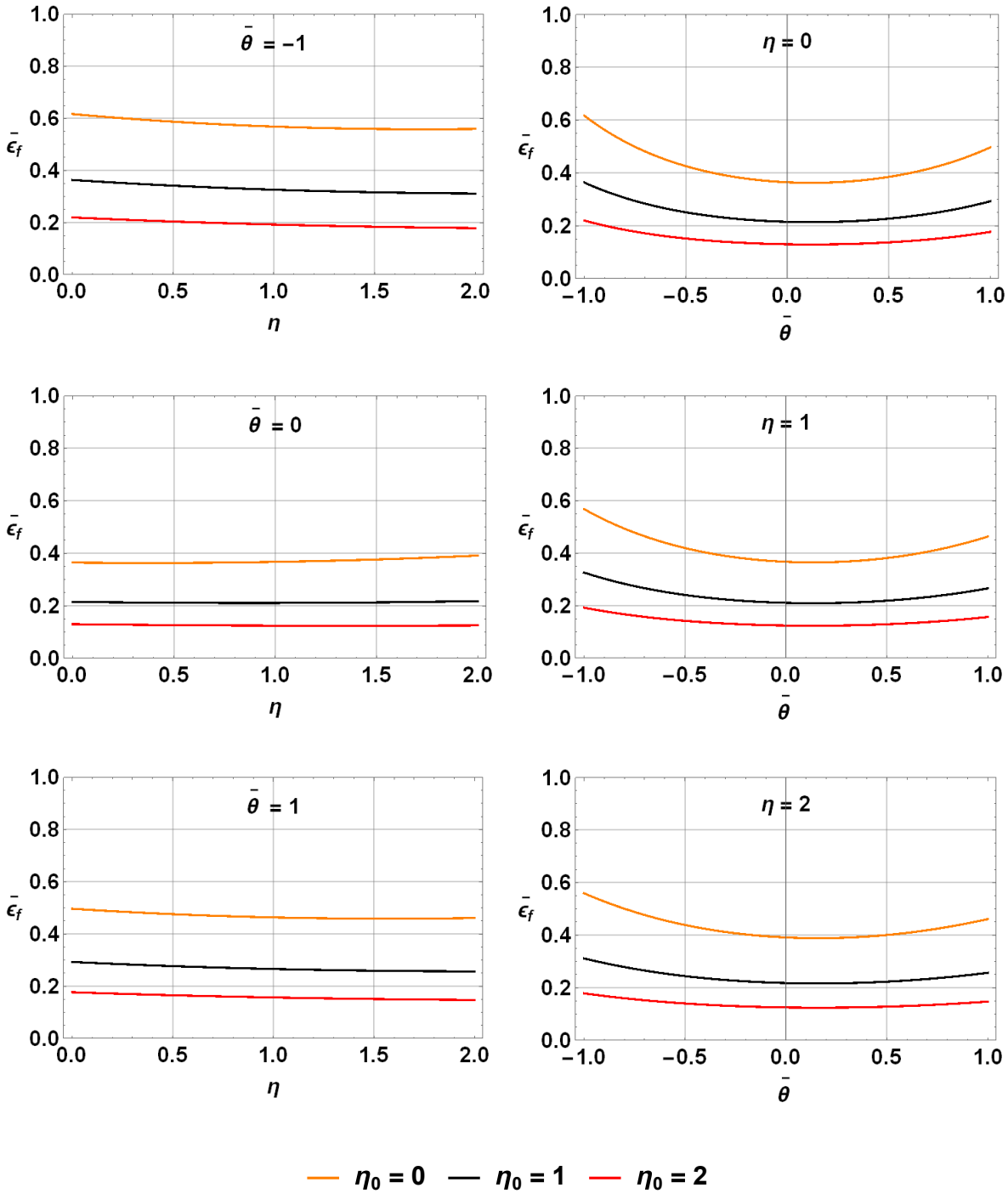

Figure 4-9. Effect of η_0 (based on $c_\eta = 0.05$) on MMC fracture criterion.

4.5 Implementation in XFEM

One currently built-in damage initiation criterion in XFEM capability of Abaqus/Standard assumes the damage occurs when the maximum principal strain ε_{maxp} of an enriched element reaches a user defined maximum allowable principal strain ε^{o}_{maxp}, i.e., the damage initiation criterion f reaches 1.0 within a given tolerance[5] f_{tol}. The numerical ε_{maxp} and fixed ε^{o}_{maxp} can be respectively replaced by the numerical equivalent plastic strain PEEQ and variable damage strain $\bar{\varepsilon}_f$ defined by Eq. (4-10). The novel damage criterion is defined using a Fortran code (Appendix A) programmed in Abaqus user subroutine-UDMGINI [30].

$$1.0 \leq f = \left\{\frac{\varepsilon_{maxp}}{\varepsilon^{o}_{maxp}}\right\} \leq 1.0 + f_{tol} \tag{4-11}$$

$$1.0 \leq f = \left\{\frac{PEEQ}{\bar{\varepsilon}_f}\right\} \leq 1.0 + f_{tol} \tag{4-12}$$

The new damage initiation criterion should be paired with a damage evolution law to constitute a failure mechanism. To implement the user's subroutine file (.for), the damage initiation and evolution information stored in an input file (.inp) generated by Abaqus/CAE should be replaced by bold text following this paragraph. The following is the calibrated optimal sets of parameters (c_1, c_2, c_3, c_4, n, G_c) = (0.03, 1.9, 0.9, 1.0, 0.0923, 100) according to Eq.(4-10) specific to X100 based on SENT models described in Chapter 5. The judicious use of damage initiation tolerance and damage stabilization option can aid in convergence in a damage model. The damage initiation tolerance of 0.1 and the viscosity coefficient of 1e-05 are appropriate values to overcome convergence difficulties while having minimal effect on the response.

[5] A smaller damage initiation tolerance value may result in convergence difficulty due to the small increment size, while a larger tolerance value may result in initiating multiple cracks simultaneously. A value of f_{tol} = 0.1 is selected in models in Chapters 5.

***Damage Initiation, criterion=user,tol=0.1,properties=5,failure mechanisms=1**

0.03, 1.9, 0.9, 1.0, 0.0923

***Damage Evolution, type=ENERGY,failure index=1**

100.,

***Damage Stabilization**

1e-05

The user-defined code has been validated in a side-grooved SENT model with a shallow crack (crack depth to specimen width a/W = 0.25) [2]. The model configuration was the same as the shallow-cracked and side-grooved model described in Chapter 5 but with an initial planar crack instead of a notch created in the middle length of model. In this model, the damage initiation criterion was defined by $\bar{\varepsilon}_f(A, n, c_1, c_2, c_3, c_4) = \bar{\varepsilon}_f$ (1129.6, 0.0923, 0.03, 535, 0.9, 1) according to Eq. (4-10), and the damage evolution law was defined by a linearly decreasing traction separation law with G_c = 300 N/mm. Theses parameters were used for validation of UDMIGINI Fortran code and not calibrated with experiments. The simulation with variable strain damage criterion produced better results than the simulation with fixed Maxpe damage criterion in predicting experimental crack propagating path and fracture profile. The irregular fracture profile ductile tearing generated using the fixed strain damage criterion was improved by variable strain damage criterion which generating a basically parabolic curve with slight growth at side groove identical to the experimental measurement. This work serves the basis of Chapter 5.

5. Variable Strain Damage Model for Predicting Fracture of Small-scale SENT and Full-scale Pipe Tests[6]

5.1 Abstract

The tensile train capacity (TSC) of welded pipeline is paramount in the pipeline integrity assessment and the J-R curves plays a key role in predicting the TSC. The single edge notched tension (SENT) tests have been recommended for fracture toughness measurement of pipelines due to the similar low constraint geometries. The extended finite element method (XFEM) has been increasingly implemented in predicting the fracture of pipelines from small-scale to full-scale tests since the last decade, but current damage criteria based on fixed critical stress or strain value have not been well calibrated. Previous studies have shown some limitations. This chapter develops a novel XFEM variable strain-based damage model by adopting a critical varying strain profile considering the crack-tip constraint derived from a modified Mohr-Coulomb fracture criterion. The novel damage criterion is calibrated by reproducing similar results with those measured from small-scale SENT tests of X100 pipe steel and full-scale pressurized tests of X52 circumferentially surface-cracked pipeline. Two optimal set of damage parameters are calibrated specific to X100 and X52 respectively. The initial crack in each model is simulated by cutting a notch instead of typically inserting a planar crack into the mesh

[6] The main content of this chapter is prepared for a research article to be submitted for a Journal-Engineering Fracture Mechanics, while part content is derived from another article that has been submitted for publication in 2021 Technology for Future and Aging Pipelines Conference [3]:

M. Lin, Y. Li, J.J.R. Cheng, S. Koduru, M. Kainat, A. Samer, Novel XFEM variable strain damage criterion for predicting tensile strain capacity of API X52 (under review), in: Technology for Future and Ageing Pipelines, Gent, Belgium, 2021.

which would bring artificial cohesion around the crack-tip field affecting the crack-tip constraint and fracture resistance. The predictions are compared with those using the simple fixed damage criterion.

Keywords: XFEM-based cohesive segments method; modified Mohr-Coulomb fracture criterion; crack-tip constraint; X100 SENT tests; X52 full-scale tests.

5.2 Introduction

Pipelines are usually made from low carbon steel and are ubiquitously used for transporting natural gas and petroleum across the world. Cracks constitute the most hazardous threat to the ability of pipelines to transport the oil and gas resources safely and reliably. The girth welds including the heat-affected zones (HAZ) establish the weakest link in the capability of a pipeline to resist the longitudinal tensile and/or bending loading due to the seasonal changes in soil temperature and soil differential movement, with this capability often measured by the longitudinal tensile strain capacity (TSC). Canadian Standard Association (CSA) used to adopt conservative equations (Rupture, Tier 2 approach in Annex C of CSA Z662-11) in predicting the longitudinal TSC of a circumferentially cracked pipeline [16]. These equations were solely developed from high strength steel pipes not accounting for the effect of biaxial loading due to the internal pressure. Due to the distinct drawbacks, these equations were withdrawn in the revision CSA Z662-15 while any attested approach validated by experiments was recommended [17]. Meanwhile, other empirical equations were available in the Canadian pipeline industry, such as that proposed by Pipeline Research Council International (PRCI) covering pipeline grades between API X65 and X100 [19], and that proposed by ExxonMobil covering pipeline grades between X65 and X80 [25–27]. The equations were developed based on modern pipelines and might not be applicable to vintage pipelines manufactured prior to the modern manufacturing techniques and testing processes implemented as early as 1950s.

Although the vintage pipelines were no longer manufactured, they still existed in current Canadian pipeline network, especially the vintage X52 pipeline.

A key role in predicting the longitudinal TSC of welded pipeline is the tearing resistance curve (R-curve)–in the form of stress intensity factor (K), J-integral, or crack tip opening displacement (CTOD)–against stable crack extension, which quantifies the material's inherent resistance to fracture in the presence of an existing crack. The measure of fracture toughness for a given pipeline material varies with temperature and testing technique, and should be indicative of the pipe body, HAZ, or weld metal regarding where the crack is located. Traditionally, a fracture toughness test specimen containing a fatigue pre-cracked notch is loaded with opening mode (Mode-I) at a low (quasi-static) strain rates and the fracture toughness is evaluated from the force versus load-line displacement and/or crack-mouth opening displacement (CMOD) monitored during the test [54]. The deep-cracked specimens such as the compact tension (CT) and single edge notched bending (SENB) specimens concomitant with high levels of constraints at the crack-tip were recommend in the past. However, the results of these experiments contributed to over conservatism of fracture resistance curves as well as the crack acceptance criteria of a given pipeline, especially when the pipeline is subjected to plastic straining during either installation or service. The actual fracture toughness of a pressurized pipe is higher and can rather be predicted by low crack-tip constrained specimens such as the curved wide plate test (CWPT) and single edge notched tension (SENT) specimens as illustrated in Figure 5-1. Recently, the SENT specimens, either pin-loaded or clamped, have been highly recommended, which can produce a relatively lower level of crack-tip constraint similar to that of a circumferentially cracked pipeline (e.g., girth weld imperfections) subjected to tension or even if it is globally loaded in bending [60,63]. Experimental and numerical research conducted by ExxonMobil have validated that the CTOD-R curves in SENT tests and full-scale tests are closely matched [61]. A few SENT test

procedures have been developed over the past two decades. The currently widely used test procedures are multiple-specimen technique recommended by Det Norske Veritas [62] and single-specimen technique recommended by CANMET Materials Technology Laboratory (CANMET-MTL) [63], and both techniques are described in the British Standard BS 8571 [64].

At present, the integrity decisions for cracked pipelines are either based on engineering experiences making the decisions inconsistent or based on numerical tools, mostly developed from conventional finite element method (FEM). This method is generally challenging to implement and computationally expensive in dealing with discontinuous geometry problems. The mesh needs to be refined continuously near crack tip field to match the geometric discontinuities as the crack progresses along a pre-defined crack path, thus the singular asymptotic fields can be captured adequately [30,31]. The mesh contribution and maintenance are significant for the success of FEM. The extended finite element method (XFEM) was proposed in 1999 by Belytschko and collaborators [32,33] based on the partition of unity method of Melenk and Babuska [34]. XFEM is a revolutionary technique since it addressed the limitation of conventional FEM in modelling the discontinuities by adding special enrichment functions in conjunction with additional degrees of freedom into standard FEM functions [30]. The finite element analysis commercial software Abaqus has a variety of fracture mechanics capabilities including the XFEM supported in Abaqus/Standard which employs the implicit integration scheme to solve structural static and low-speed dynamic events [30]. Both stationary crack analysis and propagating or moving crack analysis along an arbitrary solution-dependent path can be modelled using this technique. The propagating crack analysis can be performed using the XFEM-based cohesive segments method, i.e., cohesive zone model (CZM) within the XFEM framework. The CZM as illustrated in Figure 5-2 (a), considers the formation of fracture as a gradual phenomenon and describes a relation between cohesive traction acting on crack surfaces resisted by crack propagation and the corresponding

separation of crack surfaces across an extended crack tip which is also known as the traction–separation law (TSL). The crack grows when the separation at the tail of the cohesive zone (physical crack tip) reaches a critical value (δ_c), at which the cohesive traction (T_n) disappeared. The idea of phantom nodes was proposed by Belytschko and collaborators [35] to represent the discontinuities of cracked elements, based on the superposed element formulation of Hansbo and Hansbo [36]. Once a crack cuts through an enriched element, the phantom nodes and their superposed original real nodes move apart. The level set method offers a way to track the motion of interfaces and was used to model the arbitrary crack propagation without remeshing, in which the crack surface and crack front are determined by two level set signed distance functions [30,31]. Since the crack propagation in XFEM is freely lied within finite element (interior) instead of binding to element boundaries in conventional FEM, the meshing effort and strong dependence were significantly reduced. This makes XFEM more powerful in solving discontinuous geometry problems.

The history of increased applications of the XFEM-based cohesive segments in the crack propagation analysis in pipelines can be traced back to the last decade, nevertheless, current damage criteria have not been well calibrated. Available damage initiation criteria within the XFEM procedure assume a fixed critical stress or strain value such as the critical maximum principal stress (Maxps) or strain (Maxpe) damage initiation [30]. Once the initiation criterion is satisfied, the material cohesive stiffness is degraded with damage evolution law. As illustrated in Figure 5-2 (b), the built-in damaged TSL within the XFEM procedure can model linear or exponential softening based on either the energy dissipated due to fracture (i.e., critical fracture energy release rate G_c) or the effective displacement at failure (i.e., complete surface separation δ_c). $G_c = \int_0^{\delta_c} T_n(\delta_n) d\delta_n$ is the work needed to create an extended unit area of crack surfaces and is equivalent to the area under the TSL curve. The work [1] described in Chapter 3 has demonstrated success in implementing the XFEM-based cohesive segment method in

Abaqus/Standard, where a fixed damage initiation criterion with Maxps of 750 MPa and G_C of 900 N/mm was employed, using the results of 8 full-scale tests on circumferentially surface-cracked X52 pipe specimens subjected to internal pressure and external eccentric tension [37]. Howbeit the tensile strains along the pipe length direction were successfully predicted at pipe burst, some limitations were identified in predicting ductile crack behavior such as the growth of crack mouth opening displacement (CMOD) and pipe wall thickness reduction after fracture. In addition, the Maxps damage initiation criterion was extended to 6 small-scale SENT tests on X42 pipe steel by Ameli et al. [38]. An optimal set of Maxps of 1400 MPa and G_C of 200 N/mm was calibrated to predict similar experimental CTOD-R curves. However, this calibrated damage initiation stress value may be impractical because it is approximately 4.5 times the yield stress of X42. This led me to believe that a strain-based rather than a stress-based damage criterion may be more appropriate in predicting both brittle and ductile fracture of pipelines. Subsequent work by Agbo et al. [39] based on the maximum principal strain (Maxpe) damage initiation criterion demonstrated its success in predicting the TSC of circumferentially cracked X42 pipes based on 8 full-scale four-point bending tests. The calibrated Maxpe and G_C were 0.013 and G_C= 450 N/mm. In addition, the Maxpe damage initiation criterion was extended to the prediction of burst pressure of longitudinally cracked X60 pipes by Okodi et al. [40]. Due to the limited test data, three sets of damage parameters were calibrated from three full-scale burst tests containing different crack size (Maxpe = 0.02, G_C= 50 N/mm; Maxpe = 0.03, G_C= 10 N/mm; Maxpe = 0.065, G_C= 10 N/mm, and one set of damage parameters were calibrated from a SENT test for a specimen cut from X60 pipe (Maxpe = 0.034, G_C= 150 N/mm). This Maxpe criterion was further extended to the prediction of burst pressure of X42 and X52 pipes containing cracks in corrosion (CIC) defects by Zhang et al. [41]. One set of damage parameters (Maxpe = 0.02, G_C= 150 N/mm) were calibrated for both pipe grades.

Overall, it seems that the calibrated damage parameters may be fairly case dependent. This

motivated me to develop a novel XFEM variable strain-based damage criterion that is more accurate and applicable to various pipe grades for cracks with/without any other anomalies. The major limitation of using either fixed Maxps or Maxpe criterion is the simplicity by ignoring important factors such as the crack-tip constraint, which has a profound effect on fracture resistance. The novel criterion has been introduced in my previous work and validated on a side-grooved X100 SENT model (Chapter 4) [2]. The novel criterion successfully simulated the experimental fracture profile of ductile tearing showing a basically parabolic curve with slight growth at side groove and modified inaccurate crack propagating path and irregular fracture profile generated using the fixed Maxpe criterion. By virtue of the novel criterion accounting for constraint, the interior of the specimen (center region) is equally or more likely to suffer from crack extension than the outer free surface of the specimen although higher strain values are generated due to the presence of side groove.

Researchers and practitioners in the literature, including all research mentioned above, typically adopt the use of XFEM crack by inserting a planar crack into the finite element mesh. It was the firstly proposed by Zhang et al. [41] that such simulation accompanied by an unintended initial cohesion around the crack tip field would artificially increase the fracture resistance for crack opening. Noticeable differences were found between the simulation of a planar crack and a V-shape notch in the prediction of burst pressure of X42 and X52 pipes containing crack-in-corrosion defects using the same fixed Maxpe damage initiation criterion. Although the experimental data can be accurately predicted in simulations with XFEM planar crack, the calibrated damage parameters might not be practically representative of the actual material performance.

This chapter develops a novel XFEM variable strain-based damage model by adopting a critical varying strain profile taking into account the crack-tip constraint derived from a modified

Mohr-Coulomb fracture criterion. The novel damage criterion is validated by comparing with the results measured from small-scale SENT tests and full-scale tests. An optimal set of damage parameters is calibrated specific to X100 in predicting experimental J-R curves, force-CMOD curves and fracture profiles in SENT tests. The numerical J-integrals are computed from the two methods with one evaluated from surface strains and the other evaluated from CMOD using equations published by CANMET-MTL. Another optimal set of damage parameter is calibrated specific to X52 in predicting experimental TSC, force-CMOD curves, force-rotation curves, and reduction of pipe wall thickness in full-scale tests. The initial crack in each model is simulated by cutting a notch instead of typically inserting a planar crack into the mesh and the effect of crack tip simulation using notch or planar crack is discussed. The predictions are also compared with those using the simple fixed damage criterion. At the end, the calibrated damage parameters of X100 and X52 are compared with those calibrated for other pipe grades in the literature.

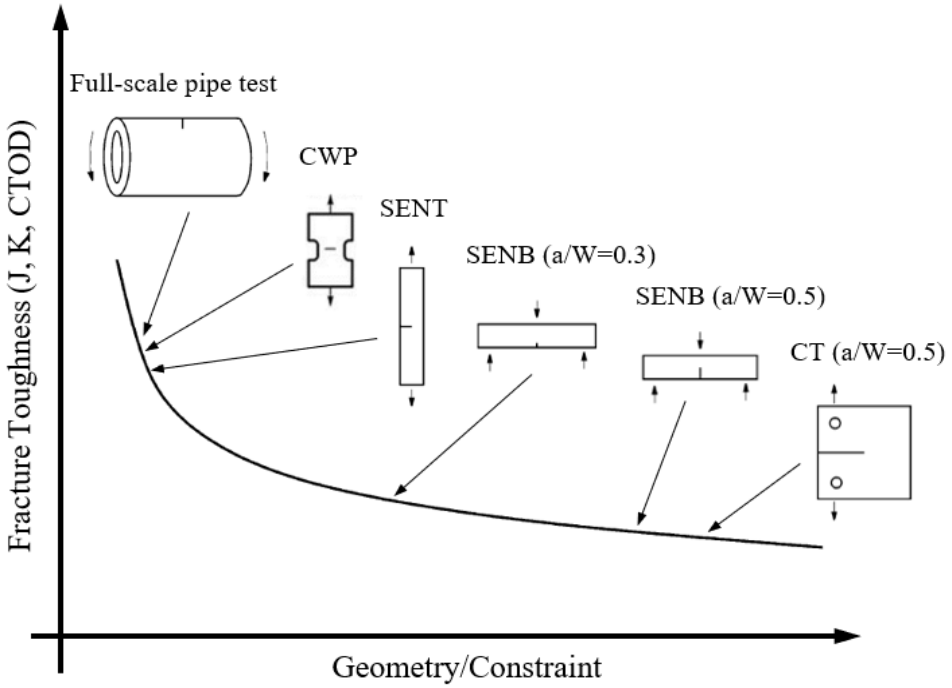

Figure 5-1. Effect of specimen geometry and constraint on fracture toughness. (Adapted from Chiesa et al. [56] and Kang et al. [57].) Note CWP, SENT, SENB, CT represents curved wide

plate test, single edge notched tension test, single edge notched bending test, and compact tension test, respectively.

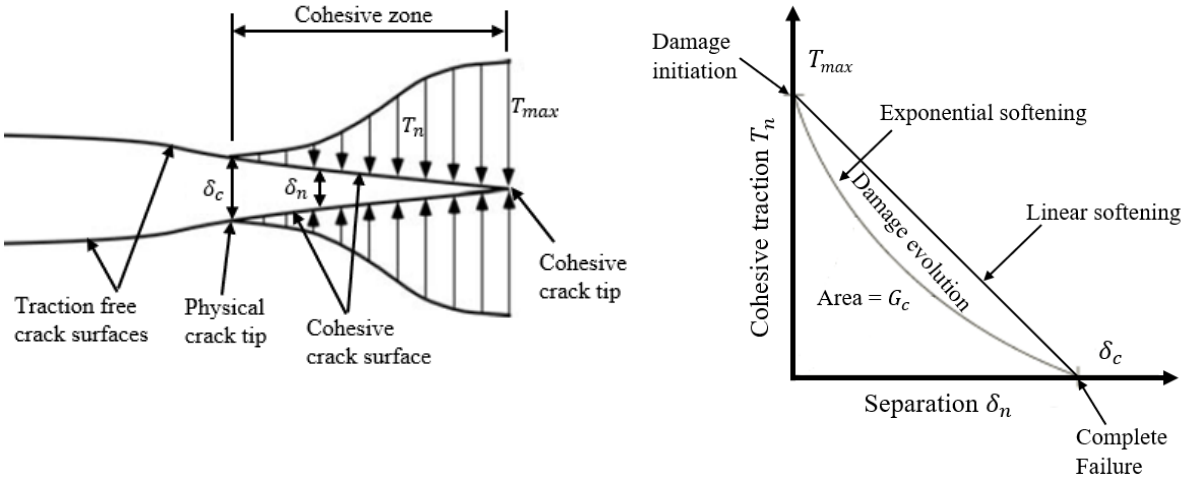

(a) (b)

Figure 5-2. (a) Concept of cohesive zone model; and (b) damaged traction-separation response in XFEM. [Adapted (a) from Anderson [49] and (b) from Abaqus documentation [30].]

5.3 Methodology

The hydrostatic pressure p, von Mises stress q, and the third stress invariant r are the three invariants of stress tensor $[\sigma]$, which can be determined from the three principal stresses σ_1, σ_2 and σ_3 given by Eqs. (*5-1*) to (5-3). The two stress state parameters, stress triaxiality parameter (η) and Lode angle parameter ($\bar{\theta}$) can be formulated in terms of p, q and r given by Eqs. (5-4) to (5-6). Here, $\bar{\theta}$ is actually normalized from Load angle θ with the range $0 \leq \theta \leq \pi/3$ and related to the normalized third deviatoric stress invariant ξ with the range $-1 \leq \xi \leq 1$. The range of $\bar{\theta}$ (referred to Lode angle parameter hereinafter) is $-1 \leq \bar{\theta} \leq 1$, and $\bar{\theta} = -1$, 0, and 1 respectively correspond to axisymmetric compression or equi-biaxial tension, plastic plane strain or generalized shear, and axisymmetric tension [75].

The Mohr–Coulomb (MMC) fracture criterion has been extensively employed to describe the brittle fracture of geo-materials in a stress-based form. It was extended by Bai and Wierzbicki [75] into a strain-based form to determine the equivalent fracture strain $\bar{\varepsilon}_f$ to describe the ductile fracture of uncracked bodies, as a function of triaxiality parameter (η) and Lode angle parameter ($\bar{\theta}$) to account for specimen constraints given by Eq. (5-7).

$$p = -\frac{1}{3}(\sigma_1 + \sigma_2 + \sigma_3) \tag{5-1}$$

$$q = \sqrt{\frac{1}{2}[(\sigma_1 - \sigma_2)^2 + (\sigma_2 - \sigma_3)^2 + (\sigma_1 - \sigma_3)^2]} \tag{5-2}$$

$$r = \left[\frac{27}{2}(\sigma_1 + p)(\sigma_2 + p)(\sigma_3 + p)\right]^{1/3} \tag{5-3}$$

$$\eta = -\frac{p}{q} \tag{5-4}$$

$$\xi = \left(\frac{r}{q}\right)^3 = cos(3\theta) \text{ and } 0 \le \theta \le \frac{\pi}{3},\ -1 \le \xi \le 1 \tag{5-5}$$

$$\bar{\theta} = 1 - \frac{6\theta}{\pi} = 1 - \frac{2}{\pi} arccos\xi \text{ and } -1 \le \bar{\theta} \le 1 \tag{5-6}$$

$$\bar{\varepsilon}_f = \left\{\frac{A}{c_2}\left[1 - c_\eta(\eta - \eta_0)\right] \times \left[c_\theta^s + \frac{\sqrt{3}}{2-\sqrt{3}}(c_\theta^{ax} - c_\theta^s)\left(sec\left(\frac{\bar{\theta}\pi}{6}\right) - 1\right)\right]\left[\sqrt{\frac{1+c_1^2}{3}} cos\left(\frac{\bar{\theta}\pi}{6}\right) + c_1\left(\eta + \frac{1}{3} sin\left(\frac{\bar{\theta}\pi}{6}\right)\right)\right]\right\}^{-\frac{1}{n}} \text{ and } c_\theta^{ax} = \begin{cases} 1 \text{ for } \bar{\theta} \ge 0 \\ c_\theta^c \text{ for } \bar{\theta} < 0 \end{cases} \tag{5-7}$$

$$\bar{\varepsilon}_f = \left\{c_2 \times \left[c_3 + \frac{\sqrt{3}}{2-\sqrt{3}}(c_4 - c_3)\left(sec\left(\frac{\bar{\theta}\pi}{6}\right) - 1\right)\right]\left[\sqrt{\frac{1+c_1^2}{3}} cos\left(\frac{\bar{\theta}\pi}{6}\right) + c_1\left(\eta + \frac{1}{3} sin\left(\frac{\bar{\theta}\pi}{6}\right)\right)\right]\right\}^{-\frac{1}{n}} \text{ and } c_4 = 1 \text{ for } 0 \le \bar{\theta} \le 1 \tag{5-8}$$

where A and n are the material strain hardening parameters; c_1 and c_2 are primary fracture parameters in original stress-based from with the range $c_1 \ge 0$ and $c_2 > 0$; c_η and η_0 are additional fracture parameters of pressure dependence; c_θ^s and c_θ^c are additional fracture

parameters of Lode angle dependence; by fixing $c_\eta = 0$ and $c_\theta^c = 1$, $c_\theta^s = 1$ and $\sqrt{3}/2$ respectively correspond to the von-Mises yield condition and Tresca yield condition [75].

The new equation introduced in this chapter and given by Eq. (5-8), consists of five unknown parameters: n, c_1, c_2, c_3 and c_4. The equation simply neglects the component $\left[1 - c_\eta(\eta - \eta_0)\right]$ due to the similarity of c_η and η_0 with c_1 in terms of pressure dependence effect as suggested [75]. An equivalent new c_2 is adopted to replace the original A/c_2 thus the strength coefficient A can be removed. In addition, c_3 and c_4 are adopted to equivalently replace the original c_θ^s and c_θ^c respectively. The strain hardening exponent n is determined from curve fitting of a power law to the strain hardening region of the true stress-strain curve measured in material tensile coupon tests as $\sigma = A\varepsilon^n$ or $\sigma = A{\varepsilon_p}^n$. c_1, c_2, c_3 and c_4 are four calibrated fracture parameters in fracture tests and c_4 can be simply taken as 1 if the loading condition is known to be dominated by $\bar{\theta} \geq 0$.

One currently built-in damage initiation criterion in XFEM-based cohesive segments method implemented in Abaqus/Standard assumes the damage occurs when Maxpe of an enriched element reaches a user defined maximum allowable principal strain, i.e., the damage initiation criterion f reaches 1.0 within a given tolerance f_{tol}. The numerical Maxpe and fixed maximum allowable Maxpe can be respectively replaced by the numerical equivalent plastic strain (PEEQ) and variable damage strain $\bar{\varepsilon}_f$ given by Eq. (5-9). The novel XFEM variable strain damage initiation criterion is implemented using a Fortran code programmed in Abaqus user subroutine-UDMGINI [30].

$$1.0 \leq f = \left\{\frac{PEEQ}{\bar{\varepsilon}_f}\right\} \leq 1.0 + f_{tol} \tag{5-9}$$

5.4 Small-scale SENT simulations and results

5.4.1 Model Setup

The three-dimensional finite-element models were developed using Abaqus/Standard to simulate the small-scale SENT tests conducted by Shen et al. in CANMET-MTL [63] for 11 clamped specimens cut from the base metal of a API 5L X100 pipeline with an outer diameter of 1219 mm (NPS 48) and a wall thickness of 14.3 mm. Each specimen had a square cross section (width W = thickness B = 12.7 mm) and a total length ($18W$ = 228.6 mm) consisted of a daylight distance between the grips of 10 times width ($H = 10W$ = 127 mm) and additional grip length of 4 times width ($4W$ = 50.8 mm) required at each end to impose fixed-grip loading. Each specimen was machined either plain-sided or side-grooved providing a net specimen thickness of $B_N = 90\%B$ (side groove depth = $5\%B$). All specimens were fatigue precracked to a depth of either $0.25W$ or $0.5W$. In total, 6 specimens were machined for a "deep crack" with 3 side-grooved (Deep, SG-1/2/3) and 3 plain-sided (Deep, PS-1/2/3), while 5 specimens were machined for a "shallow crack" with 3 side-grooved (Shallow, SG-1/2/3) and 2 plain-sided (Shallow, PS-1/2). The measured initial crack size of each deep-cracked specimen was the same as the target value of $0.5W$, while that of each shallow-cracked specimen was slightly different from the target value of $0.25W$ (respectively $0.27W$, $0.26W$, $0.25W$, $0.22W$, $0.31W$ for SG-1, SG-2, SG-3, PS-1, PS-2).

A total of 4 SENT specimen with the following configurations were modelled: deep-cracked and side-grooved (Deep, SG) (Figure 5-3), deep-cracked and plain-sided (Deep, PS), shallow-cracked and side-grooved (Shallow, SG), and shallow-cracked and plain-sided (Shallow, PS). The side groove was created with an angle of 45° with a root radius of 0.5 mm as recommended by CANMET-MTL [124]. The initial fatigue crack was particularly simulated by cutting a 0.1 mm-wide u-shaped notch with a depth of $0.25W$ [Figure 5-4 (a)] or $0.5W$ at the middle length

of the model. The notch tip was meshed with a square shape for simplicity. In this way, the initial location of the crack was not pre-specified but determined by the software during the analysis based on the calculated critical strain values in the crack domain. This 0.1 mm-wide notched SENT model could further represent current widely used SENT specimens prepared using electrical discharge machining (EDM) with a fine wire of 0.1 mm diameter to machine the notch directly to the target crack depth, as a practical alternative of fatigue pre-cracking. Experiments conducted by CANMET-MTL [125] demonstrated that the fine EDM notched SENT specimens (blunt crack) produced slightly higher J-resistance curves than those of fatigue pre-cracked specimens (sharp crack) due to the differences in crack tip blunting process, but this difference was minor in comparison with normal scatters in SENT tests. An additional side-grooved model with an initial planar crack inserted into the finite element mesh [Figure 5-4 (b)] was developed to investigate the effect of using such approach on the simulation of crack propagation.

Due to the symmetry around the X-Z plane, only half of the specimen was modelled to reduce the computational burden. The grip at one end was completely fixed, while the grip at the other end was constrained to an assigned reference node loaded with a cyclic tensile displacement along the X-axis (Figure 5-3). The mesh partition technique was employed in the model allowing a finer mesh size as small as 0.2 mm in a partitioned region fully covering the potential crack propagating region and coarser mesh size up to 2.54 mm in other regions (Figure 5-4). The solid or continuum meshing was generated in the entire model using predominantly structured hexahedral or brick elements C3D8R and a lesser number of tetrahedral elements C3D4 in two connected partitioned regions transiting the mesh size from smallest to largest. C3D8R indicates continuum, 3-D, 8-node linear brick element with reduced integration (1 integration point located in the middle of the element) and hourglass control algorithm, while C3D4 indicates a continuum, 3-D, 4-node linear tetrahedron element.

The SENT specimen was simulated as an elastoplastic isotropic material. The elasticity was defined with the Young's modulus of 210 GPa and the Poisson's ratio of 0.3. The tensile properties of the X100 pipe steel were measured from 4 round bar specimens oriented in the longitudinal direction of the pipe by CANMET-MTL [63]. The averaged measurement of the engineering stress-strain curve and the converted true stress-strain up to the ultimate tensile stress are shown in Figure 5-5 (a). The damage initiation criterion was defined when the PEEQ of an enriched element reached $\bar{\varepsilon}_f$ determined by Eq. (5-9) within a given tolerance of 0.1 and implemented using a Fortran code programmed in Abaqus user subroutine-UDMGINI [30]. The damage evolution criterion was defined by a linearly softening TSL with a mode-independent critical energy release rate G_c. The value of the hardening parameter n was taken from the calibration of the true stress-strain curve of X100 with a correlation coefficient (R^2) of 0.9933 performed by CANMET-MTL for the same pipe steel [126]. Based on the known n (0.0923) and c_4 (simply taken as 1), other damage parameters c_1, c_2, c_3 and G_c (Table 5-1) were calibrated by performing numerous simulations to generate similar experimental results. My calibrated c_1, c_2 and c_3 are expectedly but rather surprisingly close to the calibration performed by Kofiani et al. [72] for another X100 pipe steel with a different n (0.0384) based on small-scale tests on uncracked specimens (Table 5-8). A 3D damage initiation locus in the space of $\bar{\varepsilon}_f$, η, and $\bar{\theta}$ based on above calibrated set of damage parameters was displayed in Figure 5-5 (b). $\bar{\varepsilon}_f$ exponentially decreases as η increases, and the near-parabolic locus of $\bar{\varepsilon}_f$ is slightly asymmetric with respect to $\bar{\theta}$.

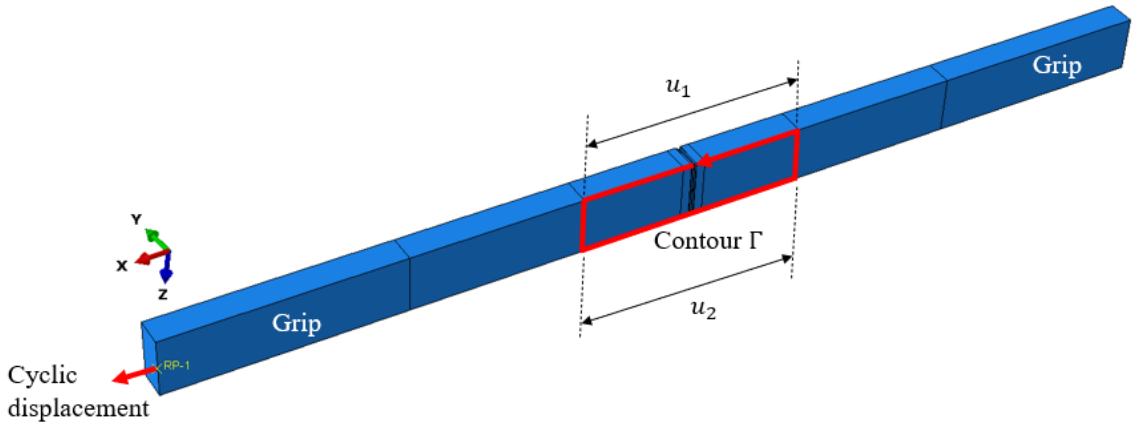

Figure 5-3. Illustration of a model configuration and contour Γ in calculating the J-integral.

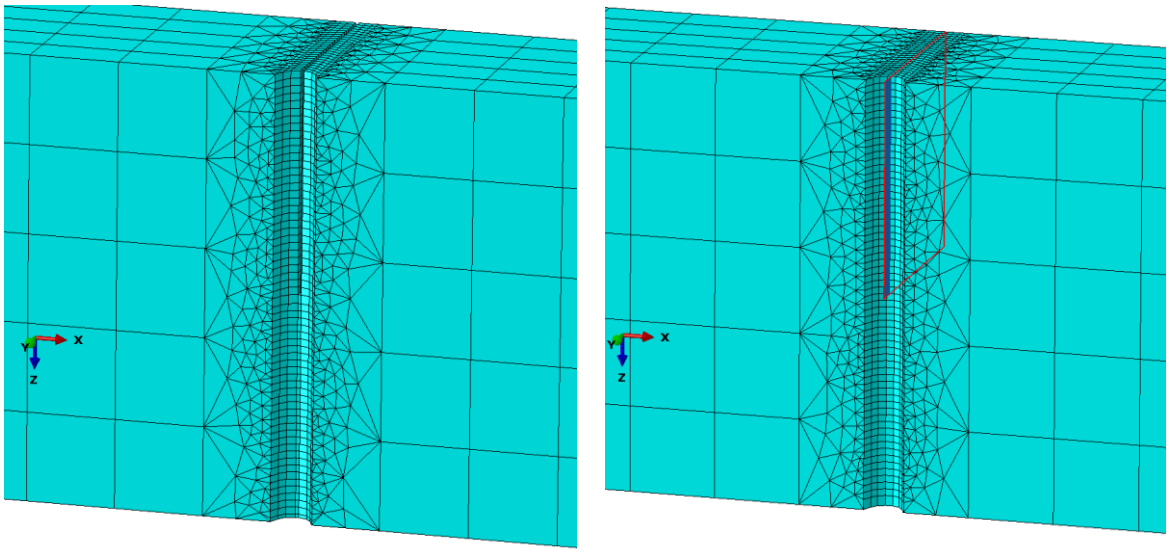

(a) (b)

Figure 5-4. Mesh distribution near a (a) notch or (b) planar crack in a side-grooved SENT model.

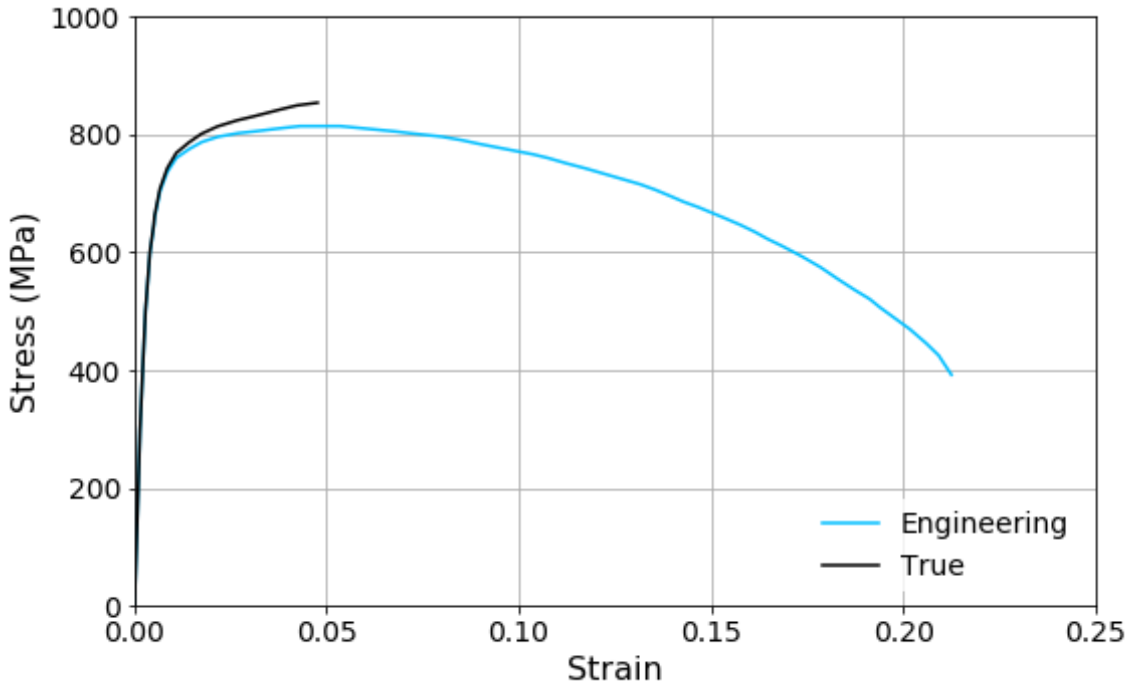

(a)

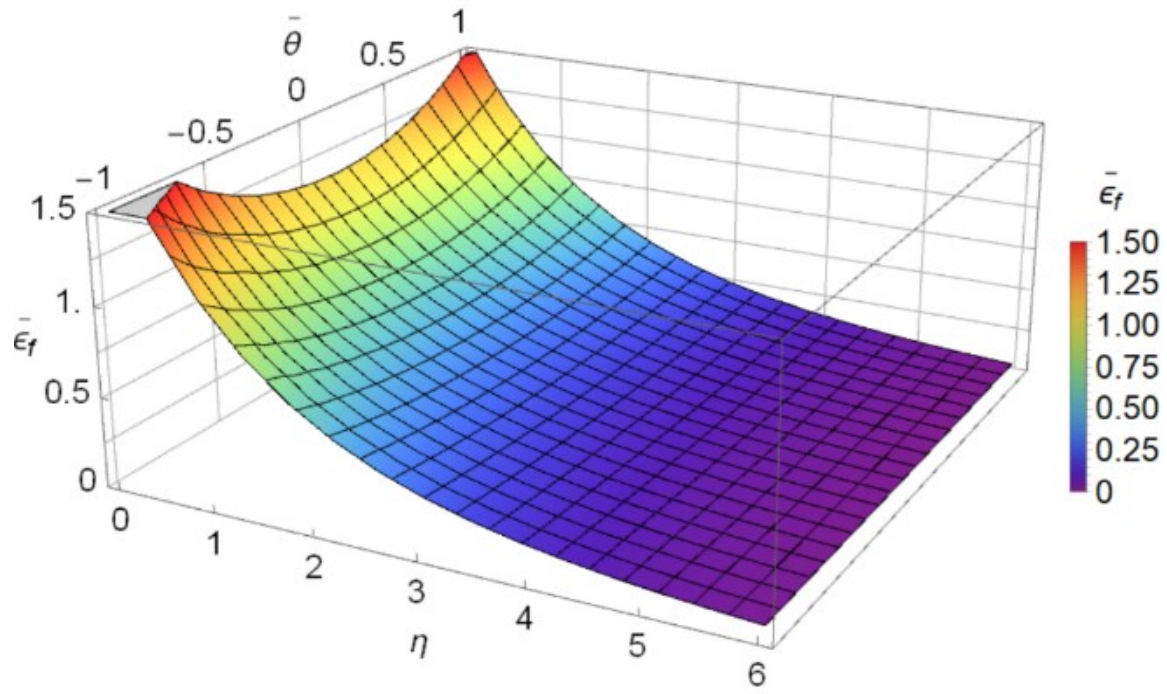

(b)

Figure 5-5. Properties of X100 (a) stress-strain curve; and (b) damage initiation locus curve.

Table 5-1. Calibrated parameters of novel XFEM damage criterion for X100.

Pipe Grade	n	c_1	c_2	c_3	c_4	G_c (N/mm or mJ/mm^2)
X100	0.0923	0.03	1.9	0.9	1	100

5.4.2 Comparison with Tests and Fixed Damage Criterion

The results generated from the 4 SENT models adopting the novel variable strain-based damage criterion with above calibrated set of damage parameter were compared with the experimental results [63] in terms of the force-CMOD curves, J-R curves (J versus Δa), and fracture profiles. In the XFEM capability of Abaqus/Standard, the contour integral evaluation is available in the stationary crack analysis, but unavailable in the propagating crack analysis because the crack-tip enrichment is not considered. Alternatively, two methods were adopted to calculate the J-integral.

The first method evaluates the J-integral from the numerical surface strains, which is a replication of the experimental evaluation from strain gages data, following the procedures described by Weeks et al. [127]. Theoretically, J is an energetic contour path integral around a crack and its mathematical expression is given by Eq. (5-7). For my purpose, Γ was chosen as a far-field contour (Figure 5-3) along the axial centerline of the specimen which was spaced at $4W$ (50.8 mm) and symmetric about the notch-plane at the center, encompassing the top-face surface, through-thickness surface, and back-face surface. The first component $\int_\Gamma W_\varepsilon dx_2$ was calculated by integrating the strain energy density function W_ε, where x_2 was taken from the Abaqus coordinate output variable COOR1 (coordinate in x direction) and W_ε was taken as the sum of the ESEDEN (total elastic strain energy density in the element) and EPDDEN (total plastic dissipation energy density in the element). The second component -$\int_\Gamma \vec{T} \cdot \frac{d\vec{u}}{dx_1} ds$ could be approximated by the product of the averaged tensile stress (P/A) and the difference in the

axial extensions between the top-face and back-face surface ($u_1^s - u_2^s$) in the deformed shape, where P was taken from the 2 times reaction force measured by the loading point, A is the specimen total cross sectional area, and $u_1^s - u_2^s$ was simply calculated by $u_1 - u_2$ as specimen deforms (Figure 5-3). The J-integral calculated using this method was termed as J_{Model}.

$$J_{Model} = \oint_{\Gamma} \left(W_\varepsilon dx_2 - \vec{T} \cdot \frac{d\vec{u}}{dx_1} ds \right) \approx \int_{\Gamma} W_\varepsilon dx_2 + \frac{P}{A}(u_1^s - u_2^s) \quad (5\text{-}10)$$

The second method (Appendix A) evaluates the J-integral from the CMOD using equations published by CANMET-MTL [63,91] that were developed based on their previous FEA models using the area under the curve of the load versus plastic CMOD and validated for SENT specimens with H/W=10 and $0.1 \leq a/W \leq 0.7$. In this method, at each unloading sequence, the numerical load P, CMOD, and crack size (a) were obtained from the model and used to compute the J-integral using equations published by CANMET-MTL and their FEA calibrated coefficients. The J-integral calculated using this method was termed as $J_{Equation}$.

J_{Test} were obtained by data fitting of the J-R curves published by Shen et al. [63] which were computed from same CANMET-MTL equations but a was evaluated from CMOD unloading compliance C at each unloading sequence based on their calibrated coefficients. The unloading compliance method was proposed due to the relation between the instantaneous crack size and unloading compliance: as crack extends further, the unloading slope reduces, thus the compliance which is equivalent to the inverse of the slope increases. It is worth mentioning that a difference between $J_{Equation}$ and J_{Test} is the measurement of instantaneous crack size which are directly measured from my models for $J_{Equation}$, but are evaluated from rotation corrected CMOD unloading compliance based on FEA calibrated coefficients for J_{Test}[63].

The numerical force-CMOD curves throughout the loading-unloading cycles are compared with experimental curves in Figure 5-6. Since Shen et al. [63] only provided two force-CMOD

curves respectively for shallow-cracked and deep-cracked specimens, without indicating whether they were measured from side-grooved or plain-sided specimen, these experimental curves were compared with numerical curves generated from both SG and PS models. The numerical load capacity described by the maximum force (P_{max}) was 0.3% lower (deep, SG) and 4.8% higher (deep, PS) than the experimental maximum force for deep-cracked specimen, and it was 0.1% higher (shallow, SG) and 2.2% higher (shallow, PS) than the experimental maximum force for shallow-cracked specimen. In addition, Shen et al. [63] provided normalized unloading compliance (BCE) values of each unloading sequence, and we replotted these BCE values and added in the force-CMOD curves to illustrate the unloading compliance more clearly and compared them with numerical BCE in Figure 5-6. Here, B is the specimen's thickness (12.7 mm) for a plain-sided specimen or the effective thickness (12.573 mm) calculated by $\mathrm{B} - (\mathrm{B} - \mathrm{B_N})^2/\mathrm{B}$ and $\mathrm{B_N}$ = 90%B for a side-grooved specimen, C is the CMOD compliance equivalent to the inverse of the slope of force-CMOD curves and E is young's modulus. Both deep-cracked models showed a higher BCE values than those reported in the tests, but the BCE in the deep PS model was closer to those in the tests after CMOD exceeded 1.4 mm. Both Shallow-cracked models showed almost identical BCE values as those in tests, but BCE in the shallow PS model was slightly lower than those in the tests after CMOD exceeded 2.0 mm. Such differences in BCE would not affect numerical J-integral calculations because the instantaneous crack size was measured directly from models, not from the CMOD unloading compliance as adopted in the tests.

A total of 11 experimental J-R curves [63] extracted from Δa = 0.2 mm were fitted with 4 power-law curves (J_{Test} in Figure 5-7) for each specimen configuration with a minimum R^2 of 0.96 expect for the shallow PS model which has smaller R^2 of 0.873. This lower correlation coefficient was caused by the large initial crack depth difference measured in the two specimens ($0.22W$ and $0.31W$ for Shallow PS-1 and PS-2). The numerical crack extension Δa

was defined by two methods (centered Δa and averaged Δa) in Figure 5-8. Centered Δa was measured from the damaged elements located at specimen center, which corresponded to the crack tip element E5 as shown in Figure 5-11(b1) and subsequent elements along the crack depth direction. Averaged Δa was measured using the nine-point-average techniques [55] at the crack front from the damage elements respectively located at crack tip elements E1 to E5. Since centered Δa was more consistent than averaged Δa between PS and SG models, centered Δa referred as Δa thereafter was adopted for comparing the numerical and experimental results. STATUSXFEM (status of the enriched element) can be used to indicate a damage-free element (STATUSXFEM = 0), partially damaged element (0 < STATUSXFEM <1), or fully damaged element (STATUSXFEM =1). To avoid a sudden jump of Δa in the J-R curves, we proposed Δa calculated by the product of damaged element depth and STATUSXFEM value. If a 0.2 mm deep element was damaged with STATUSXFEM = 0.5, Δa was considered as 0.1 mm. Figure 5-9 compares J_{Test}, J_{Model} and $J_{Equation}$ after eliminating the unloading data. J_{Model} and $J_{Equation}$ were fitted with power-law curves for each specimen configuration except for the deep PS model where logarithmic curves provided a better fit. Excellent matchings were achieved for the SG models among J_{Test}, J_{Model} and $J_{Equation}$ for the deep crack, and between J_{Test} and J_{Model} for the shallow crack, while some differences were observed in the PS models. All the fitting curves are listed in Table 5-2. The strain distribution around the crack for both SG models are shown in Figure 5-10. The crack propagation was consistently along the Z-axis perpendicular to the loading direction in the shallow SG model (b) throughout the simulation, while it slightly but rather unnoticeably deviated in the deep SG model (a) and this perhaps could be attributed to some asymmetries induced by the mesh or other numerical approximation factors. A black line along the Y-axis in the high strain region in (a) indicated the path where the crack propagation deviated from the centerline elements to the neighbouring elements.

Table 5-2. Comparisons of fitted J-R curves.

Specimens / (kJ/m^2)	Deep, SG	Deep, PS	Shallow, SG	Shallow, PS
J_{Test}	$1088.1\Delta a^{0.469}$ ($R^2 = 0.96$)	$1141.479\Delta a^{0.397}$ ($R^2 = 0.97$)	$1292.531\Delta a^{0.505}$ ($R^2 = 0.974$)	$1446.597\Delta a^{0.427}$ ($R^2 = 0.873$)
J_{Model}	$1025.596\Delta a^{0.52}$ ($R^2 = 0.957$)	$642.651\ln(\Delta a) + 1269.029$ ($R^2 = 0.979$)	$1282.222\Delta a^{0.561}$ ($R^2 = 0.983$)	$1337.553\Delta a^{0.62}$ ($R^2 = 0.978$)
$J_{Equation}$	$1054.368\Delta a^{0.452}$ ($R^2 = 0.952$)	$532.809\ln(\Delta a) + 1269.029$ ($R^2 = 0.979$)	$1382.051\Delta a^{0.59}$ ($R^2 = 0.981$)	$1331.299\Delta a^{0.671}$ ($R^2 = 0.97$)

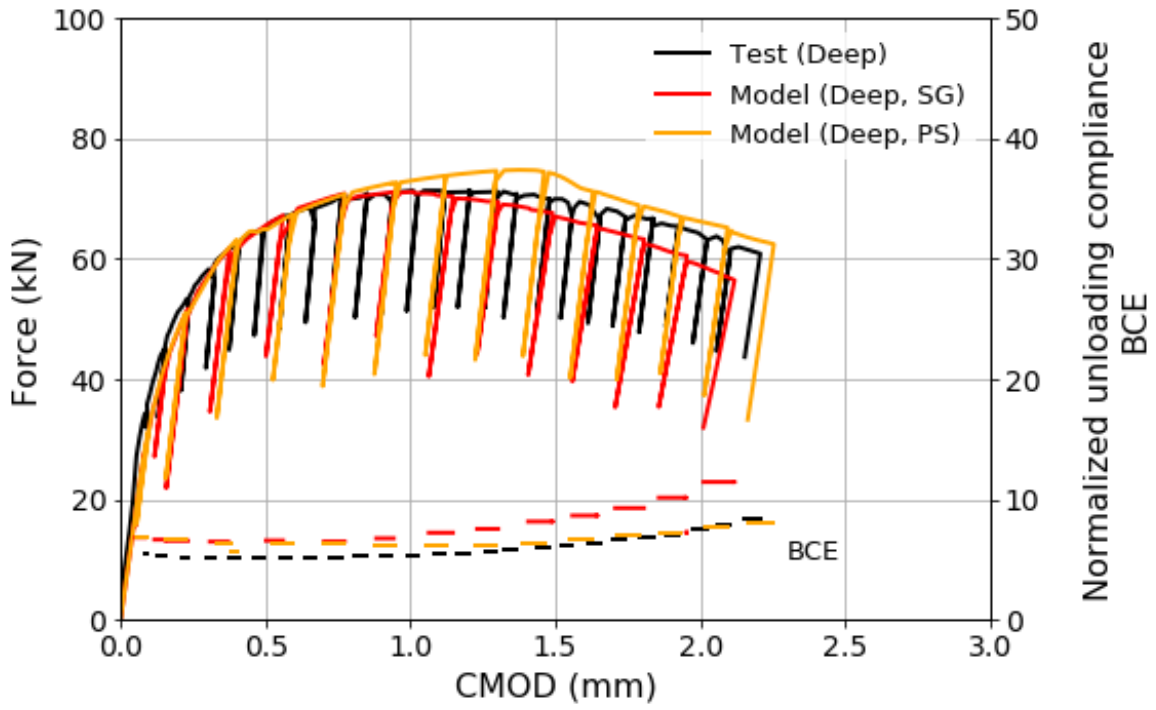

(a)

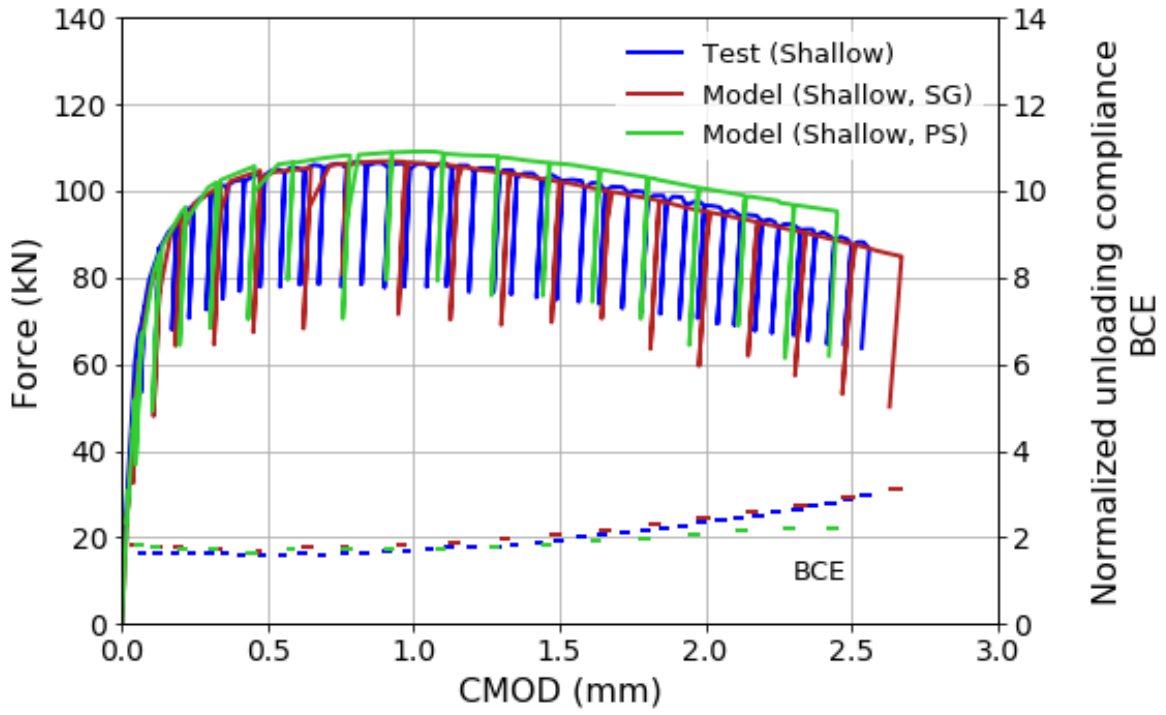

(b)

Figure 5-6. Comparisons of experimental and numerical force-CMOD throughout theloading-unloading cycles for (a) deep crack; and (b) shallow crack. Note the normalized unloading compliance BCE is computed from each unloading sequence, where B is effective thickness of specimen calculated by $(B - B_N)^2/B$, C is CMOD compliance equivalent to the inverse of the slope of force-CMOD curves, and E is young's modulus.

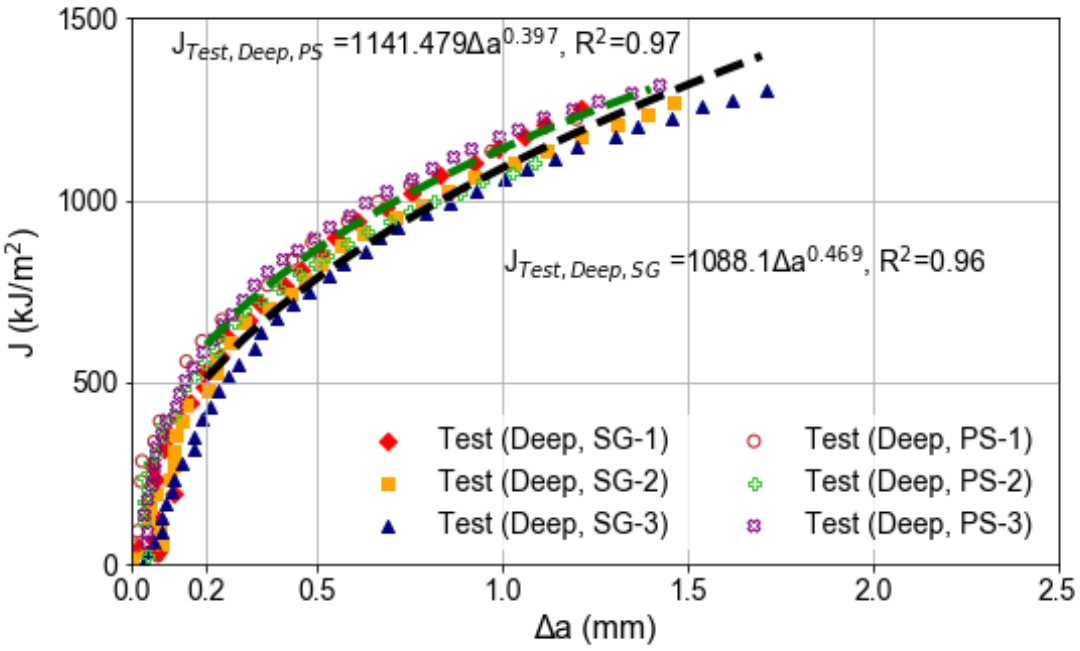

(a)

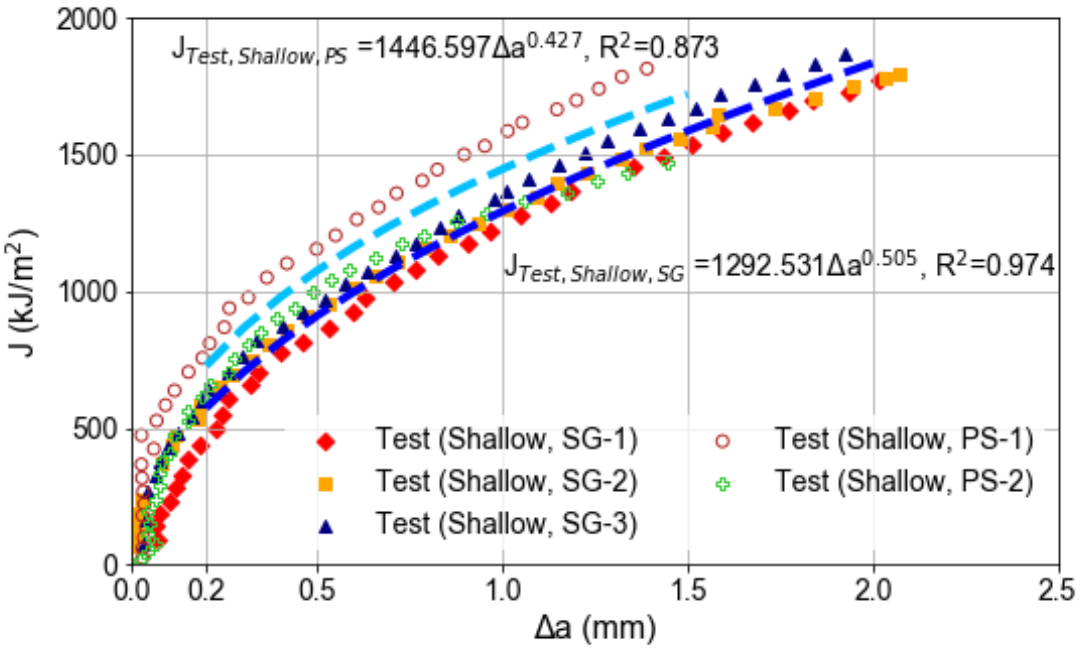

(b)

Figure 5-7. Curve fitted J_{Test} from experimental data beginning from Δa = 0.2 mm for (a) deep crack; and (b) shallow crack.

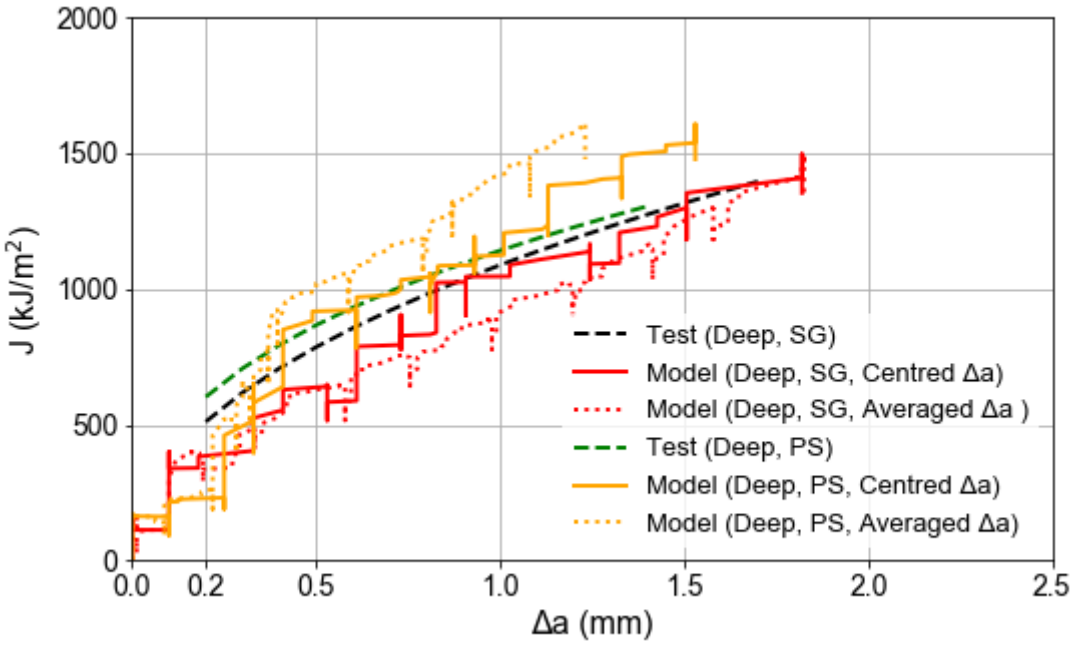

(a)

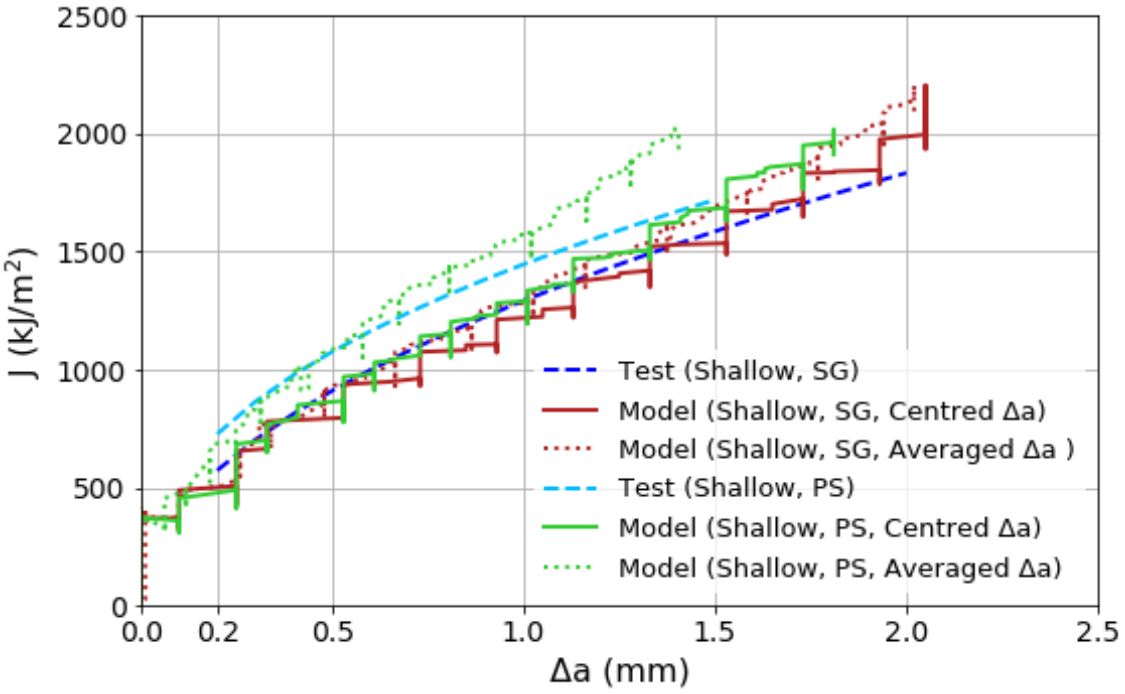

(b)

Figure 5-8. Comparisons of curve fitted J_{Test} and J_{Model} throughout the loading-unloading cycles for (a) deep crack; and (b) shallow crack.

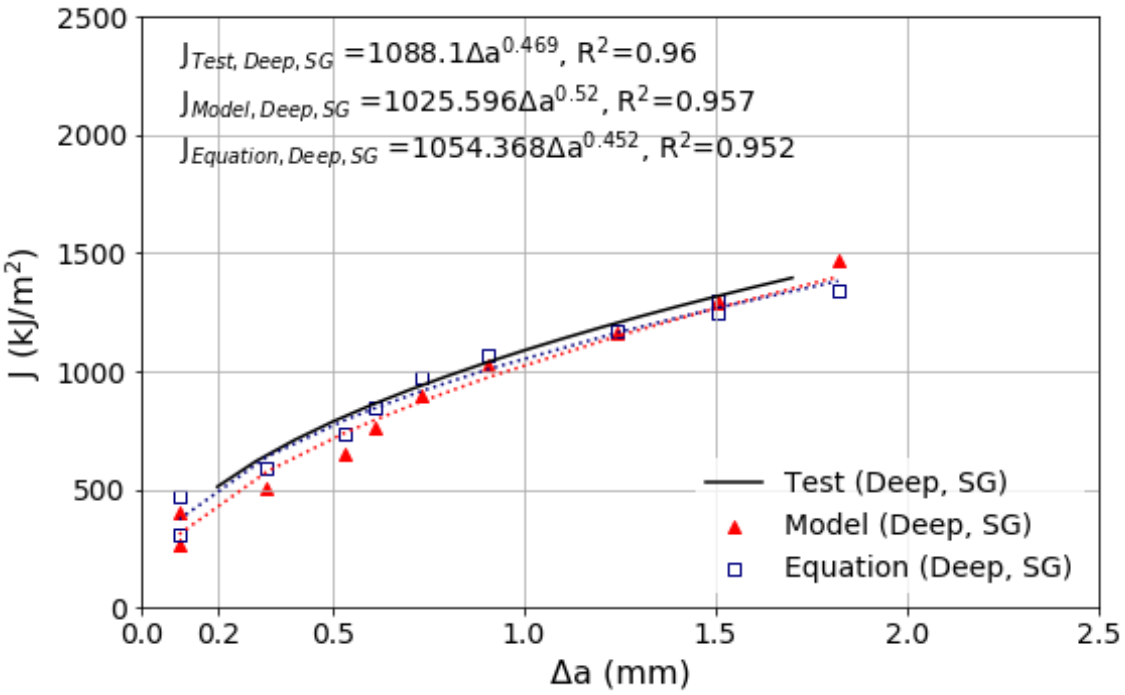
$J_{Test, Deep, SG}$ =1088.1Δa$^{0.469}$, R^2=0.96
$J_{Model, Deep, SG}$ =1025.596Δa$^{0.52}$, R^2=0.957
$J_{Equation, Deep, SG}$ =1054.368Δa$^{0.452}$, R^2=0.952
Test (Deep, SG)
Model (Deep, SG)
Equation (Deep, SG)
J (kJ/m^2)
Δa (mm)
0
500
1000
1500
2000
2500
0.0
0.2
0.5
1.0
1.5
2.0
2.5

(a)

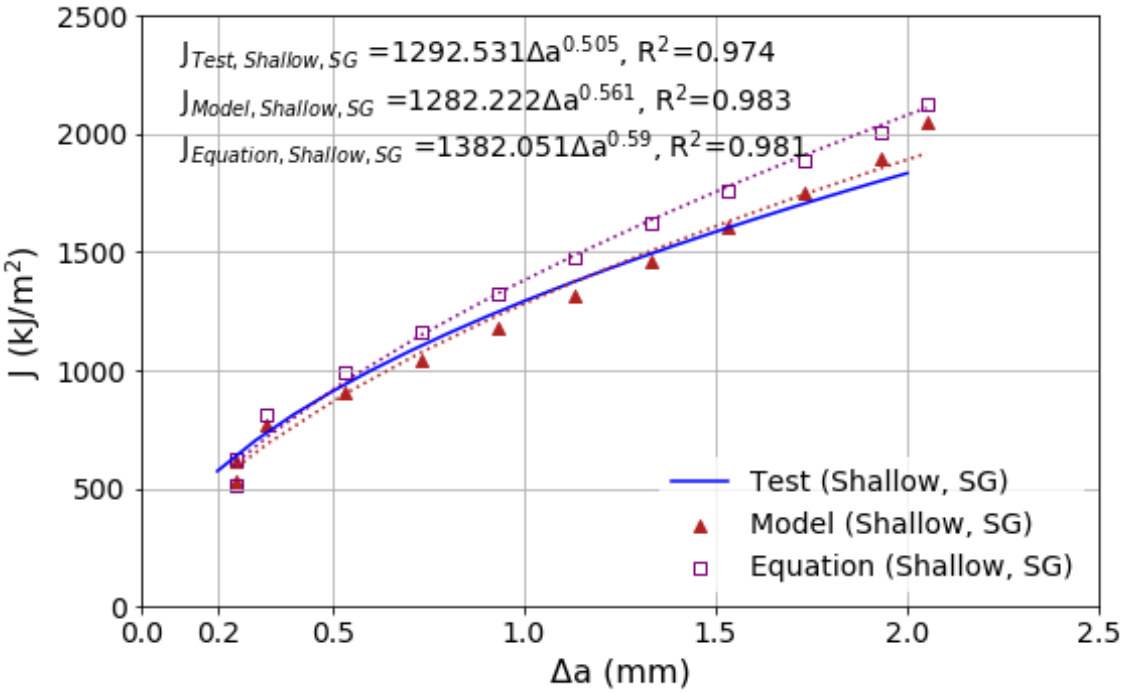
$J_{Test, Shallow, SG}$ =1292.531Δa$^{0.505}$, R^2=0.974
$J_{Model, Shallow, SG}$ =1282.222Δa$^{0.561}$, R^2=0.983
$J_{Equation, Shallow, SG}$ =1382.051Δa$^{0.59}$, R^2=0.981
Test (Shallow, SG)
Model (Shallow, SG)
Equation (Shallow, SG)
J (kJ/m^2)
Δa (mm)
0
500
1000
1500
2000
2500
0.0
0.2
0.5
1.0
1.5
2.0
2.5

(b)

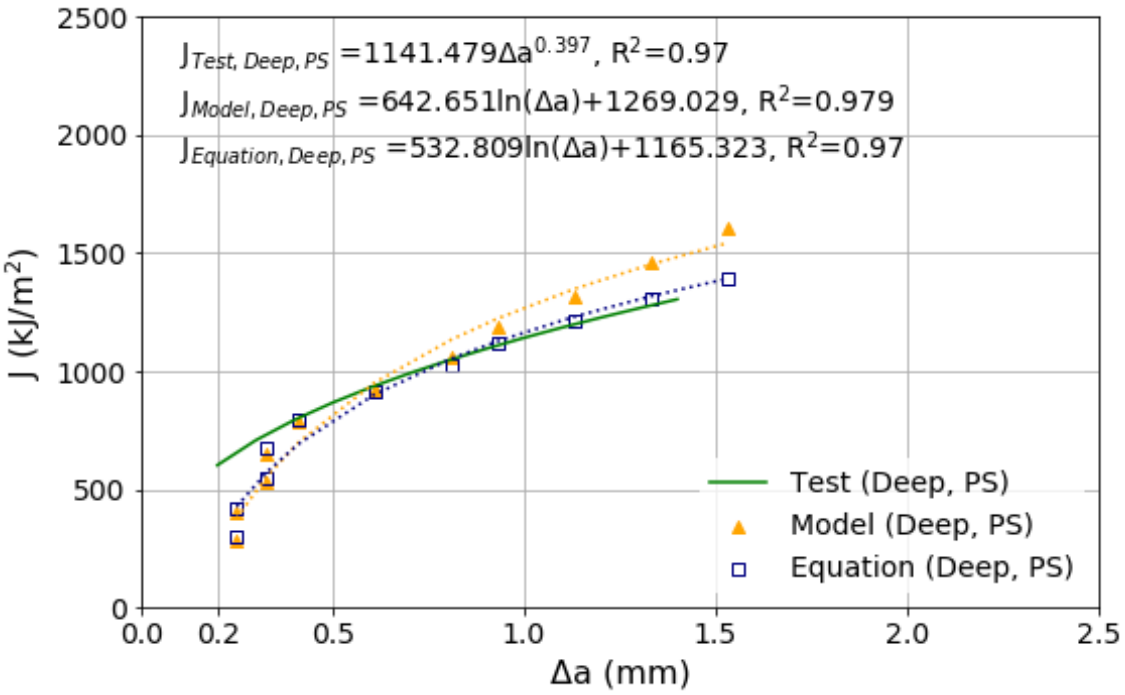

(c)

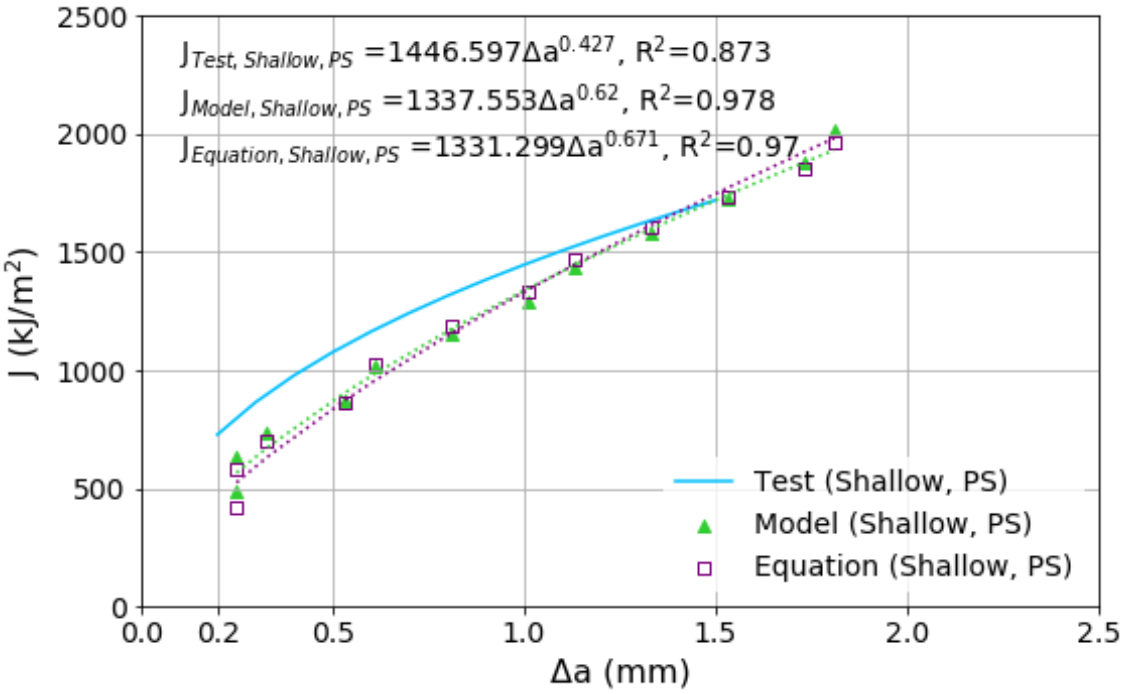

(d)

Figure 5-9. Comparison of curve fitted J_{Test}, J_{Model} and $J_{Equation}$ for (a) SG deep crack; (b) SG shallow crack; (c) PS deep crack; and (d) PS shallow crack.

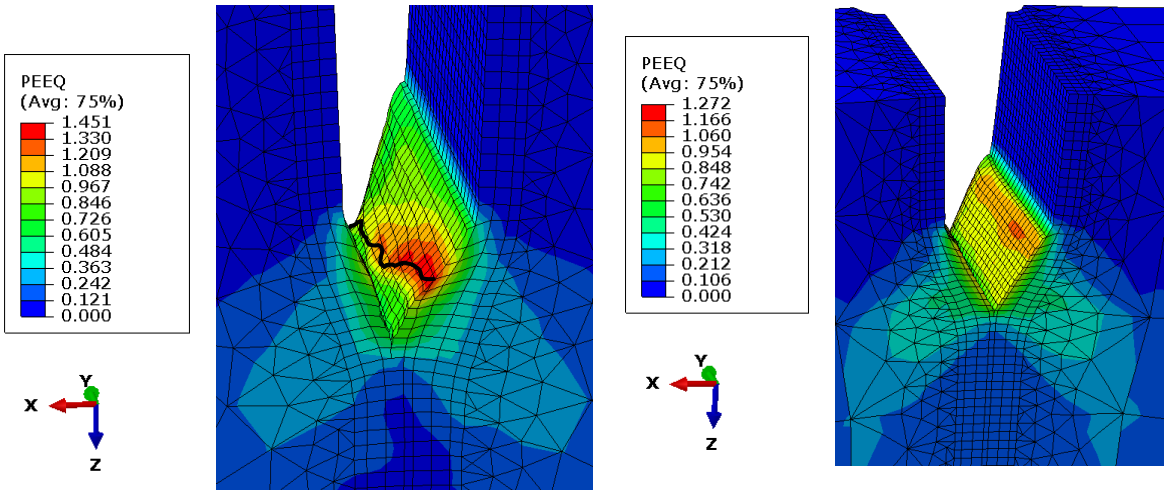

(a) (b)

Figure 5-10. Strain distribution around the crack in SG model with a (a) deep crack; and (b) shallow crack.

The limitation of a fixed Maxpe damage initiation criterion on a side-grooved SENT model were discussed in previous work [2]. Due to the presence of the side-groove, the fixed criterion resulted in very fast crack propagation at the edge of specimen in which high strains were concentrated due to the presence of side groove. However, experimental work demonstrated that 5%B side-groove on each side could promote straight-fronted crack extension without causing excessive crack growth on the edge [63]. To illustrate the effect, I repeated the deep and shallow SG models using a fixed damage criterion with allowable Maxpe = 0.2 and G_c =100 N/mm and compared the results when the novel variable criterion was used. As demonstrated in Figure 5-11, both SG models with novel variable strain-base damage criterion demonstrated a basically straight (b1) or half parabolic-shape (b2) crack extension with slight growth at the edge, agreeing with the experimental ductile crack extension as shown in (a). This was a major improvement in predicting the crack propagation path from models with fixed strain-based damage criterion as shown in (c1) and (c2).

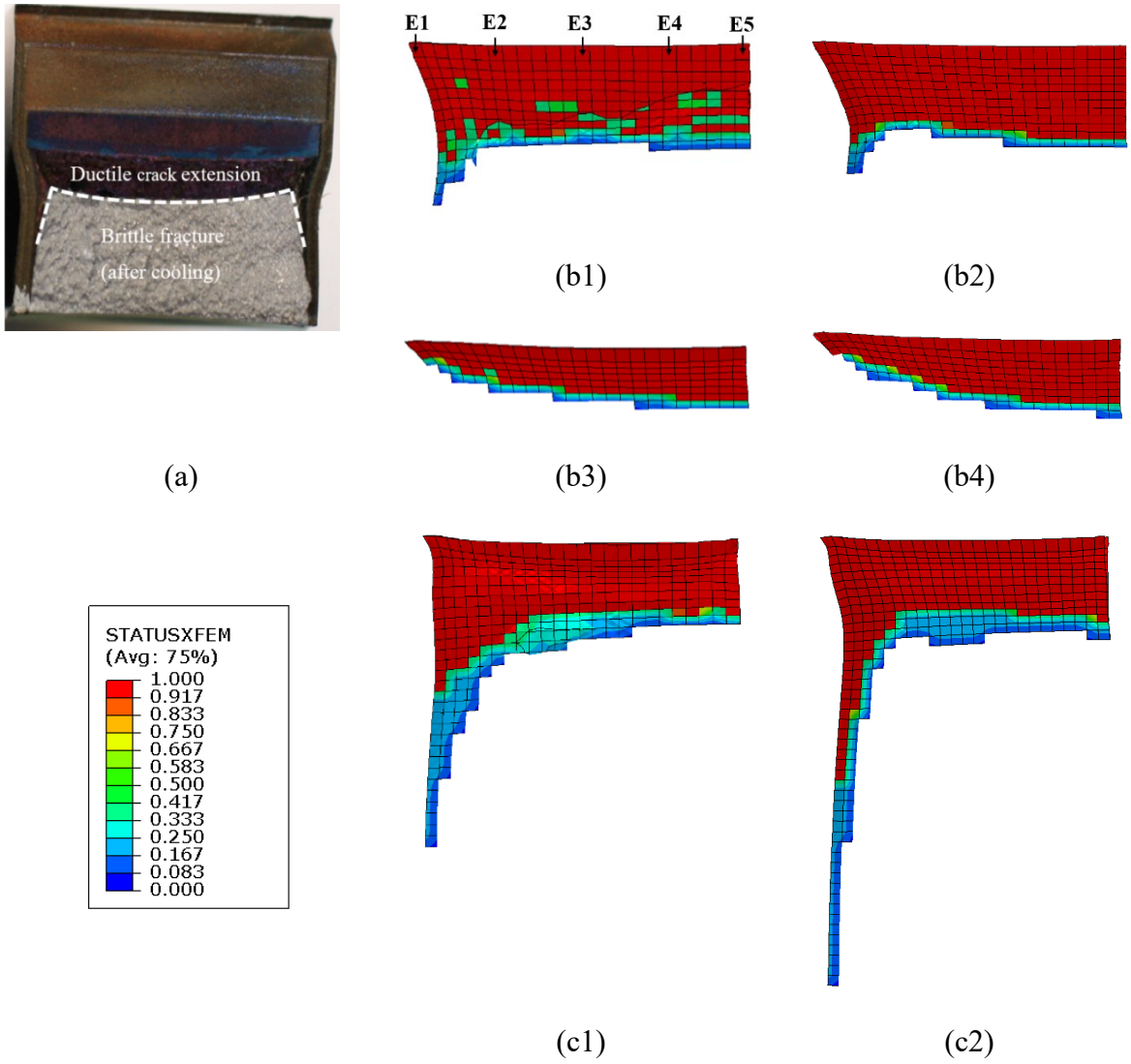

Figure 5-11. Comparisons of fracture profile from (a) test with a SG fatigue crack [63]; (b) model using novel variable strain damage criterion with (b1) SG deep crack, (b2) SG shallow crack, (b3) PS deep crack, (b4) PS shallow crack; and (c) model using fixed Maxpe damage criterion with (c1) SG deep crack and (c2) SG shallow crack. Note the right edge of numerical profiles is the specimen centerline, while the left edge is the specimen side. 5 crack tip elements along the crack front from side to center are marked by E1 to E5.

5.4.3 Investigation of Crack-tip Constraint

Figure 5-12 illustrates the damage strain (i.e., equivalent plastic strain), stress triaxiality, and Lode angle of every damaged element at the instance of reaching the damage criterion for the

4 notch models and 1 additional SG deep planar crack model adopting the novel variable strain damage criterion. The only difference between the SG deep notch model and the SG deep planar crack model is the simulation of initial crack. For the 4 notch models, the stress triaxiality values of the inner crack-tip elements along the crack front E2 to E5 where damage initiated were approximately around 4 for the deep notch while they were approximately around 3 for the shallow notch. In comparison with two SG deep models, the crack-tip elements E1 to E5 showed relatively high stress triaxiality between 3.6 and 4.4 at a force level around 45 kN in the notch model [Figure 5-12 (a)], while they showed relatively low stress triaxiality between 0.7 and 1.2 at a force level around 77 kN (reaching the maximum load) in the planar crack model [Figure 5-12 (e)]. The model with planar crack exhibited lower crack tip constrains as reflected in the lower stress triaxiality values at the crack tip resulting in higher resistance to crack propagation. Of all models, the Lode angle values of damaged elements where damage initiated seemed very scattered between -1.0 and 1.0.

Figure 5-13 illustrates the distribution of stress triaxiality and the equivalent plastic strain along the crack front of each model at different force levels before any damage occurred while the dashed line represented the instance when the first element was damaged in the model. For all models before damage initiation, the stress triaxiality of 4 inner crack-tip elements E2 to E5 were similar at any force levels and higher than that of the edge crack-tip element E1. In other word, the specimen center where the “plane strain” fracture mode is potentially dominating always has higher constraints than the outer free surface of the specimen. Since the stress triaxiality values are correlated with the expected failure strain, the inner elements at the crack front are expected to fail earlier, which can be clearly observed in the PS models [Figure 5-13 (b) and (d)]. The lower constraint at the plain-sided specimen outer surfaces can be removed by the side grooves and ideally a relatively straight crack front can be produced using appropriate side grooves. However, in the current 2 SG notch models [Figure 5-13 (a) and (c)],

the edge element E1 failed earlier due to the local high stress triaxiality which resulted in a low failure strain at the side groove. This perhaps indicates that the experimentally chosen side groove may be too deep resulting in the lateral singularities, which promote the crack to propagate more rapidly at the outer edges. Figure 5-14 (e) displays the distribution for a planar crack model, in which the edge element E1 still failed earlier despite that the value of its stress triaxiality was lower than that of the inner elements.

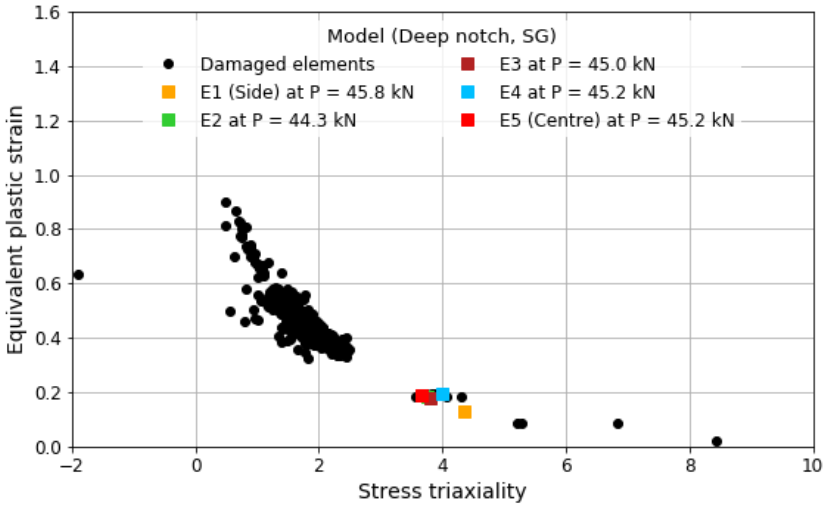
Model (Deep notch, SG)
Damaged elements
E1 (Side) at P = 45.8 kN
E2 at P = 44.3 kN
E3 at P = 45.0 kN
E4 at P = 45.2 kN
E5 (Centre) at P = 45.2 kN
Equivalent plastic strain
Stress triaxiality

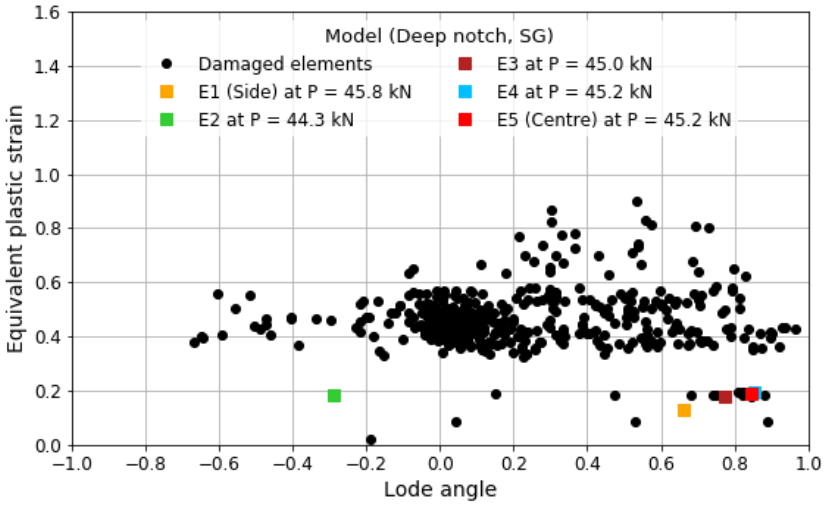
Model (Deep notch, SG)
Damaged elements
E1 (Side) at P = 45.8 kN
E2 at P = 44.3 kN
E3 at P = 45.0 kN
E4 at P = 45.2 kN
E5 (Centre) at P = 45.2 kN
Equivalent plastic strain
Lode angle

(a)

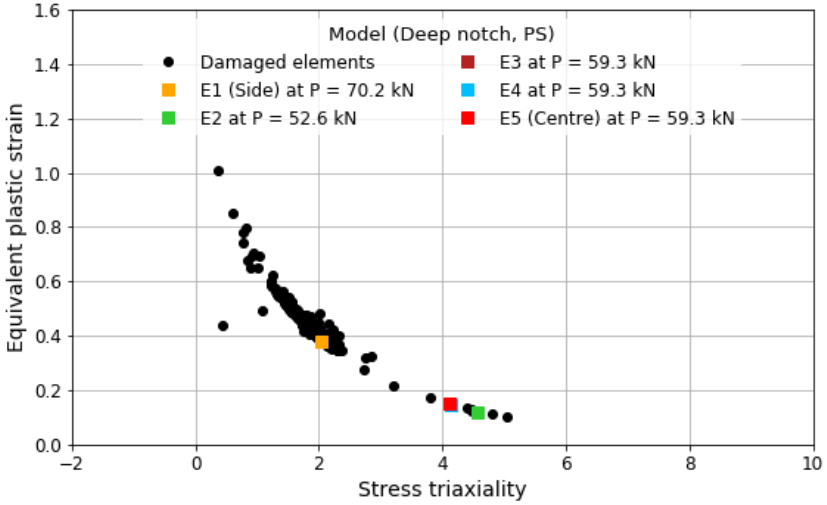
Model (Deep notch, PS)
Damaged elements
E1 (Side) at P = 70.2 kN
E2 at P = 52.6 kN
E3 at P = 59.3 kN
E4 at P = 59.3 kN
E5 (Centre) at P = 59.3 kN
Equivalent plastic strain
Stress triaxiality

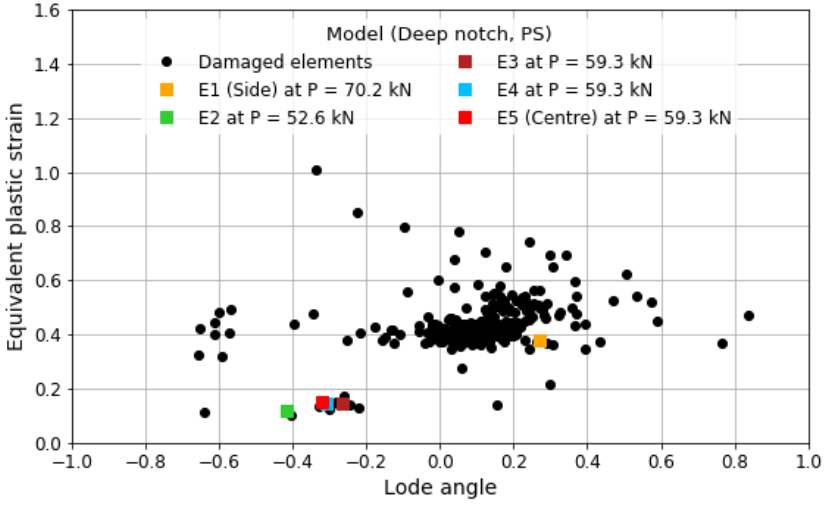
Model (Deep notch, PS)
Damaged elements
E1 (Side) at P = 70.2 kN
E2 at P = 52.6 kN
E3 at P = 59.3 kN
E4 at P = 59.3 kN
E5 (Centre) at P = 59.3 kN
Equivalent plastic strain
Lode angle

(b)

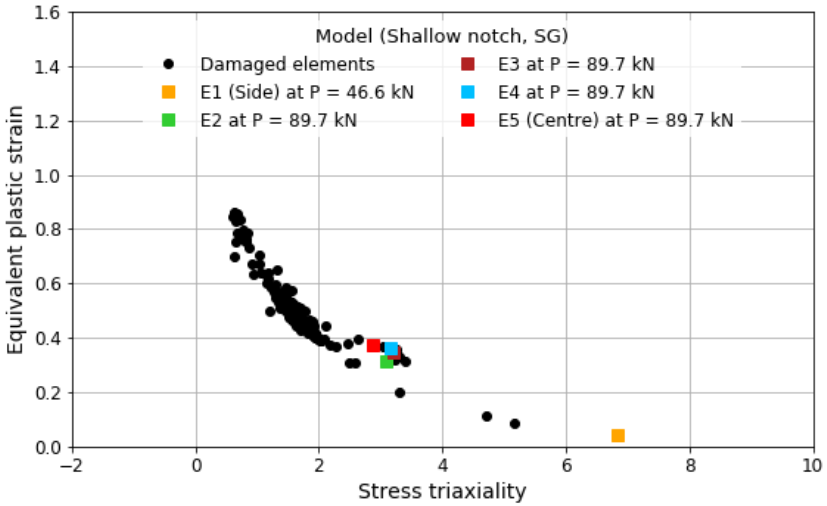
Model (Shallow notch, SG)
Damaged elements
E1 (Side) at P = 46.6 kN
E2 at P = 89.7 kN
E3 at P = 89.7 kN
E4 at P = 89.7 kN
E5 (Centre) at P = 89.7 kN
Equivalent plastic strain
Stress triaxiality

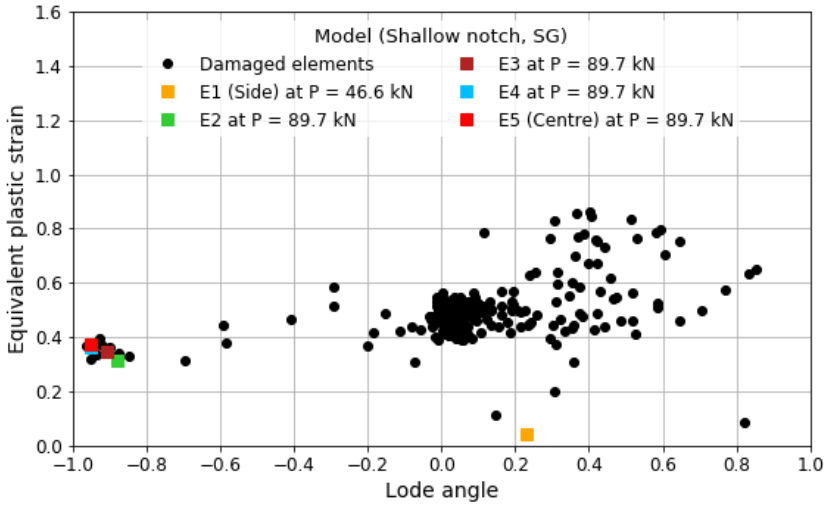
Model (Shallow notch, SG)
Damaged elements
E1 (Side) at P = 46.6 kN
E2 at P = 89.7 kN
E3 at P = 89.7 kN
E4 at P = 89.7 kN
E5 (Centre) at P = 89.7 kN
Equivalent plastic strain
Lode angle

(c)

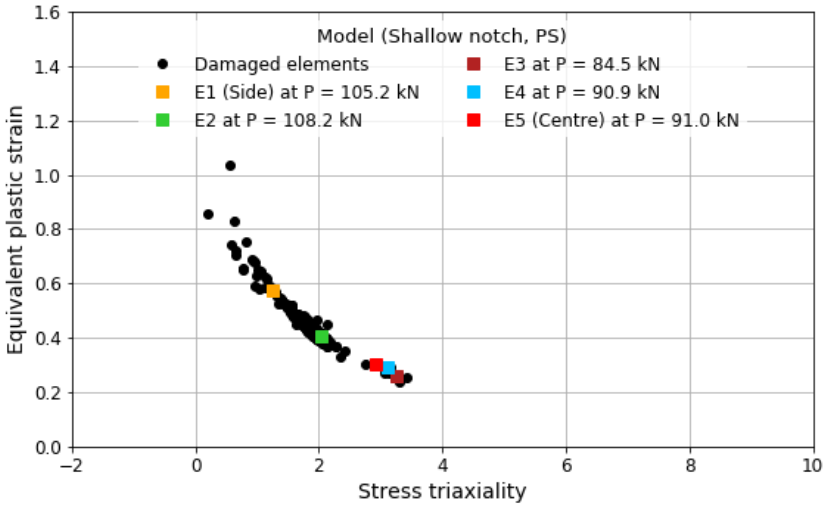
Model (Shallow notch, PS)
Damaged elements
E1 (Side) at P = 105.2 kN
E2 at P = 108.2 kN
E3 at P = 84.5 kN
E4 at P = 90.9 kN
E5 (Centre) at P = 91.0 kN
Equivalent plastic strain
Stress triaxiality

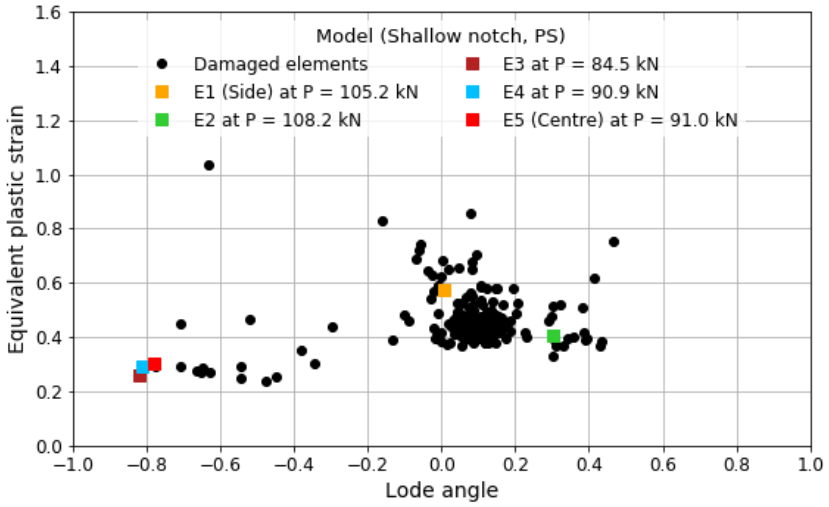
Model (Shallow notch, PS)
Damaged elements
E1 (Side) at P = 105.2 kN
E2 at P = 108.2 kN
E3 at P = 84.5 kN
E4 at P = 90.9 kN
E5 (Centre) at P = 91.0 kN
Equivalent plastic strain
Lode angle

(d)

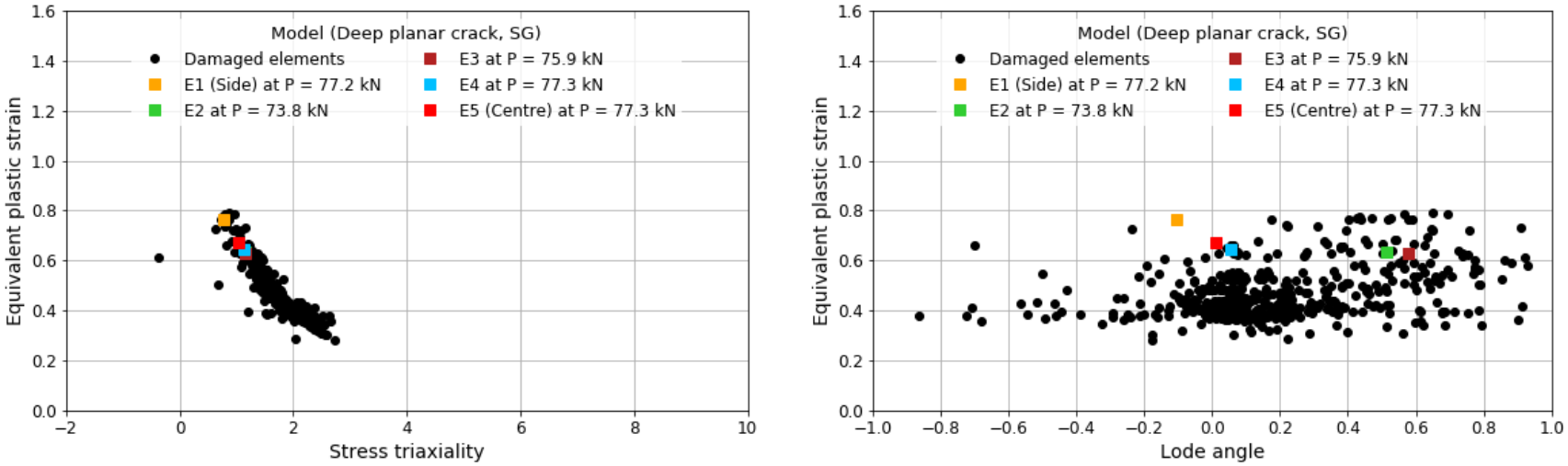

(e)

Figure 5-12. Damage locus of model with a (a) SG deep notch; (b) PS deep notch; (c) SG shallow notch; (d) PS shallow notch; and (e) SG deep planar crack.

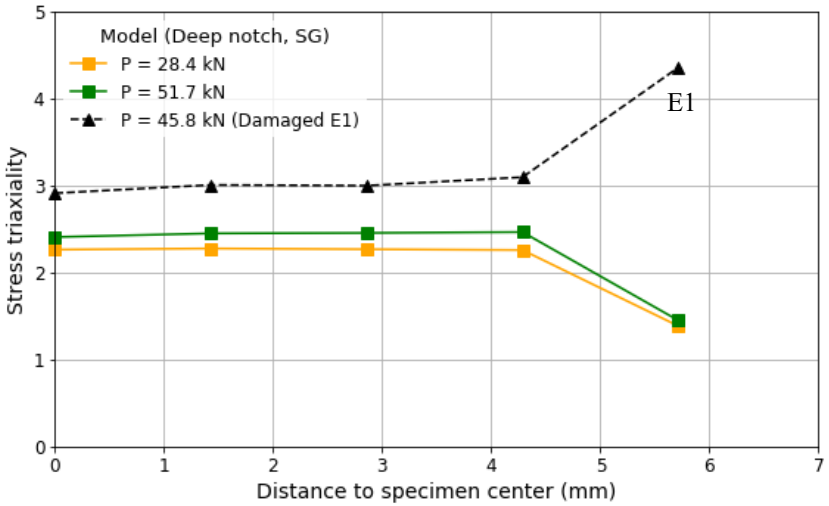
Model (Deep notch, SG)
P = 28.4 kN
P = 51.7 kN
P = 45.8 kN (Damaged E1)
E1
Stress triaxiality
Distance to specimen center (mm)

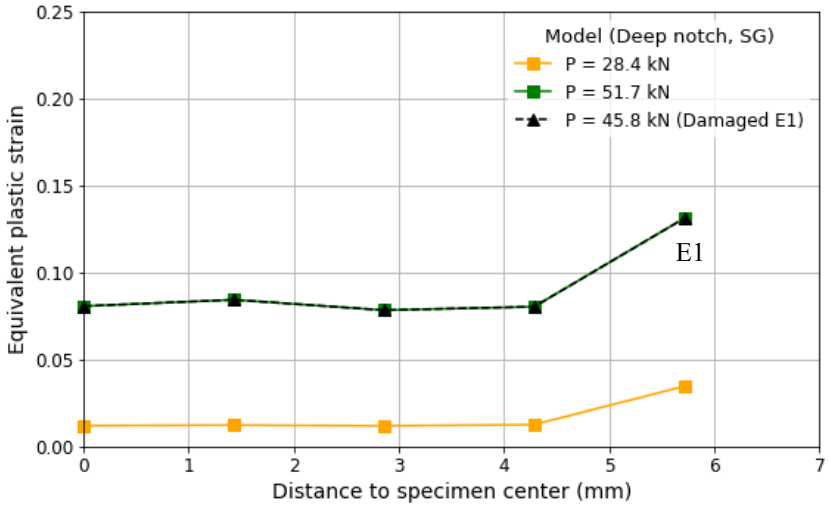
Model (Deep notch, SG)
P = 28.4 kN
P = 51.7 kN
P = 45.8 kN (Damaged E1)
E1
Equivalent plastic strain
Distance to specimen center (mm)

(a)

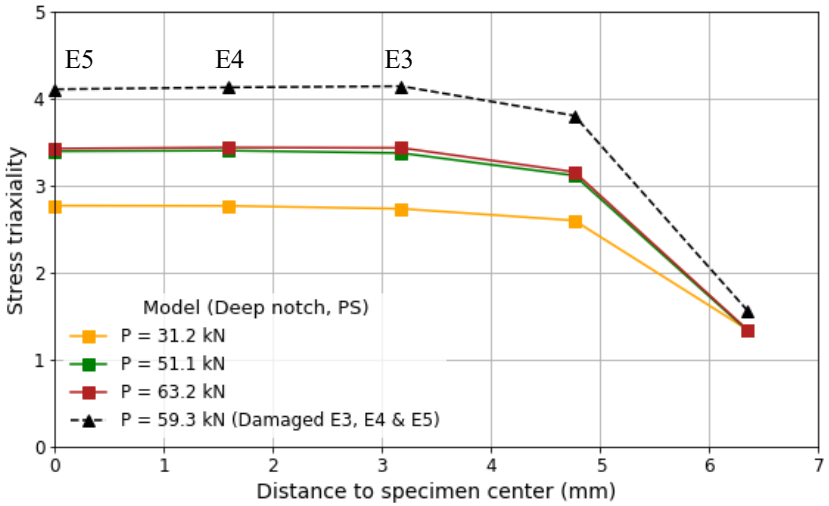
E5
E4
E3
Model (Deep notch, PS)
P = 31.2 kN
P = 51.1 kN
P = 63.2 kN
P = 59.3 kN (Damaged E3, E4 & E5)
Stress triaxiality
Distance to specimen center (mm)

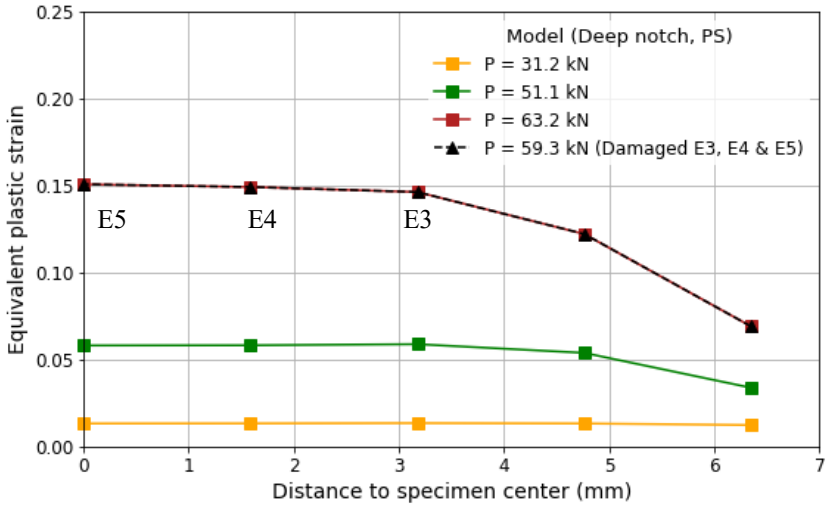
Model (Deep notch, PS)
P = 31.2 kN
P = 51.1 kN
P = 63.2 kN
P = 59.3 kN (Damaged E3, E4 & E5)
E5
E4
E3
Equivalent plastic strain
Distance to specimen center (mm)

(b)

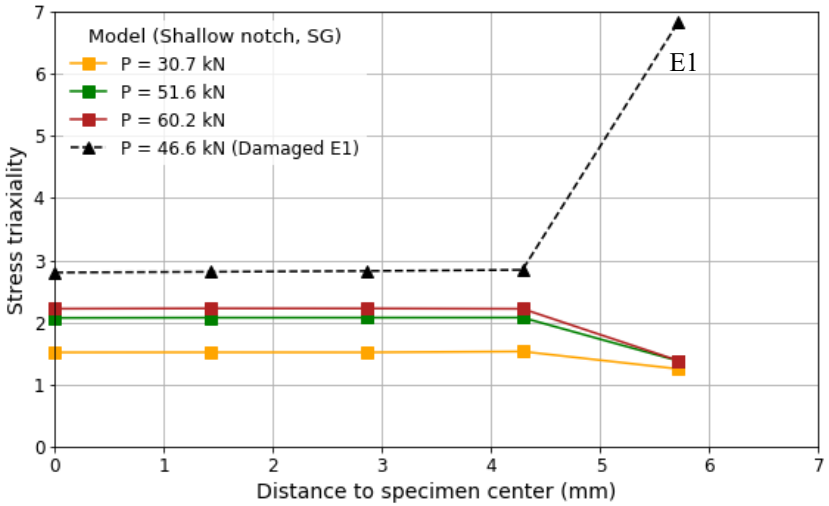
Model (Shallow notch, SG)
P = 30.7 kN
P = 51.6 kN
P = 60.2 kN
P = 46.6 kN (Damaged E1)
E1
Stress triaxiality
Distance to specimen center (mm)

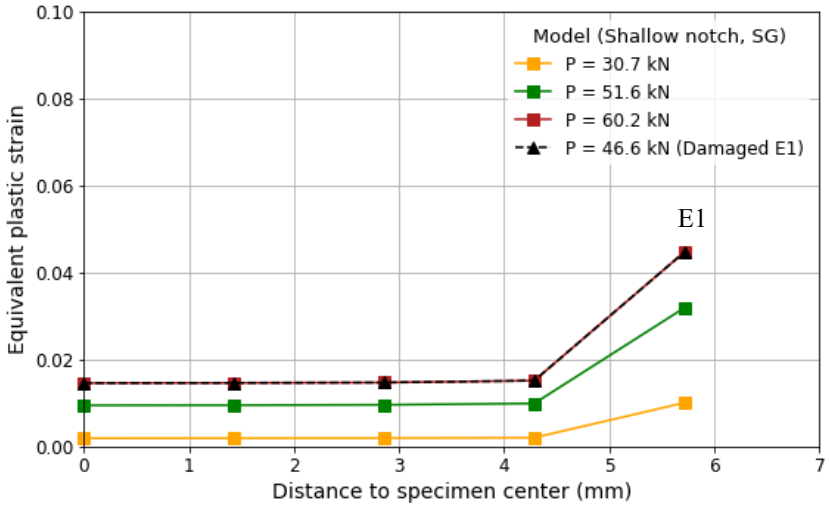
Model (Shallow notch, SG)
P = 30.7 kN
P = 51.6 kN
P = 60.2 kN
P = 46.6 kN (Damaged E1)
E1
Equivalent plastic strain
Distance to specimen center (mm)

(c)

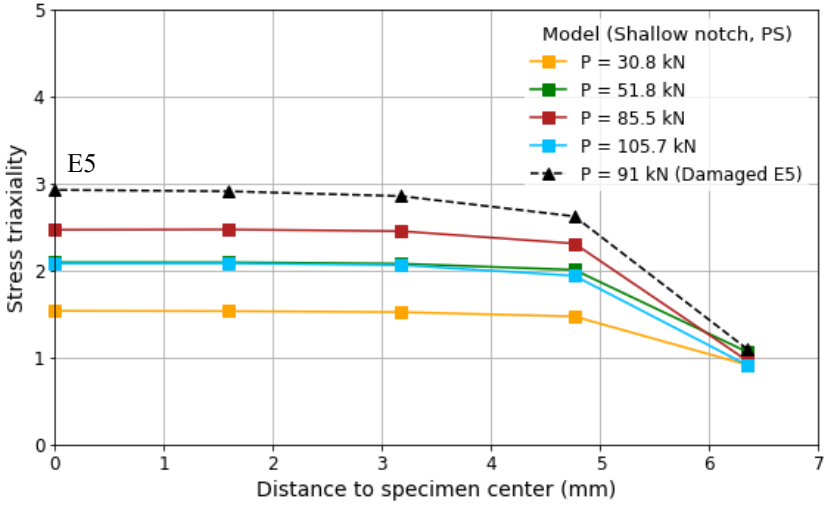
Model (Shallow notch, PS)
P = 30.8 kN
P = 51.8 kN
P = 85.5 kN
P = 105.7 kN
P = 91 kN (Damaged E5)
E5
Stress triaxiality
Distance to specimen center (mm)

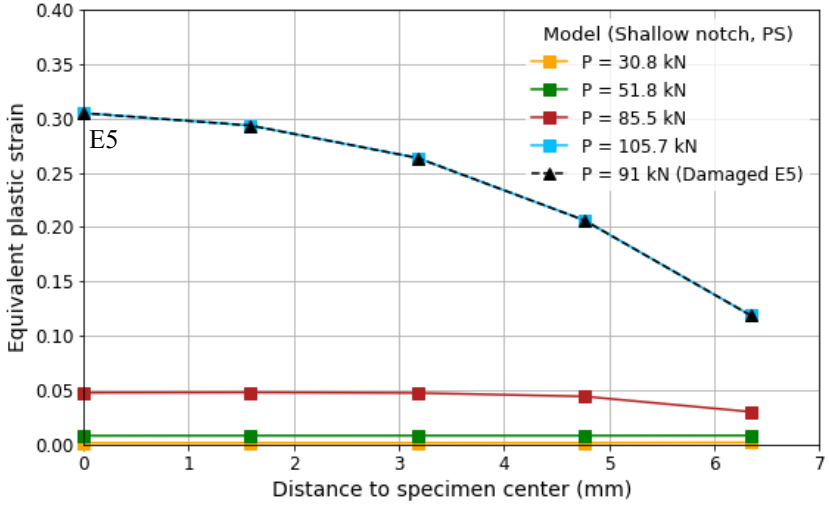
Model (Shallow notch, PS)
P = 30.8 kN
P = 51.8 kN
P = 85.5 kN
P = 105.7 kN
P = 91 kN (Damaged E5)
E5
Equivalent plastic strain
Distance to specimen center (mm)

(d)

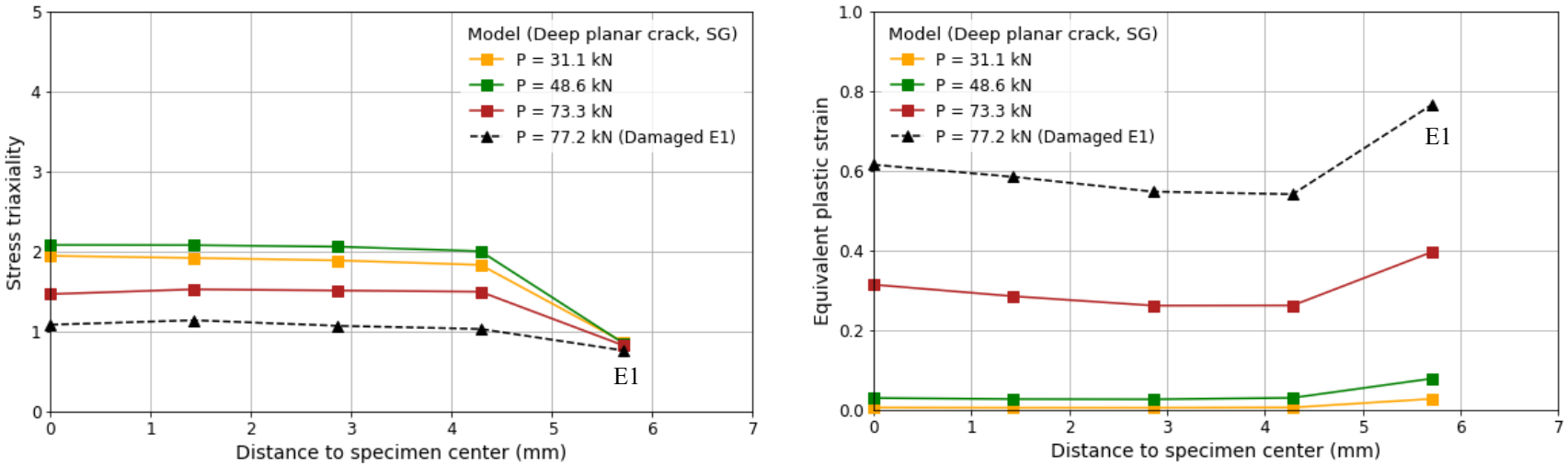

(e)

Figure 5-13. Distribution of stress triaxiality and equivalent plastic strain along crack front of model with a (a) SG deep notch; (b) PS deep notch; (c) SG shallow notch; (d) PS shallow notch; and (e) SG deep planar crack.

5.4.4 Initial Notch vs. Planar Crack

As mentioned earlier, researchers in the past traditionally implemented XFEM by inserting a planar crack into the finite element mesh, unintentionally including the artificial initial cohesion surrounding the crack-tip field. To illustrate this effect, I repeated the deep SG model with an initial XFEM planar deep crack, utilizing the novel variable strain-based damage criterion with the calibrated optimal set of damage parameters (Table 5-1) or a fixed strain-based damage criterion with Maxpe = 0.2 and G_c = 100 N/mm. As demonstrated in Figure 5-14, the J-integral computed form the model with planar crack using the variable criterion was considerably higher than those computed from the other models before crack propagation occurred. In this model, the loading capacity or maximum force was reached before any crack extension. The difference in the J-integral between the models with planar crack and notch using the fixed criterion is smaller than those using the variable criterion because of the independence on the crack tip constraints in the fixed criterion, but some differences were still seen when Δa < 0.3 mm.

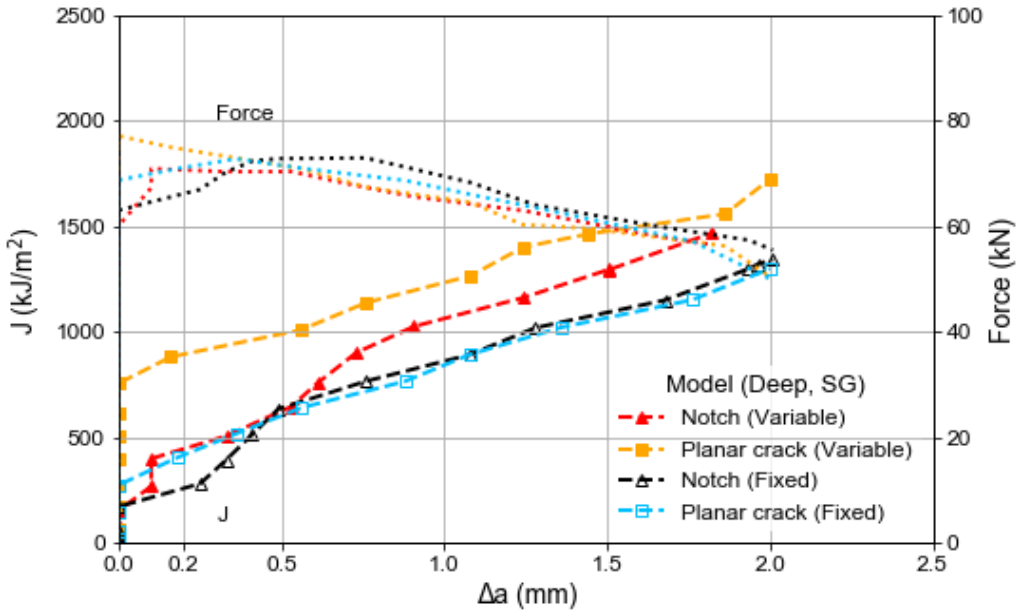

Figure 5-14. Comparisons of J-R curves of SG models for deep notch or planer crack.

5.5 Full-scale simulation and results

5.5.1 Model Setup

The results of 8 experimental full-scale tests on API 5L X52 vintage pipe samples [37] were used to calibrate and validate three-dimensional finite element models using Abaqus/Standard. The vintage pipes has an outside diameter of 324 mm (NPS 12) and a wall thickness of 6.9 mm (0.27”). Electrical discharge machining (EDM) was employed to fabricate the initial notch to the desired size along the circumferential direction of the pipe outer surface prior to the tests. In the work described in Chapter 3 [1], the initial notch was simply generated by inserting an XFEM planar crack into the finite element mesh as it has been typically used by numerous researchers in the literature. In this chapter, the initial notch was particularly simulated by cutting a 0.5 mm-wide U-shaped notch in the middle of the pipe model [Figure 5-15 (a)]. For simplicity, the notch tip was meshed with square elements.

For the purpose of reducing the computational burden, only half of the pipe was modelled taking advantage of the symmetry around the Y-Z plane. The shell-solid coupling constraint was selected to couple a relatively small solid part which was also the user-defined crack domain with the remaining larger shell part to constitute the total simulated pipe The shell meshing was generated using S4R elements (a shell, 4-node, general-purpose linear quadrilateral element with reduced integration i.e., 1 integration point located in the middle of the element, and accounting for finite membrane strains) with a uniform mesh size of 5 mm. The solid meshing was generated using C3D8R elements (a continuum, 3-D, 8-node linear brick element with reduced integration and hourglass control algorithm) with a varying meshing size from 0.5 to 2 mm. The crack propagation path is restricted to a blocked partitioned region in the solid part of pipe, where a fine mesh was employed with the sizes along the pipe thickness direction (crack propagation), longitudinal direction (perpendicular to the crack

plane), and circumferential direction (parallel to the crack plane) of 0.5 mm × 0.5 mm× 2 mm. A tie constraint was used to tie the end plates and tongues together at each end. All end plates and tongues were simulated as rigid bodies and represented by two reference nodes with an eccentricity of 50 mm to the longitudinal axis of the pipe. The pipe was first under internal pressure load, after that subjected to a tensile displacement assigned at one reference node while the other reference node fixed only allowing rotation about the X-axis. Figure 5-16 illustrates a typical model configuration while Table *5-3* summarizes the general information of each test and model. Interested readers can review the experimental study details that has been published previously [37].

The pipe was simulated as an elastoplastic isotropic material. The input true stress-plastic strain data in the model was obtained from averaged measurement of six tension coupons tests [111] where specimens were cut from the base metal of X52 pipeline in the longitudinal direction. Initially, the notch in each test pipe specimen was expected to be located within the heat affected zone (HAZ), but finally determined to be at the base metal in post-failure fractographic examination. The Young's modulus was given by 199 GPa, and the Poisson's ratio was taken as 0.3. The 0.2% offset yield strength was 411 MPa while the ultimate tensile strength was 573 MPa corresponding to a true plastic strain of 0.15. The relationship between the true stress and true plastic strain with a power law fit of strain hardening $\sigma = A \cdot {\varepsilon_p}^n = 720 \cdot {\varepsilon_p}^{0.119}$ are illustrated in Figure 5-17. If a power law relationship was related to the true strain instead of true plastic strain, $\sigma = A \cdot \varepsilon^n = 718 \cdot \varepsilon^{0.119}$ fitted the true stress-strain curve while the value of n = 0.119 remained unchanged. The novel XFEM variable strain damage initiation criterion was defined by $f = \text{PEEQ}/\bar{\varepsilon}_f$ reaching 1 within a tolerance of 0.1 as provide in Eq. (5-9), where $\bar{\varepsilon}_f$ was determined from Eq. (5-8). Such criterion is implemented using a Fortran code programmed in Abaqus user subroutine-UDMGINI [30]. For the damage evolution, a linearly decreasing TSL with a mode-independent G_c was adopted. With the determined n (0.119) and

c_4 (simply taken as 1), other 4 damage parameters c_1, c_2, c_3, and G_c were calibrated by trail and error through extensive simulations for tests 3-6, especially in matching with the experimental tensile strain profiles at failure and the force-CMOD curves, and finally validated for tests 1-2. It was noted that for Model 1 and Model 2, respectively 100 mm and 200 mm long pipe segment at both ends were particularly defined to linear elastic only to avoid excessive deformation at pipe ends due to unintentional stress concentrations. The 3D asymmetric damage initiation locus [Figure 5-17 (b)] in the space of the $\bar{\varepsilon}_f$, η, and $\bar{\theta}$ are generated based on n, c_1, c_2, c_3, and c_4 listed in Table 5-4.

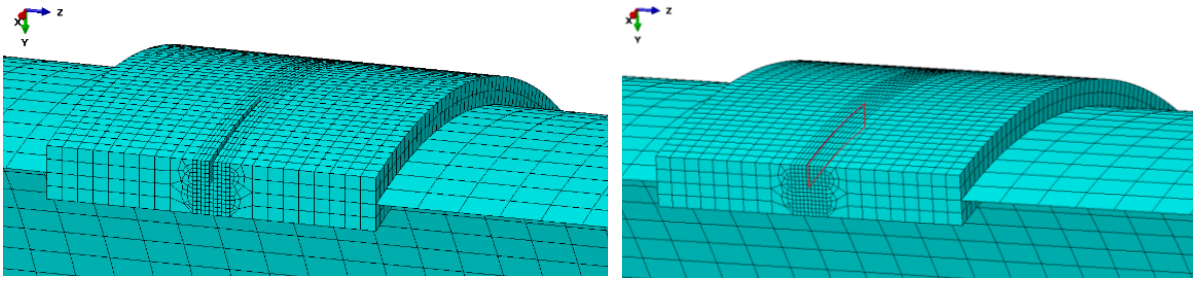

(a) (b)

Figure 5-15. Mesh distribution near a notch or planar crack in model.

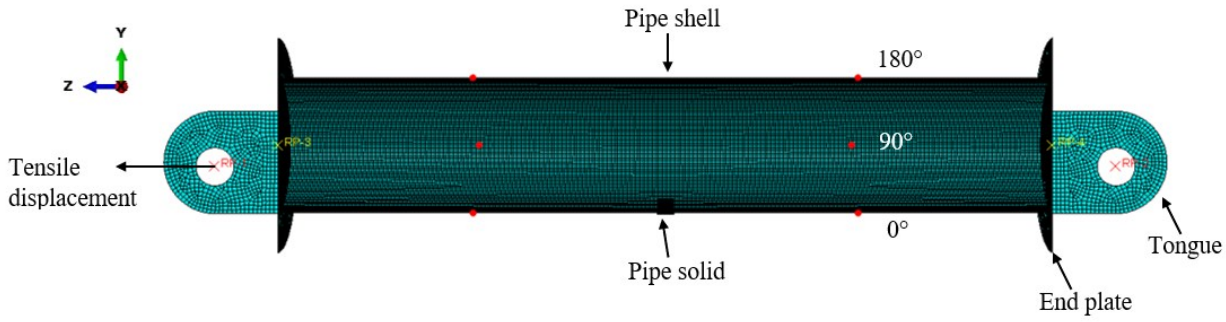

Figure 5-16. Illustration of model configuration and mesh distribution.

Table 5-3. Basic information of tests and models

Test or Model	Pipe specimen dimensions			Crack dimensions		Internal pressure level	
	Outer diameter (mm)	Total length (mm)	Wall thickness (mm)	Crack depth (mm)	Crack length[a] (mm)	Internal pressure (Mpa)	Hoop stress/SMYS[b] (%)
Test 1	324	1828.8	6.95	1.7	50	11.65	75
Model 1	324	1828.8	6.8	1.7	50	11.65	77
Test 2	324	1828.8	6.8	1.5	50	3.47	23
Model 2	324	1828.8	6.8	1.5	50	3.5	23
Test 3	324	1828.8	6.8	3.1	50	11.67	77
Model 3	324	1828.8	6.8	3.1	50	11.65	77
Test 4	324	1828.8	6.8	3.3	50	4.74	31
Model 4	324	1828.8	6.8	3.3	50	4.65	31
Test 5	324	1219.2	6.8	1.4	150	11.65	77
Model 5	324	1219.2	6.8	1.4	150	11.65	77
Test 6	324	1219.2	6.8	1.8	150	4.61	31
Model 6	324	1219.2	6.8	1.8	150	4.65	31

Test 7	324	1219.2	6.8	3.5; 3.0[c]	150	11.65	77
Model 7	324	1219.2	6.8	3.3	150	11.65	77
Test 8	324	1219.2	6.8	2.7; 2.8[c]	150	4.65	31
Model 8	324	1219.2	6.8	2.7	150	4.65	31

[a] Actual initial crack length of each pipe specimen was not measured, and the target values (5% or 15% pipe circumference) were used. Simulated initial crack length of each model was half of the value in the table due to the symmetry around the Y-Z -plane.

[b] For these API 5L X52 pipe specimens, SMYS was taken as 360 MPa (52,200 psi) provided by API Spec 5L [4].

[c] Actual initial crack depths were measured from two samples cut from test pipe specimens 7 and 8 after pipe failure using fractography [37].

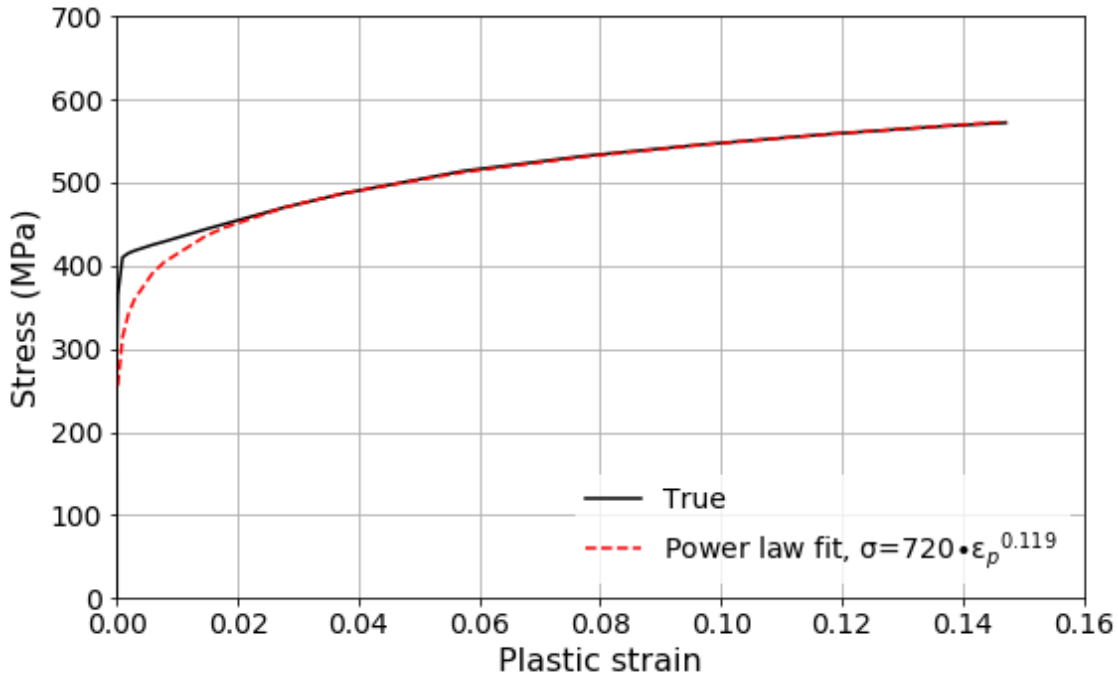

(a)

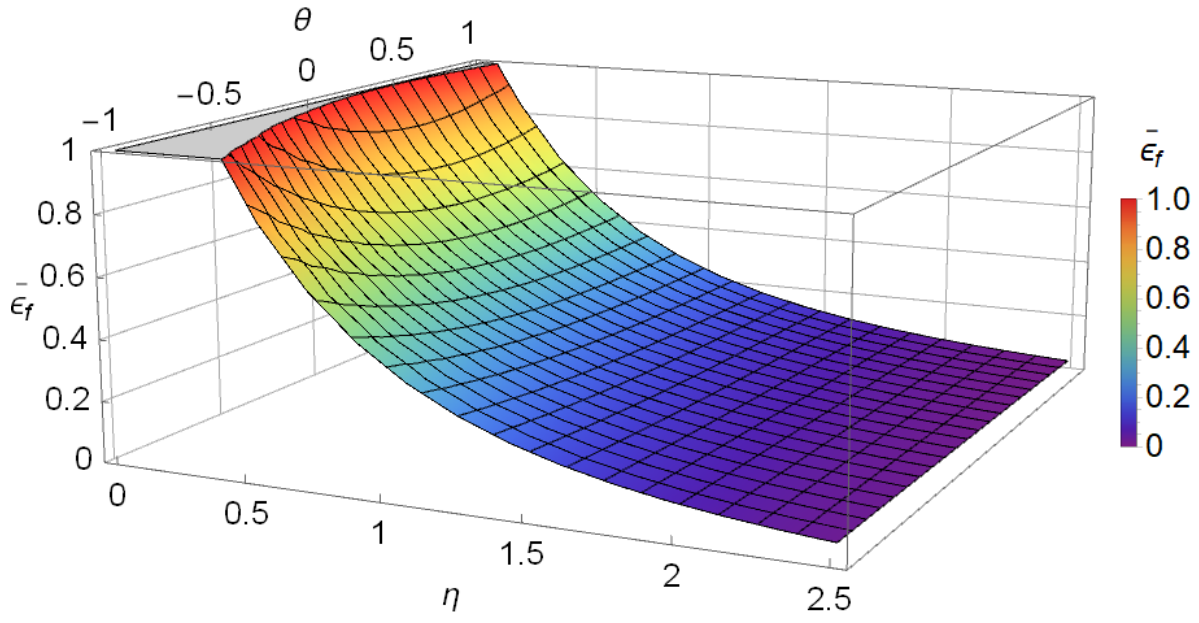

(b)

Figure 5-17. Properties of X52 (a) true stress-strain curve; and (b) damage initiation locus curve.

Table 5-4. Calibrated parameters of novel XFEM damage criterion for X52.

Pipe Grade	n	c_1	c_2	c_3	c_4	G_c (N/mm or mJ/mm^2)
X52	0.119	0.1	1.9	0.9	1	200

5.5.2 Comparison with Tests and Fixed Damage Criterion

A comparison was carried out between the numerical and experimental results in Figure 5-18 to Figure 5-21 regarding the tensile strains along the pipe length, force, CMOD, end plate rotation, and fracture surfaces appearance to calibrate the novel XFEM variable strain damage criterion. The fracture surface was measured by means of pipe wall thickness reduction [wall thickness - reduced wall thickness)/wall thickness]. Since tests was considered failed when the water seeped out of the crack, the model failure was predicted to occur when the crack propagated through the entire pipe wall, i.e., the innermost element [Figure 5-21 (b)] of pipe wall was damaged (STATUSXFEM > 0). In Table *5-5*, two strain terms $\varepsilon_{0.5L}$ and ε_{avg} characterize the tensile strains measured at an angle of 0° from the crack at onset of failure. $\varepsilon_{0.5L}$ refers to the tensile strains located at a quarter of total pipe length ($2L$) away from the end plate, corresponding to the strain gauge measurements during the tests (shown by red points in Figure 5-14). ε_{avg} refers to the averaged tensile strain of the pipe outer surface along the pipe length at an angle of 0° from the crack ranging from 10% to 40% of the total pipe segment length (from $0.2L$ to $0.8L$) away from crack on both sides (approximately 185–730 mm for tests and models 1–4 and 120–490 mm for tests and models 5–8). The experimental strain profile was evaluated using a digital image correlation (DIC) system by tracking the movements of a speckle pattern produced by black and white spray paint on the pipe surface from a sequence of recorded images. Additionally, DIC was used to measure the experimental growth of the CMOD by tracking the displacements of two selected reference points on each side of the crack. The numerical CMOD employed the same measurement by tracking the

displacement of two nodes distanced 10 mm. $CMOD_{critical}$ refers to the CMOD when its value increases sharply but with an almost constant applied load, which is simply represented by the time when the load reaches the 98% of the maximum value in each test or model.

All eight models fractured after the maximum force was exceeded. Of each model and test, the differences in the maximum force were less than 5% while that in burst force was higher and up to 16% in Model 5. Although some differences up to 23% were found in tensile strains $\varepsilon_{0.5L}$ and ε_{avg} between models and tests, their tensile strain distribution along the pipe length were closely matched as shown in Figure 5-18. In this figure, the tensile strains of models and tests 1-6 used were those corresponding to the burst force level, while those of models and tests 7-8 corresponded to the maximum force level. At failure, the numerical rotation measured at the reference nodes of the end plates and tongues were generally smaller than those measured by clinometers attached to the end plates in the tests, except for models 5-6 (Figure 5-20).

In comparison to previous simulations with initial planar crack and fixed Maxps damage criterion [1], considerable improvements were achieved when predicting the CMOD-force curve and reduction of pipe wall at failure. In previous study, differences as high as 31% were found between numerical and experimental results of the $CMOD_{critical}$ in Model 4. Similarly, a 23% difference were reported in the reduction of pipe wall in Model 1. However, in current simulation with initial notch and variable strain damage criterion, the numerical and experimental CMOD-force curves were closely matched (Figure 5-19) with a maximum 10% difference in the $CMOD_{critical}$ in Model 4. At the onset of failure, the maximum difference of reduction of pipe wall thickness was 9% between Model and Test 1, while the difference was less than 6% for all other models and tests. The fracture surface appearances of Test 1 and Model 1 are shown in Figure 5-21 and that of previous Model 1 with planar crack and fixed Maxps damage criterion is also included for comparison. In the previous study, I erroneously attributed the lower observed plastification in the models to the lack of immense impact caused

from sudden release of internal pressure when fracture occurred during tests. However, results here suggest that the previous large difference in plasticity was primarily a limitation of the stress-based damage criterion.

To investigate the effect between the proposed novel variable and fixed strain-based damage initiation criteria on the numerical predictions, I performed additional calibration of an optimal set of Maxpe = 0.15 and G_c =200 N/mm using the same data set (results in Appendix C). Surprisingly, the numerical results generated between the calibrated two damage criteria were similar. This could due to fact that the current experimental data (forces, end plate rotation, CMOD and tensile strain profiles) used for calibration mostly represented the global behaviour during the full-scale X52 pipe tests. The difference, however, can be observed in the local scale, such as the reduction of pipe wall thickness at failure, which were slightly higher (up to 4% reported for Model 6) in simulations using variable strain damage criterion than those in fixed Maxpe damage criterion. Another difference can be seen in the numerical damage locus as discussed in Section 5.5.4 below. However, the localized experimentally measured data were scarce for the validation of the local numerical difference.

It is worthy to mention that every set of 8 models adopting the fixed Maxps, fixed Maxpe or variable strain damage criterion, produced similar experimental TSC represented by ε_{avg} through current optimal calibration. Figure 5-22 illustrates the value of ε_{avg} obtained from each model and test.

Table 5-5. Comparisons between numerical and experimental results

Test or model	$CMOD_{critical}$ (mm)	Burst force (Max force) (kN)	Rotation at end plate at failure (°)	Tensile strain at 0° from crack at failure (%)		Reduction of wall thickness at failure (%)
				$\varepsilon_{0.5L}$	ε_{avg}	
Test 1	1.13	2284 (2299)	5.08	—	3	32.4
Model 1	1.12	2281 (2393)	4.49	2.67	2.93	23.4
Difference	-0.9%	-0.1% (+4.1%)	-11.6%	—	-2.3%	-9.0
Test 2	1.09	3100 (3109)	6.82	—	8	27.9
Model 2	1.12	3091 (3178)	6.04	7.30	7.30	22.6
Difference	+2.8%	-0.3% (+2.2%)	-11.4%	—	-8.8%	-5.3
Test 3	1.18	1623 (1664)	0.98	0.51	0.53	19.1
Model 3	1.07	1698 (1740)	0.79	0.41	0.42	15.3
Difference	-9.4%	+4.6% (+4.6%)	-19.7%	-19.6%	-20.8%	-3.8
Test 4	1.16	2061 (2075)	1.04	0.53	0.53	20.6
Model 4	1.04	2012 (2047)	0.88	0.44	0.46	15.0
Difference	-10.3%	-2.4% (-1.4%)	-15.5%	-16.6%	-13.2%	-5.6

Test 5	0.77	1934 (1962)	1.86	—	1.84	26.5
Model 5	0.80	1623 (2000)	2.08	1.57	1.60	26.2
Difference	+3.9%	-16.1% (+1.9%)	+11.8%	—	-13.0%	-0.3
Test 6	0.90	2261 (2268)	1.40	1.20	1.32	27.9
Model 6	0.93	1904 (2220)	1.72	1.29	1.34	22.6
Difference	3.3%	-15.8% (-2.1%)	+22.9%	+7.5%	+1.5%	-5.3
Test 7	0.90	1304 (1304)	0.26 (0.26)	0.21(0.22)	0.22 (0.22)	19.1
Model 7 [a]	0.99	1196 (1342)	0.24 (0.21)	0.13 (0.17)	0.13 (0.17)	14.3
Difference	+10.0%	-8.3% (+2.9%)	-7.7% (-19.2%)	-38.1% (-19.0%)	-40.9% (-22.7%)	-4.8
Test 8	0.85	1831 (1844)	0.42 (0.41)	0.29 (0.30)	— (0.30)	20.6
Model 8 [a]	0.84	1552 (1807)	0.36 (0.31)	0.20 (0.26)	0.19 (0.25)	18.1
Difference	-1.2%	-15.2% (-2.0%)	-14.3% (-24.4%)	-31.0% (-13.3%)	— (-16.7%)	-2.5

[a] in tests 7 and 8, the values in parentheses referred to the maximum force level.

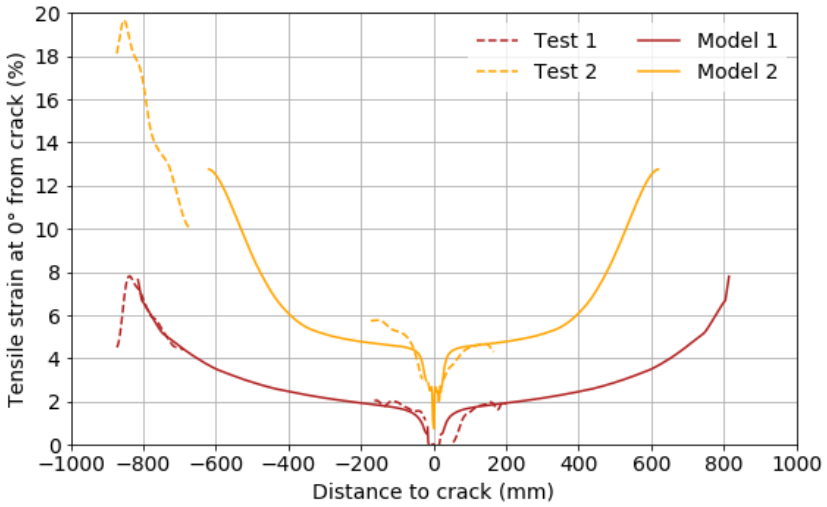

(a)

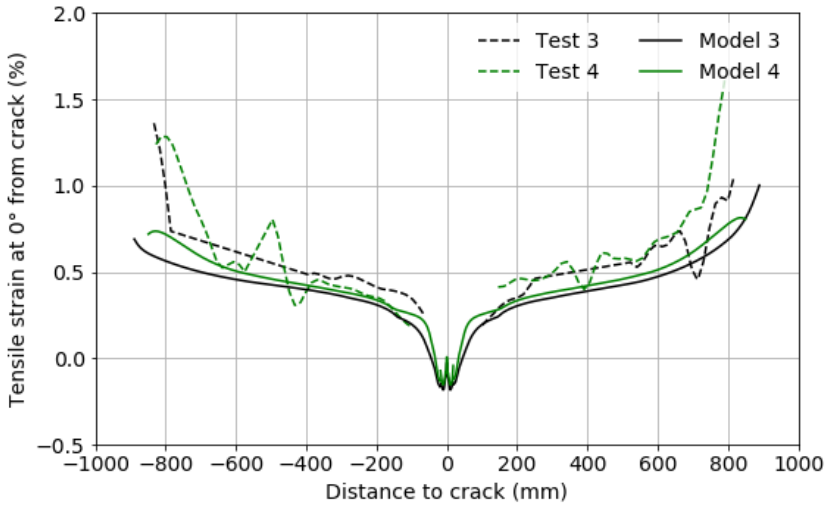

(b)

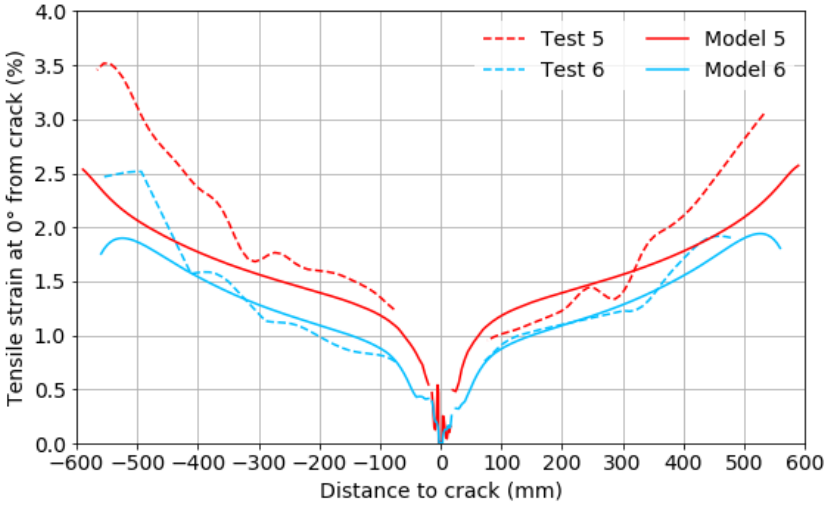

(c)

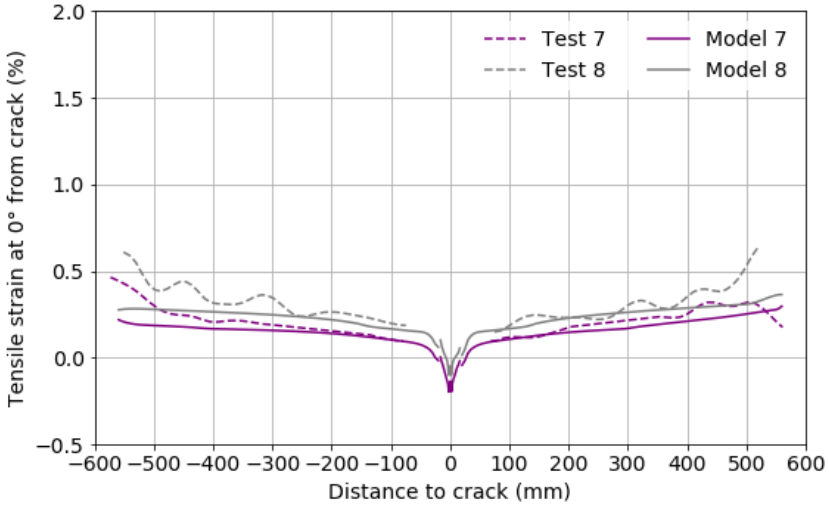

(d)

Figure 5-18. Comparison of tensile strains along the pipe length from Models and Tests (a) 1-2; (b) 3-4; (c) 5-6; and (d) 7-8.

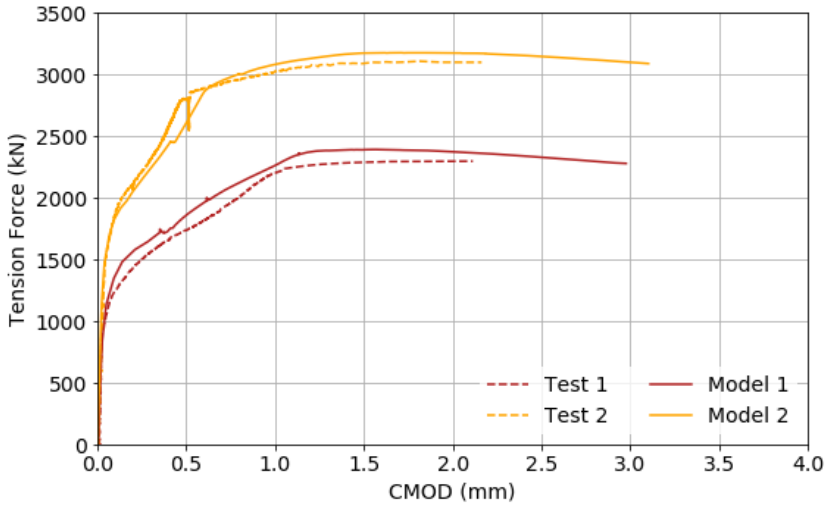

(a)

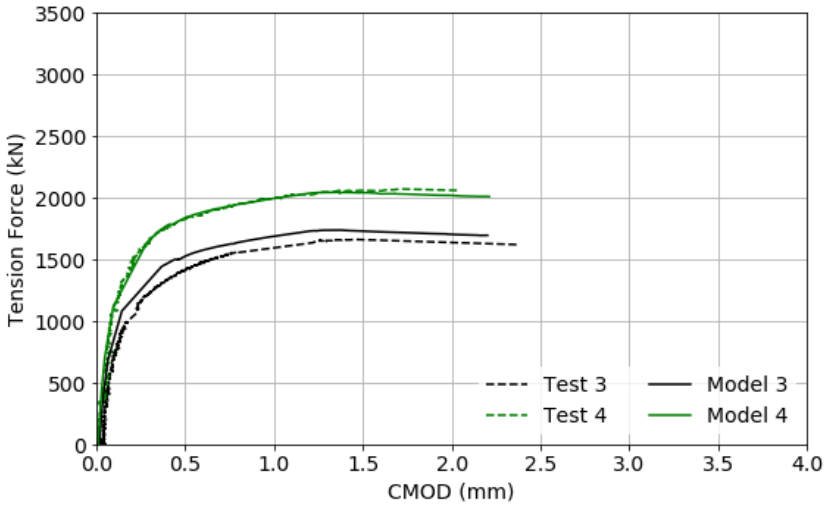

(b)

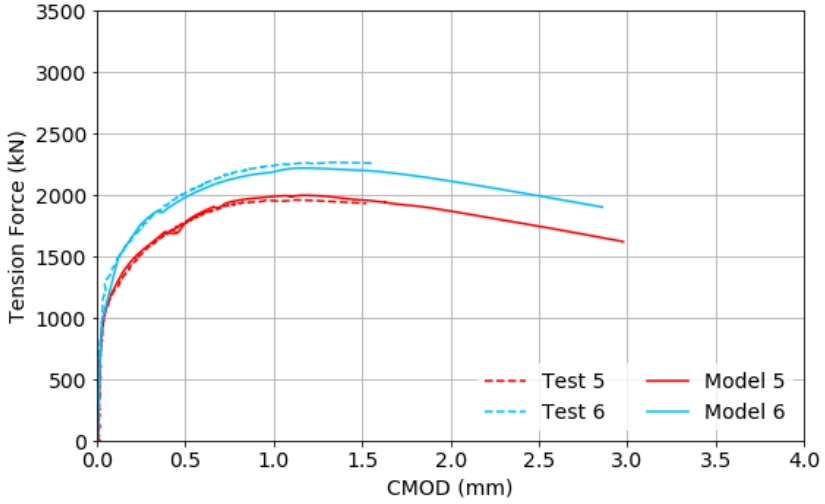

(c)

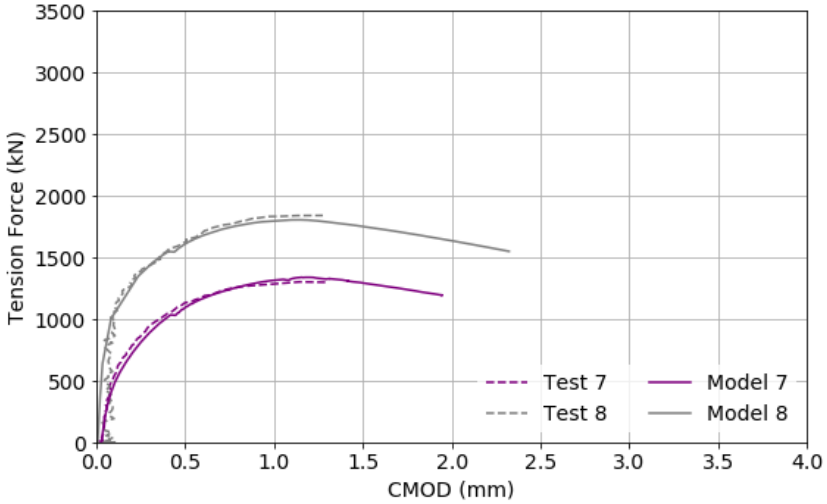

(d)

Figure 5-19. Comparison of force-CMOD curves from Models and Tests (a) 1-2; (b) 3-4; (c) 5-6; and (d) 7-8.

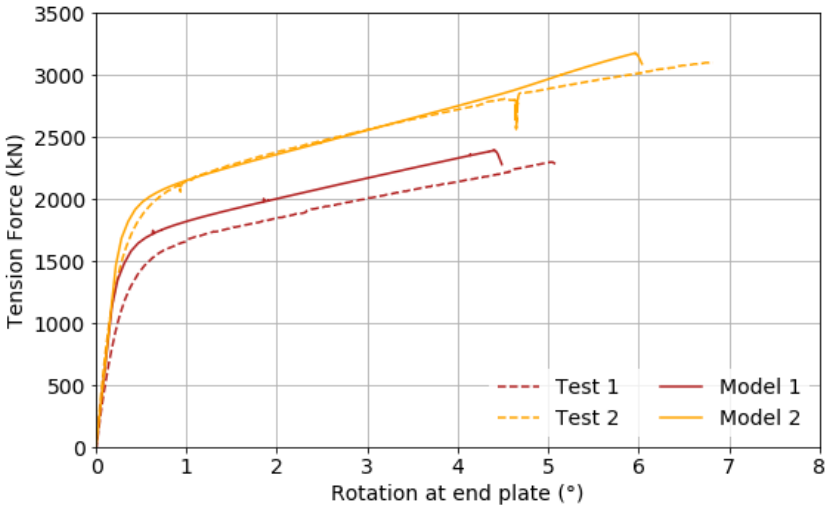

(a)

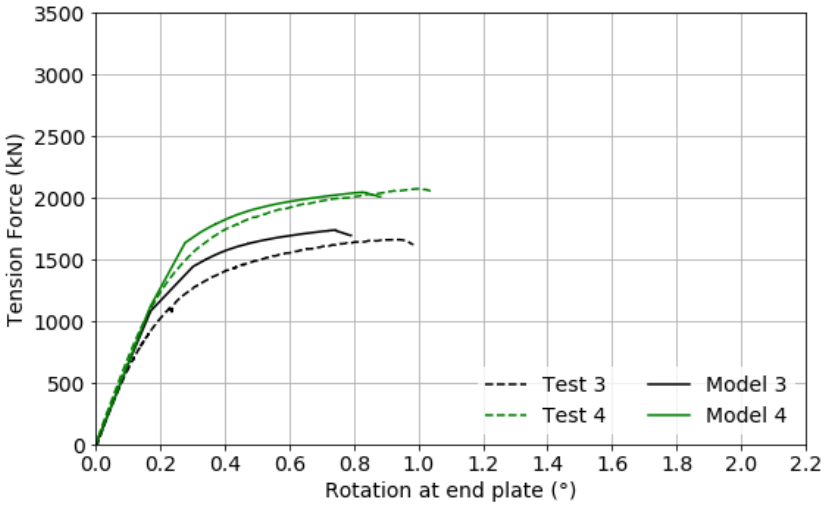

(b)

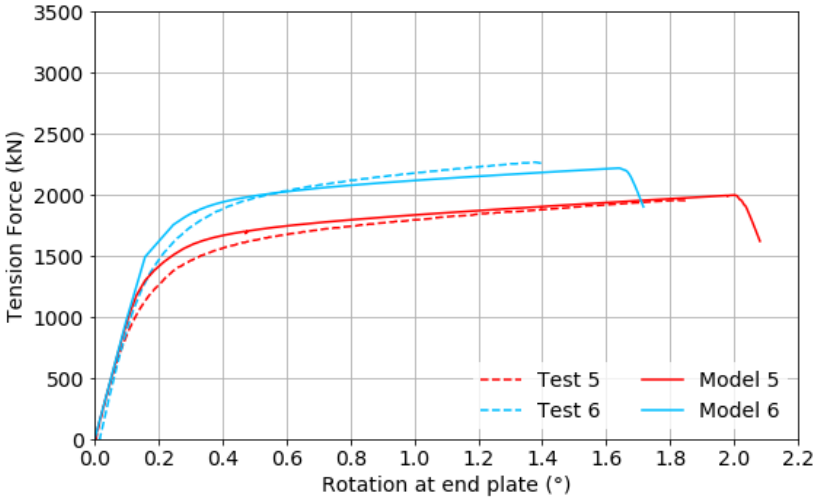

(c)

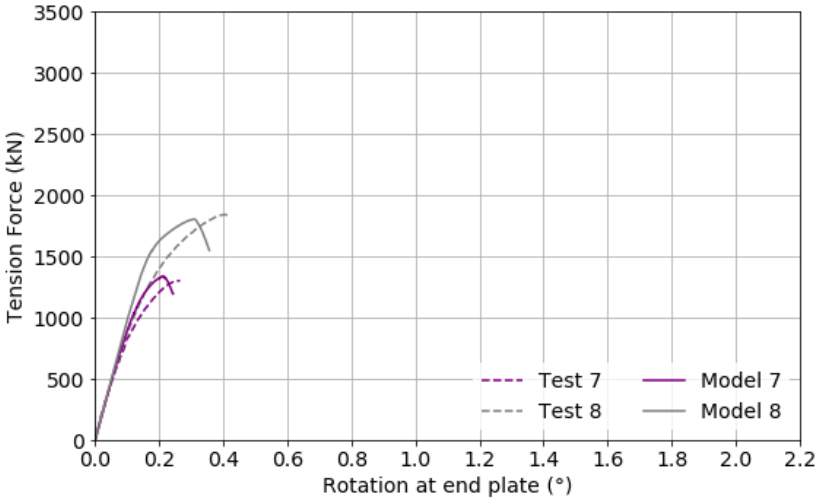

(d)

Figure 5-20. Comparison of force-rotation curves Models and Tests (a) 1-2; (b) 3-4; (c) 5-6; and (d) 7-8.

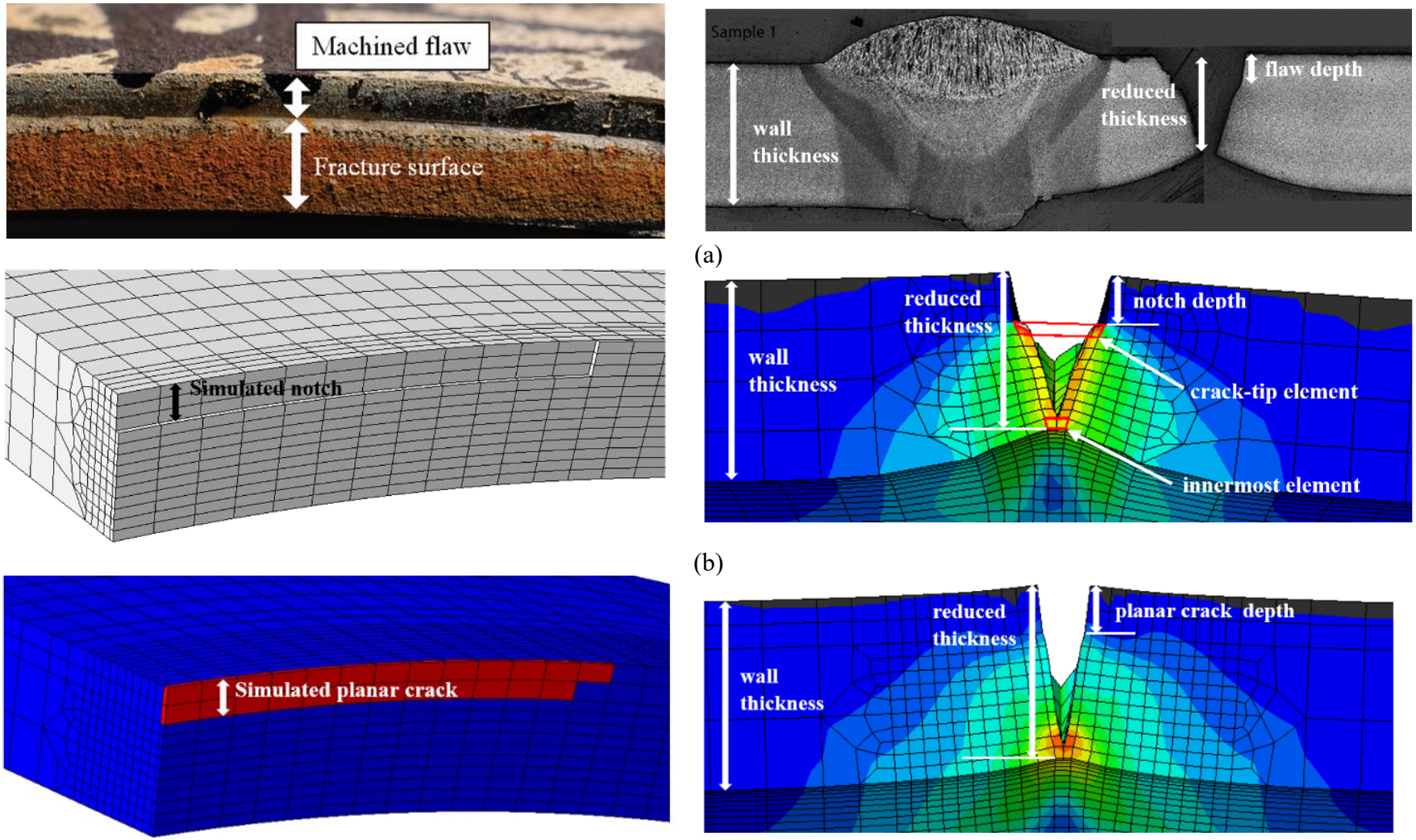

Figure 5-21. Comparison of fracture surfaces obtained from (a) Test 1; (b) Model 1 with notch using novel variable strain damage criterion; and (c) Model 1 with planar crack using fixed Maxps damage criterion

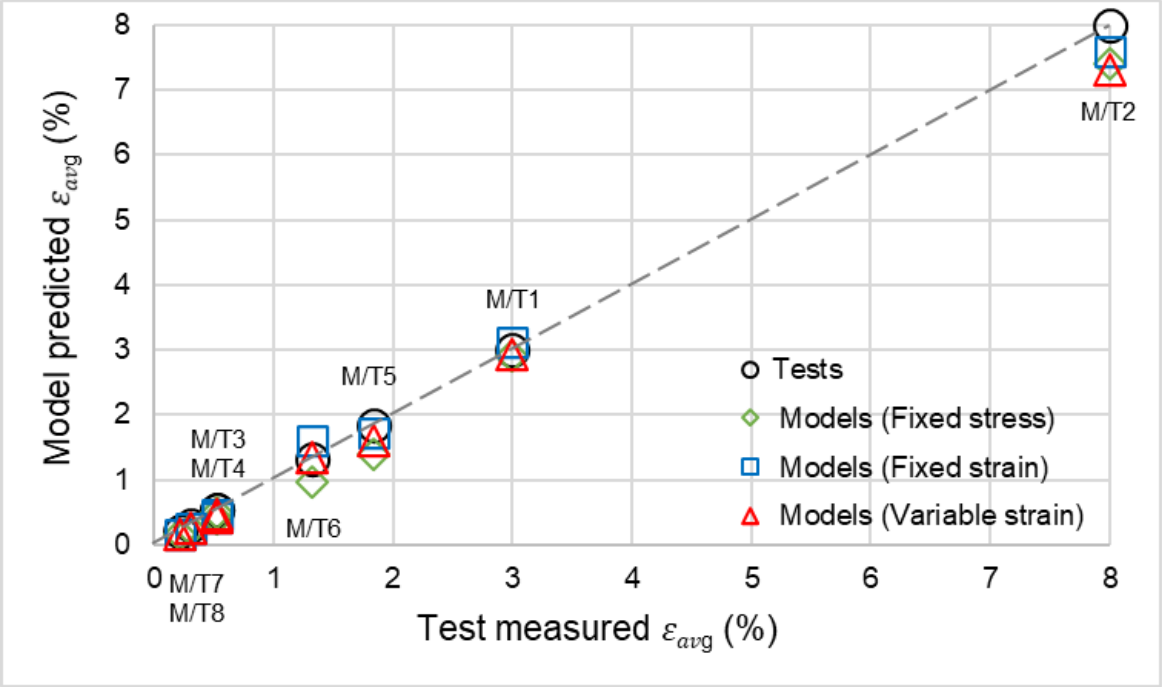

Figure 5-22. Comparison of ε_{avg} obtained from models and tests adopting different damage criteria. Note that M/T1 to M/T8 indicate Model/Test 1 to Model/Test 8.

5.5.3 Relationship between Crack Growth and TSC

The experimental TSC is defined as the strain at which the pipe fails to contain the inner fluid. It is difficult, however, in XFEM to identify the corresponding failure criterion. In particular, the elements go through an initial step of reaching the damage initiation criterion followed by a degrading stiffness until full separation. The failure of the pipe can thus be determined when the innermost element of the pipe wall is either damaged (i.e., STATUSXFEM > 0) or fully damaged (i.e., STATUSXFEM = 1). To better investigate the different phases of crack growth and their effect on TSC, four crack phases were identified, including the two crack initiation phases, i.e., when the crack-tip element is damaged and when it is fully damaged, and two pipe failure phases, i.e., when the innermost element is damaged and when it is fully damaged. Of all models, the tensile strain profiles along the pipe length at these four crack phases plus additional phase when the maximum force is reached are illustrated in Figure 5-23. The values of corresponding force and strain (i.e.,

$\varepsilon_{0.5L}$ and ε_{avg}) of each phase are listed in

Table *5-6*. For Models 1, 2 and 5, the last phase (innermost element fully damaged) was not obtained from Models 1, 2 and 5 because the simulation aborted due to convergence problems, but results obtained from the previous phase (innermost element damaged) were enough to predict pipeline failure.

It is interesting to observe that the tensile strain profiles of both pipe failure phases are almost identical. Therefore, the pipe failure determined by either phase was reasonable. The difference of tensile strain profiles of both crack initiation phases was remarkable in models 1-6 but minor in models 7-8. For models 1-6, the crack initiation criterion on the pipe wall should be chosen carefully. If the numerical crack initiation criterion is determined by the damaged crack-tip element, the pipe could continue to resist significant tensile strains during crack propagation, while if it is determined by fully damaged crack-tip element, there is considerably lesser tensile strains to grow. For models 7-8, the tensile strain profiles were reduced after the crack initiation occurred on the pipe wall. This is perhaps because these two models had the deepest and longest notch which led to the fastest crack propagation and most brittle fracture behavior among all the models. For all models, the maximum force occurred after the crack-tip element is fully damaged and before the innermost element is damaged. In general, the longitudinal tensile strain values of circumferentially cracked pipeline increase as the crack propagates through the pipe wall, and they grow along the pipe longitudinal direction from the crack location at the middle of the pipe to both pipe ends. Exceptions occur in models 7-8 where the crack size is large enough that it immediately threatens the pressure containment capacity resulting in a relatively low and similar TSC along the pipe length.

Table 5-6 Numerical force and tensile strains at difference phases

Model	Phases	Force (kN)	Tensile strain at 0° from crack (%)	
			$\varepsilon_{0.5L}$	ε_{avg}
1	crack tip element is damaged	1721	0.41	0.44
	crack tip element is fully damaged	2242	2.17	2.32
	max force	2393	2.69	2.95
	innermost element is damaged	2281	2.67	2.93
	innermost element is fully damaged	—	—	—
2	crack tip element is damaged	2454	2.04	1.95
	crack tip element is fully damaged	3150	6.87	6.87
	max force	3178	7.31	7.30
	innermost element is damaged	3091	7.30	7.30
	innermost element is fully damaged	—	—	—
3	crack tip element is damaged	1502	0.25	0.25
	crack tip element is fully damaged	1712	0.38	0.39
	max force	1740	0.42	0.43
	innermost element is damaged	1698	0.41	0.42
	innermost element is fully damaged	1676	0.40	0.41
4	crack tip element is damaged	1784	0.27	0.27
	crack tip element is fully damaged	2043	0.45	0.42
	max force	2047	0.45	0.46
	innermost element is damaged	2012	0.44	0.46
	innermost element is fully damaged	2001	0.44	0.45

	crack tip element is damaged	1690	0.42	0.43
	crack tip element is fully damaged	1980	1.55	1.59
5	max force	2000	1.65	1.69
	innermost element is damaged	1623	1.57	1.60
	innermost element is fully damaged	—	—	—
	crack tip element is damaged	1867	0.31	0.31
	crack tip element is fully damaged	2180	1.15	1.19
6	max force	2220	1.36	1.41
	innermost element is damaged	1904	1.29	1.34
	innermost element is fully damaged	1705	1.25	1.30
	crack tip element is damaged	1037	0.15	0.15
	crack tip element is fully damaged	1321	0.17	0.17
7	max force	1342	0.17	0.17
	innermost element is damaged	1196	0.13	0.13
	innermost element is fully damaged	1055	0.09	0.09
	crack tip element is damaged	1551	0.19	0.19
	crack tip element is fully damaged	1799	0.26	0.25
8	max force	1807	0.26	0.25
	innermost element is damaged	1552	0.20	0.19
	innermost element is fully damaged	1398	0.16	0.15

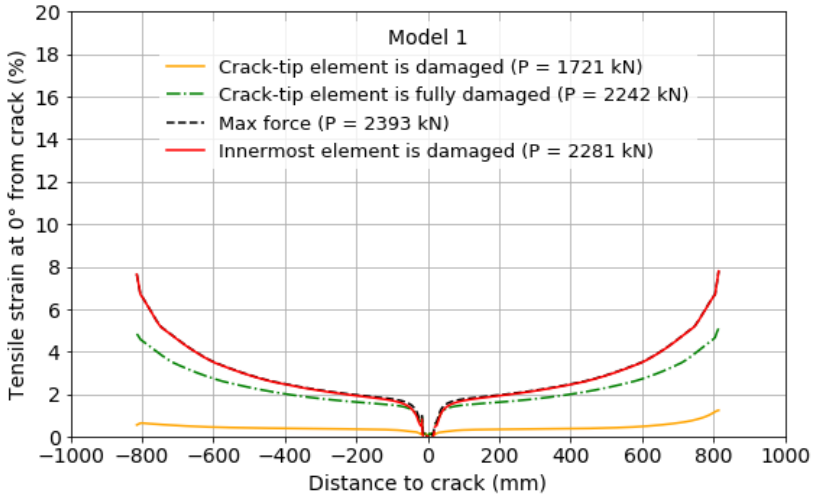
Model 1
Crack-tip element is damaged (P = 1721 kN)
Crack-tip element is fully damaged (P = 2242 kN)
Max force (P = 2393 kN)
Innermost element is damaged (P = 2281 kN)
Tensile strain at 0° from crack (%)
Distance to crack (mm)

(a)

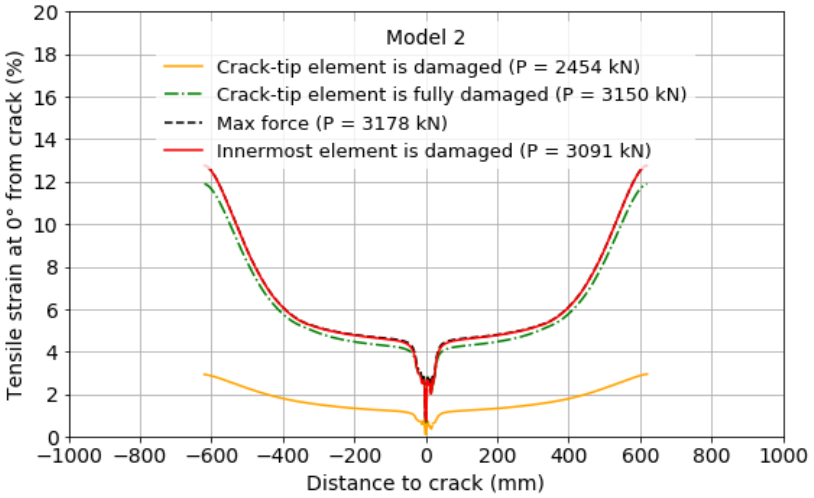
Model 2
Crack-tip element is damaged (P = 2454 kN)
Crack-tip element is fully damaged (P = 3150 kN)
Max force (P = 3178 kN)
Innermost element is damaged (P = 3091 kN)
Tensile strain at 0° from crack (%)
Distance to crack (mm)

(b)

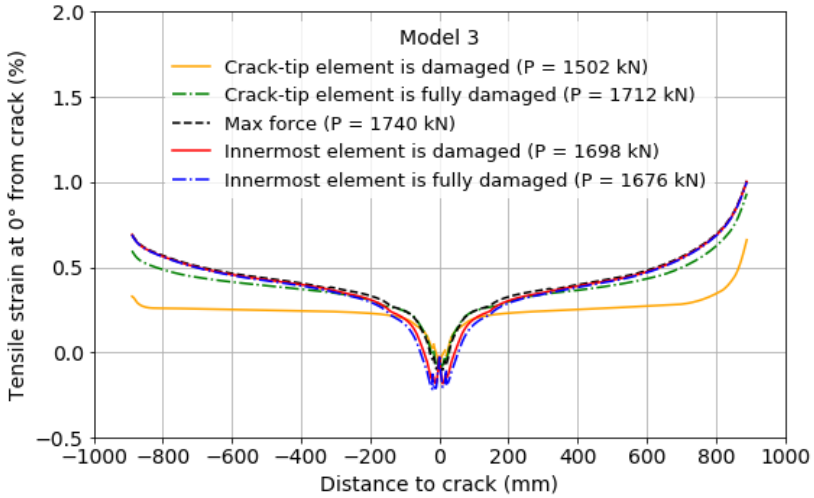
Model 3
Crack-tip element is damaged (P = 1502 kN)
Crack-tip element is fully damaged (P = 1712 kN)
Max force (P = 1740 kN)
Innermost element is damaged (P = 1698 kN)
Innermost element is fully damaged (P = 1676 kN)
Tensile strain at 0° from crack (%)
Distance to crack (mm)

(c)

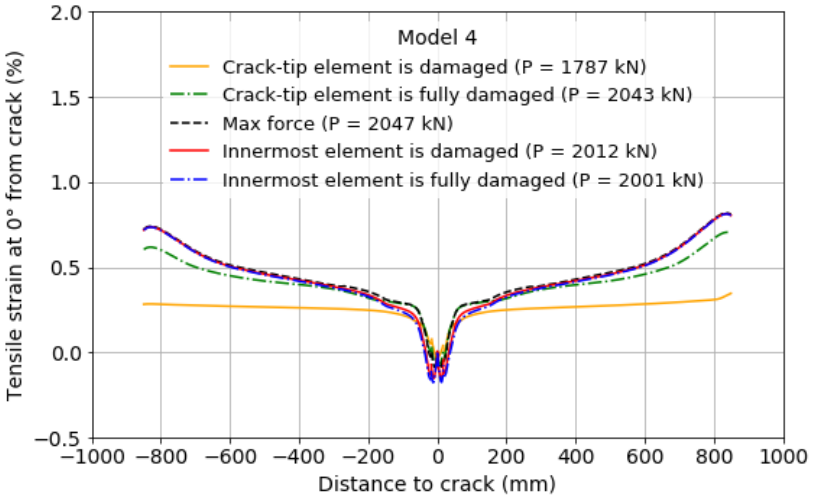
Model 4
Crack-tip element is damaged (P = 1787 kN)
Crack-tip element is fully damaged (P = 2043 kN)
Max force (P = 2047 kN)
Innermost element is damaged (P = 2012 kN)
Innermost element is fully damaged (P = 2001 kN)
Tensile strain at 0° from crack (%)
Distance to crack (mm)

(d)

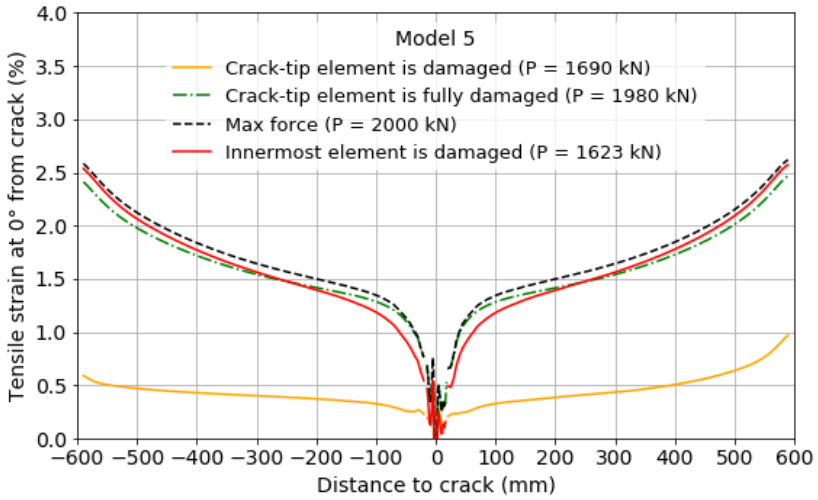

(e)

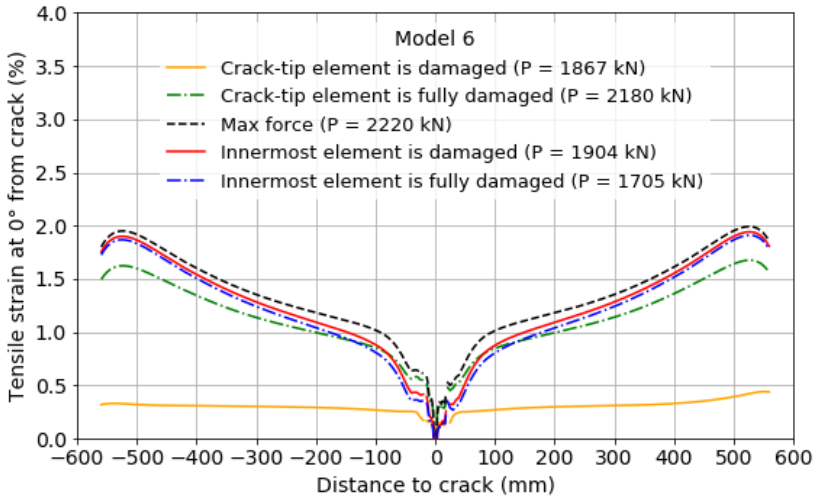

(f)

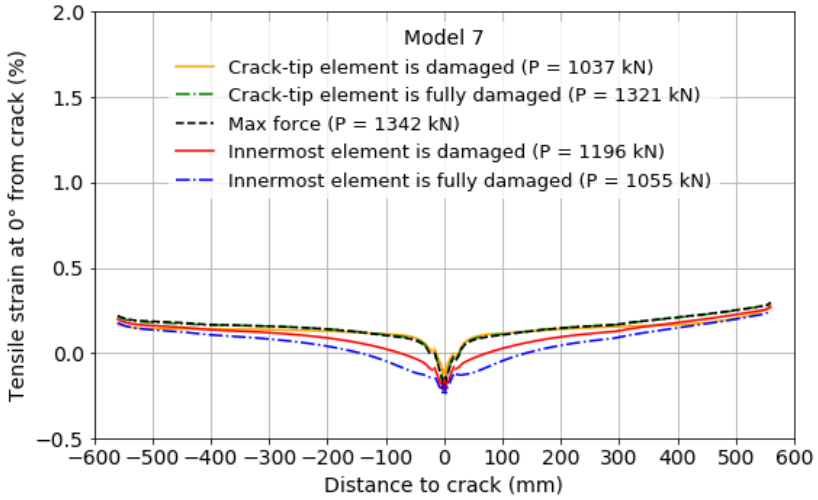

(g)

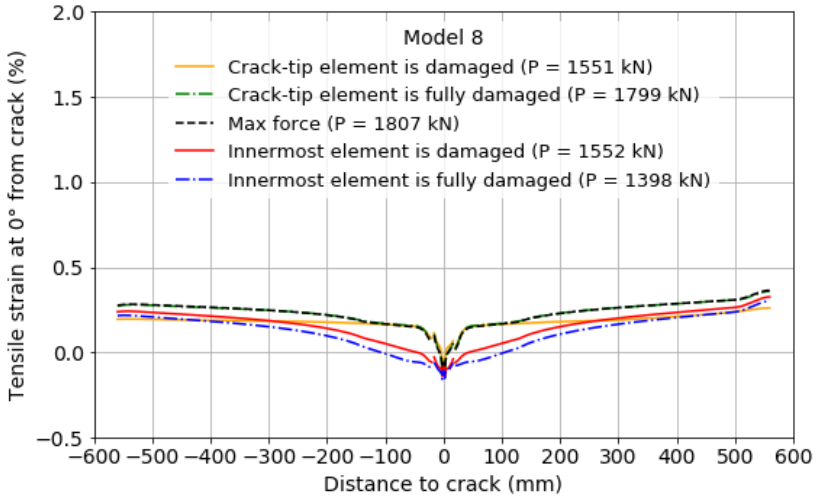

(h)

Figure 5-23. Tensile strains along the pipe length at different phases from Models (a) 1; (b) 2; (c) 3; (d) 4; I 5; (f) 6; (g) 7; and (h) 8. Note the last phase was not obtained from Models 1, 2 and 5.

5.5.4 Investigation of Crack-tip Constraint

Figure 5-24 illustrates the damage strain (i.e., equivalent plastic strain), stress triaxiality, and Lode angle of every damaged element at the instance of reaching the damage criterion for the 8 notch models adopting the novel variable strain damage criterion. Of all models, the overall stress triaxiality values of all damage elements was from 0.7 to 1.7 and that of each crack-tip element was approximately around 1.5. The overall Lode angle values of all damage elements varied between -0.2 to 0.2 and that of crack-tip element was approximately around 0. These values were very similar to those obtained from the other 8 notch models adopting the fixed Maxpe damage criterion (Figure C-4). This perhaps contributed to the observation that a fixed strain criterion is also adequate for predicting the global behaviour of these pipes. Despite these similarities, the damage strain values vary in the two damage criteria, which would alter fracture resistance such as changing the crack propagating path. It is expected that the fixed strain criterion would only be geometry specific and would not be widely applicable for other situations.

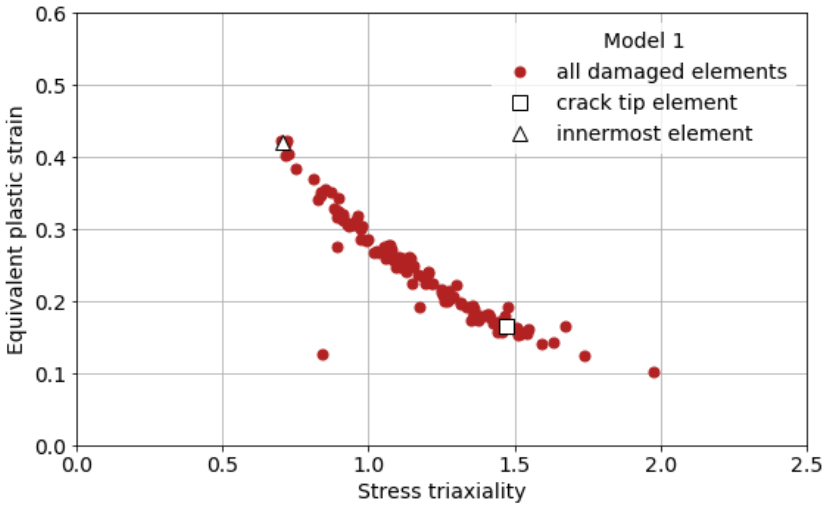
Model 1
all damaged elements
crack tip element
innermost element
Equivalent plastic strain
Stress triaxiality
0.0
0.1
0.2
0.3
0.4
0.5
0.6
0.0
0.5
1.0
1.5
2.0
2.5

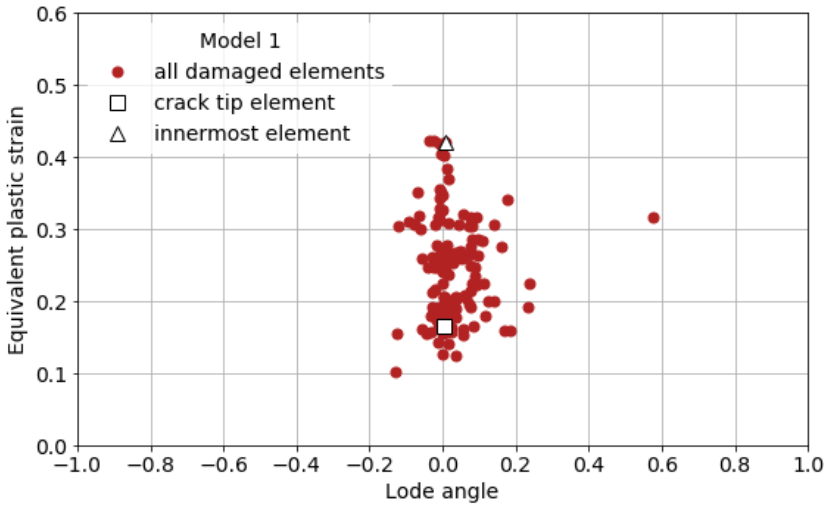
Model 1
all damaged elements
crack tip element
innermost element
Equivalent plastic strain
Lode angle
0.0
0.1
0.2
0.3
0.4
0.5
0.6
−1.0
−0.8
−0.6
−0.4
−0.2
0.0
0.2
0.4
0.6
0.8
1.0

(a)

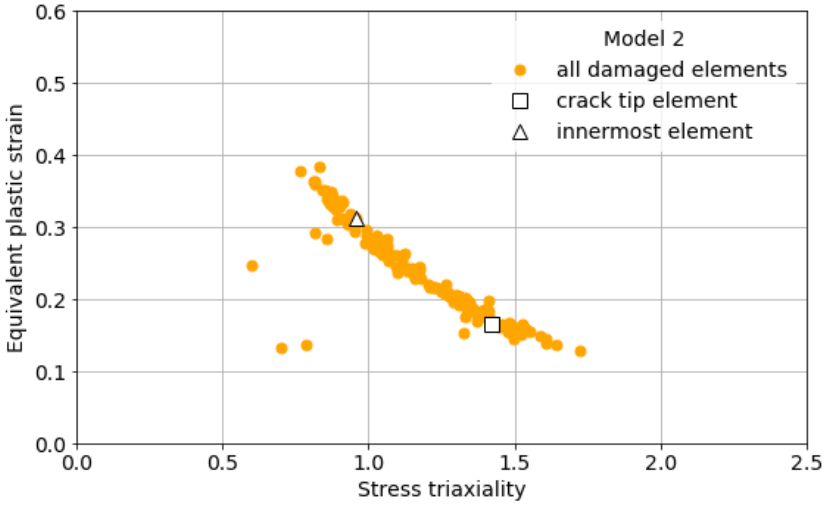
Model 2
all damaged elements
crack tip element
innermost element
Equivalent plastic strain
Stress triaxiality
0.0
0.1
0.2
0.3
0.4
0.5
0.6
0.0
0.5
1.0
1.5
2.0
2.5

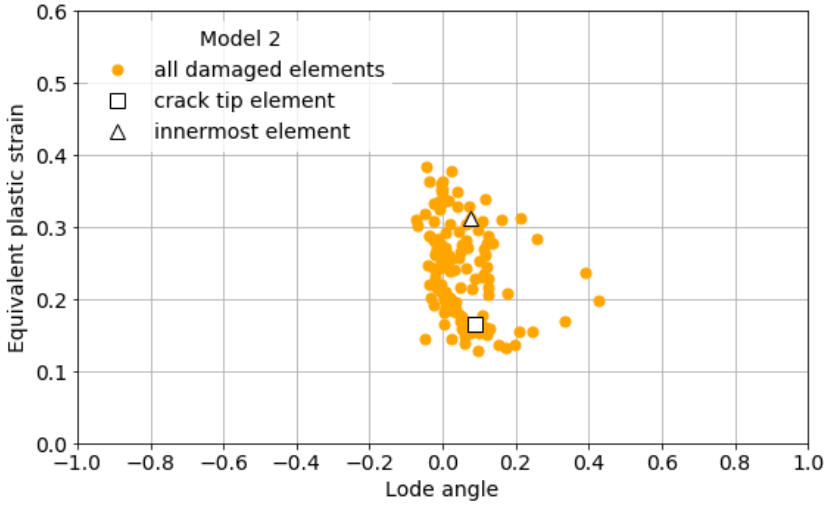
Model 2
all damaged elements
crack tip element
innermost element
Equivalent plastic strain
Lode angle
0.0
0.1
0.2
0.3
0.4
0.5
0.6
−1.0
−0.8
−0.6
−0.4
−0.2
0.0
0.2
0.4
0.6
0.8
1.0

(b)

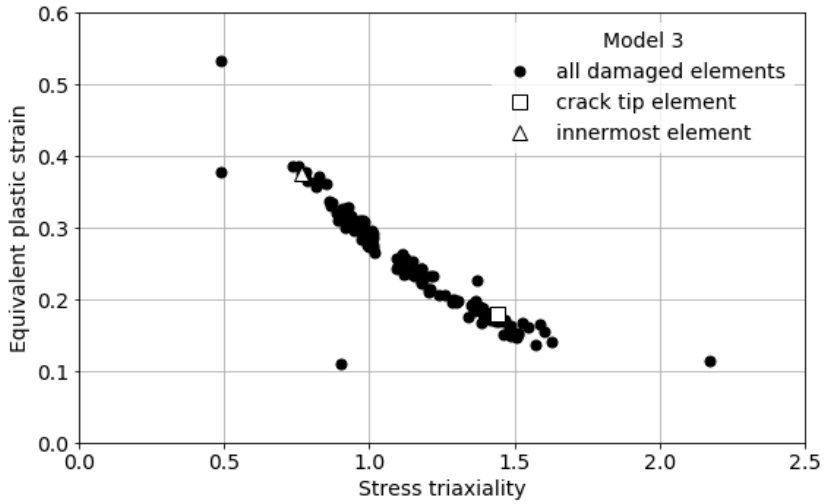
Model 3
all damaged elements
crack tip element
innermost element
Equivalent plastic strain
Stress triaxiality
0.0
0.1
0.2
0.3
0.4
0.5
0.6
0.0
0.5
1.0
1.5
2.0
2.5

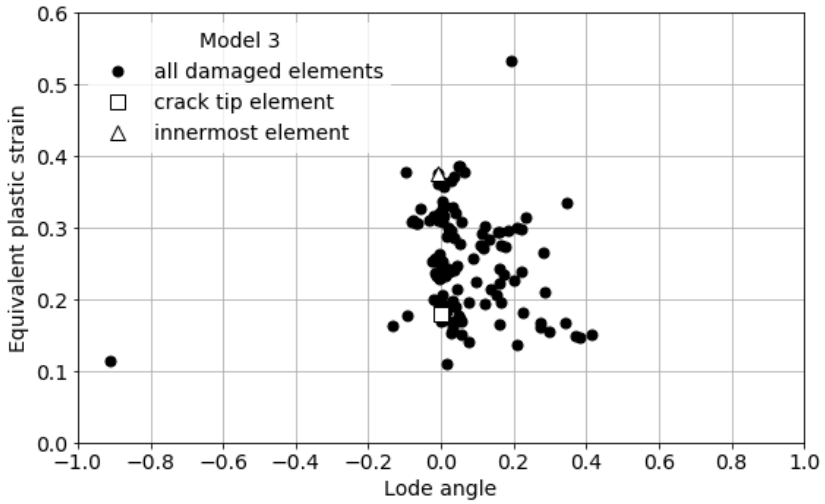
Model 3
all damaged elements
crack tip element
innermost element
Equivalent plastic strain
Lode angle
0.0
0.1
0.2
0.3
0.4
0.5
0.6
−1.0
−0.8
−0.6
−0.4
−0.2
0.0
0.2
0.4
0.6
0.8
1.0

(c)

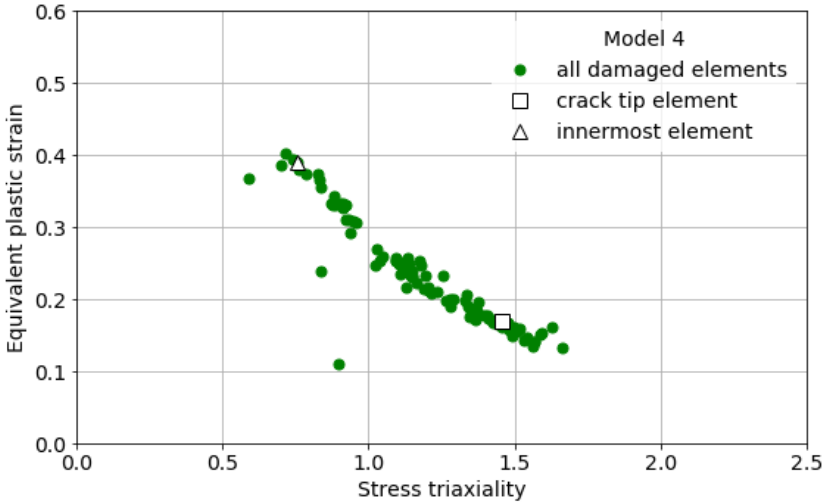
Model 4
all damaged elements
crack tip element
innermost element
Equivalent plastic strain
Stress triaxiality
0.0
0.1
0.2
0.3
0.4
0.5
0.6
0.0
0.5
1.0
1.5
2.0
2.5

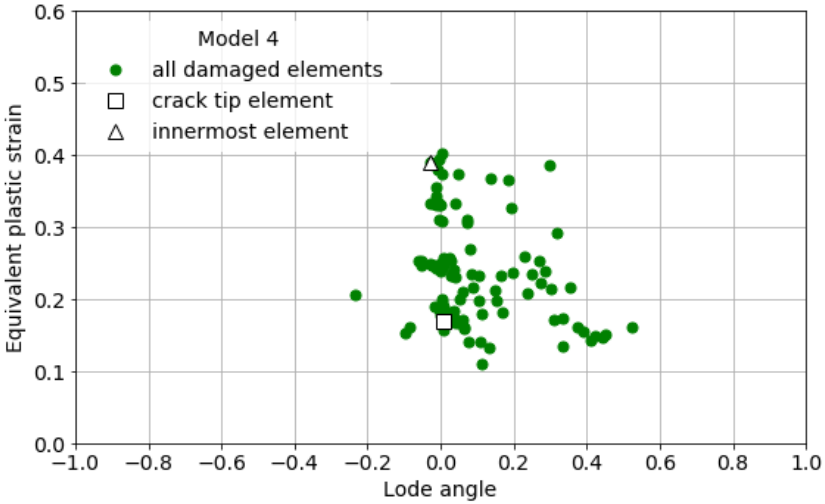
Model 4
all damaged elements
crack tip element
innermost element
Equivalent plastic strain
Lode angle
0.0
0.1
0.2
0.3
0.4
0.5
0.6
−1.0
−0.8
−0.6
−0.4
−0.2
0.0
0.2
0.4
0.6
0.8
1.0

(d)

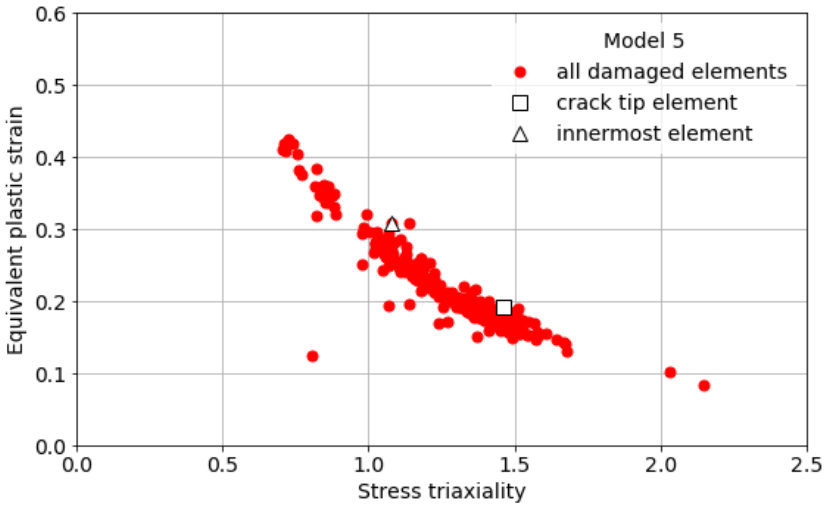
Model 5
all damaged elements
crack tip element
innermost element
Equivalent plastic strain
Stress triaxiality
0.0
0.1
0.2
0.3
0.4
0.5
0.6
0.0
0.5
1.0
1.5
2.0
2.5

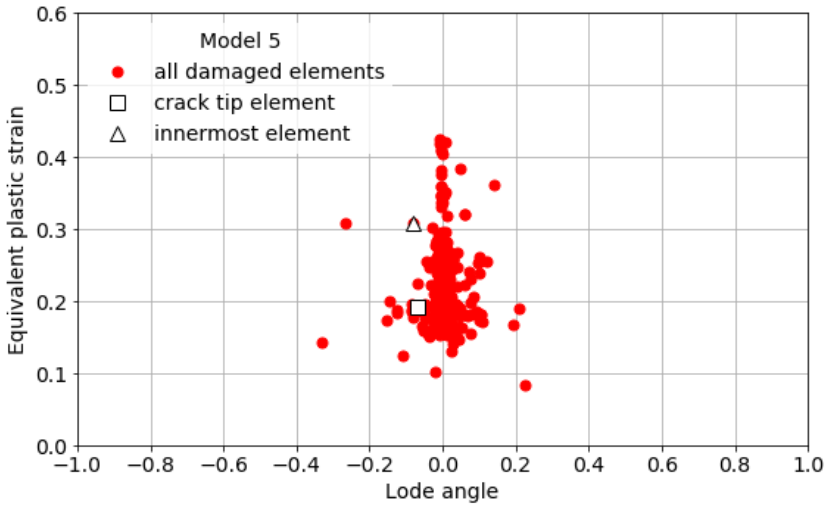
Model 5
all damaged elements
crack tip element
innermost element
Equivalent plastic strain
Lode angle
0.0
0.1
0.2
0.3
0.4
0.5
0.6
−1.0
−0.8
−0.6
−0.4
−0.2
0.0
0.2
0.4
0.6
0.8
1.0

(e)

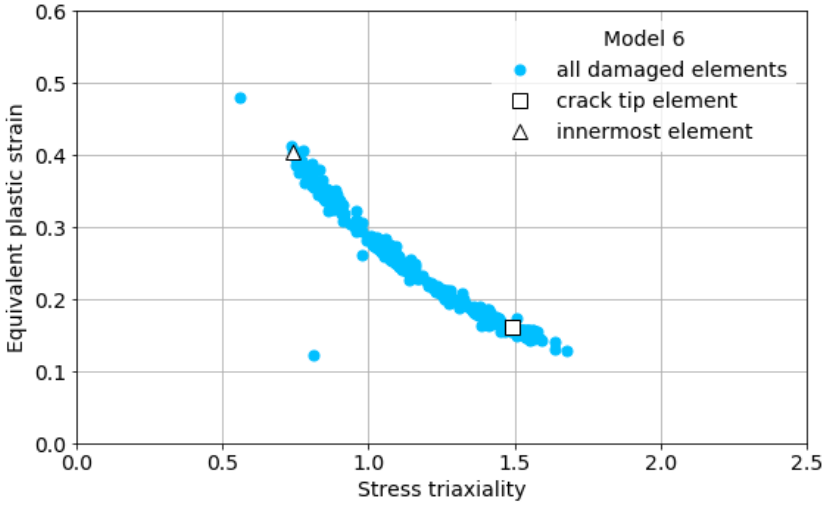
Model 6
all damaged elements
crack tip element
innermost element
Equivalent plastic strain
Stress triaxiality
0.0
0.1
0.2
0.3
0.4
0.5
0.6
0.0
0.5
1.0
1.5
2.0
2.5

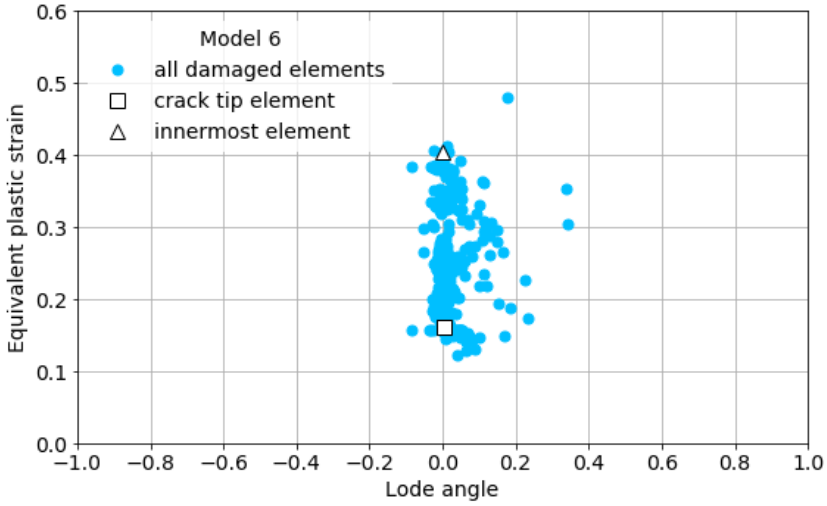
Model 6
all damaged elements
crack tip element
innermost element
Equivalent plastic strain
Lode angle
0.0
0.1
0.2
0.3
0.4
0.5
0.6
−1.0
−0.8
−0.6
−0.4
−0.2
0.0
0.2
0.4
0.6
0.8
1.0

(f)

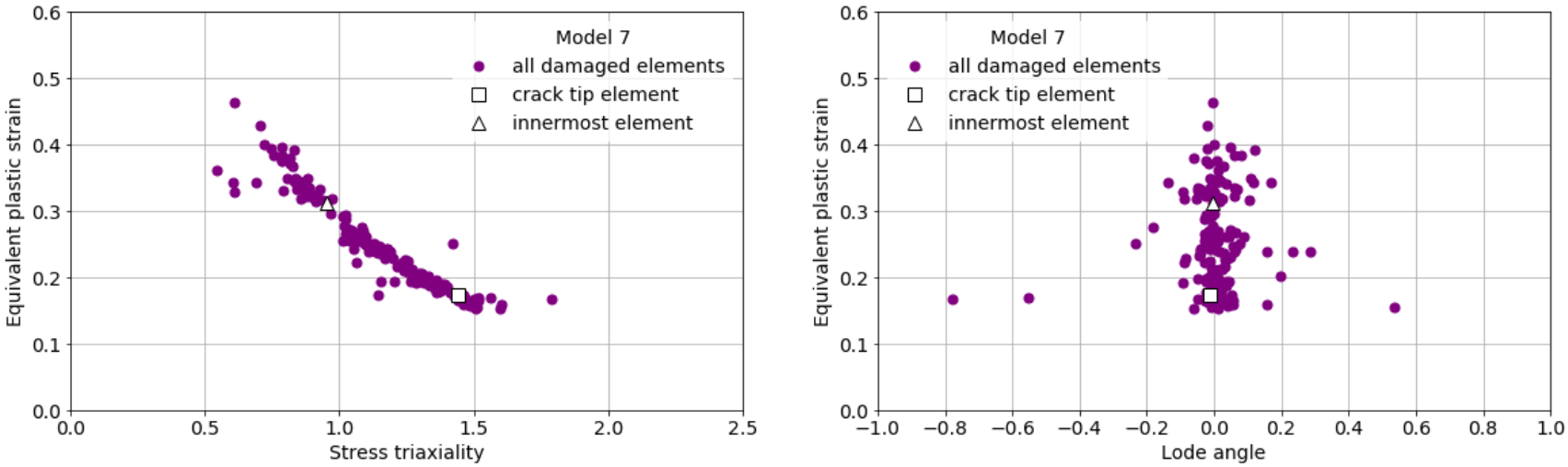

(g)

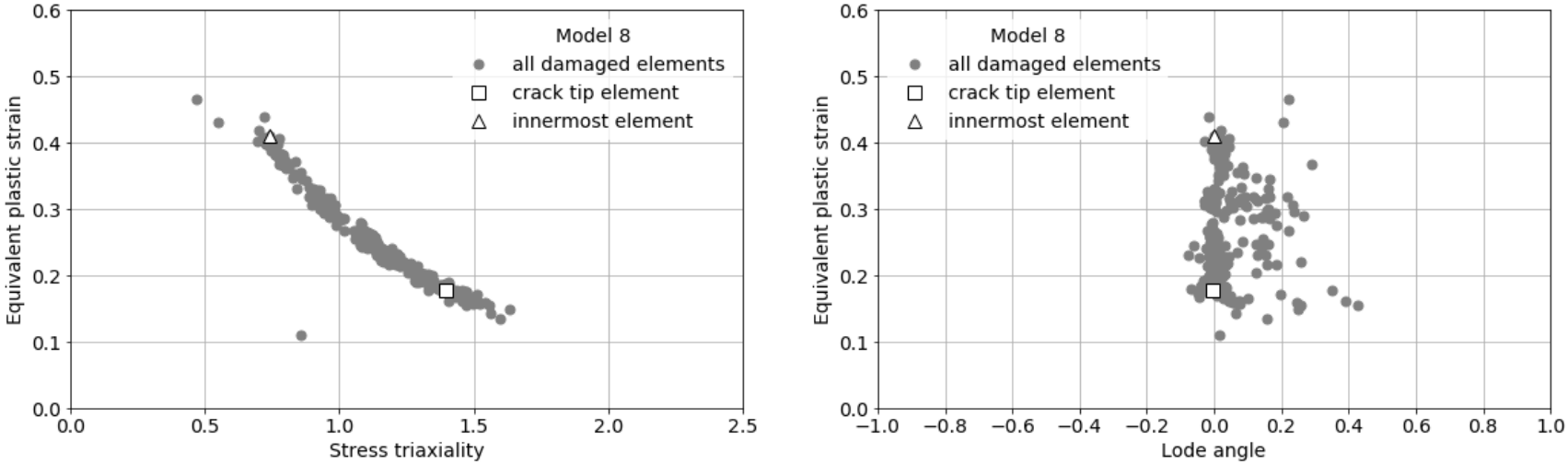

(h)

Figure 5-24. Damage locus of X52 full-scale models from Model (a) 1; (b) 2; (c) 3; (d) 4; (e) 5; (f) 6; (g) 7; and (h) 8.

5.5.5 Initial Notch vs. Planar Crack

To investigate the effect of crack-tip simulation on the numerical predictions, an additional model, termed "Model 3 (planar crack)" was developed with an initial planar crack but having the same other model configuration with "Model 3 (notch)." Both models were analyzed with either variable or fixed strain-based damage criterion. Both the force-CMOD curve and tensile stain profile at failure for planar crack and variable damage criterion were significantly higher than those in the other three simulations (Figure 5-25). The difference between the models with planar crack or notch adopting the fixed damage criterion was smaller than that using the variable damage criterion because of the independence of crack tip constraints. A seen in Figure 5-26 (b), identical tensile strain profiles were found in the planar crack model using variable criterion from the crack initiation to pipe failure. This could be explained by the simulation of planar crack accompanied by artificial cohesion around the crack tip field, generating high resistance for crack initiation, while the crack propagation in the pipe wall thereafter would not effectively reduce the calculated tensile strain capacity.

For models adopting the variable damage criterion in Figure 5-27 (a) and (b), the stress triaxiality and equivalent plastic strain of the initial crack-tip element at the instance of satisfying the damage initiation criterion was 1.44 and 0.18 corresponding a force level of 1502 kN in the notched model while they were 0.94 and 0.30 corresponding to a force level of 1925 kN in the planar cracked model. This indicated that the initial crack-tip constraint quantified by the values of the stress triaxiality with an initial planar crack is artificially lower (i.e., less constrained) than the case of modelling a notch, which resulted in higher local damage strain. Such decrease in stress triaxiality was also shown for the models adopting the fixed damage criterion in Figure 5-27 (c) and (d), where the stress triaxiality and equivalent plastic strain of the initial crack-tip element at the onset of damage were 1.43 and 0.18 corresponding to a force level of 1496 kN in the notched model, while they were 1.07 and 0.17 corresponding to a force

level of 1651 kN in the planar cracked model. There was no big difference in all models in terms of the stress triaxiality of the innermost element at the onset of damage (i.e., onset of pipe failure), which ranged from 0.60 to 0.77. The Lode angle of both the initial crack-tip and the innermost elements of all models were all around 0 indicating a general consistent loading condition, i.e., plastic plane strain or generalized shear, at two moments when the damage occurred on the pipe wall and when the crack propagated through the total pipe wall. Related data are listed in Table 5-7.

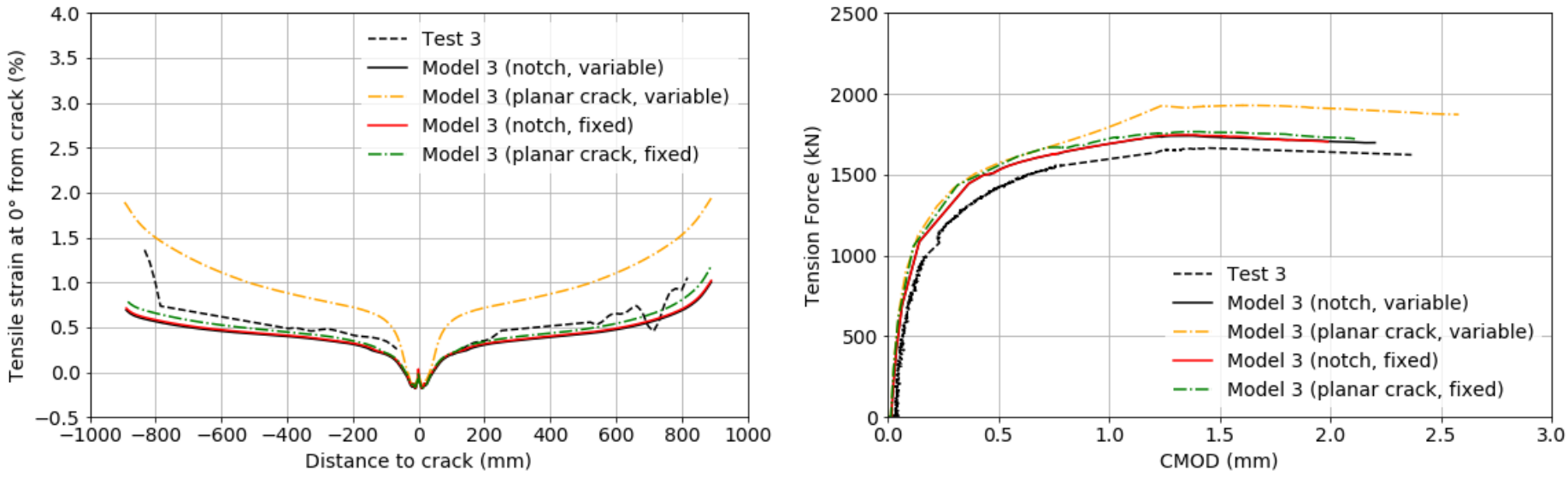

(a) (b)

Figure 5-25. Comparisons of (a) tensile strains along the pipe length at failure; and (b) CMOD against force from models with an initial notch or planar crack and variable or fixed strain-based damage criterion.

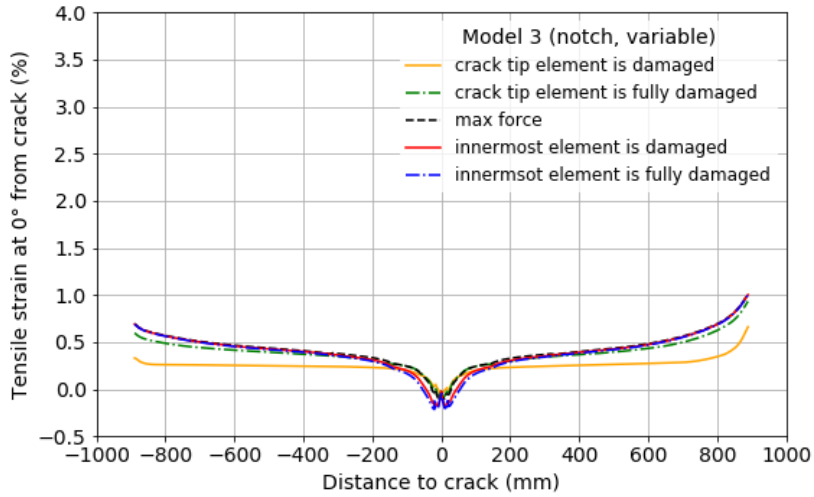

(a)

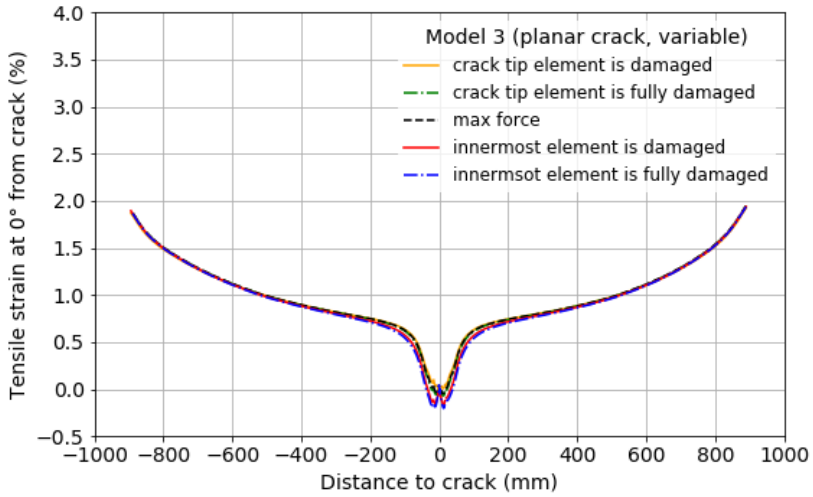

(b)

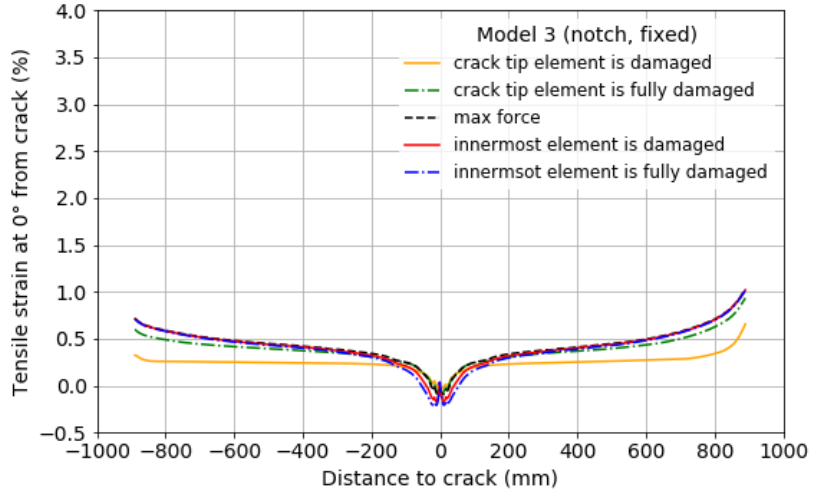

(c)

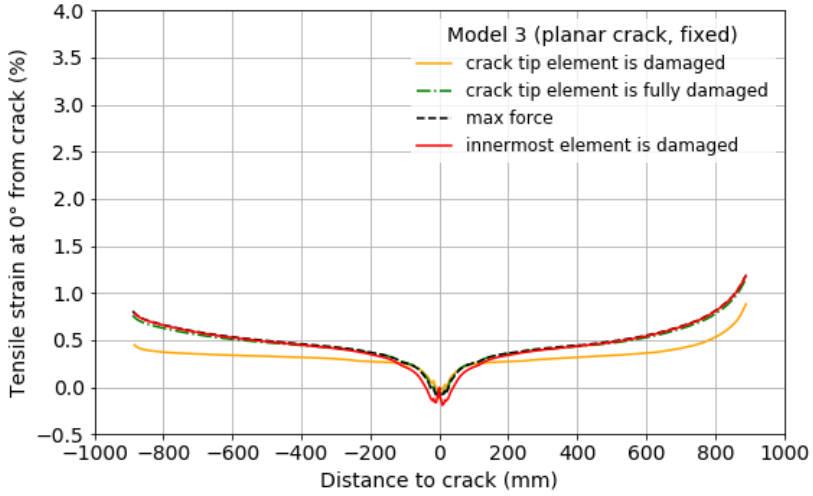

(d)

Figure 5-26. Comparisons of tensile strains at different stages from model 3 with initial (a) notch and variable criterion; (b) planar crack and variable criterion; (c) notch and fixed criterion; and (d) planar crack and fixed criterion.

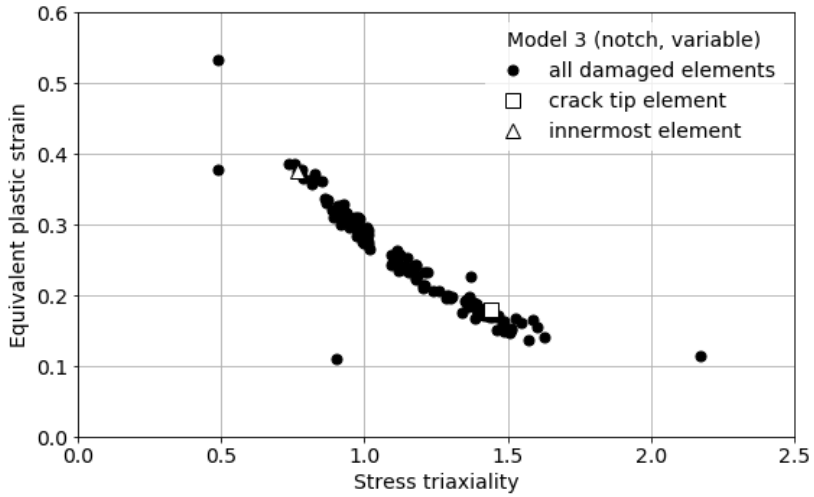
Model 3 (notch, variable)
all damaged elements
crack tip element
innermost element
Equivalent plastic strain
Stress triaxiality
0.0
0.1
0.2
0.3
0.4
0.5
0.6
0.0
0.5
1.0
1.5
2.0
2.5

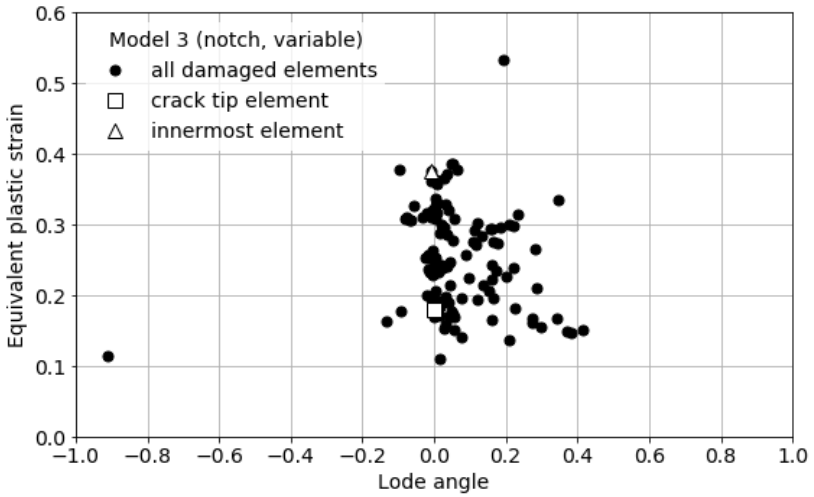
Model 3 (notch, variable)
all damaged elements
crack tip element
innermost element
Equivalent plastic strain
Lode angle
0.0
0.1
0.2
0.3
0.4
0.5
0.6
−1.0
−0.8
−0.6
−0.4
−0.2
0.0
0.2
0.4
0.6
0.8
1.0

(a)

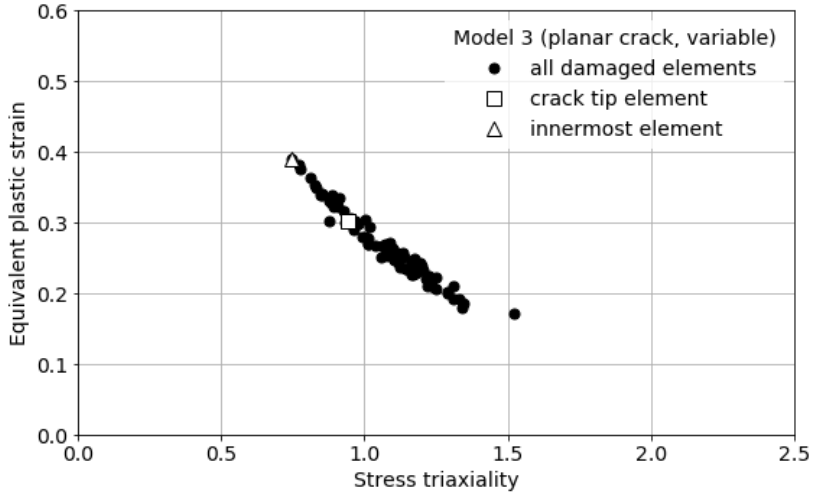
Model 3 (planar crack, variable)
all damaged elements
crack tip element
innermost element
Equivalent plastic strain
Stress triaxiality
0.0
0.1
0.2
0.3
0.4
0.5
0.6
0.0
0.5
1.0
1.5
2.0
2.5

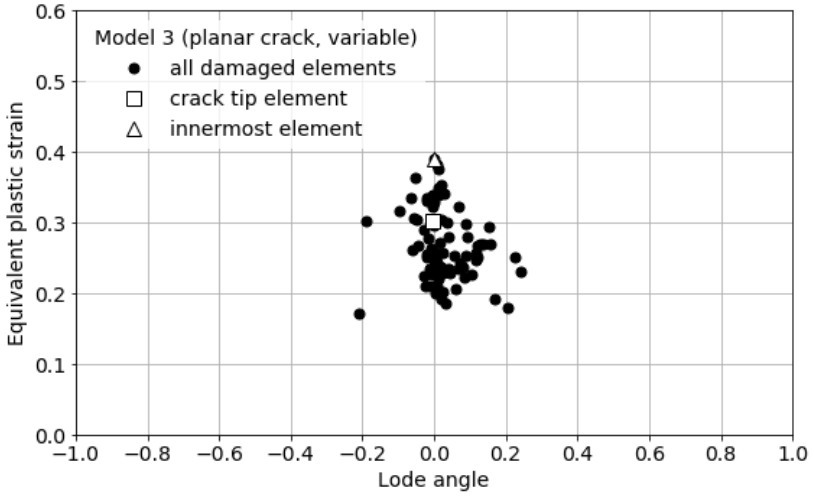
Model 3 (planar crack, variable)
all damaged elements
crack tip element
innermost element
Equivalent plastic strain
Lode angle
0.0
0.1
0.2
0.3
0.4
0.5
0.6
−1.0
−0.8
−0.6
−0.4
−0.2
0.0
0.2
0.4
0.6
0.8
1.0

(b)

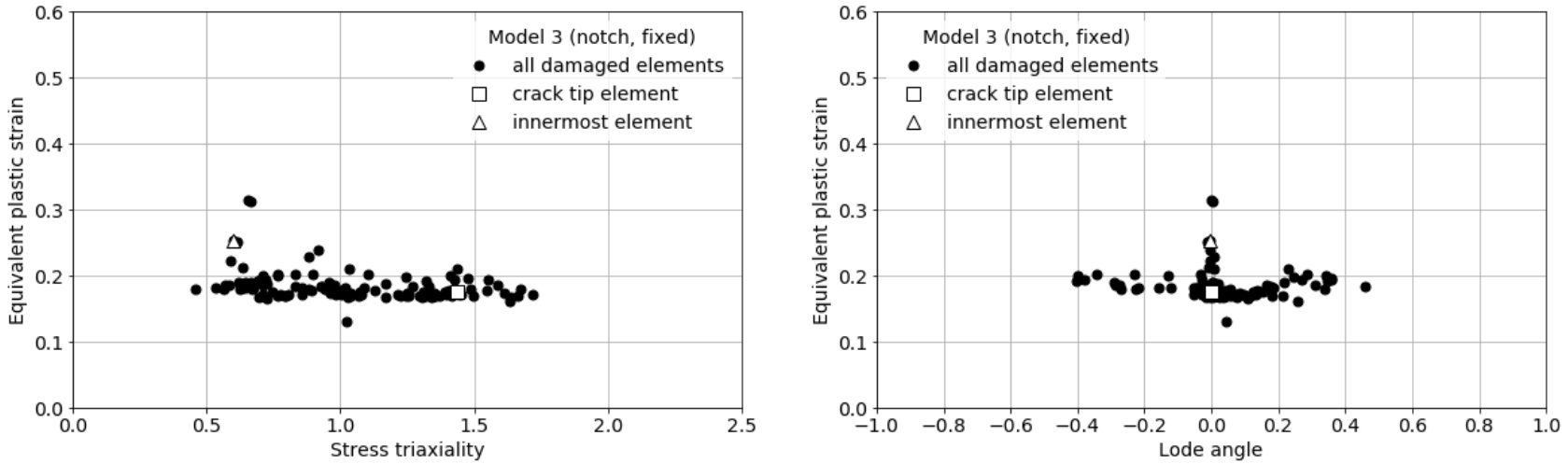

(c)

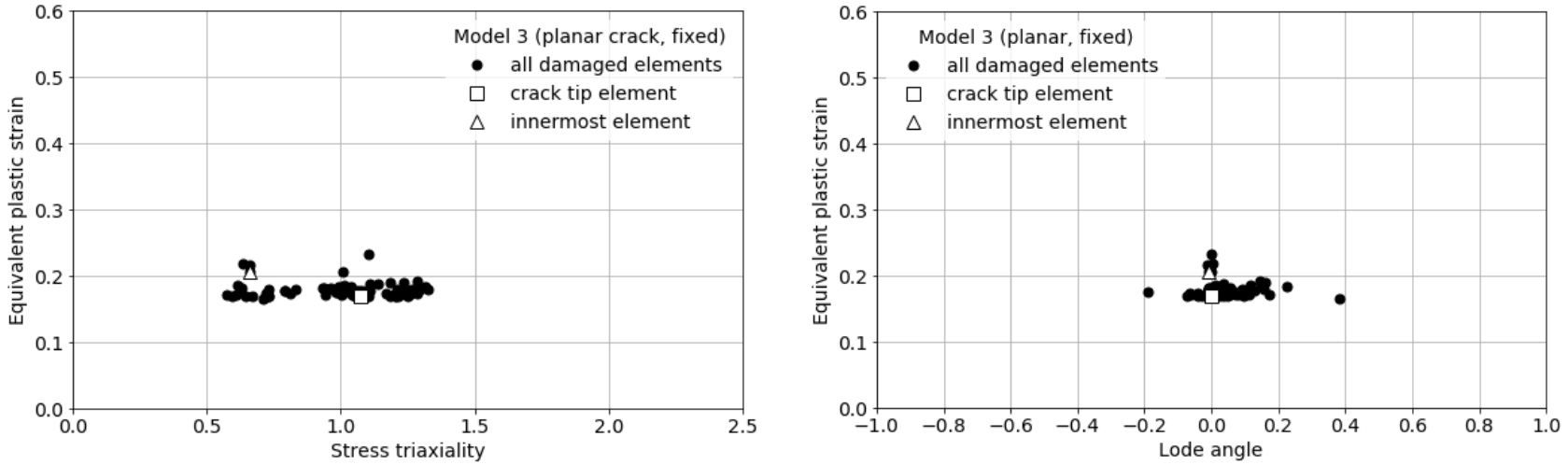

(d)

Figure 5-27. Damage locus of Model 3 with an initial (a) notch and variable damage criterion; (b) planar crack and variable damage criterion; (c) notch and fixed damage criterion; and (d) planar crack and fixed damage criterion.

Table 5-7. Comparison between Model 3 with initial notch and planar crack using variable or fixed damage strain criterion

Model 3	Stage	Force (kN)	Tensile strain at 0° from crack (%)		PEEQ (Maxpe)	η
			$\varepsilon_{0.5L}$	ε_{avg}		
Notch, Variable	crack tip element is damaged	1502	0.25	0.25	0.18	1.44
	crack tip element is fully damaged	1712	0.38	0.39	—	—
	max force	1740	0.42	0.43	—	—
	innermost element is damaged	1698	0.41	0.42	0.38	0.77
	innermost element is fully damaged	1676	0.40	0.41	—	—
Planar crack, Variable	crack tip element is damaged	1925	0.94	0.97	0.30	0.94
	max force[a]	1929	0.94	0.97	—	—
	crack tip element is fully damaged	1925	0.94	0.97	—	—
	innermost element is damaged	1872	0.93	0.96	0.39	0.75
	innermost element is fully damaged	1846	0.92	0.96	—	—
Notch, fixed	crack tip element is damaged	1496	0.25	0.25	0.18 (0.16)	1.43
	crack tip element is fully damaged	1712	0.38	0.39	—	—
	max force	1746	0.43	0.44	—	—
	innermost element is damaged	1704	0.42	0.43	0.25 (0.16)	0.60
	innermost element is fully damaged	1668	0.41	0.42	—	—
Planar crack, fixed	crack tip element is damaged	1651	0.32	0.33	0.17 (0.15)	1.07
	crack tip element is fully damaged	1756	0.45	0.47	—	—
	max force	1766	0.47	0.48	—	—
	innermost element is damaged	1722	0.46	0.47	0.21 (0.15)	0.66
	innermost element is fully damaged	—	—	—	—	—

[a]Max force is reached before the crack tip element is fully damaged in this model.

5.6 Comparison with literature available MMC strain-based fracture model parameters

The calibrated power-law fit plasticity parameters and fracture parameters of the modified MMC fracture criterion for API 5LX pipe steels available in the literature are listed in Table 5-8. Kofiani et al. [72,73] calibrated each set of fracture parameters for steel cut from X100 pipe and X70 seamless pipe based on numbers of experiments on uncracked specimens covering a wide range of stress triaxiality $0 \leq \eta \leq 2$ and lode angle $\bar{\theta} = -1$ and $0 \leq \bar{\theta} \leq 1$. They also validated their respective fracture locus on pin-loaded SENT tests. Tests for stress triaxiality lower than 1 included tensile tests on central hole or notched flat specimens, tensile and shear tests on flat butterfly specimens, and punch tests on circular disk specimens, while tests for stress triaxiality higher than 1 included tensile tests on notched round bar and SENT specimens. Paredes et al. [76] conducted similar fracture tests and calibrated two sets of parameters for steel respectively cut from X65 seamless pipe (NPS 16, D/t=10) and X65 seam welded pipe (NPS 24, D/t=32). Mohajer Rahbari et al. [77] calibrated a set of parameters for steel cut from X65 seam welded pipe (NPS 30) based on tensile tests of flat round bar and grooved plate specimens. Table 5-8 also included my calibrated parameters for X100 pipe (NPS 48, D/t = 85) based on SENT tests and X52 pipe (NPS 12, D/t = 47) based on full-scale tests. Figure 5-28 demonstrates the plotted relationship between $\bar{\varepsilon}_f$ and η of the listed studied keeping $\bar{\theta}$ constant at 0 corresponding to a loading type of plastic plane strain or generalized shear.

Of all above studies in the literature, the calibrations were performed on uncracked specimens, while current calibrations were performed on cracked specimens. Surprisingly, the calibrated values of c_2 (i.e., new c_2), c_3 and c_4 are almost identical for all studies, and c_1 and n seem to control the difference between all the listed models. This finding perhaps led to further

simplification of Eq. (5-8) by making the component $c_2 \times \left[c_3 + \frac{\sqrt{3}}{2-\sqrt{3}}(c_4 - c_3)\left(sec\left(\frac{\bar{\theta}\pi}{6}\right) - 1\right)\right]$ determined through inputting the constants, e.g., c_2 = 1.85, c_3 = 0.9 and c_4 = 1. In this way, the unknown variables will be reduced to only c_1 and n. Further work would also look at replacing the plasticity parameter n appearing in the fracture model with a different variable independent of the power law. To the best of my knowledge, this work is the first to incorporate XFEM with a ductile fracture criterion of intact specimens into full-scale and small-scale pre-cracked specimens. The success of this work attempts to unify classical fracture mechanics assuming a pre-existing crack and damage mechanics of intact metals.

Table 5-8. Calibrated parameters of strain-based MMC fracture model for API 5LX pipes

Pipe	Plasticity parameters		Fracture parameters					Literature
	A (Mpa)	n	c_1	old c_2 (Mpa)	new c_2 = $\frac{A}{\text{Old } c_2}$	c_3	c_4	
X100	1006.5	0.0384	0.029	535	1.88	0.9	1	Kofiani et al. [73]
X100	—	0.0923	0.03	—	1.9	0.9	1	Lin et al. (This thesis)
X70 (seamless)	844.6	0.0984	0.050	454	1.86	0.91	1	Kofiani et al. [72]
X65 (seamless)	991.19	0.2	0.12	598.44	1.66	0.9	1	Paredes et al. [76]
X65 (seam welded)	722.35	0.054	0.029	381.77	1.89	0.87	1	Paredes et al. [76]
X65 (seam welded)	830.96	0.0834	0.0499	458.98	1.81	0.912	1.031	Mohajer Rahbari et al. [77]
X52	—	0.119	0.1	—	1.9	0.9	1	Lin et al. (This thesis)

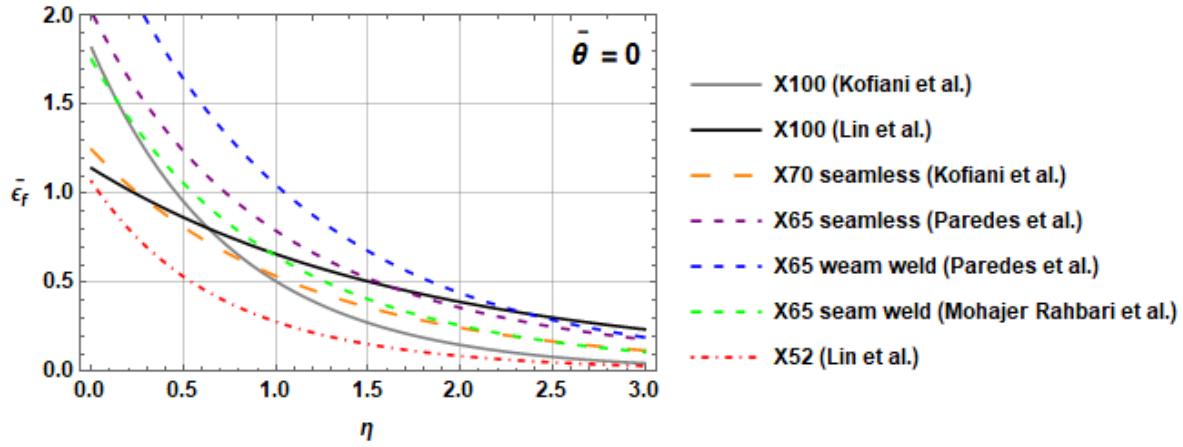

Figure 5-28. Calibrated fracture locus curves of API 5LX pipes when $\bar{\theta} = 0$.

5.7 Conclusions

This chapter validated the novel XFEM variable strain damage model in predicting the fracture behaviour of pipeline steel in both small-scale and full-scale tests. The criterion was modified from Mohr–Coulomb fracture criterion as function of stress triaxiality and lode angle parameters to account for the crack tip constraint. An optimal set of damage parameters (c_1 = 0.03, c_2 = 1.9, c_3 = 0.9, c_4 = 1, and G_c = 100 N/mm) was obtained specific to X100 with a given strain hardening exponent (n = 0.0923), based on experimental data including force-CMOD and J-R curves. Two methods were adopted to evaluate the numerical J-integral, with one computed from surface strain and the other computed from CMOD using empirical equations developed by CANMET-MTL. These methods compensated for the unavailability of contour integral evaluation in the XFEM propagating crack analysis. The novel variable strain-based damage criterion demonstrated significant improvements in predicting the actual crack propagating path in side-grooved SENT models in comparison with that predicted by the fixed strain-based damage criterion. Another optimal set of damage parameters (c_1 = 0.1, c_2 = 1.9, c_3 = 0.9, c_4 = 1, and G_c = 200 N/mm) was obtained specific to X52 with a given strain hardening exponent (n = 0.119), based on experimental data including force-CMOD curves

and tensile strain capacity along the pipe length.

Since during the calibration process, the experimental data mostly indicated the global behaviour of X52 pipe in full-scale tests, it was noticed that the numerical results obtained using the calibrated variable strain and fixed strain (Maxpe = 0.15 and G_c =200 N/mm) damage criteria were similar. The local numerical differences could not be validated due to the scarcity of localized experimental measurements. Nevertheless, significant improvements were achieved for both variable and fixed strain-based damage criteria in predicting the growth of CMOD and pipe wall thickness reduction at failure in comparison with those predicted by fixed stress-based damage criterion. For each model, the initial crack was modelled as a three-dimensional notch instead of typically inserting a planar two-dimensional crack. It was found that when using the novel variable strain damage criterion, the crack-tip constraint posed a remarkable effect on the results, whereas such effect was insignificant when using the fixed strain damage criterion. Lastly, my calibrated damage parameters of X100 and X52 were compared with those calibrated for other pipe grades in the literature. One limitation of my calibrated models was the absence of validation on a different data set. To the best of my knowledge, this work is the first to ever incorporate XFEM with a ductile fracture criterion of intact specimens into full-scale and small-scale cracked specimens. This work successfully attempts to unify classical fracture mechanics assuming a pre-existing crack and damage mechanics of intact metals.

Future work may focus on updating the variable strain-based damage model, such as reducing the variables to only predominated c_1 and n and replacing the plasticity parameter n with a different variable independent of the power law. Further research direction may also include exhaustively exploring the damage initiation criterion to account for strain rate and temperature and the damage evolution criterion to consider mixed mode fracture. The updated advanced XFEM damage model would be validated on various fracture tests covering wide range of

crack-tip constraint, such as the small-scale SENT, SENB and CT tests, the medium-scale CWP tests, and full-scale tests on either circumferentially or longitudinally cracked pipe. In addition, the model may be extended to hybrid defects such as the dent-crack defect and crack-in-corrosion defect. Further extensive calibration work specific to each of various pipeline grades would make significant contribution in the pipeline crack assessment.

6. Summary, Conclusions, Contributions and Recommendations

6.1 Summary

Cracking is the most dangerous integrity threat in steel pipelines potentially resulting in the immediate loss of pressure containment capacity. Circumferential cracking affects the longitudinal tensile strain capacity of pipelines, while longitudinal cracking affects the burst pressure of pipelines. The only Canadian code-based equation (Rupture, Tier 2 approach) proposed in CSA Z662-11 in predicting the TSC of a circumferentially cracked pipeline has been removed in the revision and a guideline was proposed instead to adopt proven methods validated from physical tests. Meanwhile, other empirical equations available in the Canadian pipeline industry, such as that proposed by PRCI or ExxonMobil validated on modern pipelines are not applicable to vintages pipelines. For example, the vintage X52 pipeline is ubiquitous in current Canadian pipeline network. The small-scale SENT test has been recently recommended in the pipeline industry to measure the tearing resistance curve, which serves as a key input to evaluate the TSC in the analytical equations. Extensive experimental and research in the literature have validated the SENT tests can produce similarly low level of crack-tip constraint and R-curves measured from full-scale tests on circumferentially cracked pipes loaded in globally bending.

At present, numerical tools have been favored in the pipeline integrity crack assessment. XFEM is a revolutionary technique to overcome the difficulties occurred in solving the discontinuous geometry problems in conventional FEM. Although the XFEM-based cohesive segments method provided by Abaqus/Standard has been increasingly employed in the pipeline crack propagation analysis since the last decade, current damage criteria have not been well calibrated. The built-in damage initiation criterion assumes a fixed critical stress or strain value

as the damage initiation, such as Maxps or Maxpe. However, these damage criteria ignore the crack-tip constraint which is known to have a profound effect on fracture resistance. By accounting of crack-tip constraint, a novel XFEM variable strain damage initiation criterion has been developed in this doctoral thesis. The novel criterion was derived from a modified stain-based MMC fracture criterion as a function of stress triaxiality and Lode angle. It was implemented using a Fortran code programmed in Abaqus user subroutine-UDMGINI.

This doctoral research includes the evaluation of fixed Maxps, fixed Maxpe and novel variable strain-based damage criteria in predicting the Mode I (opening mode) fracture of pipeline in full-scale tests and small-scale SENT tests. One optimal set of damage parameters (Maxps = 750 and G_c = 900 N/mm) was calibrated through eight full-scale models of circumferentially surfaced-cracked X52 pipeline with an initial XFEM planar crack inserted into the mesh to predict similar TSC measured from eight full-scale tests. Limitations of the fixed stress-based damage criterion were found in predicting the plasticity indicated by growth of CMOD and reduction of pipe wall thickness at failure. Another optimal set of damage parameters (Maxpe = 0.15 and G_c = 200 N/mm) was calibrated through similar eight full-scale models but with an 0.5 mm-wide notch cut in the model instead of inserting planar crack. The fixed strain-based damage criterion was found adequate for predicting all experimental results. The final recommended optimal set of damage parameters (c_1 = 0.1, c_2 = 1.9, c_3 = 0.9, c_4 = 1, and G_c = 200 N/mm) within the novel variable strain damage criterion specific to X52 with a given strain hardening exponent (n = 0.119), was calibrated through the eight full-scale notched models as same as those using Maxpe. The difference between the numerical results adopting the fixed Maxpe and variable strain damage criterion were similar because the current experimental data used for calibration are mostly an indication of global behaviour of X52 pipe in full-scale tests. The local numerical differences could not be validated due to the lack of localized experimental measurements. It is expected that the optimal Maxpe damage parameters would be geometry

and case specific and not widely applicable to other situations for the same material, whereas the optimal variable strain damage parameters may be applicable to any situation for X52. A unique feature of pressurised pipelines that TSC increased by the crack propagating through the pipe wall thickness was discussed. In addition, a detailed investigation of crack-tip constraint and initial crack-tip simulation using either planar crack or notch on the numerical predictions was performed. The notch simulation could remove the artificial cohesion in the crack tip field generated by typically inserting the XFEM planar crack, which had remarkable effect in application of novel variable strain damage criterion depended on the crack-tip constraint.

This research also evaluated the performance of novel variable strain-based damage criteria in predicting the J-R curves of X100 pipe steel in SENT tests. A recommend optimal set of damage parameters (c_1 = 0.03, c_2 = 1.9, c_3 = 0.9, c_4 = 1, and G_c = 100 N/mm) was calibrated specific to X100 with a given strain hardening exponent (n = 0.0923) through four SENT models with an initial 0.1 mm-wide notch. Two methods were adopted to calculate the J-integral, with one computed from surface strain and the other computed from CMOD using empirical equations developed by CANMET-MTL for SENT specimens. Both methods compensated for the unavailability of contour integral evaluation in the XFEM propagating crack analysis. The novel criterion demonstrated significant improvements in predicting the actual crack propagating path in two side-grooved models in comparison with that predicted by the fixed Maxpe damage criterion. An irregular ductile extension fracture profile was obtained from the model with fixed Maxpe damage criterion, whereas a basically parabolic or flat curve with only slight growth at the side groove was obtained from the model with novel damage criterion which was identical to the experimental measurement. Detailed investigations of crack-tip constraint at crack front and initial crack-tip simulation using either planar crack or notch adopting fixed Maxpe or variable strain damage criterion were all performed.

Lastly, the above two optimal sets of damage parameters in the novel damage criterion calibrated to X100 and X52 were compared with literature available MMC strain-based fracture model parameters calibrated to X65, X70 and X100 based on uncracked small-scale specimens. To the best of my knowledge, this research is first to incorporate XFEM with a ductile fracture criterion of uncracked specimens into both small and full-scale cracked specimens. The success of this work attempts to unify classical fracture mechanics assuming a pre-existing crack and damage mechanics of uncracked metals.

6.2 Conclusions

This doctoral thesis evaluated the most common adopted damage initiation criteria (Maxps or Maxpe) available in XFEM framework supported in Abaqus/Standard and developed novel variable strain damage initiation criterion accounting for the crack-tip constraint, with each paired with a linearly softening damage evolution law characterized by a mode-independent critical energy release rate (G_c) to predict the Mode I fracture of API 5L X52 and X100 pipeline steel. The new criterion was derived from the modified strain-based Mohr-Coulomb (MMC) fracture criterion as a function of stress triaxiality and Lode angle. It was implemented using a Fortran code programmed in Abaqus user subroutine-UDMGINI and calibrated through models based on experimental data. The tensile strain capacity of circumferentially surfaced-cracked X52 pipe specimens in full-scale pressurized tests and the J-R curves of X100 pipe specimens in small-scale SENT tests were well predicted with novel damage criterion.

The following are the main conclusions of this doctoral thesis.

1. An optimal set of damage parameters (Maxps = 750 and G_c = 900 N/mm) was calibrated specific to X52 pipeline through eight models with an initial crack inserted by XFEM planar crack into the mesh based on experimental full-scale test results.

Limitations of the fixed stress-based damage criterion were found in predicting the plasticity indicated by the growth of CMOD and reduction of pipe wall thickness at failure.

2. An optimal set of damage parameters (Maxpe = 0.15 and G_c = 200 N/mm) was calibrated specific to X52 pipeline through eight models with an initial 0.5 mm-wide notch created in the model based on experimental full-scale test results. The fixed strain-based damage criterion was adequate for predicting global behaviour of these X52 tests. However, it is expected to be geometry and case specific and not widely applicable to other situations for the same material.

3. A recommended optimal set of damage parameters (c_1 = 0.1, c_2 = 1.9, c_3 = 0.9, c_4 = 1, and G_c =200 N/mm) was calibrated specific to X52 pipeline with a given strain hardening exponent (n = 0.119) through eight models with an initial 0.5 mm-wide notch created in the model based on experimental full-scale test results. This novel variable strain damage criterion is expected to be applicable to any situation for X52.

4. A recommended optimal set of damage parameters (c_1 = 0.03, c_2 = 1.9, c_3 = 0.9, c_4 = 1, and G_c = 100 N/mm) was calibrated specific to X100 with a given strain hardening exponent (n = 0.0923) through four models with an initial 0.1 mm-wide notch created in the model based on experimental SENT test results. This novel variable strain damage criterion is expected to be applicable to any situation for X100.

5. Both calibrated variable strain-based and fixed strain-based damage criteria demonstrated significant improvements in predicting the ductile behaviour in X52 full-scale models, in comparison with those utilizing fixed stress-based damage criterion.

6. The calibrated variable strain-based damage criterion demonstrated significant

improvements in predicting the actual crack propagation path in X100 SENT models in comparison with that utilizing fixed strain-based damage criterion. The irregular ductile crack extension profile and excessive crack growth at side groove generated by Maxpe damage criterion was largely improved by novel damage criterion where a basically parabolic or flat fracture profile with only slight growth at side groove was obtained identical to experimental measurement.

7. The numerical J-integral in X100 SENT models was computed by two methods, with one computed from surface strain and the other computed from CMOD using empirical equations developed by CANMET-MTL. These methods compensated for the unavailability of contour integral evaluation in the XFEM propagating crack analysis.

8. The effect of crack-tip simulation using either notch or planar crack was remarkable in both X52 full-scale models and X100 SENT models utilizing the variable strain damage initiation criterion dependent of crack-tip constraint, but smaller in models utilizing the fixed strain damage initiation criterion independent of crack-tip constraints.

9. The parameters involved in defining the fracture locus of the novel damage model include a strain-hardening parameter n and four dimensionless fracture parameters c_1, c_2, c_3, c_4. c_1 is a coefficient relating the fracture strain to the hydrostatic pressure and Lode angle, with the range of $c_1 \geq 0$. c_2 is a coefficient only affecting the magnitude of the fracture locus without changing its shape, and it has the range of $c_2 > 0$. c_3 is a coefficient relating the fracture strain to Lode angle in loading condition $-1 < \bar{\theta} < 1$, but has no impact on fracture strain at $\bar{\theta}$ = -1 (axisymmetric compression or equi-biaxial tension) and $\bar{\theta}$ = 1 (axisymmetric tension or equi-biaxial compression). c_4 is another coefficient relating the fracture strain to Lode angle in loading condition $\bar{\theta} <$ 0, but has no impact on fracture strain at $\bar{\theta} \geq 0$. Note that c_1= 0 corresponds to a

maximum shear stress fracture criterion, $c_3 = c_4 = 1$ correspond to a von Mises yield condition, and $c_3 = \sqrt{3}/2$ and $c_4 = 1$ correspond to a Tresca yield condition. My work and literature study improve the applicable range of fracture parameters for pipeline steel grade between X52 and X100: $0.03 \leq c_1 \leq 0.12$, $1.66 \leq c_2 \leq 1.9$ (average value of $c_2 = 1.85$), $c_3 = 0.9$ and $c_4 = 1$. To use this novel damage model for various pipe material, n should be calibrated from curve fitting of a power law stress-strain relationship of specific pipeline, c_1 should be calibrated from fracture tests cut from specific pipeline, $c_2 = 1.85$, $c_3 = 0.9$ and $c_4 = 1$ may be simply adopted.

10. The novel damage model developed in this research was carried out in the commercial finite element software ABAQUS but not restricted to this software. The model is applicable to any other finite element analysis software that supports the XFEM framework.

11. My doctoral thesis is the first to implement a ductile fracture criterion (i.e., strain-based MMC fracture criterion) of uncracked specimens into full-scale and small-scale cracked specimens.

6.3 Contributions

This doctoral thesis contributed to both engineering and academic aspects. From the engineering or pipeline industry viewpoints, this work provides a novel XFEM variable strain-based damage model dependent on crack-tip constraint to predict the fracture in both small- and full-scale pipeline fracture tests. The model is expected to be widely applicable to a given pipeline material under any testing configuration, independent of specimen geometry, pre-cracking size, and loading conditions. This would significantly benefit current crack assessment methods for pipeline integrity. Although this novel damage model was validated

for predominated fracture mode I, it is not restricted to this fracture mode. This model is applicable to other fracture modes and mixed fracture mode. From the academic or scientific viewpoints, this work is the first to couple XFEM with strain-based modified Mohr-Coulomb fracture criterion developed from uncracked specimens into full-scale and small-scale models of cracked specimens and validated from experiments. This work was successful in its attempts to unify the classical fracture mechanics assuming a pre-existing crack and damage mechanics of uncracked bodies to form a unified theory in predicting fracture. In the unified theory, there is no need to define the critical fracture toughness parameters in predicting the crack propagation.

6.4 Recommendations

Future work may focus on updating the variable strain-based damage model, such as reducing the variables to only predominated c_1 and n and replacing the plasticity parameter n with a different variable independent of the power law. Further research direction may also include exhaustively exploring the damage initiation criterion to account for strain rate and temperature and the damage evolution criterion to consider mixed mode fracture. It would also be advantageous to control both damage initiation and evolution criteria for predicting the fracture of pipeline steel. The updated advanced XFEM damage model would be validated on various fracture tests covering wide range of crack-tip constraint, such as the small-scale SENT, SENB and CT tests, the medium-scale CWP tests, and full-scale tests on either circumferentially or longitudinally cracked pipe. In addition, the model may be extended to hybrid defects such as the dent-crack defect and crack-in-corrosion defect. Future work may attempt to provide specific critical values of CTOD to facilitate the field fracture control plan in the pipeline industry. Further extensive calibration work specific to each of various pipeline grades would make significant contribution in current crack assessment methods in pipeline industry. The

unified theory in combining the fracture mechanics and damage mechanics would be explored further.

References

[1] M. Lin, S. Agbo, D.-M. Duan, J.J.R. Cheng, S. Adeeb, Simulation of crack propagation in API 5L X52 pressurized pipes using XFEM-based cohesive segment approach, Journal of Pipeline Systems Engineering and Practice. 11 (2020) 04020009. https://doi.org/10.1061/(asce)ps.1949-1204.0000444.

[2] M. Lin, Y. Li, M. Salem, J.J.R. Cheng, S. Adeeb, M. Kainat, A parametric study of variable crack initiation criterion in XFEM on pipeline steel, in: Pressure Vessels and Piping Conference Volume 6: Materials and Fabrication, American Society of Mechanical Engineers (ASME), Virtual, Online, 2020. https://doi.org/10.1115/PVP2020-21664.

[3] M. Lin, Y. Li, J.J.R. Cheng, S. Koduru, M. Kainat, A. Samer, Novel XFEM variable strain damage criterion for predicting tensile strain capacity of API X52 (under review), in: Technology for Future and Ageing Pipelines, Gent, Belgium, 2021.

[4] American Petroleum Institute, API SPEC 5L Line Pipe, 46th ed., Washington, DC, USA, 2018.

[5] J.F. Kiefner, C.J. Trench, Oil pipeline characteristics and risk factors: Illustrations from the decade of construction, American Petroleum Institute, 2001.

[6] L.J. Smart, Review of materials property data for nondestructive characterization of pipeline materials [MSc thesis], Iowa State University, 2015.

[7] B. Vyvial, Crack management in vintage pipelines, (2021) 1–7. https://www.stress.com/crack-management-in-vintage-pipelines/.

[8] J.F. Kiefner, M.J. Rosenfeld, The role of pipeline age in pipeline safety, INGAA Foundation Final Report No.2012.04, 2012.

[9] H. Ghaednia, S. Das, R. Wang, R. Kania, Dependence of burst strength on crack length of a pipe with a dent-crack defect, Journal of Pipeline Systems Engineering and Practice.

8 (2017). https://doi.org/10.1061/(asce)ps.1949-1204.0000259.

[10] J.F. Kiefner, W.A. Maxey, R.J. Eiber, A.R. Duffy, Failure stress levels of flaws in pressurized cylinders, in: progress in flaw growth and fracture toughness testing, in: Progress in Flaw Growth and Fracture Toughness Testing, STP536, ASTM International, West Conshohocken, PA, 1973: pp. 461–481. https://doi.org/10.1520/STP49657S.

[11] C.E. Jaske, J.A. Beavers, B.A. Harle, Effect of stress corrosion cracking on integrity and remaining life of natural gas pipelines, in: National Association of Corrosion Engineers (NACE) Annual Corrosion Conference and Exposition, NACE International, Houston, Texas, 1996.

[12] I. Milne, R. Ainsworth, A. Dowling, A. Stewart, Assessment of the integrity of structures containing defects, International Journal of Pressure Vessels and Piping. 32 (1988) 3–104. https://doi.org/10.1016/0308-0161(88)90071-3.

[13] EDF Energy Nuclear Generation Limited, Assessment of the integrity of structure containing defects, EDF Energy Nuclear Generation Limited Report R6, Revision 4, Gloucester, UK, 2011.

[14] British Standard Institution, BS 7910:2013 Guide to methods for assessing the acceptability of flaws in metallic structures, BSI Standards Limited 2015, London, UK, 2013.

[15] American Petroleum Institute, API 579-1/ASME FFS-1 Fitness-For-Service, American Petroleum Institute/American Society of Mechanical Engineers, New York, USA, 2016.

[16] Canadian Standards Association, CAN/CSA Z662-11 Oil and gas pipeline systems, 6th ed., CSA Group, Ottawa, ON, Canada, 2011.

[17] Canadian Standards Association, CAN/CSA-Z662-15 Oil and gas pipeline systems, 7th ed., CSA Group, Ottawa, ON, Canada, 2015.

[18] Y.Y. Wang, M. Liu, X. Long, M. Stephens, R. Petersen, R. Gordon, Validation and

documentation of tensile strain limit design models for pipelines (PR-ABD-1-Project 1 report), Pipeline Research Council International. Inc., 2011.

[19] Y.Y. Wang, M. Liu, Y. Song, Second generation models for strain-based design (Contract PR-ABD-1-Project 2 report), Pipeline Research Council International. Inc., 2011.

[20] Y.Y. Wang, M. Liu, F. Zhang, D. Horsley, S. Nanney, Multi-tier tensile strain models for strain-based design: Part 1 — Fundamental basis, in: Proceedings of the 2012 9th International Pipeline Conference. Volume 4: Pipelining in Northern and Offshore Environments; Strain-Based Design; Risk and Reliability; Standards and Regulations, Calgary, Alberta, Canada, 2012: pp. 447–458. https://doi.org/10.1115/IPC2012-90690.

[21] M. Liu, Y.-Y. Wang, Y. Song, D. Horsley, S. Nanney, Multi-tier tensile strain models for strain-based design: Part 2 — Development and formulation of tensile strain capacity models, in: Volume 4: Pipelining in Northern and Offshore Environments; Strain-Based Design; Risk and Reliability; Standards and Regulations, American Society of Mechanical Engineers, Calgary, Alberta, Canada, 2012: pp. 415–425. https://doi.org/10.1115/IPC2012-90659.

[22] M. Liu, Y. Wang, D. Horsley, S. Nanney, Multi-tier tensile strain models for strain-based design: Part 3 — Model evaluation against experimental data, in: Proceedings of the 2012 9th International Pipeline Conference. Volume 4: Pipelining in Northern and Offshore Environments; Strain-Based Design; Risk and Reliability; Standards and Regulations, American Society of Mechanical Engineers, Calgary, Alberta, Canada, 2012: pp. 427–438. https://doi.org/10.1115/IPC2012-90660.

[23] Y. Wang, M. Liu, Y. Song, D. Horsley, Tensile strain models for strain-based design of pipelines, in: Proceedings of the ASME 2012 31st International Conference on Ocean, Offshore and Arctic Engineering. Volume 6: Materials Technology; Polar and Arctic Sciences and Technology; Petroleum Technology Symposium, American Society of

Mechanical Engineers, 2012: pp. 353–363. https://doi.org/10.1115/OMAE2012-84241.

[24] Y. Wang, F. Zhang, M. Liu, W.-Y. Cho, D.-H. Seo, Tensile strain capacity of X80 and X100 welds, in: Proceedings of the ASME 2012 31st International Conference on Ocean, Offshore and Arctic Engineering. Volume 6: Materials Technology; Polar and Arctic Sciences and Technology; Petroleum Technology Symposium, American Society of Mechanical Engineers, Rio de Janeiro, Brazil, 2012: pp. 345–351. https://doi.org/10.1115/OMAE2012-84240.

[25] S. Kibey, X. Wang, K. Minnaar, M.L. Macia, D.P. Fairchild, W.C. Kan, S.J. Ford, B. Newbury, Tensile strain capacity equations for strain-based design of welded pipelines, in: Proceedings of the 2010 8th International Pipeline Conference. 2010 8th International Pipeline Conference, Volume 4, Calgary, Alberta, Canada, 2010: pp. 355–363. https://doi.org/10.1115/IPC2010-31661.

[26] D.P. Fairchild, S.A. Kibey, H. Tang, V.R. Krishnan, X. Wang, M.L. Macia, W. Cheng, Continued advancements regarding capacity prediction of strain-based pipelines, in: Proceedings of the 2012 9th International Pipeline Conference. Volume 4: Pipelining in Northern and Offshore Environments; Strain-Based Design; Risk and Reliability; Standards and Regulations, American Society of Mechanical Engineers, Calgary, Alberta, Canada, 2012: pp. 297–305. https://doi.org/10.1115/IPC2012-90471.

[27] H. Tang, D. Fairchild, M. Panico, J. Crapps, W. Cheng, Strain capacity prediction of strain-based pipelines, in: Proceedings of the 2014 10th International Pipeline Conference, ASME, Calgary, Alberta, Canada, 2014. https://doi.org/10.1115/IPC2014-33749.

[28] B. Wang, B. Liu, Y.-Y. Wang, O.J. Huising, Estimation of tensile strain capacity of vintage girth welds, in: Proceedings of the 2020 13th International Pipeline Conference. Volume 2: Pipeline Safety Management Systems; Project Management, Design,

Construction, and Environmental Issues; Strain Based Design; Risk and Reliability; Northern, Offshore, and Production, Virtual, Online, 2020: p. V002T06A008. https://doi.org/10.1115/IPC2020-9664.

[29] Pipeline and Hazardous Materials Safety Administration (PHMSA), Miles by decade of installation inventory reports, (2020). https://www.phmsa.dot.gov/data-and-statistics/pipeline-replacement/decade-inventory.

[30] Abaqus Documentation, Dassault Systèmes, 2019.

[31] A.R. Khoei, Extended finite element method: theory and applications, 2015. https://doi.org/10.1002/9781118869673.

[32] T. Belytschko, T. Black, Elastic crack growth in finite elements with minimal remeshing, International Journal for Numerical Methods in Engineering. 45 (1999) 601–620. https://doi.org/10.3760/cma.j.issn.0366-6999.2011.18.023.

[33] N. Moës, J. Dolbow, T. Belytschko, A finite element method for crack growth without remeshing, International Journal for Numerical Methods in Engineering. 46 (1999) 131–150. https://doi.org/10.1002/(SICI)1097-0207(19990910)46:1<131::AID-NME726>3.0.CO;2-J.

[34] J.M. Melenk, I. Babuška, The partition of unity finite element method: Basic theory and applications, Computer Methods in Applied Mechanics and Engineering. 139 (1996) 289–314. https://doi.org/10.1016/S0045-7825(96)01087-0.

[35] J. Song, P.M.A.. Areias, T. Belytschko, A method for dynamic crack and shear band propagation with phantom nodes, International Journal for Numerical Methods in Engineering. 67 (2006). https://doi.org/https://doi.org/10.1002/nme.1652.

[36] A. Hansbo, P. Hansbo, A finite element method for the simulation of strong and weak discontinuities in solid mechanics, Computer Methods in Applied Mechanics and Engineering. 193 (2004) 3523–3540. https://doi.org/10.1016/j.cma.2003.12.041.

[37] D. Abdulhameed, C. Cakiroglu, M. Lin, J.J.R. Cheng, J. Nychka, M. Sen, S. Adeeb, The effect of internal pressure on the tensile strain capacity of X52 pipelines with circumferential flaws, ASME Journal of Pressure Vessel Technology. 138 (2016) 061701. https://doi.org/10.1115/1.4033436.

[38] I. Ameli, B. Asgarian, M. Lin, S. Agbo, R. Cheng, D. Duan, S. Adeeb, Estimation of the CTOD-crack growth curves in SENT specimens using the eXtended finite element method, International Journal of Pressure Vessels and Piping. 169 (2019) 16–25. https://doi.org/10.1016/j.ijpvp.2018.11.008.

[39] S. Agbo, M. Lin, I. Ameli, A. Imanpour, D.M. Duan, J.J.R. Cheng, S. Adeeb, Evaluation of the effect of internal pressure and flaw size on the tensile strain capacity of X42 vintage pipeline using damage plasticity model in extended finite element method (XFEM), in: Proceedings of the . Volume 5: High-Pressure Technology; Rudy Scavuzzo Student Paper Symposium and 27th Annual Student Paper Competition; ASME Nondestructive Evaluation, Diagnosis and Prognosis Division (NDPD)., ASME, San Antonio, Texas, USA, 2019: pp. 1–9. https://doi.org/10.1115/PVP2019-94005.

[40] A. Okodi, M. Lin, N. Yoosef-ghodsi, M. Kainat, S. Hassanien, S. Adeeb, Crack propagation and burst pressure of longitudinally cracked pipelines using extended finite element method, International Journal of Pressure Vessels and Piping. 184 (2020). https://doi.org/10.1016/j.ijpvp.2020.104115.

[41] X. Zhang, M. Lin, A. Okodi, L. Tan, J.Y. Leung, S. Adeeb, Numerical analysis of API 5L X42 and X52 vintage pipes with cracks in corrosion defects using extended finite element method, Journal of Pressure Vessel Technology. 143 (2021) 061302. https://doi.org/https://doi.org/10.1115/1.4050988.

[42] M.M.. Shahzamanian, M. Lin, M. Kainat, N. Yousef-Ghodsi, S. Adeeb, Systematic literature review of the application of extended finite element method in failure

prediction of pipelines, Journal of Pipeline Science and Engineering. (2021). https://doi.org/10.1016/j.jpse.2021.02.003.

[43] Canadian Standards Association, CSA Z662:19 Oil and gas pipeline systems, 8th ed., CSA Group, Ottawa, ON, Canada, 2019.

[44] American Society of Mechanical Engineers, ASME B31.8S-2018 Managing system integrity of gas pipelines, American Society of Mechanical Engineers, New York, NY, USA, 2018.

[45] American Petroleum Institute, API RP 1176 Recommended practice for assessment and management of cracking in pipelines, 1st ed., American Petroleum Institute, Washington, DC, USA, 2016.

[46] American Petroleum Institute, API RP 1160 Managing system integrity for hazardous liquid pipelines, 3rd ed., American Petroleum Institute, Washington, DC, USA, 2019.

[47] P. Rajeev, J. Kodikara, D. Robert, P. Zeman, B. Rajani, Factors contributing to large daimeter water pipe failure, Water Asset Management International. 10 (2014) 9–14.

[48] P.W. McMullin, General principles of fatigue and fracture Part 1, Structure Magazine. (2016) 10–13.

[49] T.L. Anderson, Fracture mechanics foundamentals and applications, 3rd ed., Boca Raton, FL, USA, 2005.

[50] S. Adeeb, Introduction to solid mechanics and finite element analysis using Mathematica, Kendall Hunt, Dubuque, IA, USA, 2011.

[51] Y.H. Wang, G.Z. Wang, S.T. Tu, F.Z. Xuan, In-plane and out-of-plane constraint characterization of different constraint parameters for semi-elliptical surface cracks in pipes, Engineering Fracture Mechanics. 235 (2020) 107161. https://doi.org/10.1016/j.engfracmech.2020.107161.

[52] M. Mostafavi, D.J. Smith, M.J. Pavier, A micromechanical fracture criterion accounting

for in-plane and out-of-plane constraint, Computational Materials Science. 50 (2011) 2759–2770. https://doi.org/10.1016/j.commatsci.2011.04.023.

[53] J. Yang, G.Z. Wang, F.Z. Xuan, S.T. Tu, Unified characterisation of in-plane and out-of-plane constraint based on crack-tip equivalent plastic strain, Fatigue and Fracture of Engineering Materials and Structures. 36 (2013) 504–514. https://doi.org/10.1111/ffe.12019.

[54] ASTM International, ASTM E1820-20b Standard test method for measurement of fracture toughness, ASTM International, West Conshohocken, PA, USA, 2020. https://doi.org/10.1520/E1820-20B.

[55] ISO 12135, Metallic materials — Unified method of test for the determination of quasistatic fracture toughness, International Organization of Standardization, Vernier, Geneva, Switzerland, 2016.

[56] M. Chiesa, B. Nyhus, B. Skallerud, C. Thaulow, Efficient fracture assessment of pipelines. A constraint- corrected SENT specimen approach, Engineering Fracture Mechanics. 68 (2001) 527–547. https://doi.org/10.1016/S0013-7944(00)00129-6.

[57] J. Kang, J.A. Gianetto, W.R. Tyson, Recent development in low-constraint fracture toughness testing for structural integrity assessment of pipelines, Frontiers of Mechanical Engineering. 13 (2018) 546–553. https://doi.org/10.1007/s11465-018-0501-2.

[58] M.A. Verstraete, W. De Waele, K. Van Minnebruggen, S. Hertelé, Comparison of girth weld tearing resistance obtained from Curved Wide Plate and Single Edge Notch Tensile testing, ENGINEERING FRACTURE MECHANICS. 148 (2015) 406–420. https://doi.org/10.1016/j.engfracmech.2015.03.041.

[59] Y. Bai, Qiang; Bai, ed., 12 - Fatigue and Fracture, in: Subsea Pipeline Design, Analysis, and Installation, Gulf Professional Publishing, 2014: pp. 283–318.

https://doi.org/10.1016/B978-0-12-386888-6.00012-2.

[60] Z. Zhang, J. Xu, B. Nyhus, E. Østby, SENT (single edge notch tesion) methodology for pipeline applications, in: Proceedings of the 18th European Conference on Fracture, Dresden, Germany, 2010.

[61] X. Wang, S. Kibey, H. Tang, W. Cheng, K. Minnaar, M.L. Macia, W.C. Kan, S.J. Ford, B. Newbury, Strain-based design-advances in prediction methods of tensile strain capacity, International Journal of Offshore and Polar Engineering. 21 (2011) 1–7.

[62] DNV-RP-F108, Fracture control for pipeline installation methods introducing cyclic plastic strain, Det Norske Veritas, Høvik, Norway, 2006.

[63] G. Shen, J.A. Gianetto, W.R. Tyson, Measurement of J-R curves using single-specimen technique on clamped SE(T) specimens, in: Proceedings of the Nineteenth (2009) International Offshore and Polar Engineering Conference, ISOPE, Osaka, Japan, 2009: pp. 92–99.

[64] British Standards Institution, BS 8571:2014 Method of test for determination of fracture toughness in metallic materials using single edge notched tension (SENT) specimens, BSI Standards Limited, 2014.

[65] W. Zhang, Y. Cai, Continuum damage mechanics and numerical applications, Springer-Verlag Berlin Heidelberg, 2010. https://doi.org/10.1007/978-3-642-04708-4.

[66] A.L. Gurson, Continuum theory of ductile rupture by void nucleation and growth: Part 1 — yield criteria and flow rules for porous ductile media, ASME Journal of Engineering Materials and Technology. 99 (1977) 2–15. https://doi.org/10.1115/1.3443401.

[67] V. Tvergaard, On localization in ductile materials containing spherical voids, International Journal of Fracture. 18 (1982) 237–252. https://doi.org/10.1007/BF00015686.

[68] V. Tvergaard, A. Needleman, Analysis of the cup-cone fracture in a round tensile bar,

Acta Metallurgica. 32 (1984) 157–169. https://doi.org/10.1016/0001-6160(84)90213-X.

[69] K. Nahshon, J.W. Hutchinson, Modification of the Gurson model for shear failure, 27 (2008) 1–17. https://doi.org/10.1016/j.euromechsol.2007.08.002.

[70] K.L. Nielsen, V. Tvergaard, Failure by void coalescence in metallic materials containing primary and secondary voids subject to intense shearing, International Journal of Solids and Structures. 48 (2011) 1255–1267. https://doi.org/10.1016/j.ijsolstr.2011.01.008.

[71] J. Jackiewicz, Use of a modified Gurson model approach for the simulation of ductile fracture by growth and coalescence of microvoids under low, medium and high stress triaxiality loadings, Engineering Fracture Mechanics. 78 (2011) 487–502. https://doi.org/10.1016/j.engfracmech.2010.03.027.

[72] K. Kofiani, A. Nonn, T. Wierzbicki, C. Kalwa, C. Walters, Experiments and fracture modeling of high-strength pipelines for high and low stress triaxialities, in: Proceedings of the International Offshore and Polar Engineering Conference, International Society of Offshore and Polar Engineers (ISOPE), Rhodes, Greece, 2012: pp. 511–518.

[73] K. Kofiani, A. Nonn, T. Wierzbicki, New calibration method for high and low triaxiality and validation on SENT specimens of API X70, International Journal of Pressure Vessels and Piping. 111–112 (2013) 187–201. https://doi.org/10.1016/j.ijpvp.2013.07.004.

[74] Y. Bai, T. Wierzbicki, A new model of metal plasticity and fracture with pressure and Lode dependence, International Journal of Plasticity. 24 (2008) 1071–1096. https://doi.org/10.1016/j.ijplas.2007.09.004.

[75] Y. Bai, T. Wierzbicki, Application of extended Mohr – Coulomb criterion to ductile fracture, International Journal of Fracture. 161 (2010) 1–20. https://doi.org/10.1007/s10704-009-9422-8.

[76] M. Paredes, J. Lian, T. Wierzbicki, M.E. Cristea, S. Münstermann, P. Darcis, Modeling of plasticity and fracture behavior of X65 steels: seam weld and seamless pipes,

International Journal of Fracture. 213 (2018) 17–36. https://doi.org/10.1007/s10704-018-0303-x.

[77] N. Mohajer Rahbari, M. Xia, X. Liu, J.J. Roger Cheng, S. Adeeb, Experimental and numerical investigation on ductile fracture of steel pipelines, Journal of Pressure Vessel Technology. 142 (2020). https://doi.org/10.1115/1.4045449.

[78] S.E. Benzley, Representation of singularities with isoparametric finite elements, International Journal for Numerical Methods in Engineering. 8 (1974) 537–545. https://doi.org/10.1002/nme.1620080310.

[79] N. Sukumar, N. Moës, B. Moran, T. Belytschko, Extended finite element method for three-dimensional crack modelling, International Journal for Numerical Methods in Engineering. 48 (2000) 1549–1570. https://doi.org/10.1002/1097-0207(20000820)48:11<1549::AID-NME955>3.0.CO;2-A.

[80] P.M.A. Areias, T. Belytschko, Non-linear analysis of shells with arbitrary evolving cracks using XFEM, International Journal for Numerical Methods in Engineering. 62 (2005) 384–415. https://doi.org/10.1111/1365-2435.12153.

[81] P.M.A. Areias, J.H. Song, T. Belytschko, Analysis of fracture in thin shells by overlapping paired elements, Computer Methods in Applied Mechanics and Engineering. 195 (2006) 5343–5360. https://doi.org/10.1016/j.cma.2005.10.024.

[82] L. Gigliotti, Assessment of the applicability of XFEM in Abaqus for modeling crack growth in rubber [MSc thesis], Royal Institute of Technology, 2012.

[83] G.I. Barenblatt, The formation of equilibrium cracks during brittle fracture. General ideas and hypotheses. Axially-symmetric cracks, Journal of Applied Mathematics and Mechanics. 23 (1959) 434–444. https://doi.org/10.1016/0021-8928(59)90157-1.

[84] G.I. Barenblatt, The mathematical theory of equilibrium cracks in brittle fracture, Advances in Applied Mechanics. 7 (1962) 55–129. https://doi.org/10.1016/S0065-

2156(08)70121-2.

[85] D.S. Dugdale, Yielding of steel sheets containing slits, Journal of the Mechanics and Physics of Solids. 8 (1960) 100–104. https://doi.org/10.1016/0022-5096(60)90013-2.

[86] A. Hillerborg, M. Modéer, P.-E. Petersson, Analysis of crack formation and crack growth in concrete by means of fracture mechanics and finite elements, Cement and Concrete Research. 6 (1976) 773–781. https://doi.org/10.1016/0008-8846(76)90007-7.

[87] G.N. Wells, L.J. Sluys, A new method for modelling cohesive cracks using finite elements, International Journal for Numerical Methods in Engineering. 50 (2001) 2667–2682. https://doi.org/10.1002/nme.143.

[88] E.M. Wu, R.C. Reuter Jr., Crack extension in fiberglass reinforced plastics. T. & A.M Report No.275, 1965.

[89] M.L. Benzeggagh, M. Kenane, Measurement of mixed-mode delamination fracture toughness of unidirectional glass/epoxy composites with mixed-mode bending apparatus, Composite Science and Technology. 56 (1996) 439–449.

[90] J. Billingham, J.V. Sharp, J. Spurrier, P.J. Kilgallon, Review of the performance of high strength steels used offshore, HSE Research Report 105, United Kingdom, 2003.

[91] E. Wang, W. Zhou, G. Shen, D. Duan, An experimental study on J(CTOD)-R curves of single edge tension specimens for X80 steel, Proceedings of the Biennial International Pipeline Conference, IPC. 4 (2012) 241–248. https://doi.org/10.1115/IPC2012-90323.

[92] G. Shen, R. Bouchard, J.A. Gianetto, W.R. Tyson, Fracture toughness evaluation of high strength steel pipe, in: Proceedings of PVP2008 ASME Pressure Vessel and Piping Division Conference. Volume 6: Materials and Fabrication, Parts A and B., ASME, Chicago, Illinois, USA, 2008: pp. 1275–1282. https://doi.org/https://doi.org/10.1115/PVP2008-61100.

[93] A. Needleman, A continuum model for void nucleation by inclusion debonding, ASME

Journal of Applied Mechanics. 54 (1987) 525–531. https://doi.org/10.1115/1.3173064.

[94] V. Tvergaard, J.W. Hutchinson, The relation between crack growth resistance and fracture process parameters in elastic-plastic solids, Journal of the Mechanics and Physics of Solids. 40 (1992) 1377–1397. https://doi.org/10.1016/0022-5096(92)90020-3.

[95] H. Jiang, Cohesive zone model for carbon nanotube adhesive simulation and fracture/fatigue crack growth [PhD thesis], University of Akron, Akron, OH, USA, 2010.

[96] Z.-H. Jin, C.T. Sun, A comparison of cohesive zone modeling and classical fracture mechanics based on near tip stress field, International Journal of Solids and Structures. 43 (2006) 1047–1060. https://doi.org/10.1016/j.ijsolstr.2005.06.074.

[97] Y. Zeng, Feasibility study of cohesive zone model on crack propagation in pipeline steel under monotonic and fatigue loading [MSc thesis], Delft University of Technology, Delft, Netherlands, 2015.

[98] K.-H. Schwalbe, I. Scheider, A. Cornec, Guidelines for applying cohesive models to the damage behaviour of engineering materials and structures, Springer, 2013. https://doi.org/10.1007/978-3-642-29494-5.

[99] I. Scheider, W. Brocks, The effect of the traction separation law on the results of cohesive zone crack propagation analyses, Key Engineering Materials. 251–252 (2003) 313–318. https://doi.org/10.4028/www.scientific.net/KEM.251-252.313.

[100] I. Scheider, Simulation of cup-cone fracture in round bars using the cohesive zone model, in: Computational Fluid and Solid Mechanics, Elsevier, 2001: pp. 460–462. https://doi.org/10.1016/B978-008043944-0/50681-8.

[101] J. Dolbow, An extended finite element method with discontinuous enrichment for applied mechanics [PhD Thesis], Northwestern University, USA, 1999.

[102] D. Shim, M. Uddin, F. Brust, G. Wilkowski, Cohesive zone modeling of ductile crack

growth in circumferential through-wall cracked pipe tests, in: Proceedings of the ASME 2011 Pressure Vessels and Piping Conference. Volume 3: Design and Analysis, ASME, Baltimore, Maryland, USA, 2011: pp. 685–690. https://doi.org/https://doi.org/10.1115/PVP2011-57947.

[103] A. Nonn, C. Kalwa, Simulation of ductile crack propagation in high-strength pipeline steel using damage models, in: Proceedings of the 2012 9th International Pipeline Conference. Volume 3: Materials and Joining, ASME, Calgary, Alberta, Canada, 2012: pp. 597–603. https://doi.org/10.1115/IPC2012-90653.

[104] A. Nonn, C. Kalwa, Analysis of dynamic ductile fracture propagation in pipeline steels: a damage-mechanics' approach, in: Proceedings of the 6th International Pipeline Technology Conference, Ostend, Belgium, 2013. https://doi.org/10.13140/2.1.4370.3046.

[105] I. Scheider, A. Nonn, A. Völling, A. Mondry, C. Kalwa, A damage mechanics based evaluation of dynamic fracture resistance in gas pipelines, Procedia Materials Science. 3 (2014) 1956–1964. https://doi.org/10.1016/j.mspro.2014.06.315.

[106] P.F. Liu, B.J. Zhang, J.Y. Zheng, Finite element analysis of plastic collapse and crack behavior of steel pressure vessels and piping using XFEM, Journal of Failure Analysis and Prevention. 12 (2012) 707–718. https://doi.org/10.1007/s11668-012-9623-8.

[107] Y.M. Zhang, M. Fan, Z.M. Xiao, W.G. Zhang, Fatigue analysis on offshore pipelines with embedded cracks, Ocean Engineering. 117 (2016) 45–56. https://doi.org/10.1016/j.oceaneng.2016.03.038.

[108] R. Hojjati-Talemi, Numerical simulation of dynamic brittle fracture of pipeline steel subjected to DWTT using XFEM-based cohesive segment technique, Frattura Ed Integritá Strutturale (Fracture and Structural Integrity). 36 (2016) 151–159. https://doi.org/10.3221/IGF-ESIS.36.15.

[109] R. Hojjati-Talemi, S. Cooreman, D. Van Hoecke, Finite element simulation of dynamic brittle fracture in pipeline steel: A XFEM-based cohesive zone approach, Proceedings of the Institution of Mechanical Engineers, Part L: Journal of Materials: Design and Applications. 0 (2016) 1–14. https://doi.org/10.1177/1464420715627379.

[110] J.M. Barsom, S.T. Rolfe, Correlations between KIc and Charpy V-notch test results in the transition-temperature range, in: Impact Testing of Metals, ASTM International, West Conshohocken, PA, 1970: pp. 281–302. https://doi.org/10.1520/STP32067S.

[111] M. Lin, Characterization of tensile and fracture properties of X52 steel pipes and their girth weld [MSc thesis], University of Alberta, 2015. https://doi.org/10.7939/R3X05XM68.

[112] B. Ken, Tensile testing, 2nd ed., ASM International, Materials Park, OH, USA, 2004.

[113] M. Lin, S. Agbo, J.J. Roger Cheng, N. Yoosef-Ghodsi, S. Adeeb, Application of the extended finite element method (XFEM) to simulate crack propagation in pressurized steel pipes, in: American Society of Mechanical Engineers, Pressure Vessels and Piping Division (Publication) PVP, 2017. https://doi.org/10.1115/PVP2017-65575.

[114] S. Agbo, M. Lin, A. Arman, J.J.R. Cheng, S. Adeeb, Prediction of burst load in pressurized pipelines using extended finite element method (XFEM), in: CSCE 6th International Conference on Engineering Mechanics and Materials, CSCE, Vancouver, Canada, 2017.

[115] A. Cornec, I. Scheider, K.H. Schwalbe, On the practical application of the cohesive model, Engineering Fracture Mechanics. 70 (2003) 1963–1987. https://doi.org/10.1016/S0013-7944(03)00134-6.

[116] M. Anvari, I. Scheider, C. Thaulow, Simulation of dynamic ductile crack growth using strain-rate and triaxiality-dependent cohesive elements, Engineering Fracture Mechanics. 73 (2006) 2210–2228. https://doi.org/10.1016/j.engfracmech.2006.03.016.

[117] T. Siegmund, W. Brocks, A numerical study on the correlation between the work of separation and the dissipation rate in ductile fracture, Engineering Fracture Mechanics. 67 (2000) 139–154. https://doi.org/10.1016/S0013-7944(00)00054-0.

[118] I. Scheider, Derivation of separation laws for cohesive models in the course of ductile fracture, Engineering Fracture Mechanics. 76 (2009) 1450–1459. https://doi.org/10.1016/j.engfracmech.2008.12.006.

[119] A. Carpinteri, Softening and snap-back instability in cohesive solids, International Journal for Numerical Methods in Engineering. 28 (1989) 1521–1537. https://doi.org/10.1002/nme.1620280705.

[120] A. Carpinteri, G. Colombo, Numerical analysis of catastrophic softening behaviour (snap-back instability), Computers and Structures. 31 (1989) 607–636. https://doi.org/10.1016/0045-7949(89)90337-4.

[121] N. Moës, T. Belytschko, Extended finite element method for cohesive crack growth, Engineering Fracture Mechanics. 69 (2002) 813–833. https://doi.org/10.1016/S0013-7944(01)00128-X.

[122] S. Mojiri, Numerical analysis of cohesive crack growth using extended finite element method (X-FEM) [Msc Thesis], Numerical analysis of cohesive crack growth using extended finite element method (X-FEM)., 2010.

[123] F. Oliveira, Crack modelling with the extended finite element method [MSc thesis], Instituto Superior Técnico, Lisboa, Portugal, 2013.

[124] D. Park, W.R. Tyson, J.A. Gianetto, R.S. Eagleson, Fracture toughness of X100 pipe girth welds using SE(T) and SE(B) test, in: Proceedings of the 2012 9th International Pipeline Conference, ASME, Clagary, Alberta, Canada, 2012: pp. 221–231. https://doi.org/doi.org/10.1115/IPC2012-90289.

[125] J. Kang, G. Shen, J. Liang, J. Gianetto, Influence of constraint on J-resistance curves for

an X100 pipe steel, Procedia Materials Science. 3 (2014) 239–244. https://doi.org/10.1016/j.mspro.2014.06.042.

[126] J. Kang, G. Shen, J. Liang, K. Brophy, A. Mendonca, J. Gianetto, Evaluation of fracture toughness test methods for linepipe steels, Application of Automation Technology in Fatigue and Fracture Testing and Analysis. (2014) 101–115. https://doi.org/10.1520/stp157120130074.

[127] T.S. Weeks, D.T. Read, Comparison of J-integral from single specimen SE (T) tests on API-5L X100 line pipe steel, in: Proceedings of the 25th International Offshore (Ocean) and Polar Engineering Conference, 2015.

[128] N. Elyasi, M. Shahzamanian, M. Lin, L. Westover, Y. Li, M. Kainat, N. Yoosef-Ghodsi, S. Adeeb, Prediction of tensile strain capacity for X52 steel pipeline materials using the Extended Finite Element Method, Applied Mechanics. 2 (2021) 209–225. https://doi.org/10.3390/applmech2020013.

Appendix A - Variable Strain Damage Initiation Criterion Code

This appendix includes the user-defined Fortran code (.for) in defining the variable strain damage initiation criterion modified from Mohr-Coulomb fracture criterion which is programmed in Abaqus user subroutine-UDMGINI. The sentence beginning with Letter "C" are comments for explaining the codes. [128]

```
C USER SUBROUTINE UDMGINI

C FINDEX(NFINDEX)- A VECTOR DEFINING INDICES FOR ALL FAILURE MECHANISMS (NUMBERS
OF INDICES FOR ALL FAILURE MECHANISMS)
C FNORMAL(NDI,NFINDEX)-AN ARRAY DEFINING NORMAL DIRECTION TO FRACTURE PLANE FOR
EACH FAILURE MECHANISM (NUMBER OF DIRECT COMPONENTS, NUMBERS OF INDICES FOR ALL
FAILURE MECHANISMS)

      SUBROUTINE UDMGINI(FINDEX,NFINDEX,FNORMAL,NDI,NSHR,NTENS,PROPS,
     1 NPROPS,STATEV,NSTATEV,STRESS,STRAIN,STRAINEE,LXFEM,TIME,
     2 DTIME,TEMP,DTEMP,PREDEF,DPRED,NFIELD,COORDS,NOEL,NPT,
     3 KLAYER,KSPT,KSTEP,INC,KDIRCYC,KCYCLELCF,TIMECYC,SSE,SPD,
     4 SCD,SVD,SMD,JMAC,JMATYP,MATLAYO,LACCFLA,CELENT,DROT,ORI)

      INCLUDE 'ABA_PARAM.INC'

      PARAMETER(ZERO=0.0d0,ONE=1.0d0,PI=3.1415926535897932d0)

      DIMENSION FINDEX(NFINDEX),FNORMAL(NDI,NFINDEX),COORDS(*),
     1 STRESS(NTENS),STRAIN(NTENS),STRAINEE(NTENS),PROPS(NPROPS),
     2 STATEV(NSTATEV),PREDEF(NFIELD),DPRED(NFIELD),TIME(2),
     3 JMAC(*),JMATYP(*),DROR(3,3),ORI(3,3)

C USING CODING TO DEFINE FINDEX AND FNORMAL

C TO SPECIFIES THE VARIABLES RETURNED FROM UTILITY ROUTINE GETVRM
C ARRAY/JARRAY-REAL/INTEGER ARRAY CONTAINING INDIVIDUAL COMPONENTS OF OUTPUT
VARIABLE;FLGRAY-CHARACTER ARRAY CONTAINING FLAGS CORRESPONDING TO INDIVIDUAL
COMPONENTS. FLAG WILL CONTAIN EITHER YES, NO, OR N/A
      DIMENSION ARRAY(15), JARRAY(15)
      CHARACTER*3 FLGRAY(15)
C TO SPECIFY THE VARIABLES TO BE DOUBLE PRECISION 8-BYTE REAL NUMBERS WHICH HAS 15
DIGITS OF ACCURACY AND A MAGNITUDE RANGE OF 10 FROM -308 TO +308
      REAL*8 EPMAX,MISES,PRESS,INV3,TRIAX,XI,THETA,NTHETA,EPF1,EPF2,PI
C TO SPECIFY THE NUMBER OF DIMENSIONS FOR AN ARRAY, INCLUDING THE NUMBER OF
ELEMENTS IN EACH DIMENSION
C SP(I) AND EP(I), I=1,2,3-THREE PRINCIPAL STRESS AND STRAIN VALUES; AS(3,3) AND
AE(3,3)-TWO DIMENSIONAL STRESS AND STRAIN ARRAYS OF 3*3=9 REAL NUMBERS; REALV(*)-
ARRAY OF REAL VARIABLES TO BE OUTPUT
      DIMENSION EP(3), AE(3,3), SP(3), AS(3,3), REALV(17)
      EP(1)=0.0
      EP(2)=0.0
      EP(3)=0.0
      SP(1)=0.0
```

```
      SP(2)=0.0
      SP(3)=0.0

C MAXIMUM PRINCIPAL STRAIN CRITERION
C CALL SPRIND(S,PS,AN,LSRT,NDI,NSHR)-CALCULATE PRINCIPAL STRAIN VALUES AND
DIRECTIONS; S-STRESS OR STRAIN TENSOR; PS(I),I=1,2,3-THREE PRINCIPAL VALUES;
LSRT=1 INDICATES S CONTAINS STRESSES WHILE LSRT=2 INDICATES S CONTAINS STRAINS;
NDI-NUMBER OF DIRECT COMPONENTS; NSHR-NUMBER OF SHEAR COMPONENTS
      CALL SPRIND(STRAIN,EP,AE,2,NDI,NSHR)
C TO DETERMINE THE MAXIMUM PRINCIPAL STRAIN VALUE (EPMAX) BY COMPARING EP1,EP2,EP3
C ASSUME EPMAX=EP1
      KMAX=1
      EPMAX = EP(KMAX)
C IF EP2>EPMAX, THEN EPMAX=EP2; NDI=3
      DO K1 = 2, NDI
         IF(EP(K1).GT.EPMAX) THEN
            EPMAX = EP(K1)
            KMAX = K1
         END IF
      END DO

C CALL GETVRM('VAR',ARRAY,JARRAY,FLGRAY,JRCD,JMAC,JMATYP,MATLAYO,LACCFLA)-UTILITY
ROUTINE GETVRM CAN BE CALLED FROM UDMGINI TO ACCESS MATERIAL INTEGRATION POINT
INFORMATION
C VAR-OUTPUT VARIABLE KEY; ARRAY/JARRAY-REAL/INTEGER ARRAY CONTAINING INDIVIDUAL
COMPONENTS OF OUTPUT VARIABLE;FLGRAY-CHRACTER ARRAY CONTANING FLAGS CORRESPONDING
TO INDIVIDUAL COMPONENTS (FLAG WILL CONTAIN EITHER YES, NOT, OR N/A);JRCD-RETURN
CODE (0-NO ERROR, 1-OUTPUT REQUEST ERROR OR ALL COMPONENTS OF OUTPUT REQUEST ARE
ZERO);JMAC, JMATYP,MATLAYO,LACCFLA-VARIABLES THAT MUST BE PASSED INTO GETVRM
UTILITY ROUTINE
C IF IDENTIFIED SINV IS SPECIFIED, ARRAY WILL BE RETURNED WITH STRESS INVARIANT
COMPONENTS (MISES,TRESC,PRESS,INV3)
      CALL GETVRM('SINV',ARRAY,JARRAY,FLGRAY,JRCD,JMAC,JMATYP,MATLAYO,
     $     LACCFLA)
C OUTPUT MISES STRESS, PRESSURE STRESS
      MISES=ARRAY(1)
      PRESS=ARRAY(3)
      INV3=ARRAY(4)
C CALCULATE NOMINALIZED THIRD INVARIANT (XI)LODE ANGLE(THETA),
      XI=(INV3/MISES)**3.0
      THETA=ACOS(XI)/3
C CALCULATE STRESS TRIAXIALITY AND NORMALIZED LODE ANGLE (NTHETA)
      TRIAX=-PRESS/MISES
      NTHETA=1.0-2.0/PI*ACOS(XI)

C IF IDENTIFIED PE IS SPECIFIED, ARRAY WILL BE RETURNED WITH PLASTIC STRAIN
COMPONENTS (PE11, PE22, PE33, PE12, PE13, PE23, PEEQ, PEMAG)
C JARRAY WILL BE 0. FLGRAY ARRAY WILL HAVE N/A FOR FIRST SIX COMPONENTS, EITHER
YES OR NO IN THE SEVENTH COMPONENT (PEEQ) INDICATING WHETHER THE MATERIAL IS
CURRENTLY YIELDING, AND N/A IN THE EIGHT COMPONENTS (PEMAG).
      CALL GETVRM('PE',ARRAY,JARRAY,FLGRAY,JRCD,JMAC,JMATYP,MATLAYO,
     $     LACCFLA)
C OUTPUT EQUIVALENT PLASTIC STRAIN PEEQ
      PEEQ=ARRAY(7)

C A FAILURE MECHANISM IS COMBINED FROM A DAMAGE INITIATION CRITERION AND A
CORRESPONDING DAMAGE EVOLUTION LAW; DAMAGE IS ASSUMED TO INITIATE WHEN
1.0<=FINDEX(1)<=1.0+TOLERANCE, DEFAULT TOLERANCE=0.05.
C VARIABLE STRAIN CRITERION
```

```
C EPF-PREDEFINED MAXIMUM ALLOWABLE PRINCIPAL STRAIN VALUE (FRACTURE STRAIN) AS A
FUNCTION OF STRESS TRIAXIALITY AND LOAD ANGLE, DERIVED FROM MODIFIED MOHR-COULOMB
FRACTURE CRITERION)
C C1,C2,C3,C4 ARE MODIFIED MOHR-COULOMB FRACTURE CRITERION CONSTANTS
C A AND N ARE STRENGTH COEFFICIENT AND STRAIN HARDENING EXPONENT USED IN
CALCULATIONS FOR STRESS-STRAIN BEHAVIOUR IN WORK HARDENING
C PROPS(1)=C1,PROPS(2)=A/C2,PROPS(3)=C3,PROPS(4)=C4, PROPS(5)=N
      EPF1=(PROPS(2)*(PROPS(3)+SQRT(3.0)/(2.0-SQRT(3.0))*
     $ (1.0-PROPS(3))*(1.0/COS(NTHETA*PI/6.0)-1.0))*
     $ (SQRT((1.0+PROPS(1)**2.0)/3.0)*COS(NTHETA*PI/6.0)+PROPS(1)*
     $ (TRIAX+1.0/3.0*SIN(NTHETA*PI/6.0))))**(-1.0/PROPS(5))

      EPF2=(PROPS(2)*(PROPS(3)+SQRT(3.0)/(2.0-SQRT(3.0))*
     $ (PROPS(4)-PROPS(3))*(1.0/COS(NTHETA*PI/6.0)-1.0))*
     $ (SQRT((1.0+PROPS(1)**2.0)/3.0)*COS(NTHETA*PI/6.0)+PROPS(1)*
     $ (TRIAX+1.0/3.0*SIN(NTHETA*PI/6.0))))**(-1.0/PROPS(5))
C IF THETA >=0, EPF=EPF1; IF THETA <0, EPF=EF2
      IF(NTHETA.GE.0.0d0) THEN
          EPF=EPF1
      ELSE IF(NTHETA.LT.0.0d0) THEN
          EPF=EPF2
      END IF

C IF MAX PRINCIPAL STRAIN IS USED AS FRACTURE STRAIN
C       FINDEX(1) = EPMAX/EPF

C IF PEEQ IS USED AS FRACTURE STRAIN
      FINDEX(1) = PEEQ/EPF


C NORMAL DIRECTION TO FRACTURE PLANE
C AN(KMAX,I),I=1,2,3-THE DIRECTION COSINES OF MAXIMUM PRINCIPAL DIRECTIONS
      DO K1=1, NDI
       FNORMAL(K1,1) = AE(KMAX,K1)
      END DO

C FOLLOWING SECTION WAS USED TO CHECK RESULTS USING CODE. THE RESULTS ARE PRINTED
OUT IN ABAQUS .MSG FILE
C AFTER CHECKING, THIS SECTION IS COMMENTED AND RESULTS ARE NOT PRINTED OUT
IN .MSG FILE.

!C DOUBLE CHECK MISES, PRESS VALUES
!       CALL SPRIND(STRESS,SP,AS,1,NDI,NSHR)
!       SPRESS=-1.0/3.0*(SP(1)+SP(2)+SP(3))
!       SMISES=SQRT(1.0/2.0*((SP(1)-SP(2))**2+(SP(2)-SP(3))**2+
!      $ (SP(1)-SP(3))**2))
!       SINV3=(27.0/2.0*(SP(1)+PRESS)*(SP(2)+PRESS)*(SP(3)+PRESS))
!      $ **(1.0/3.0)

!C PRINTING MESSAGES TO .MSG FILE
!       REALV(1)= PROPS(1)
!       REALV(2)= PROPS(2)
!       REALV(3)= PROPS(3)
!       REALV(4)= PROPS(4)
!       REALV(5)= PROPS(5)
!       REALV(6)= MISES
!       REALV(7)= SMISES
!       REALV(8)= PRESS
!       REALV(9)= SPRESS
```

```
!       REALV(10)= INV3
!       REALV(11)= SINV3
!       REALV(12)= TRIAX
!       REALV(13)= NTHETA
!       REALV(14)= XI
!       REALV(15)= THETA
!       REALV(16)= THETA*57.2958
!
!       Call STDB_ABQERR(1,"C1=%R,C2=%R,C3=%R,C4=%R,N=%R,MISES=%R,
!      $ SMISES=%R,PRESS=%R,SPRESS=%R,INV3=%R,SINV3=%R,TRIAX=%R,
!      $ NETHETA=%R,XI=%R,THETA=%R,THETA(DEG)=%R",,REALV,)
!
!       Write (7,*) "PI=", PI
!       Write (7,*) "KMax =", KMAX
!       Write (7,*) "CALCULATED MMC FRACTURE STRAIN,EPF=", EPF
!       Write (7,*) "CALCULATED MMC FRACTURE STRAIN,EPF1=", EPF1
!       Write (7,*) "CALCULATED MMC FRACTURE STRAIN,EPF2=", EPF2
!       Write (7,*) "NUMERICAL FRACTURE STRAIN,EPMAX=", EPMAX
!       Write (7,*) "NUMERICAL FRACTURE STRAIN,PEEQ=", PEEQ
!       Write (7,*) "THREE PRINCIPAL STRAINS", EP
!       Write (7,*) "PEEQ=", PEEQ
!       Write (7,*) "NORMAL DIRECTION TO FRACTURE PLANE,FNORMAL=", FNORMAL
!       Write (7,*) "STRAIN ARRAY,AE(transpose)=", AE
!       Write (7,*) "STRAIN TENSOR=", STRAIN
!       Write (7,*) "THREE PRINCIPAL STRESS=", SP
!       Write (7,*) "STRESS TENSOR=", STRESS
!       Write (7,*) "STRESS ARRAY,AS(transpose)=", AS

!       Write (7,*) "CALCULATED MMC FRACTURE STRAIN,EPF=", EPF
!       Write (7,*) "NUMERICAL FRACTURE STRAIN,PEEQ=", PEEQ
!       Write (7,*) "NUMERICAL TRIAXIALITY PARAMETER=", TRIAX
!       Write (7,*) "NUMERICAL LODE ANGLE PARAMETER =", NTHETA

      RETURN
      END
```

Appendix B - CANMET-MTL Equations of J-integral for SENT specimen

This appendix summarize the equations of J-integral published by CANMET-MTL [63,91] for SENT specimens with H/W=10 and $0.1 \leq a/W \leq 0.7$. J-integral value is calculated at i_{th} unloading at instantaneous crack size $a_{(i)}$, crack mouth opening displacement $\mathrm{CMOD}_{(i)}$, and load $P_{(i)}$. The calibrated coefficients t_x (valid for $0.05 \leq a/W \leq 0.95$), ϕ_x (valid for $0.05 \leq a/W \leq 0.7$), Ψ_x (valid for $0.1 \leq a/W \leq 0.7$) and r_x (valid for $0.05 \leq a/W \leq 0.95$) are listed in Table B-*1*.

$$J_{(i)} = J_{el(i)} + J_{pl(i)} \tag{A-1}$$

$$J_{el(i)} = \frac{K_{(i)}^2 (1-\nu)^2}{E} \tag{A-2}$$

$$K_{(i)} = \left[\frac{P_{(i)}\sqrt{\pi a_{(i)}}}{(BB_N)^{1/2}W}\right] G\left(\frac{a_{(i)}}{W}\right) \tag{A-3}$$

$$G\left(\frac{a_{(i)}}{W}\right) = \sum_{x=1}^{12} t_x \left(\frac{a_{(i)}}{W}\right)^{x-1} \tag{A-4}$$

$$J_{pl(i)} = \left[J_{pl(i-1)} + \frac{\eta_{CMOD(i-1)}}{b_{(i-1)}} \frac{A_{pl(i)} - A_{pl(i-1)}}{B_N}\right]\left[1 - \frac{\gamma_{LLD(i-1)}(a_{(i)} - a_{(i-1)})}{b_{(i-1)}}\right] \tag{A-5}$$

$$\eta_{CMOD(i)} = \sum_{x=0}^{10} \phi_x \left(\frac{a_{(i)}}{W}\right)^x \tag{A-6}$$

$$\gamma_{LLD(i)} = \eta_{LLD(i)} - 1 - \left(1 - \frac{a_{(i)}}{W}\right)\frac{\eta'_{LLD(i)}}{\eta_{LLD(i)}} \tag{A-7}$$

$$\eta_{LLD(i)} = \sum_{x=0}^{10} \Psi_x \left(\frac{a_{(i)}}{W}\right)^x \tag{A-8}$$

$$\eta'_{LLD(i)} = \sum_{x=1}^{10} x\Psi_x \left(\frac{a_{(i)}}{W}\right)^{x-1} \quad \text{(A-9)}$$

$$A_{pl(i)} = A_{pl(i-1)} + \frac{\left[P_{(i)} + P_{(i-1)}\right]\left[CMOD_{pl(i)} + CMOD_{pl(i-1)}\right]}{2} \quad \text{(A-10)}$$

$$CMOD_{pl(i)} = CMOD_{(i)} - P_{(i)}C_{(i)} \quad \text{(A-11)}$$

Table B-1. Coefficients t_x, ϕ_x, Ψ_x used in J-integral equations published by CANMET-MTL for SENT specimens

x	0	1	2	3	4	5	6
t_x	-	1.197	-2.133	23.886	-69.051	100.462	-41.397
ϕ_x	1.000	-1.089	9.519	-48.572	109.225	-73.116	-77.984
Ψ_x	-0.880	15.190	-35.440	18.644	18.399	-1.273	-12.756
x	7	8	9	10	11	12	
t_x	-36.137	51.215	-6.607	-52.322	18.574	19.465	
ϕ_x	38.487	101.401	43.306	-110.770	-	-	
Ψ_x	-12.202	-4.447	5.397	14.187			

Appendix C - Results of X52 Full-scale Pipe Models With Fixed Maxpe Damage Criterion

This appendix includes numerical results of eight X52 full-scale pipe models with initial notch adopting the fixed damage criterion with Maxpe = 0.15 and G_c =200 N/mm.

Table C-1. Comparison between numerical and experimental results

Test or model	$CMOD_{critical}$ (mm)	Burst force (Max force) (kN)	Rotation at end plate at failure (°)	Tensile strain at 0° from crack at failure (%)		Reduction of wall thickness at failure (%)
				$\varepsilon_{0.5L}$	ε_{avg}	
Test 1	1.13	2284 (2299)	5.08	—	3	32.4
Model 1	1.15	2341 (2440)	4.78	2.84	3.12	20.2
Difference	+1.8%	+2.5% (+6.1%)	-5.9%	—	+4%	-12.2
Test 2	1.09	3100 (3109)	6.82	—	8	27.9
Model 2	1.18	3109 (3195)	6.11	7.60	7.59	19.7
Difference	+8.3%	+0.3% (+2.8%)	-10.4%	—	-5.1%	-8.2
Test 3	1.18	1623 (1664)	0.98	0.51	0.53	19.1
Model 3	1.09	1704 (1746)	0.80	0.43	0.43	13.8
Difference	-7.6%	+5.0% (+4.9%)	-18.4%	-15.7%	-18.9%	-5.3
Test 4	1.16	2061 (2075)	1.04	0.53	0.53	20.6
Model 4	1.04	2018 (2048)	0.86	0.45	0.46	11.9

Difference	-10.3%	-2.1% (-1.3%)	-17.3%	-15.1%	-13.2%	-8.7
Test 5	0.77	1934 (1962)	1.86	—	1.84	26.5
Model 5	0.91	1721(2018)	2.20	1.69	1.72	22.8
Difference	+18.1%	-11.0% (+2.8%)	+18.3%	—	-6.5%	-3.7
Test 6	0.90	2261 (2268)	1.40	1.20	1.32	27.9
Model 6	1.01	2095 (2258)	1.95	1.54	1.60	18.8
Difference	+12.2%	-7.3% (-0.4%)	+39.3%	+28.3%	+21.2%	-9.1
Test 7	0.90	1304 (1304)	0.26 (0.26)	0.21 (0.22)	0.22 (0.22)	19.1
Model 7 [a]	1.05	1203 (1346)	0.25 (0.22)	0.13 (0.17)	0.13 (0.17)	14.8
Difference	+16.7%	-7.7% (+3.2%)	-3.8% (-15.4%)	-38.1% (-19.0%)	-40.9% (-22.7%)	-4.3
Test 8	0.85	1831 (1844)	0.42 (0.41)	0.29 (0.30)	— (0.30)	20.6
Model 8 [a]	0.85	1623 (1811)	0.35 (0.31)	0.21 (0.26)	0.20 (0.25)	15.3
Difference	0%	-11.4% (-1.8%)	-16.3% (-24.4%)	-27.6% (-13.3%)	— (-16.7%)	-5.3

[a] in tests 7 and 8, the values in parentheses referred to the maximum force level.

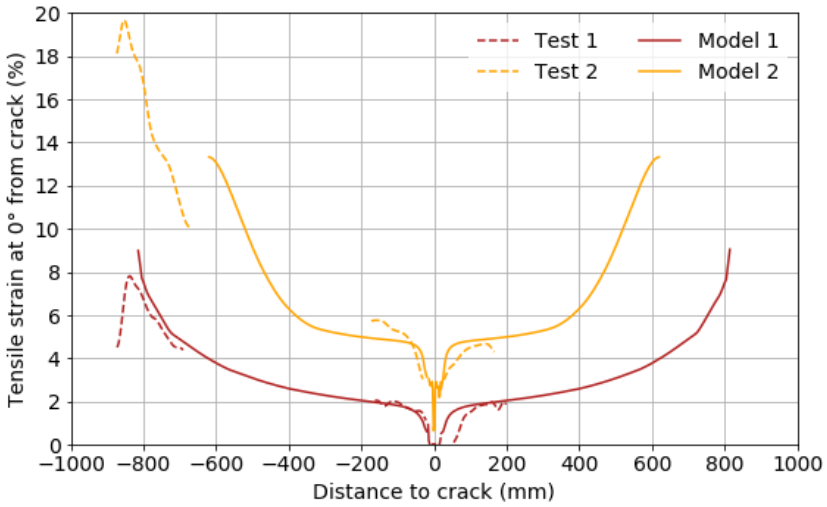

(a)

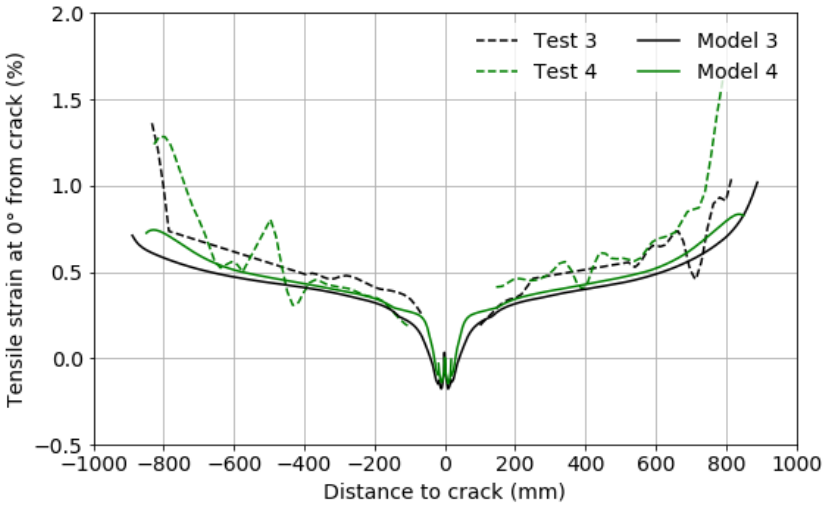

(b)

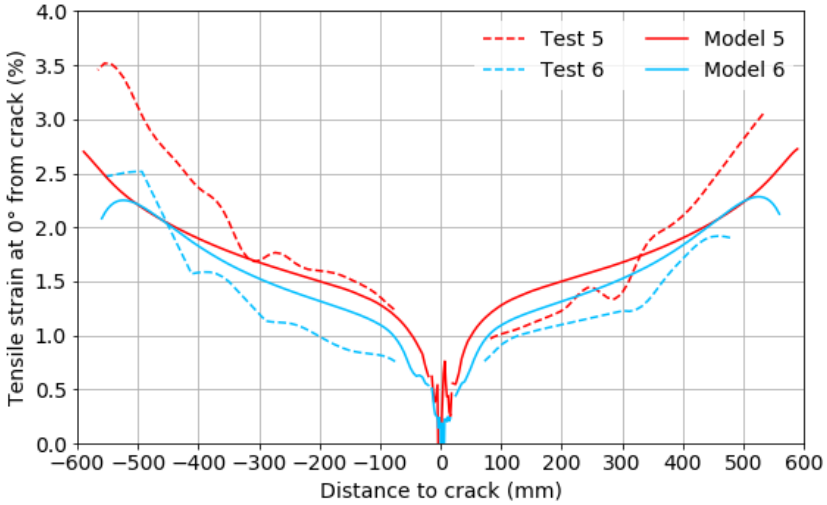

(c)

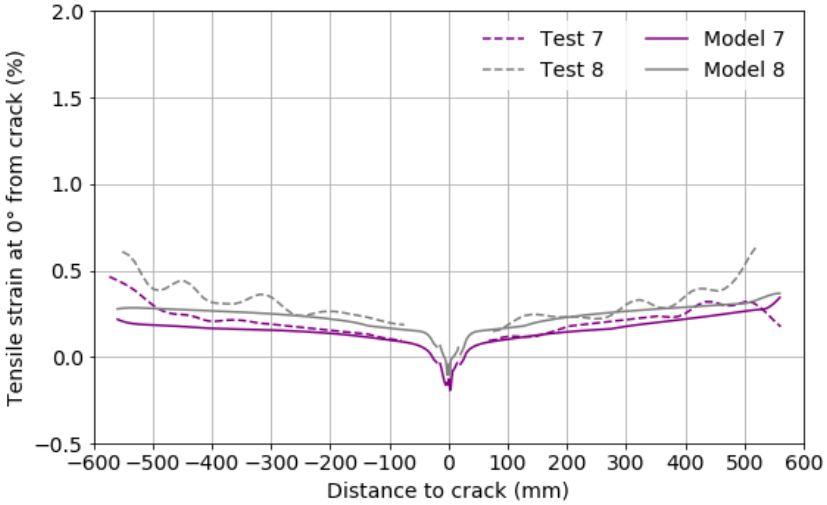

(d)

Figure C-1. Comparison of tensile strains along the pipe length from Models and Tests (a) 1-2; (b) 3-4; (c) 5-6; and (d) 7-8.

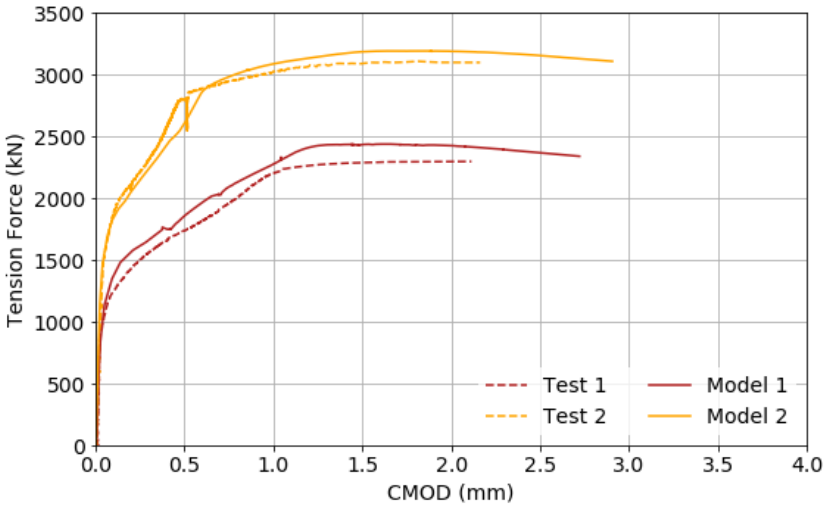

(a)

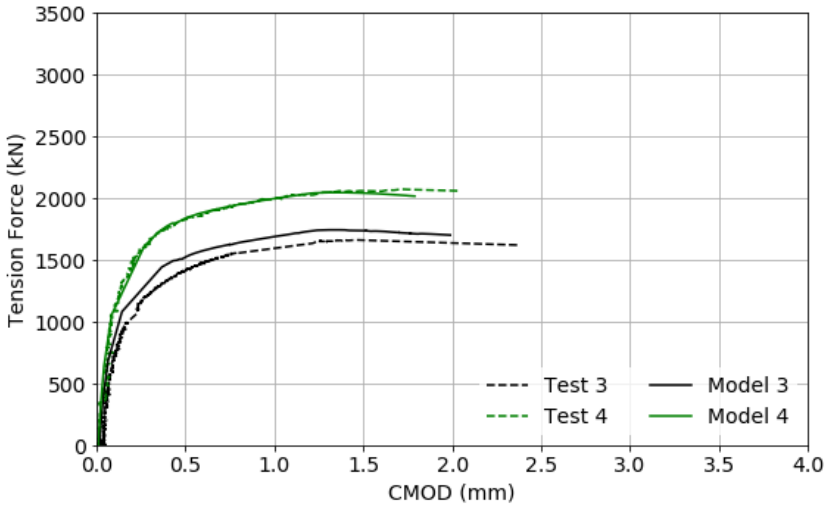

(b)

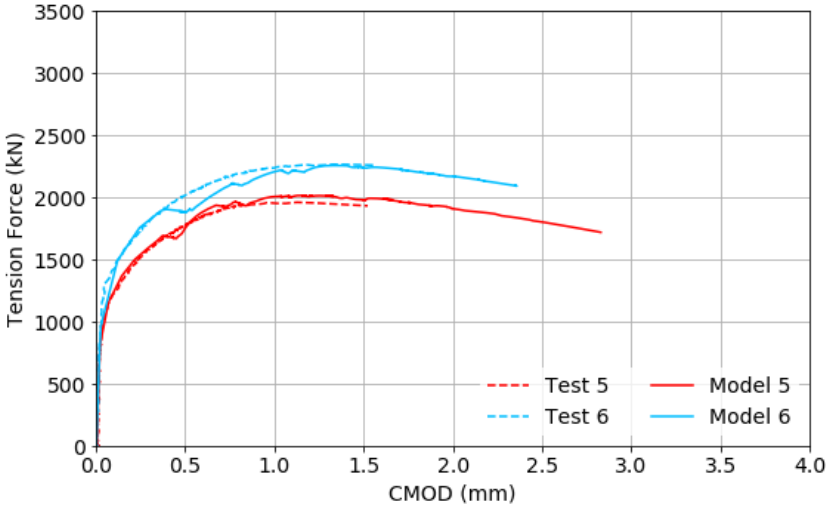

(c)

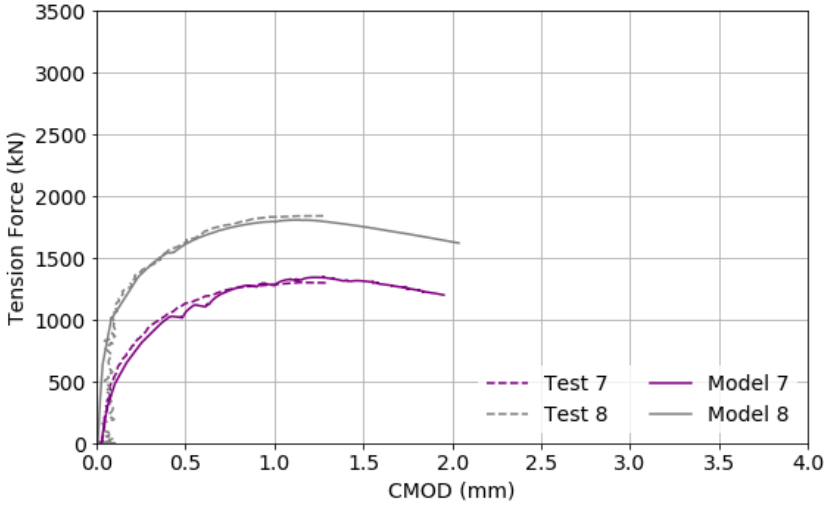

(d)

Figure C-2. Comparison of force-CMOD curves Models and Tests (a) 1-2; (b) 3-4; (c) 5-6; and (d) 7-8.

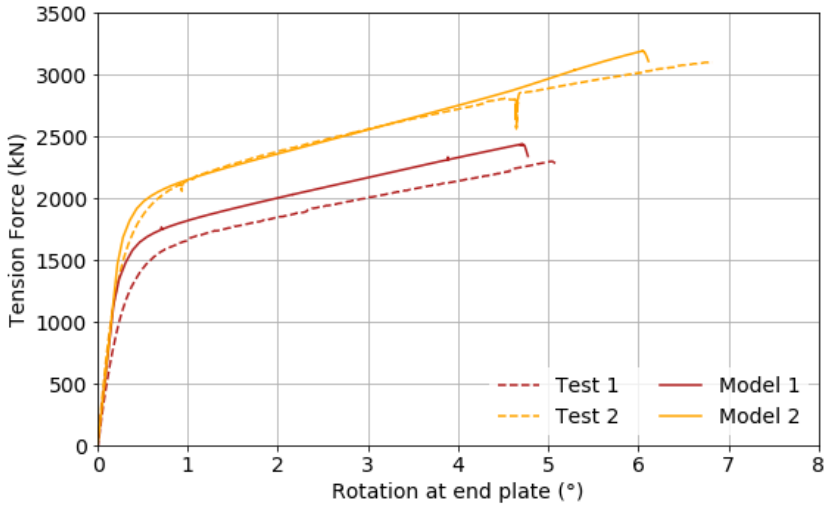

(a)

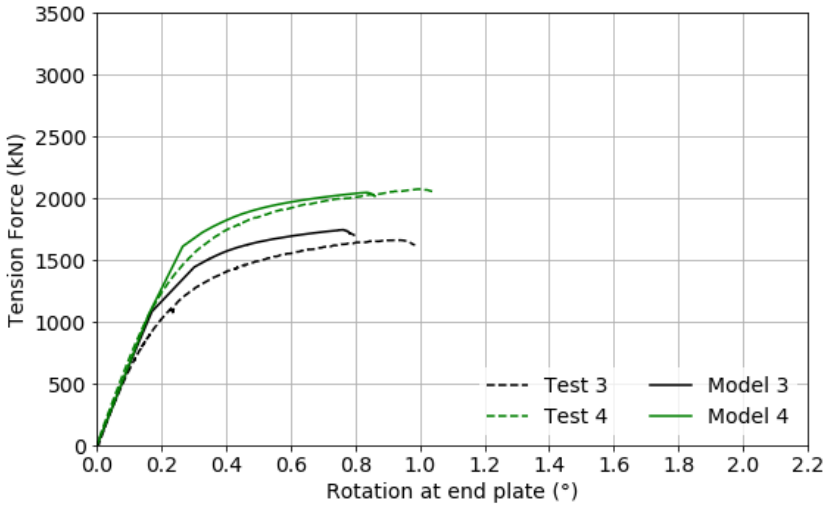

(b)

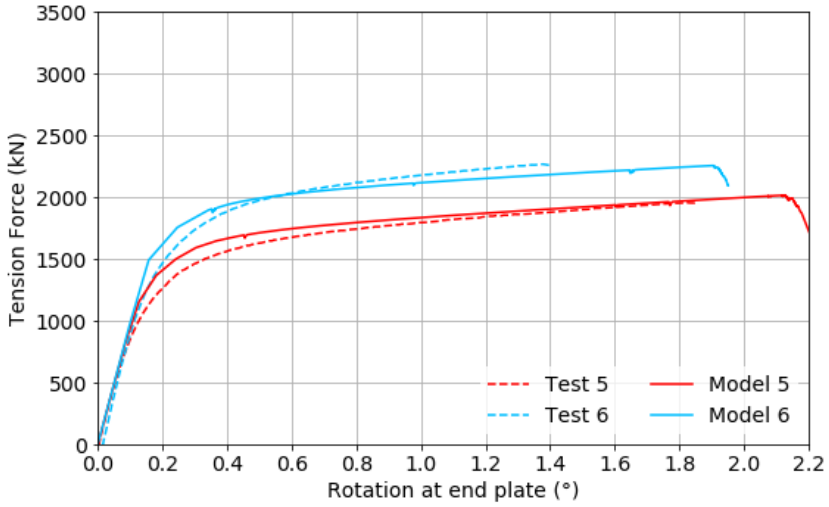

(c)

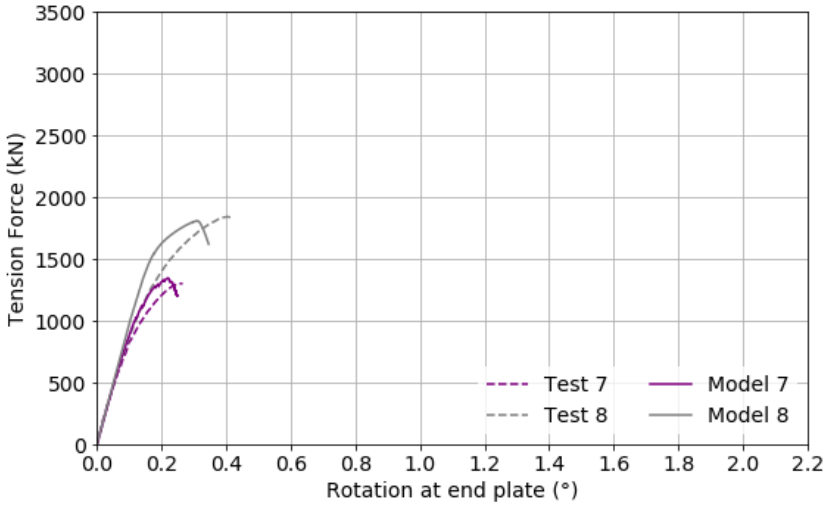

(d)

Figure C-3. Comparison of force-rotation curves from Models and Tests (a) 1-2; (b) 3-4; (c) 5-6; and (d) 7-8.

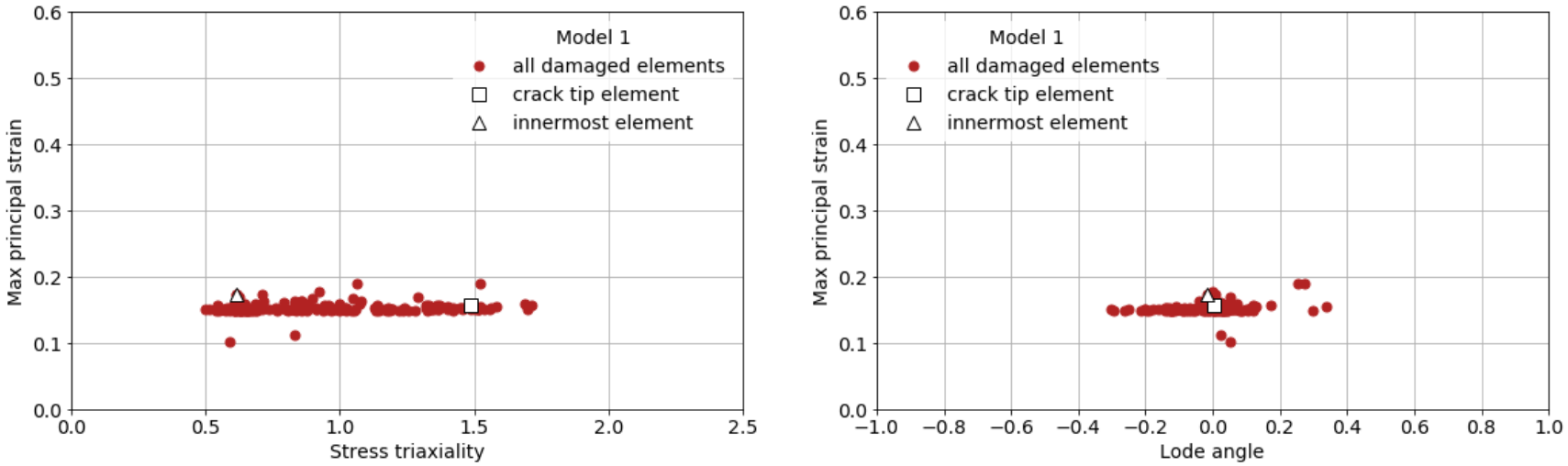
Model 1
all damaged elements
crack tip element
innermost element
Max principal strain
Stress triaxiality
Lode angle

(a)

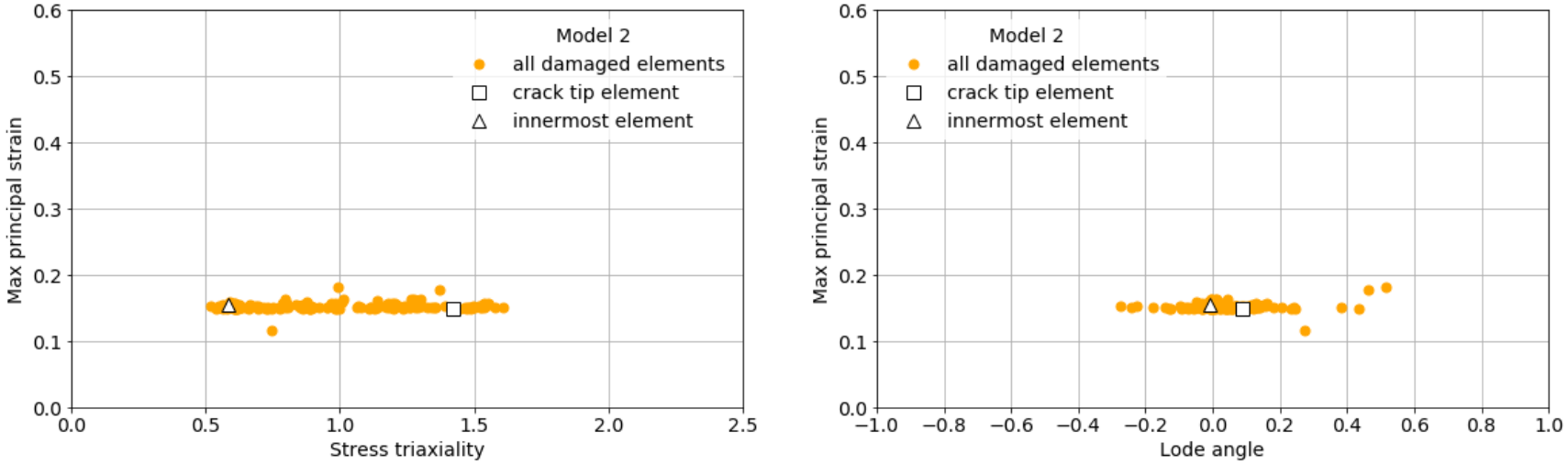
Model 2
all damaged elements
crack tip element
innermost element
Max principal strain
Stress triaxiality
Lode angle

(b)

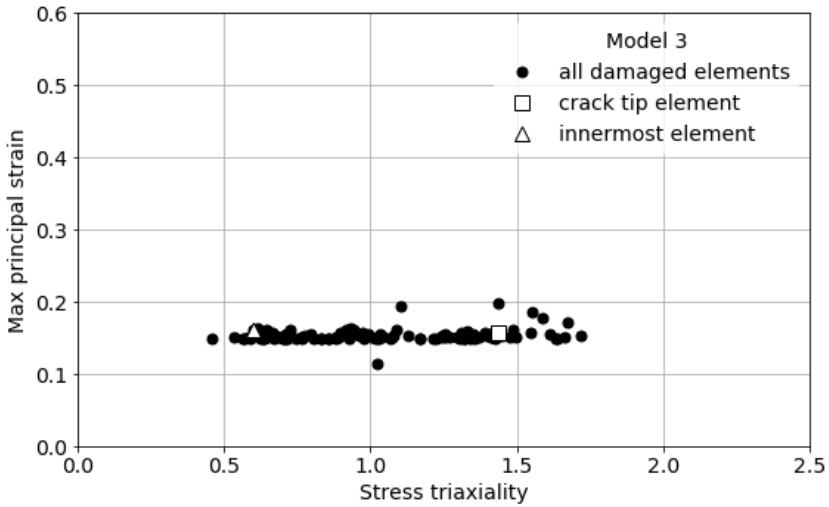
Model 3
all damaged elements
crack tip element
innermost element
Max principal strain
Stress triaxiality
0.0
0.1
0.2
0.3
0.4
0.5
0.6
0.0
0.5
1.0
1.5
2.0
2.5

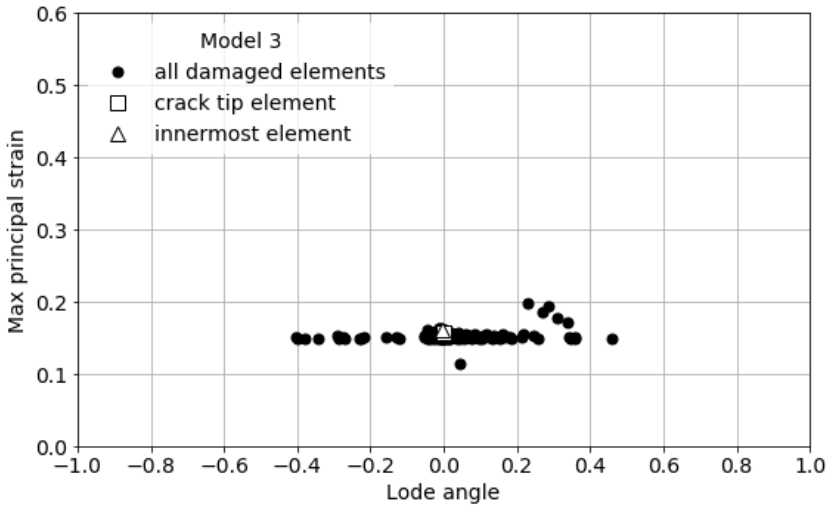
Model 3
all damaged elements
crack tip element
innermost element
Max principal strain
Lode angle
0.0
0.1
0.2
0.3
0.4
0.5
0.6
−1.0
−0.8
−0.6
−0.4
−0.2
0.0
0.2
0.4
0.6
0.8
1.0

(c)

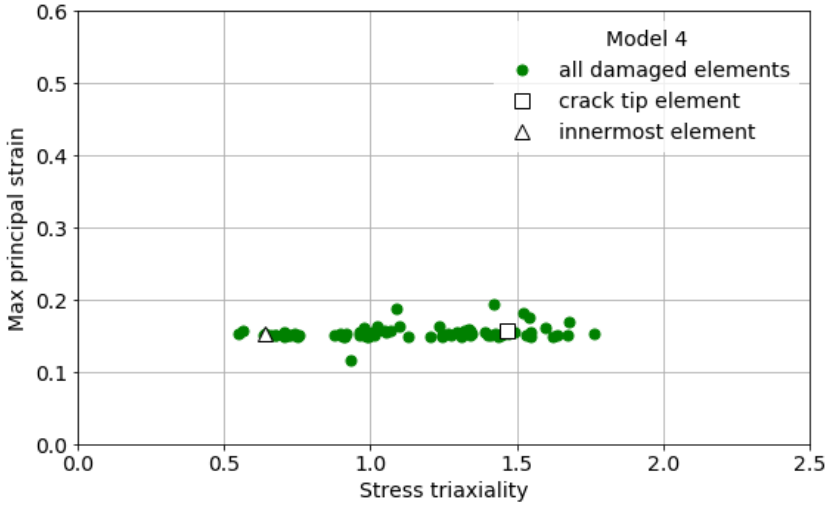
Model 4
all damaged elements
crack tip element
innermost element
Max principal strain
Stress triaxiality
0.0
0.1
0.2
0.3
0.4
0.5
0.6
0.0
0.5
1.0
1.5
2.0
2.5

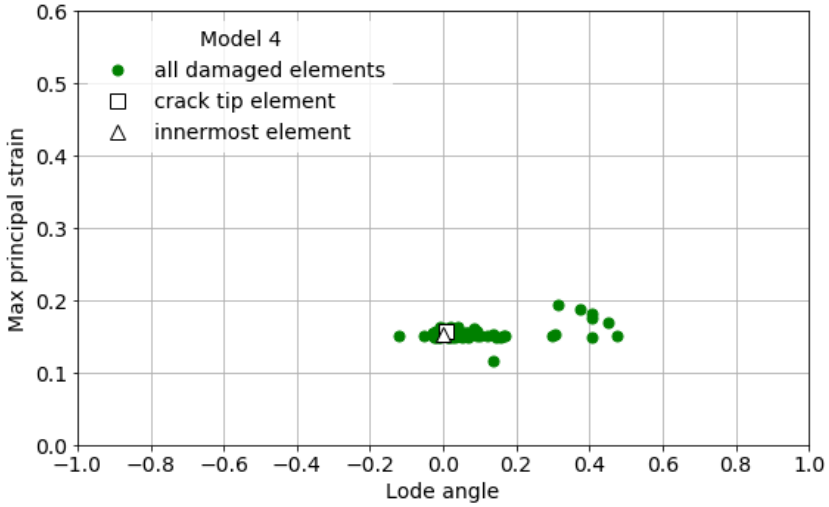
Model 4
all damaged elements
crack tip element
innermost element
Max principal strain
Lode angle
0.0
0.1
0.2
0.3
0.4
0.5
0.6
−1.0
−0.8
−0.6
−0.4
−0.2
0.0
0.2
0.4
0.6
0.8
1.0

(d)

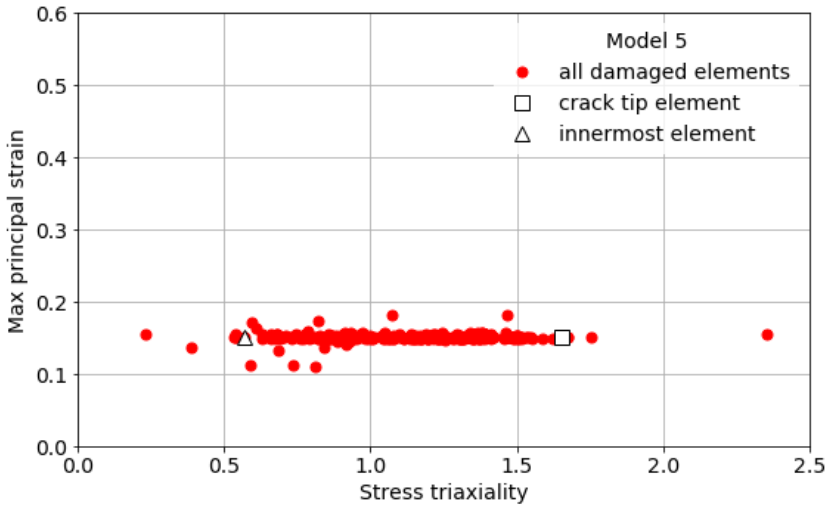
Model 5
all damaged elements
crack tip element
innermost element
Max principal strain
Stress triaxiality
0.0
0.1
0.2
0.3
0.4
0.5
0.6
0.0
0.5
1.0
1.5
2.0
2.5

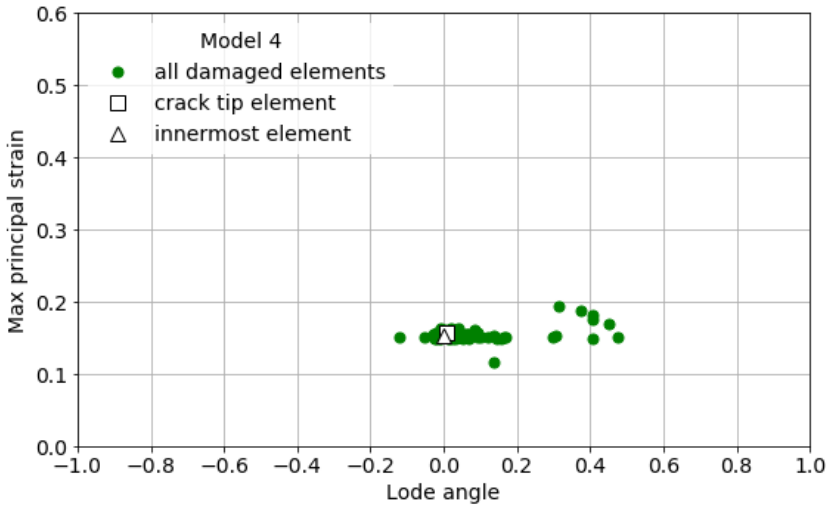
Model 4
all damaged elements
crack tip element
innermost element
Max principal strain
Lode angle
0.0
0.1
0.2
0.3
0.4
0.5
0.6
−1.0
−0.8
−0.6
−0.4
−0.2
0.0
0.2
0.4
0.6
0.8
1.0

(e)

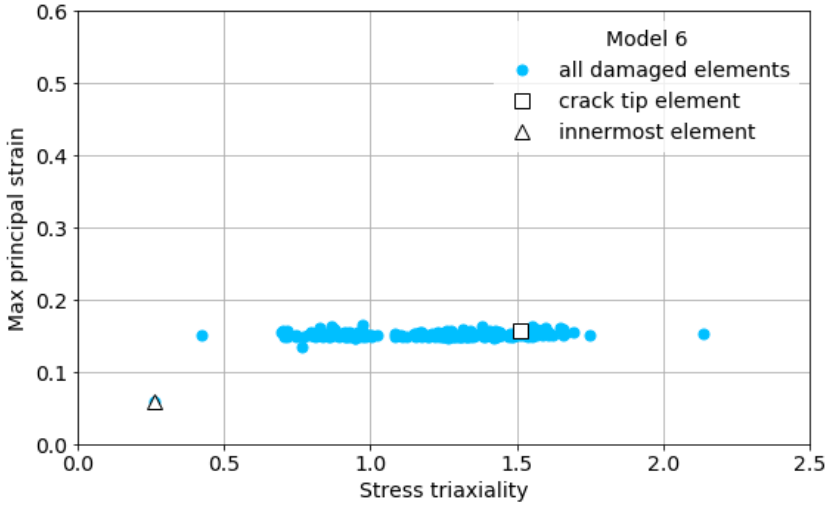
Model 6
all damaged elements
crack tip element
innermost element
Max principal strain
Stress triaxiality
0.0
0.1
0.2
0.3
0.4
0.5
0.6
0.0
0.5
1.0
1.5
2.0
2.5

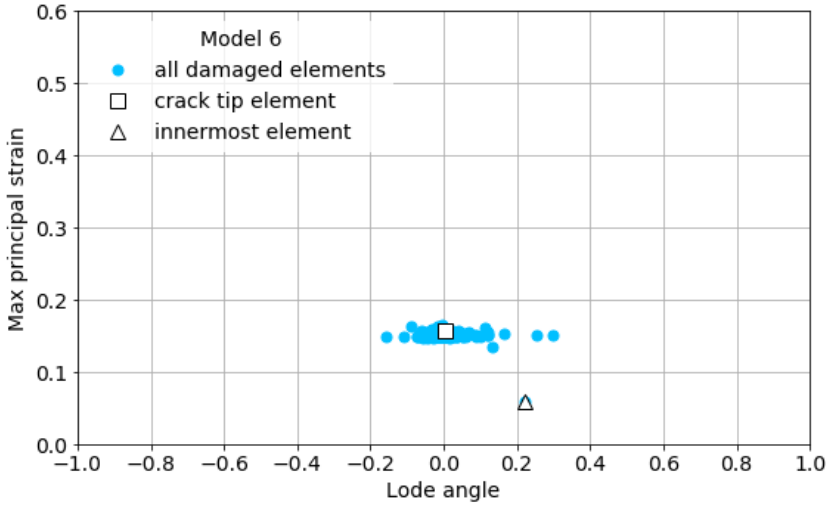
Model 6
all damaged elements
crack tip element
innermost element
Max principal strain
Lode angle
0.0
0.1
0.2
0.3
0.4
0.5
0.6
−1.0
−0.8
−0.6
−0.4
−0.2
0.0
0.2
0.4
0.6
0.8
1.0

(f)

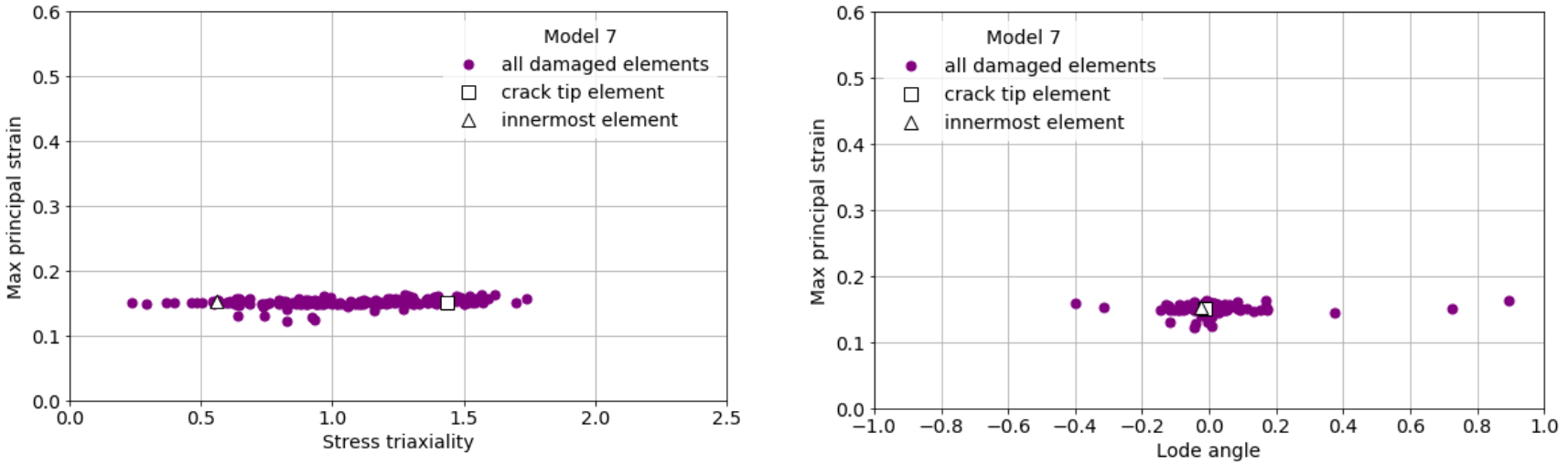

(g)

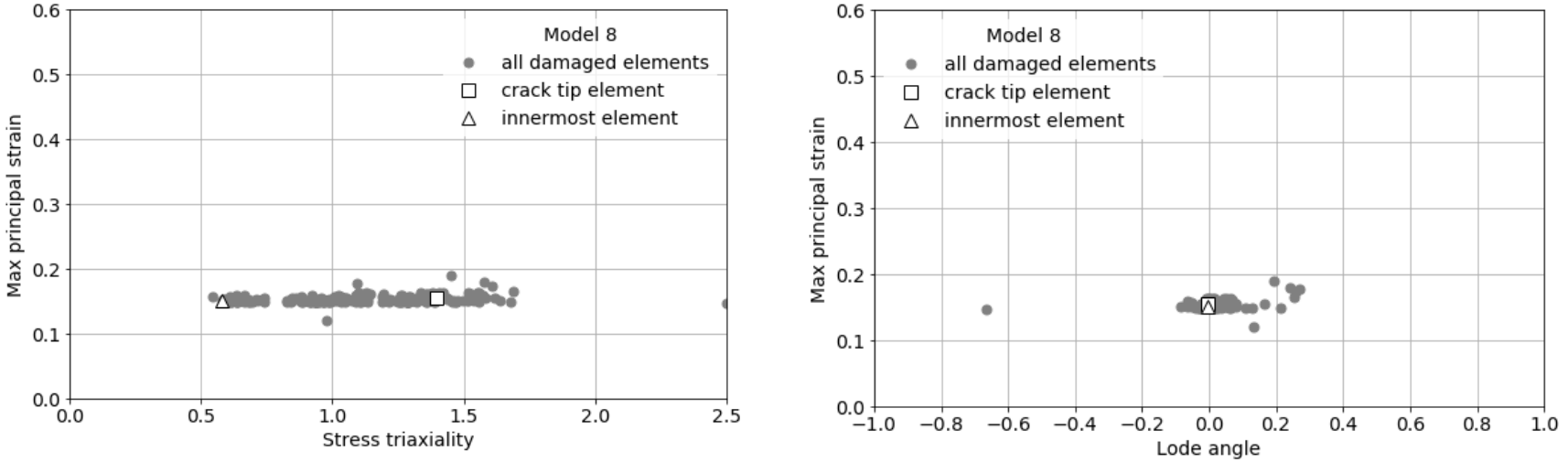

(h)

Figure C-4. Damage locus from Model (a) 1; (b) 2; (c) 3; (d) 4; (e) 5; (f) 6; (g) 7; and (h) 8.